AN INVESTIGATION OF THE CONDUCTIVITY OF PEPTIDE NANOSTRUCTURED HYDROGELS VIA MOLECULAR SELF-ASSEMBLY

A thesis submitted to The University of Manchester for the degree of

Doctor of Philosophy

in the Faculty of Engineering and Physical Sciences

2011

HAIXIA XU

School of Materials

TABLE OF CONTENTS

TABLE OF CONTENTS..... 2

LIST OF TABLES……..... 6

LIST OF FIGURES…… 7

LIST OF ABBREVIATIONS..... 14

ABSTRACT……..... 18

DECLARATION……..... 20

COPYRIGHT…….. 20

ACKNOWLEDGEMENTS..... 21

THE AUTHOR……..... 22

CHAPTER 1 INTRODUCTION 23

1.1 OVERVIEW..... 23

1.2 AIMS……..... 24

1.3 OUTLINE OF THESIS..... 25

1.4 REFERENCES:..... 26

CHAPTER 2 LITERATURE REVIEW..... 28

2.1 INTRODUCTION..... 28

2.2 PEPTIDES NANOSTRUCTURES..... 29

2.2.1 Background of Self-assembly..... 29

2.2.2 The building blocks of peptides 29

2.2.3 Peptide self-assembly 32

2.2.4 Self-assembling systems based on peptides 33

2.2.5 Systems based on peptide amphiphiles 35

2.3 CONTROL OF SELF-ASSEMBLY BY ENZYMES 43

2.3.1 Enzyme triggered assembly via hydrolysis..... 44

2.3.2 Enzyme assisted assembly by condensation 46

2.4 SUPRAMOLECULAR ELECTRONICS..... 49

2.4.1 π-electronic nanostructures from organic building block 49
2.4.2 DNA based electronics 53
2.4.3 Peptides in supramolecular electronics 54
2.5 ALIGNMENT OF SELF-ASSEMBLED PEPTIDE NANOSTRUCTURE 59
2.6 SUMMARY 64
2.7 REFERENCES: 66
CHAPTER 3 EXPERIMENTAL METHODS 75
3.1 MATERIALS AND METHODS 75
3.1.1 Suppliers 75
3.1.2 Synthesis 75
3.2 METHODS 76
3.2.1 Formation of the hydrogels 76
3.2.2 Characterization techniques 77
3.2.3 Background of electrical conductivity 82
3.3 REFERENCES: 92
CHAPTER 4 STRUCTURE AND CONDUCTIVE PROPERTIES OF FIBROUS NETWORKS PRODUCED BY ENZYME TRIGGERED SELF-ASSEMBLY 94
4.1 INTRODUCTION 94
4.2 HYDROGELS 95
4.2.1 Formation of self assembled hydrogel via ester hydrolysis 95
4.2.2 Fmoc-XY 98
4.2.3 Fmoc-L_3 105
4.3 CONDUCTIVITY OF THE HYDROGEL FILMS 112
4.3.1 Current-Voltage (I-V) and impedance characterization 112
4.3.2 Conductivity of Fmoc-L_3 xerogel 122
4.4 CONDUCTIVITY ANALYSIS AND COMPARISON 132
4.5 CONCLUSIONS 142
4.6 REFERENCES 143

CHAPTER 5 ALIGNMENT OF SELF-ASSEMBLED PEPTIDE NANOTUBES 147

5.1 INTRODUCTION 147

5.2 ELECTROSPINNING 147

5.2.1 Introduction of electrospinning 147

5.2.2 Electrospinning using Fmoc-L_3(enz) mixed with PEO 149

5.3 ALIGNMENT OF FMOC-L_3 NANOTUBES ASSEMBLED UNDER A HIGH ELECTRIC FIELD……..... 152

5.3.1 Experiments 152

5.3.2 Fmoc-L_3 (pH) aligned at various electric field strengths..... 152

5.3.3 Alignment of Fmoc-L_3 (enz) nanotubes under various electric field strengths..... 153

5.4 CONCLUSIONS 158

5.5 REFERENCES 159

CHAPTER 6 CONCLUSIONS AND FUTURE WORK 161

6.1 SUMMARY..... 161

6.2 FUTURE WORK 163

APPENDICES…….. 165

A1 PEAKS OF WAXS DATA FROM BUFFER 165

A2 ELECTRONIC AND STRUCTURAL PROPERTIES OF NANOSTRUCTURES PRODUCED BY THERMOLYSIN ASSISTED SELF-ASSEMBLY 167

A2.1 INTRODUCTION 167

A2.2 Background to the self-assembly process 167

A2.3 NANOSTRUCTURES FROM FOUR DIFFERENT FMOC-PEPTIDE ESTERS .. 169

A2.3.1 Characterization of the nanostructures..... 169

A2.3.2 Dependence of structure on gelator and formation time 173

A2.3.3 Dependence of electrical properties on gelator and formation time 178

A2.3.4 Further investigation of Fmoc-SF-OMe nanosheets..... 181

A2.4 CONCLUSIONS..... 191

A2.5 REFERENCES 193

LIST OF TABLES

Table 2.1 Energy and distance of weak intermolecular forces 29

Table 4.1 Comparison of resistance of different films between DC and AC both in air and vacuum 121

Table 4.2 Comparison of resistance of organic and inorganic conductive nano-networks from the literature 121

Table 4.3 The λ_{onset}, and band gap (E_g) of hydrogel films from UV-Vis spectra 134

Table 4.4 Electrochemical properties of peptide films 136

Table 4.5 Activation energy values of Fmoc-LL, Fmoc-L_3, Fmoc-WL and Fmoc-YL from vacuum system 138

Table A.1 Peaks and their relative intensities from WAXS data of buffers 165

Table A.2 Nanostructures of Fmoc-XY-OMe 178

Table A.3 Summary of all films with conditions, structures and resistance 193

LIST OF FIGURES

Figure 2.1 Amino acid structures with their common name and one letter abbreviation used in peptide sequences. 31

Figure 2.2 a, A two-dimensional representation of the chemical structure of the peptide subunit (D or L refers to the amino acid chirality). 34

Figure 2.3 Schematic representation of various nanostructures formed by self-assembly of FF-based building blocks and their potential applications. 35

Figure 2.4 (A) Chemical structure of the peptide amphiphile, highlighting the five key structural features. 37

Figure 2.5 A. The molecular structures of the two compounds used for the formation of hydrogels and a schematic of the gelation process. 40

Figure 2.6 Molecular structure of Fluorenylmethoxycabornyl-diphenylalanine (Fmoc-FF) 41

Figure 2.7 Fmoc-peptides nanostructures produced by various groups....43

Figure 2.8 Free energy diagram for hydrolysis of Fmoc-peptide methyl esters by enzyme triggered self-assembly systems....45

Figure 2.9 Scheme of synthetic route and the structure of 5a....45

Figure 2.10 Diagram showing the free energy profile of enzyme-assisted self-assembly of peptide derivatives....47

Figure 2.11 Proposed mechanism and chemical structures of Fmoc-amino acids....49

Figure 2.12 To show the gap between molecular electronics and plastic electronics. 50

Figure 2.13 Schematic representation of the concept of post-ROMP stabilization of self-assembled nanocoils and nanotubes from 1 (HBC). 51

Figure 2.14 A. Molecular structures and hypothetical OMARG-SHJ architecture Au-1-(2-3-)m(4-5-)n of POP-N initiator....52

Figure 2.15 Current-voltage curves measured at room temperature on a DNA molecule trapped between two metal nanoelectrodes. 54

Figure 2.16 To show the first peptide nanotubes were developed in the 1990s by M. Reza Ghadiri. 55

Figure 2.17 a) Atomic force microscopy (AFM) image of reduced cyclic peptide absorbed on mica; 56

Figure 2.18 Depiction of PA self-assembly in the presence of EDOT monomer 57

Figure 2.19 Energy-minimized illustration of b-sheets and -stacks as helical twist sense along a model aggregate. 58

Figure 2.20 Schematic representation of the self-assembly of Fmoc-KK(NDI) into nanobelts.....59

Figure 2.21 Vertically aligned diphenylalanine-based nanotubes self-assembled into a peptide nanoforest.....61

Figure 2.22 Experimental scheme and cross-sectional electron micrographs showing the growth 62

Figure 2.23 Schema of the process to obtain alignment peptide nanofibres at magnetic field.....63

Figure 2.24 AFM topography images of the residues of droplets of HFIP water solution containing FF tubes,.....63

Figure 3.1 Schematic representation of the sample used to measure electrical resistivity. 80

Figure 3.2 Sample preparation for conductivity measurement.....80

Figure 3.3 a, Surface mapping curve of the scratched film, b, 3D micrograph of scratched film...81

Figure 3.4 Schematic representation of the apparatus of the apparatus used to measure electrical resistivity. 84

Figure 3.5 The various possible electron band structures in solids at 0 K. 85

Figure 3.6 Conductivity of three kinds of materials: conductor, semiconductor and insulator. 86

Figure 3.7 Diagrammatic sketch of the thin film.....87

Figure 3.8 An impedance vector diagram. 88

Figure 3.9 Nyquist and Bode plots for the impedance of ideal conductor. 89

Figure 3.10 Nyquist and Bode plots for the impedance of a perfect capacitor.....90

Figure 3.11 Schematic of (a) equivalent circuit, (b) Nyquist plot for a parallel RC circuit.....91

Figure 3.12 Nyquist and Bode plots for the impedance with a diffusion gradient between the electrodes 92

Figure 3.13 Nyquist and Bode plots for the impedance of an electrolyte measured with two

electrodes. 92

Figure 4.1 Fluorenylmethoxycarbonyl (Fmoc) -peptide building blocks, supramolecular structures 96

Figure 4.2 Schematic diagram of the proposed mechanism for Fmoc-peptide ester hydrolysis. The gelators....97

Figure 4.3 Formation of hydrogels by hydrolysis....97

Figure 4.4 HPLC Chromatograms 98

Figure 4.5 Fluorescence emission spectra of gels (20 mM) and suspension (20 mM). 99

Figure 4.6 FT-IR spectra of Fmoc-LL, Fmoc-WL, Fmoc-YL 100

Figure 4.7 FT-IR spectra of dried films of Fmoc-peptides gels prepared enzymatically.... 101

Figure 4.8 Fluorescence spectra of dried films prepared by enzymatic hydrolysis.... 102

Figure 4.9 Atomic force microscopy (AFM) images Fmoc-peptide hydrogel film.... 103

Figure 4.10 Analysis of X-ray Scattering of Fmoc-LL, Fmoc-YL and Fmoc-WL film on a silica surface. 104

Figure 4.11 Analysis of X-ray scattering of the dried phosphate, MOPS and HEPES buffer..... 105

Figure 4.12 Scanning Electro Microscopy (SEM) image of dried Fmoc-L_3 film on the glass slide prepared for electronic properties measurements.... 106

Figure 4.13 FT-IR spectra and Fluorescence emission spectra of Fmoc-L_3 dried films 106

Figure 4.14 Transmission electron micrographs of the tubular structures formed and tapping-mode AFM analysis of peptide nanotubes on mica.... 107

Figure 4.15 Structure of Fmoc-L_3 16-mer in TIP3P water after initial minimisation and equilibration. 108

Figure 4.16 schematic of a single Fmoc-L_3 molecular layer nanotube 109

Figure 4.17 Wide angle X-ray scattering (WAXS) data of dried Fmoc-L_3 (bottom line).... 109

Figure 4.18 Chemical structure of Fmoc-L_3 molecules with β-sheet and hydrogen bonding. 110

Figure 4.19 Distribution of β-sheet distances between the Fmoc-L_3 molecules and π-π stacking distances between Fmoc residues. 111

Figure 4.20 Current versus voltage characteristics of the peptide films at a scan rate of 500 mV/s 113

Figure 4.21 Impedance spectroscopy and fitted curves of the Fmoc-peptide-ester films in air.. 115

Figure 4.22 Impedance spectroscopy and fitted curves of the hydrogels films in air 116

Figure 4.23 Equivalent circuits for Fmoc-L_3 film and Fmoc-L_3-OMe (a) in air; (b) in vacuum 116

Figure 4.24 Impedance spectroscopy and fitted curves of Fmoc-peptide-ester films under vacuum condition..... 117

Figure 4.25 Impedance spectroscopy and fitted curves of the hydrogels films under vacuum condition..... 118

Figure 4.26 Complex impedance plot data of blank glass. 119

Figure 4.27 Impedance spectra and fitted data of peptide films (Fmoc-LL, Fmoc-L_3, Fmoc-WL and Fmoc-YL)..... 120

Figure 4.28 Impedance spectroscopy measurements and fitted data of the peptide networks.. 123

Figure 4.29 a, Impedance spectra of Fmoc-L_3 film at different vacuum time from 1 to 15 following vacuum time increasing,..... 124

Figure 4.30 Complex impedance plot data (frequency ranged from 0.1 to 107 HZ) for Fmoc-L_3 film..... 124

Figure 4.31 Sheet resistance of the peptide networks as a function of amount of Fmoc-L_3-OMe 125

Figure 4.32 Impedance spectra of Fmoc-L_3 samples prepared by the same methods in air and vacuum. 126

Figure 4.33 Impedance spectra of Fmoc-L_3 samples prepared on a big glass slide in air and vacuum. 126

Figure 4.34 Impedance spectra of Fmoc-L_3 film at different relative humidity, fitted data and equivalent circuits (inset). 128

Figure 4.35 Equivalent circuits for Fmoc-L_3 film at high relative humidity (over 78.6%)..... 129

Figure 4.36 Impedance spectra of Fmoc-L_3 hydrogel 130

Figure 4.37 Resistance of Fmoc-L_3 dried film in varied relative humidity that was controlled by

saturated salt solutions and resistance of Fmoc-L_3 hydrogel. 130

Figure 4.38 Transmission electron micrographs (TEM) image of peptide Fmoc-L_3 based on pH 131

Figure 4.39 Tapping mode AFM analysis of Fmoc-L_3 network which based on pH..... 132

Figure 4.40 Complex impedance plot data (frequency ranged from 0.1 to 107 HZ) for Fmoc-L_3 pH film: a, in air, b, in vacuum..... 132

Figure 4.41 UV-Vis-NIR spectrum curves of films: Fmoc-LL, Fmoc-L_3, Fmoc-WL and Fmoc-YL134

Figure 4.42 Cyclic voltammograms of on platinum plate electrodes in acetonitrile 136

Figure 4.43 The temperature dependence of the current for the hydrogel films in vacuum system. 138

Figure 4.44 Plots of ln(I) versus 1/T: (a) heating up the sample; (b) cooling the samples 138

Figure 4.45 Currents changing at different environment at the same voltage at 3V..... 139

Figure 4.46 Impedance spectroscopy measurements of the hydrogels films at different days in air and vacuum. 141

Figure 4.47 Resistance comparisons between four samples (Fmoc-LL, Fmoc-L_3, Fmoc-WL and Fmoc-YL) at different times (a), in air, (b), in vacuum. 142

Figure 5.1 Schematic diagram of the electrospinning set up used to spin the Fmoc-L_3(enz) nanotubes. 148

Figure 5.2 A rotating cylinder collector which aligns the fibres along the rotating direction 149

Figure 5.3 Optical microscopy images of electrospun fibres 150

Figure 5.4 FT-IR spectra of Fmoc-L_3 xerogel, Fmoc-L_3 mixed with PEO (6%wt) 150

Figure 5.5 Optical images of aligned fibres of PEO (a) and Fmoc-L_3 blended with PEO (1.2% wt) by electrospinning 151

Figure 5.6 SEM images of Fmoc-L_3 mixed with PEO electrospinning fibres..... 151

Figure 5.7 Diagram of the high electronic field setup used to induce for alignment. 152

Figure 5.8 AFM images of Fmoc-L_3 (pH) 153

Figure 5.9 SEM images of Fmoc-L_3 (enz): a, b, c: aligned under a 3.75 kV/cm electric field, d: random (no field). 154

Figure 5.10 Diagram of angle to calculate Herman's orientation function (f). 155

Figure 5.11 Distribution of angle Φ between electric field direction and nanotubes aligned in 3.75 kV/cm electric field. 155

Figure 5.12 Impedance spectra of three areas on the same Fmoc-L_3 (enz) film aligned at 3.75 KV/cm electronic field 156

Figure 5.13 Impedance spectra of Fmoc-L_3 (enz) film formed at various electronic field..... 156

Figure 5.14 SEM images of Fmoc-L_3 aligned at varied electric field: a, 0.25 kV/cm, b, 1.25 kV/cm, c, 2.5 kV/cm 157

Figure 5.15 Alignment degree f of the networks versus applied electric field strength..... 158

Figure 5.16 Resistances of the Fmoc-L_3 films parallel and perpendicular to the applied electric field 158

Figure A.1 (a) Reversible amide synthesis/hydrolysis catalysed by thermolysin and building blocks 169

Figure A.2 Cryo-TEM images of the hydrogel..... 171

Figure A.3 Taping-mode AFM images of the Fmoc-XY-OMe peptide nanostructures on mica.. 172

Figure A.4 Taping-mode AFM images and cross section 173

Figure A.5 Emission spectra monitored using photoluminescence spectroscopy characterization 174

Figure A.6 FT-IR spectra of Fmoc-SF-OMe, Fmoc-SL-OMe, Fmoc-TF-OMe and Fmoc-TL-OMe gel 175

Figure A.7 Analysis of Wide Angle X-ray Scattering (WAXS) of Fmoc-peptides and buffer film on a silica..... 176

Figure A.8 Molecular lengths and spacing found from WAXS data of a dried sample (Fmoc-SF-OMe)..... 177

Figure A.9 Schematic representing distorted ~ sheets after nanoribbons twisted. 177

Figure A.10 Complex impedance plot data of 100 µL hydrogel films which have spent different times under vacuum 180

Figure A.11 Comparison of resistance of films formed from hydrogel or suspension with 6 h

formation time 181

Figure A.12 SEM images of SF-0-Gel film 182

Figure A.13 SEM images of SF-20-Gel film 183

Figure A.14 SEM images of SF-20-Gel film 184

Figure A.15 SEM images of SF-55-Gel film 185

Figure A.16 Cross polarized optical microscopy images of SF-55-Gel film in reflectance. 187

Figure A.17 SEM images of SF-55-Gel film 187

Figure A.18 Diagram of spherulite formation process from mixed solution to Fmoc-SF-OMe, to nanosheets and nanoribbons, to spherulite 188

Figure A.19 Impedance plot of film SF-0-Gel, SF-20-Gel and SF-55-Gel from 50 μL suspension. 188

Figure A.20 Resistances of a series of films SF-0-Gel, SF-20-Gel and SF-55-Gel from suspension 189

Figure A.21 SEM images of film SF-20-Sol 190

Figure A.22 Diagram of the formation process of the film from mixed solution directly. 190

Figure A.23 Impedance plot of a film made from 50 μL volume mixed solution of SF-20-Sol. .. 191

Figure A.24 Comparison of resistance between film SF-20-Gel and SF-20-sol. 191

LIST OF ABBREVIATIONS

The following abbreviations and acronyms have been used:

General:

1-D	One-dimensional
AFM	Atomic Force Microscopy
CV	Cyclic Voltammetry
$CaCl_2$	Calcium chloride
DNA	Deoxyribose nucleic acid
EIS	Electrochemical Impedance Spectroscopy
Fmoc	N-(fluorenyl-9-methoxycarbonyl)
Fmoc-LL	N-(fluorenyl-9-methoxycarbonyl)-Leucine-Leucine
Fmoc-LL-OMe	N-(fluorenyl-9-methoxycarbonyl)-Leucine-Leucine methyl ester
Fmoc-L_3	N-(fluorenyl-9-methoxycarbonyl)-Leucine-Leucine-Leucine
Fmoc-L_3-OMe	N-(fluorenyl-9-methoxycarbonyl)-Leucine-Leucine-Leucine methyl ester
Fmoc-YL	N-(fluorenyl-9-methoxycarbonyl)- Tyrosine-Leucine-Leucine
Fmoc-YL-OMe	N-(fluorenyl-9-methoxycarbonyl)-Tyrosine-Leucine-Leucine methyl ester
Fmoc-WL	N-(fluorenyl-9-methoxycarbonyl)-Tryptophan-Leucine-Leucine
Fmoc-WL-OMe	N-(fluorenyl-9-methoxycarbonyl)-Tryptophan-Leucine-Leucine methyl ester
Fmoc-SF-OMe	N-(fluorenyl-9-methoxycarbonyl)-Serine- Phenylalanine methyl ester
Fmoc-TF-OMe	N-(fluorenyl-9-methoxycarbonyl)- Threonine- Phenylalanine methyl ester
Fmoc-SL-OMe	N-(fluorenyl-9-methoxycarbonyl)- Serine-Leucine methyl ester
Fmoc-TL-OMe	N-(fluorenyl-9-methoxycarbonyl)-Threonine-Leucine methyl ester
FT-IR	Fourier transform infra-red
HCl	hydrochloric acid
HEPES	4-(2-hydroxyethyl)-1-piperazineethanesulfonic acid
HFPIP	1,1,1,3,3,3-hexafluoro-2-propanol
HOMO	highest occupied molecular orbital

HPLC	High Performance liquid chromatography
I-V	current-voltage
KCl	potassium chloride
KNO_3	potassium nitrate
LiCl	lithium chloride
LUOM	lowest unoccupied molecular orbital
MOPS	3-(N-morpholino)propanesulfonic acid
MD	molecular dynamics
$MgCl_2$	magnesium
NaOH	sodium hydroxide
NaCl	sodium chloride
NDI	naphthalenediimide
PA	peptide amphiphile
PEO	polyethylene oxide
PEG	poly-(ethylene glycol)
PNTs	peptide nanotubes
RH	relative humidity
RGD	Arginine-Glycine-Aspartic acid
SA	self-assembly
SEM	Scanning Electron Microscopy
TEM	Transmission Electron Microscopy
UV-Vis	Ultraviolet and Visible spectroscopies
WAXS	Wide angle X-ray scattering

Aromatic group:

F	fluorene
P	pyrene
N	(Nap) naphthalene

Amino acid:

A	Alanine
R	Arginine
D	Aspartic acid
E	Glutamic acid
Q	Glutamine
G	Glycine
L	Leucine
K	Lysine
F	Phenylalanine
S	Serine
W	Tryptophan
Y	Tyrosine
V	Valine

Notation:

c	speed of light
C	capacitance
E_f	Fermi level
E_g	optical band gap
$E_{g\text{-}ec}$	electrochemical band gap
E_{act}	activation energy
f	Frequency
G	Gibbs free energy
h	Planck constant
I	current
J	current density
R	Resistance
R_s	sheet resistance

T	temperature respectively
V	potential
Z’	real impedance
Z’’	imaginary impedance
|Z|	modulus of the impedance
σ	conductivity
ρ	intrinsic physical property
ε	electric field intensity
θ	phase angle
ω	angular frequency
λ	wavelength
υ	frequency of wave

ABSTRACT

Nanoscale, conductive wires fabricated from organic molecules have attracted considerable attention in recent years due to their anticipated applications in the next generation of optical and electronic devices. Such highly ordered 1D nanostructures could be made from a number of routes. One route of particular interest is to self-assemble the wires from biomolecules due to the wide range of assembly methods that can be adapted from nature. For example, biomolecules with aromatic motifs can be self-assembled so that good $\pi-\pi$ stacking is achieved in the resultant nanostructure. An additional advantage of using biomolecules is that it enables the interface of the electronic materials with biological systems, which is important for many applications, including nerve cell communication and artificial photosynthesis. In this study, nanowires were prepared by the molecular self-assembly of oligopeptides that were coupled to aromatic components. In order to achieve charge transport though the nanowires, it was imperative that the aromatic components were arranged so that there was $\pi-\pi$ stacking with very few structural defects. Therefore, enzymes were used to control the formation of the hydrogelators which subsequently self-assembled to produce nanowire networks. Two main systems were studied in this thesis.

In the first system, hydrogelators were produced from aromatic peptide amphiphiles via the enzymatic hydrolysis of the methyl ester of fluorenylmethoxycarbonyl (Fmoc)-di/tripeptides. These hydrogelators formed nanostructures due to π-π stacking between the Fmoc groups and H-bonding between the peptides. The nanostructures in turn produced macroscale gel networks. The nanostructures were analyzed by wide angle X-ray diffraction and fluorescence spectroscopy. A combination of Fourier transform infra-red (FTIR), Transmission Electron Microscopy (TEM), Cryo-TEM, and Atomic Force Microscopy (AFM) was used to characterize the networks. The charge transport properties of the dried networks were studied using impedance spectroscopy. Fmoc-L_3 was found to assemble into nanotubes whose walls consisted of 3 self-assembled layers and possessed inner and outer diameters of ~ 9 nm and ~ 18 nm, respectively. The Fmoc-L_3 networks were structurally stabile and were electronically conductive under a vacuum. The sheet

resistance of the peptide networks increased with relative humidity due to the increasing ionic conductivity. The resistance of the networks was 0.1 MΩ/sq in air and 500 MΩ/sq in vacuum (pressure: 1.03 mbar) at room temperature. The networks had a band gap of between 1 to 4 eV as measured by UV-Vis spectroscopy and the temperature-impedance studies.

Possible routes for aligning the Fmoc-L_3 networks were studied in an attempt to improve their conductivity in one direction. In particular, the peptides were assembled under an electric field (0 to 3.75 kV/cm). Random networks were produced at low field strengths, whereas a degree of alignment was obtained at a field strength of 3.75 kV/cm. The conductivity of the aligned networks in the direction of alignment was a factor of three times higher than that of the random networks.

The second system studied was Fmoc-dipeptide-OMe hydrogels produced by the enzymatic condensation of an Fmoc-amino acid and an amino acid ester. Preliminary results found that Fmoc-SF-OMe assembled into nanosheets, nanoribbons and spherulites, depending on the temperature at which self-assembly occurred. The Fmoc-XY-OMe films possessed an extremely high resistance (10^{12} Ω).

Keywords: self-assembly, peptide nanotubes, hydrogel, nanostructures, conductivity, alignment.

DECLARATION

Except where specific reference has been made to the work of others, this thesis is the result of my own work. No portion of the work referred to in the thesis has been submitted in support of an application for another degree or qualification of this or any other university or other institute of learning.

COPYRIGHT

ACKNOWLEDGEMENTS

Firstly, I would like to thank both of my supervisors for supervising my PhD project: Rein Ulijn for this opportunity to do PhD and entrusting me with this project, and Ian Kinloch for his time on my thesis and enthusiasm on my PhD project. I appreciate the opportunity Rein Ulijn offered me for international conferences which expanded my scope of scientific knowledge and inspired me. For the financial assistance, I would like to thank The Leverhulme Trust for funding this project.

I would like to thank John Walton, Alan Harvey, Judith Shackleton, Gary Harrison, Christopher Wilkins, Michael Faulkner and Polly Crook, for their assistance with AFM, TEM, WAXS, SEM, optical microscopy and FT-IR spectroscopy, respectively. I would also like to thank Stephen Furzeland and Derek Atkins in Unilever for Cryo-TEM help.

I would like to thank post-docs of the groups: Apurba Das, Andrew Smith, Majeed Shaik, Brian Cousins and Andrew Hirst for their advice and practical support. Among my colleagues and friends, I would like to thank the members of Ulijn Group, Kinloch Group, Young's Group and D4 office for contribution to such a nice work environment during these last three years.

There are a few special individuals I would like to thank Masaki from the University of Manchester Chemistry Department, for his generous help with electrochemistry and organic electronics. I would like to thank Ping Xiao and his PhD student Fan Yang from Materials Science in the University of Manchester for revolutionizing my understanding of impedance spectroscopy.

I appreciate the support from my family and friends. I would like to thank my husband Rui for his unfailing support and encouragement. I would also like to thank my parents and parents in law for their support and encouragement throughout my study.

Finally, my sincere thanks go to all who have supported me throughout this PhD project.

THE AUTHOR

Publications:

M. Hughes, **H. Xu**, P. Frederix, A. Smith, N. Hunt, T. Tuttle, I. Kinloch and R. V. Ulijn, *Biocatalytic self-assembly of 2D peptide nanostructures,* in preparation.

H. Xu, A. K. Das, M. Horie, M. S. Shaik, A. M. Smith, Y. Luo, X. Lu, R. Collins, S. Y. Liem, A. Song, P. L.A. Popelier, M. L. Turner, P. Xiao, I. A. Kinloch and R. V. Ulijn, *An investigation of the conductivity of peptide nanotube networks prepared by enzyme-triggered self-assembly*, Nanoscale, 2010, 2, 960-966.

Conference presentations:

Oral:

MRS (Materials Research Society) spring conference -- San Francisco (US), Apr. 2010

Poster:

RSC conference: Polymeric & Self-Assembling Hydrogels -- Manchester (UK), Oct. 2009

IUPAC Congress -- Glasgow (UK), Aug. 2009

MRS (Materials Research Society) -- China, Jun. 2008

CHAPTER 1 INTRODUCTION

1.1 OVERVIEW

The medical community have had a long term interest in protein aggregation as such aggregation causes many neurodegenerative diseases including Alzheimer's disease (AD) and Parkinson's disease. Within these diseases, β-sheet formation is known to drive the aggregation processes (e.g. the formation of fibrils from amyloids).[1] Recently, material scientists have also taken an interest in the self-assembly of peptides, where they have used the design rules established by the peptide community to formulate molecules which can self-assemble into nanostructures. Research interest in these peptide materials has increased rapidly due to their many potential applications including tissue engineering. One area of peptide science that is underdeveloped is the self-assembly of peptides with electronically active constituents to form nanowires. This area would be considered as part of the broader area of organic supramolecular electronics, where the self-assembly of π-conjugated materials has already attracted much attention for use in photovoltaic cells and field effect transistors. The ability to produce such nanowires using peptides both gives the opportunity to have more control over the self-assembly process and to design materials for the interface of electronics and biology.[2] For example, electronic substrates have been employed in the study of biological systems due to the prevalence of electrical signals in the function of heart muscle cells and neurons. Electrical stimulation can augment stem cell differentiation, as well as cell growth and organization.[3] It would also desirable to assemble oriented peptide nanostructures as this architecture may enable their integration into multi-array sensors, nano(electro)mechanic devices, nanofluidic devices,[4] optical devices and nanopatterning.[5]

A range of self-assembling peptide systems have been proposed and studied. Typically these systems use relatively long peptide sequences of 7 or more residues. Xu *et al.*[6] have shown that shorter peptide sequences can assemble into hydrogels when they are terminated with a Fmoc protecting group. There are two approaches which have been subsequently developed to self-

assemble the Fmoc-peptides; (i) hydrolysis of non-assembling precursors and (ii) condensation of precursor molecules. In both cases the reactions can be controlled by the use of enzymes to give more defined nanostructures. In this study, both routes were investigated with Fmoc-LL, Fmoc-WL, Fmoc-YL and Fmoc-L_3 produced from their corresponding methyl esters and Fmoc-SF-OMe, Fmoc-SL-OMe, Fmoc-TF-OMe, and Fmoc-TL-OMe were produced via bond formation from Fmoc-peptide and peptide-esters (Fmoc-S, Fmoc-T, F-OMe, and L-OMe).

In 1998, the electronic properties of self-assembled peptide nanotubes (composed of cyclic peptides) were studied by Mintmire *et al.* They confirmed that these structures were electronic insulators with a calculated band gap of 4.7 eV.[7] In 2007, Lewis *et al.* also found these cyclic peptide nanotubes were electronically insulating based upon electronic structure calculations.[8] In 2005, Ghadiri's group prepared D, L-α-peptides nanotubes bearing 1, 4, 5, 8-naphthalenetetracarboxylic acid diimide (NDI) side chains so that efficient overlap of the aromatic motifs in the structures could be achieved. Fluorescence spectra suggested that this approach had managed to partly overlap the π-orbitals to form an extended delocalised sytem.[9] In this project, the conductive properties of different types of self-assembled Fmoc-peptide nanostructures was studied. These studies were not only conducted using spectroscopy as in previous work, but also by electronic measurements.

1.2 AIMS

1. To prepare and characterise Fmoc-di/tripeptide hydrogels.

   i. To make hydrogels from Fmoc-LL, Fmoc-WL, Fmoc-YL and Fmoc-L_3 via enzyme triggered hydrolysis.

   ii. To conduct a preliminary study on the production of hydrogels from Fmoc-SF-OMe, Fmoc-SL-OMe, Fmoc-TF-OMe and Fmoc-TL-OMe via enzyme assisted reversed hydrolysis.

   iii. To study the structure of the hydrogels, including:

- Analysis of β-sheet formation and π–π stacking by fluorescence spectroscopy and FT-IR.
- Analysis of the morphology of the networks by transmission electron microscopy (TEM), cryogenic transmission electron microscopy (Cryo-TEM), scanning electron microscopy (SEM), atomic force microscopy (AFM) and optical microscopy.
- Study of the supramolecular structures by wide angle X-ray scattering (WAXS).
- Measurement of the electrical properties of the networks by electrochemical impedance spectroscopy (EIS), current-voltage studies (IV) and cyclic voltammetry (CV), ultraviolet and visible spectroscopy (UV-Vis).

2. To align the networks of the peptide nanotubes by:

1) Electrospinning
2) Assembly under an electric field.

1.3 OUTLINE OF THESIS

In Chapter 2, the literature on peptide nanostructures is discussed, including materials that are assembled from cyclic peptides, short aromatic peptides, aliphatic peptide amphiphiles and aromatic peptide amphiphiles. In particular, assembly routes via enzyme hydrolysis and condensation are reviewed. Furthermore, the progress of research into peptide and supramolecular electronics is discussed.

A guide to materials preparation and methodologies used in this study are introduced in Chapter 3.

Chapter 4 describes the enzyme hydrolysis system which uses Fmoc terminated amino acids and dipeptides to produce gelators. In this chapter, the hydrogels were formed by enzyme triggered

hydrolysis and the systems studied were Fmoc-LL, Fmoc-WL, Fmoc-YL and Fmoc-L_3. The β-sheet formation and π–π stacking in the nanostructures were studied by fluorescence, FT-IR spectra and WAXS. The nanostructures (i.e. nanotubes, nanofibres and nanospheres) were characterized by TEM, Cryo-TEM and AFM. The electronic properties of the nanostructured networks were measured using UV-Vis spectroscopy, EIS, IV studies and CV.

Chapter 5 studies two methods, electrospinning and assembly under an electric field, to align peptide nanotube networks with the aim of improving their electrical conductivity. It was found that the Fmoc-L_3 hydrogel could not be electrospun due to its low viscosity. However, alignment was achieved by assembling the gel under an electric field and the resultant anisotropy increased conductivity of peptide nanotubes networks by a factor of 3.

Chapter 6 presents the conclusions of the investigation and suggests further work which could be carried out to complete the study of the systems and bring it closer to application.

The appendix presents preliminary work on the enzyme reversed hydrolysis system. The systems studied were Fmoc-SF-OMe, Fmoc-SL-OMe, Fmoc-TF-OMe and Fmoc-TL-OMe. Cryo-TEM and AFM found that these systems self-assembled into nanostructures including nanosheets, nanoribbons and twisted nanoribbons. Fmoc-SF-OMe was studied in detail, since an unusually wide range of structures were found to be produced, depending on the conditions used.

1.4 REFERENCES:

1. E. H. Koo, P. T. Lansbury, Jr., J. W. Kelly, Amyloid diseases: Abnormal protein aggregation in neurodegeneration, Proc. Natl. Acad. Sci. USA, 1999, Vol. 96, 9989-9990.
2. H. Shao, T. Nguyen, N. C. Romano, D. A. Modarelli, J. R. Parquette, Self-assembly of 1-D n-type nanostructures based on naphthalene diimide-appended dipeptides, J. AM. CHEM. SOC. 2009, 131, 16374-16376.
3. D. A. Stone, L. Hsu, S. I. Stupp, Self-assembling quinquethiophene-oligopeptide hydrogelators, Soft Matter, 2009, 5, 1990-1993.

4. M. Reches, E. Gazit, Controlled patterning of aligned self-assembled peptide nanotubes, Nature Nanotechnology, 2006, Vol. 1, 195-200.
5. T. H. Han, J. Kim, J. S. Park, C. B. Park, H. Ihee, S. O. Kim, Liquid crystalline peptide nanowires, Adv. Mater. 2007, 19, 3924-3927.
6. Z. Yang, H. Gu, D. Fu, P. Gao, J. Kwok, B. Xu, Enzymatic formation of supramolecular hydrogels, Adv. Mater., 2004, No. 16, 1440-1444.
7. R. A. Jishi, N. C. Braier, C. T. White, J. W. Mintmire, Peptide nanotubes: An inert environment, The American Physical Society, 1998, 58, R16009-R16011.
8. R. Takahashi, H. Wang, J. P. Lewis, Electronic structures and conductivity in peptide nanotubes, J. Phys. Chem. B2007, 111, 9093-9098.
9. E. Gazit, Self-assembled peptide nanostructures: the design of molecular building blocks and their technological utilization, Chem. Soc. Rev., 2007, 36, 1263-1269.

CHAPTER 2 LITERATURE REVIEW

2.1 INTRODUCTION

Nanoscale, conductive wires fabricated by the self-assembly of organic molecules have attracted considerable attention in recent years due to their anticipated applications in the next generation of optical and (bio-) electronic devices.[1-3] Such highly ordered 1D nanostructures could be made from a number of routes. One route of particular interest is to assemble the wires from biomolecules due to the wide range of assembly methods that can be adapted from nature. For example, biomolecules with aromatic motifs can be self-assembled so that good π–π stacking is achieved in the resultant nanostructure. The construction of such biomolecular electronic nanostructures in aqueous environments remains a daunting challenge.[4] However, these nanostructures are of interest in a number of fields. For example, electrically conducting scaffolds are required for tissue growth due to the prevalence of electrical signals in the function of heart muscles cells and neurons. Furthermore, electrical signals are known to control lineage in stem cell differentiation, as well as controlling more general aspects of cell growth and organization.[5] Finally, the self-assembled π-conjugated nanostructures have attracted potential applications in organic electronic devices such as sensors, photovoltaic cells and field effect transistors.[6] For such applications, it would be desirable to orient the nanostructures as this architecture may enable their integration into multi-array sensors, nano(electro)mechanic devices, nanofluidic devices,[7] optical devices and nanopatterning.[8]

Peptide-based nanostructures are an intriguing approach to make nanowires because peptides are biocompatible, can be synthesized easily in large amounts, can be decorated with functional elements and can be used in various biological and non-biological applications.[9, 10] A detailed understanding of the electronic properties of peptide-based nanostructures is particularly important for biosensors and supramolecular devices.

2.2 PEPTIDES NANOSTRUCTURES

2.2.1 Background of Self-assembly

Molecular self-assembly is a key process in supramolecular chemistry. The molecules interact through the application of weak intermolecular forces, including hydrogen bonding, ionic interactions, van der Waals forces, π–π interactions, electrostatic interactions and hydrophobic and hydrophilic interactions (Table 2.1).[11-13] These weak interactions play a significant role in biology, but can also be exploited in supramolecular materials synthesis. Hydrogen bonds are formed between an electronegative atom or hydrogen acceptor (usually oxygen or nitrogen) and a hydrogen donor (generally hydrogen covalently linked to an electronegative atom)[14]. Ionic interactions occur between polar charged (or partially charged) groups: opposite and same charges attract and repel each other respectively. Van der Waals interactions exist between atoms which are in close proximity. In the case of interactions between aromatic groups, π electrons are involved and give rise to the π–π stacking of aromatic rings on top of each other. Therefore, due to the stacked arrangement of the aromatic moieties, this π–π interaction is highly directional.

Table 2.1 Energy and distance of weak intermolecular forces

Interaction	Energy (kJ/mol/bond)	Distance (Å)
electrostatic interactions	0.5-4	~7
hydrogen bonding	4-12	~2.8
hydrophobic effect	4-8	5~6
π–π stacking interaction	7.16	3.9

2.2.2 The building blocks of peptides

Amino acids are the basic components of peptides. There are twenty naturally occurring α amino acids which are relevant to the make-up of mammalian proteins, in principle complemented by an

infinite number of synthetic amino acids. The α amino acids in peptides and proteins (except proline) covalently bond one side to a carboxylic acid (-COOH) and bond the other side to an amino ($-NH_2$) functional group. The functional group is attached to the same tetrahedral carbon atom which is called the α carbon. Each of the 20 α amino acids (Figure 2.1) can be distinguished by the R-group substitution on the α carbon atom. Amino acids can be classified by whether the R-group is hydrophobic or hydrophilic. The hydrophobic amino acids tend to reside predominantly in the interior of proteins because they repel the aqueous environment. This type of amino acid does not ionize nor participate in the formation of H-bonds. The hydrophobic residues can be divided further into two subgroups: aliphatic residues and aromatic residues. The aliphatic residues provide a general hydrophobic environment whereas the aromatic residues can become involved in $\pi-\pi$ stacking. These aromatic interactions play an important structural role in DNA and are increasingly recognized as important interactions in protein and peptide folding. The hydrophilic amino acids are often involved in the formation of H-bonds due to the interaction with the aqueous environment. These hydrophilic amino acids are found predominantly on the exterior surfaces of proteins or in the reactive centres of enzymes. The hydrophilic uncharged residues can be involved in hydrogen bonding interactions.[15]

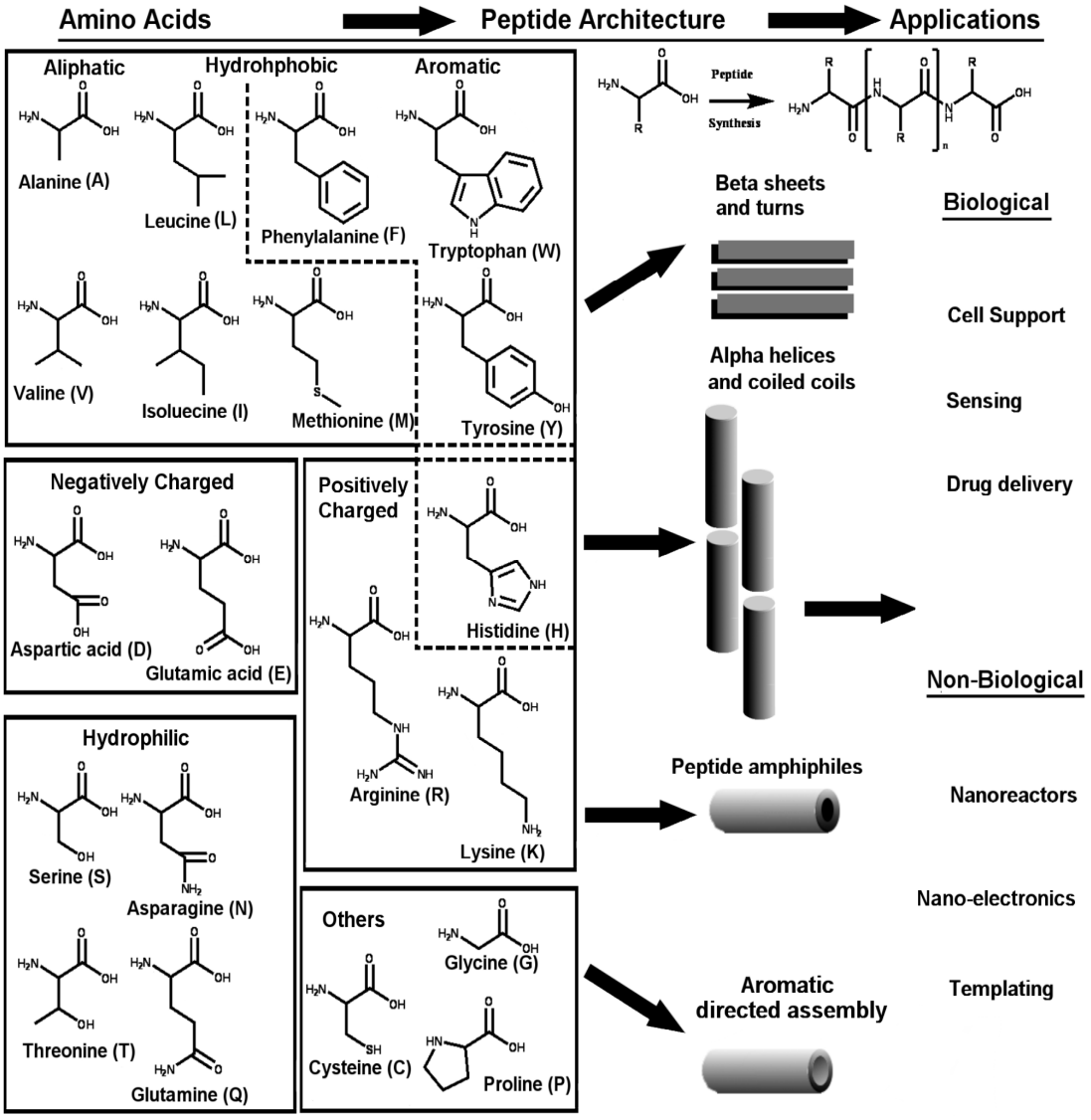

Figure 2.1 Amino acid structures with their common name and one letter abbreviation used in peptide sequences. The four main classes of possible architectures which peptides can form for potential applications [Adapted from 12].

The secondary structures of polypeptides have two main conformations: α-helices and β-sheets. The structure of an α-helix is a clockwise spiral that is stabilized by hydrogen bonding between the amide nitrogens (N-H) and carbonyl oxygens (C=O) spaced four residues apart on the same polypeptide chain. The helical coiling of the peptide backbone is oriented in such a way so that the R- group side chains are present on the helix exterior and perpendicular to its axis.[16] Unlike the single linear array of amino acids constituting the α-helices structure, β-sheets are composed

of extended regions of polypeptide chains by adopting either a parallel or anti-parallel alignment. In both cases, the alternate positioning of the α-carbon atom above and below the plane of the sheet suggests all β-sheet structures are pleated. However, similar to the α-helices, the stability of the β-sheet structure relies on the presence of hydrogen bonding between the amino and carbonyl groups of adjacent polypeptide chains.

2.2.3 Peptide self-assembly

In 1999, Hashimoto *et al*. found that α-synuclein had a potential role in the cause of synaptic damage and neurotoxicity via the formation of amyloid-like fibrils and mitochondrial dysfunction.[17] For example, α-synuclein might damage the mitochondrial membrane which could then promote aggregation. Hashimoto *et al*. confirmed later that α-synuclein is definitely a risk factor for familial Parkinson's disease (PD).[18] Neurodegenerative diseases, such as Alzheimer's disease (AD), Parkinson's disease (PD), Huntington's disease (HD), amyotrophic lateral sclerosis (ALS) and prion diseases, are now realized to have common cellular and molecular mechanisms including protein aggregation. The aggregates usually consist of fibres containing misfolded proteins with a β-sheet conformation, termed "amyloid".[19] These amyloid fibres are relevant to the design of the aromatic group containing self-assembly systems due to self-assembly process in the aggregation. Recently, material scientists have also taken an interest in the self-assembly of peptides, where they have used the design rules established by the peptide community to formulate controlled molecules which can self-assemble into nanostructures.

Since 1993, the self-assembly of peptides has emerged as a versatile method for creating nanomaterials.[20] Two general approaches have been developed. Firstly, peptide building blocks can be designed based upon an understanding of natural motifs. Secondly, amino acids may be exploited purely as chemical moieties to produce new structures which are not found in nature. As examples of the latter approach, nanofibrous hydrogels may be formed by the self-assembly of non-naturally occurring, β-amino acid derivatives.[21]

2.2.4 Self-assembling systems based on peptides

2.2.4.1 Peptide nanostructures from stacked cyclic peptides

The arrangement of a cyclic peptide assembled into a hollow tubular structure was suggested in 1974 on the basis of theoretical analysis.[22] The first peptide nanotubes were subsequently developed in 1993 by Ghadiri *et al.*[20] They designed an eight-residue cyclic peptide with the following sequence: cyclo[-(^{D}A-E-^{D}A-Q)$_2$-], in which the subunits can stack in an antiparallel fashion and participate in backbone-backbone intermolecular hydrogen bonding to produce a contiguous β-sheet structure (Figure 2.2). The design rule for these peptide nanotubes is that cyclic peptide structures are made up of an even number of alternating D- and L-amino acid residues. These residues can adopt a flat-ring conformation and stack, under favourable conditions, to provide a continuous, hydrogen-bonded, hollow tubular structure.[23] Peptide side chains must necessarily lie on the outside of the ensemble, thereby creating the desired hollow tubular core structure. This general strategy allows the design and synthesis of a wide range of tubular structures with specified internal diameters and surface chemistries. In 2003, Ghadiri *et al.*[24] tried to produce a heterocyclic peptide nanotube which had potential for molecular electronic applications. Ghadiri's group modified the cyclic D, L-α-peptides with aromatic motifs, as discussed in detail in section 2.4.3.1. In 2008, Liu *et al.* conduced molecular dynamical studies of the structures of the peptide nanotubes formed by the self-assembled of cyclo[(-D-Phe-L-Ala)$_{n=4}$-] and found that the average distance between the centres of neighbouring rings was 4.5 to 5.3 Å.[25]

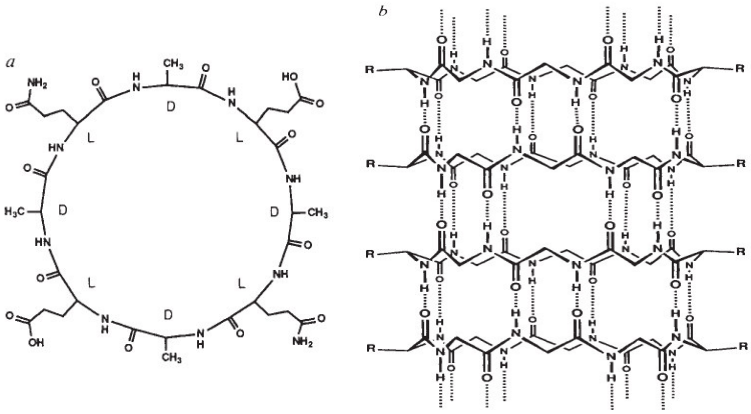

Figure 2.2 a, A two-dimensional representation of the chemical structure of the peptide subunit (D or L refers to the amino acid chirality). b, Peptide subunits are shown in a self-assembled tubular configuration emphasizing the antiparallel stacking and the extensive network of intermolecular hydrogen-bonding interaction (for clarity only backbone structure is represented) [Adapted from 25].

2.2.4.2 Peptide nanostructures from short aromatic peptides

The self-assembly of peptide nanostructures from short aromatic peptide building blocks emerged as a new approach for nanomaterial synthesis in 2003 and is now very commonly studied for a range of applications.[26] The interaction of these peptides is thought to be hydrophobic and largely driven by entropy. The geometrically restricted interactions between aromatic peptides allow them to obtain highly ordered structures whilst using very small building blocks. The most significant case of the self-assembly of such aromatic peptides is the formation of nanotubes by the diphenylalanine peptide. For example, peptide nanotubes based on FF were reported by Gazit's group in 2003.[27] Song *et al.* in 2004 investigated the formation and the structures of diphenylalanine peptide nanotubes. They also incorporated platinum nanoparticles into the nanotubes to form novel peptide-nanotube platinum-nanoparticle composites with a diameter of several tens of nanometers.[28] Furthermore, in 2009, Gazit's group demonstrated the self-assembly of a large array of diphenylalanine peptides using vapour deposition methods that will be introduced in detail in Section 2.5. Within the same year, their group studied the formation of planar nanostructures with β-sheet content from the triphenylalanine peptide (FFF). The FFF peptides self-assembled into plate-like nanostructures.[29] Recently, a variety of different supramolecular structures including nanotubes, vesicles, nanofibrils, ribbons, nanowires and

ordered molecular chains have been formed by the self-assembly of short di-phenylalanine (FF)-based peptides. These nanostructures are shown in Figure 2.3.[30]

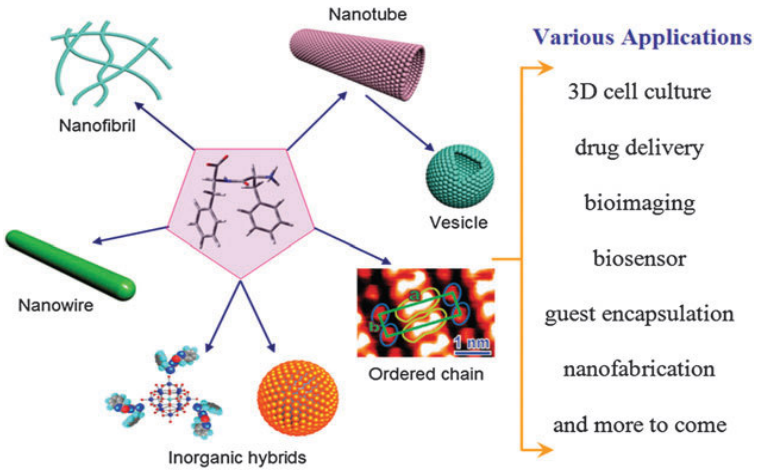

Figure 2.3 Schematic representation of various nanostructures formed by self-assembly of FF-based building blocks and their potential applications. [Adapted from 30].

2.2.5 Systems based on peptide amphiphiles

2.2.5.1 Aliphatic peptide amphiphiles

In 2001, Stupp's group reported the use of self-assembly, covalent capture and mineralization of a peptide-amphiphile (PA) to prepare a nanostructured composite material that recreates the structural orientation between collagen and hydroxy-apatite observed in bone.[31] An alkyl tail with 16 carbon atoms coupled to an ionic peptide was used to create an amphiphile that assembled into cylindrical micelles in water because of the amphiphile's overall conical shape. The alkyl tails would pack in the centre of the micelle leaving the peptide segments exposed to the aqueous environment. These cylindrical micelles can be viewed as fibres in which the chemistry of the peptide region is repetitively displayed on their surface, as shown in Figure 2.4. These fibres were easily modified through the selection of different amino acids for other applications in tissue engineering and mineralization. In 2005, Stupp's group published more detail on the assembly mechanism and structural characteristics of gels formed from PAs.[32] The self-assembly of PAs into gel-forming networks of cylindrical aggregates is triggered by counterion screening and

stabilized by van der Waals interactons, hydrophobic forces, ionic bridging and hydrogen bonding. In 2009, this group demonstrated the excellent biocompatability of hybrid nanofibres composed of heparin sulfate and a peptide amphiphile capable of binding to this biopolymer.[33] Furthermore, Stupp *et al.* also developed a new short hydrophobic-hydrophilic alternative peptide sequence which assemnled into β-sheets. This peptide sequence contained alternative tetrapeptide sequences with (i) hydrophobic and negatively charged residues (V and E) and (ii) alkyl segments with a length of 16 carbon atoms. The hydrophobic and negatively charged residues could trigger the self-assembly of the peptide amphiphiles into 1D nanostructures which possessed curvature and grew laterally to create nanobelts. Futhermore, electrostatic repulsions were found to reversibly open 2 nm grooves in the nanobelts upon changes in pH. Also, changes in peptide concentration resulted in the breakup of the nanobelts into twisted ribbons, providing an insight on the formation mechanism of nanobelts.[34]

Recently, Stupp's group investigated how the gelation kinetics, stiffness, and strain recovery of PA gels varied with the type of charge screening gelling agent used (HCl or $CaCl_2$).[35] They found that the ionic bridges in $CaCl_2$-PA gels form stronger intra- and interfibre cross-links than the hydrogen bonds in HCl-PA gels. These PA molecules consist of three segments: (1) a hydrophobic sequence, which is commonly an alkyl tail, and drives aggregation through hydrophobic collapse; (2) a β-sheet-forming peptide that promotes nanofibre formation; and (3) a peptide segment that contains ionizable side chains and an amino acid sequence of interest for biological signalling. The link between the internal structure of PA nanofibres with different amino acid sequences and stiffness of the gels was also investigated.[36] In addition to structural studies, Stupp has explored a number of biomedical applications for self-assembled peptide amphiphile molecules, including cell scaffolds, drug carriers, and bioactive networks for central nervous system regeneration, angiogenesis, and the regeneration of bone and enamel.[37]

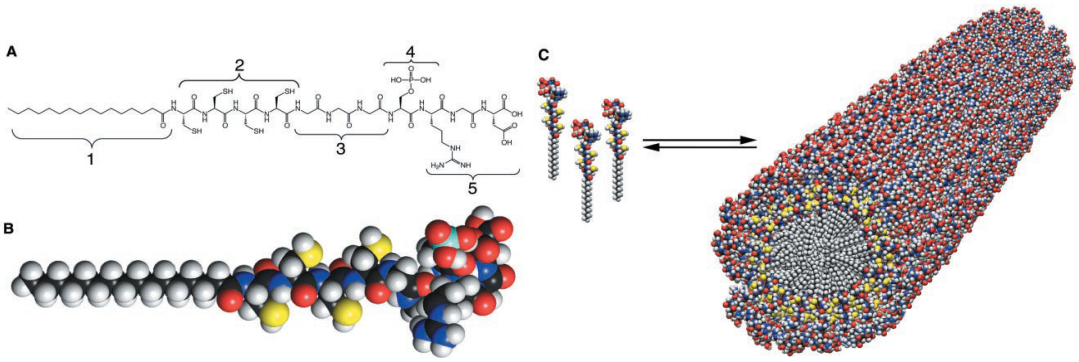

Figure 2.4 (A) Chemical structure of the peptide amphiphile, highlighting the five key structural features. Region 1 is a long alkyl tail that coveys hydrophobic character to the molecule and makes the molecule amphiphilic when combined with the peptide region. Region 2 is composed of four consecutive cysteine residues that may form disulfide bonds when oxidized to polymerize the self-assembled structure. Region 3 is a flexible linker region of three glycine residues to provide the hydrophilic head group flexibility from the more rigid cross-linked region. Region 4 is a single phosphorylated serine residue that is designed to interact strongly with calcium ions and help direct mineralization of hydroxyapatite. Region 5 displays the cell adhesion ligand RGD. (B) Molecular model of the PA showing the overall conical shape of the molecule going from the narrow hydrophobic tail to the bulkier peptide region. Colour scheme: C, black; H, white; O, red; N, blue; P, cyan; S, yellow. (C) Schematic showing the self-assembly of PA molecules into a cylindrical micelle [Adapted from 31].

Other groups, such as Deming's, also reported diblock copolypeptide amphiphiles containing charged and hydrophobic segments in 2002.[38] In 2008, Gokel's group produced amphiphilic heptapeptides which had the general formula $R^1{}_2NCOCH_2OCH_2CO$-$(Gly)_3$-Pro-(Gly)3-OR^2. Substitution at R^1 and R^2 with various aliphatic or aromatic groups was found to alter the ability of amphiphilic heptapeptides to transport chloride through a phospholipid bilayer membrane.[39] Recently, Kokkoli *et al.* developed a fibronectin mimetic peptide-amphiphile which contained both the primary binding domain RGD and the synergy binding domain PHSRN, which has shown superior cell adhesion properties over simple RGD sequences and fibronectin in 2D culture.[40]

Aliphatic peptide amphiphiles have also been explored for electronic applications, as discussed in section 2.4.3.2.

2.2.5.2 Aromatic peptide amphiphiles

Vegners and co-workers were the first group to report the formation of gels from aromatic peptide amphiphiles (N-terminal Fmoc-protected anionic dipeptide L-D) in aqueous solution. These gels were found to form at peptide concentrations as low as 2 mg/ml due to the Fmoc-peptides assembling into long, amphipathic, polyanionic filaments.[41] Xu's group then reported small molecular hydrogelators, based on Fmoc-^{D}A-^{D}A. They argued that these Fmoc-dipeptides were a new class of low-molecular weight hydrogelators that are readily available and may serve as new biomaterials. The most remarkable feature of the hydrogels was their response to a specific biological ligand – receptor interaction because the dipeptides bound to vancomycin with different affinities.[42] They also explored a new supramolecular hydrogel based on multiple components with discrete yet complementary activities, and demonstrated the gel's function *in vivo*.[43]

Xu's group in 2004 studied the role of the relative orientation of aromatic groups on the structure and spectroscopic properties of the peptide nanostructures.,[44] They initiated gelation by the dephosphorylation of Fmoc tyrosine phosphate to form a Fmoc tyrosine hydrogelator (Figure 2.5 A). Circular dichroism (CD) was used to characterize the gels (I, II) in Figure 2.5 B and C. The Cotton effect arises from π–π transition of aromatic species and is typically found at 250-315 nm in hydrogels. As can be seen in the Figure 2, the Cotton effect was observed in both gels I and II, suggesting the presence of superhelical arrangements of the L-lysine residues which induce the helical orientation of the fluorenyl groups. In the solution of II, the fluorenyl group had an emission peak at 346 nm, which shifted to ~352 nm in gel I. The small red-shift suggested that the fluorenyl group overlaps with the phenyl group (Figure 2.5 D). The shoulder at ~376 nm likely originated from the antiparallel dimerization of the fluorenyl group (Figure 2.5 E), with the small peak at ~400 nm due to the small amount of the fluorenyl groups overlapping in parallel fashion (Figure 2.5 F). The broad peak centered at 456 nm, implied that multiple fluorenyl moieties had stacked efficiently and were restricted within the hydrogel (Figure 2.5 G). Therefore, it can be concluded overall that four modes of π–π interactions are able to coexist and drive the formation of the supramolecular polymers.

In 2006, Ulijn's group demonstrated the spontaneous assembly, under physiological conditions, of Fmoc-dipeptides into fibrous hydrogels. They selected a library of seven Fmoc-dipeptides made up of the four amino acids, Glycine (G), Alanine (A), Leucine (L), and Phenylalanine (F), thus covering a range of hydrophobicities. The hydrogels were prepared by suspending the Fmoc-dipeptides in purified water. The pH was increased to a value greater than pH 8 by adding concentrated NaOH to cause the deprotonation of the carboxylic acid groups to give a clear solution. Concentrated hydrochloric acid was added to this solution dropwise until a clear gel was formed.[45] In 2008, Ulijn *et al.* reported that one member of this type of peptides, Fmoc-diphenylalanine (Fmoc-FF) (Figure 2.6), forms a hydrogel at pH 7 by self-assembly. This process produces nanotubular structures via a new molecular architecture. The structure is based mainly on both anti-parallel β-sheets and anti-parallel π-stacked fluorenyl groups, interlocking a number of β-sheets through π–π stacking interactions. The twisted nature of the β-sheets causes formation of nanotubes.[46] In 2009, they developed gels formed from a range of compositions of Fmoc-FF hydrogels (Fmoc-FF and Fmoc-FF/X where X=Fmoc-lysine (K), Fmoc-serine (S), Fmoc-glutamic acid (D) at physiological).[47] In the same year, this group introduced that self-assembly process of Fmoc-diphenylalanine (Fmoc-FF) into fibrils consisted of antiparallel β-sheets which were affected by pH. It results in two apparent pK_a shifts of 6.4 to 2.2 pH units above the theoretical pK_a (3.5).[48]

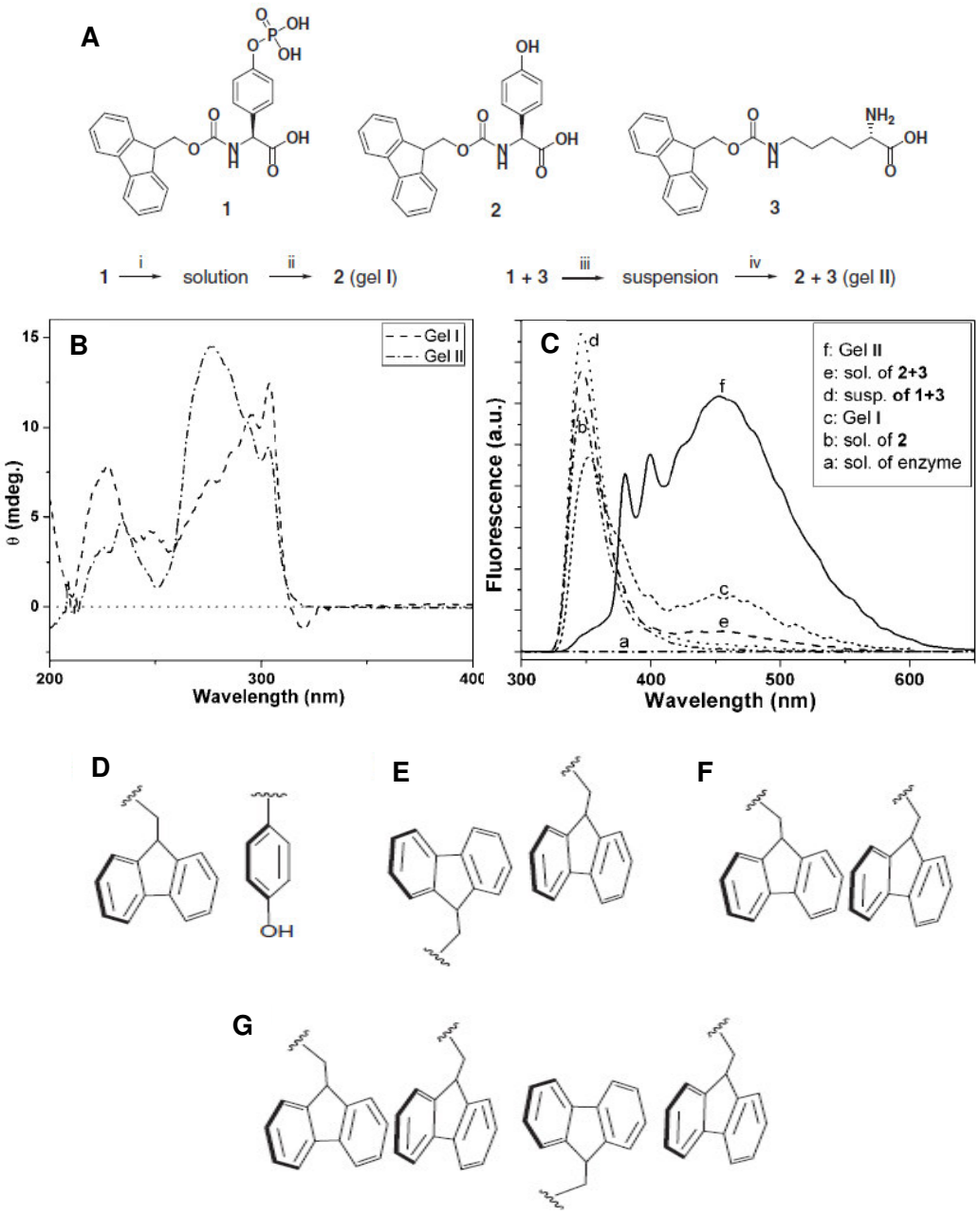

Figure 2.5 A. The molecular structures of the two compounds used for the formation of hydrogels and a schematic of the gelation process. Conditions of gelation: i) Na_2CO_3, buffer, ii) enzyme, 37 ℃; iii) Na_2CO_3, buffer, and iv) enzyme, 60 ℃ (buffer: pH-9.6, 50 mM of Tris-HCl, and 1 mM of $MgCl_2$). B, the CD spectra of the hydrogel, C, the emission spectra (λexcitation =265 nm, slit width -2.5 nm) of the hydrogels and the solutions containing the corresponding components, D, E, F, G, Some of the possible modes of π–π interactions that contribute to the emissions in the gel phase [Adapted from 44].

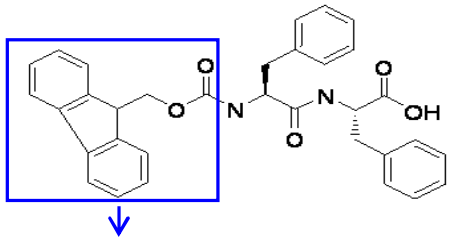

Fluorenylmethoxycarbonyl (Fmoc)

Figure 2.6 Molecular structure of Fluorenylmethoxycabornyl-diphenylalanine (Fmoc-FF) [Adapted from 46].

Naphthalene-dipeptide has also be used in a similar way to Fmoc to provide the hydrophobic driven for short peptide self-assembly. This concept was introduced by Chen and Adams *et al.* in 2010. They showed that the removal of charge allows lateral assembly of the molecules leading to $\pi-\pi$ stacking and β-sheet formation to form fibrous structures.[49] Recently, Adams and Cameron reported the electrochemically induced growth of thin, self-assembled Fmoc-LG hydrogel films. Film growth was controlled by inducing a localized pH drop at an electrode surface by the oxidation of hydroquinone.[50]

Gazit's group, in 2006, discovered that Fmoc-diphenylalanine peptides could be self-assembled by diluting an organic solvent, HFPIP, in which the peptides were initially dissolved, resulting in the formation of a rigid gel-phase material.[51] In 2009, this group described the self-assembly of nine different Fmoc-peptides (Fmoc-FRGD, Fmoc-RGDF, Fmoc-2-Nal, Fmoc-FG and Fmoc-FF) into various structures under mild conditions in an aqueous solution by using low-molecular weight building blocks. They also characterized the distinctive physical properties of these structures.[52] They demonstrated the critical role of the aromatic groups in regulating the self-assembly process and consequently influencing the structural and physical properties of the resulting hydrogels.

Other groups, such as Ripmeester's group, in 2008, described the basis of a new gelation mechanism based on dipeptide prepared from N-Fmoc-protected Leucine and C-benzoyl-protected Leucine by peptidic coupling in acetonitrile. The use of ultrasound was found to modify the morphology of the material from sheet-like particles into 3-dimensional networks of fibres or ribbons, leading to gelation.[53] Channon *et al.* described the formation of self-assembling,

nanoscale, fibrillar aggregates from an amyloidogenic peptide (YTIAALLSPYS). The peptide was conjugated to the Fmoc, which was utilized only for its fluorescent functionality in this work.[54] In 2010, a strategy to form supramolecular hydrogels triggered by electrostatic attraction of oppositely charged peptides with rigid Fmoc tails (Fmoc-VRGDV, Fmoc-GRGDG and Fmoc-KKRGDK) was introduced by Xu and Zhuo. The rigid Fmoc tails formed β-sheet structures which were induced by hydrogen bonding and π-stacking (Figure 2.7).[55] They suggested that the self-assembly only occurred when mixing the oppositely charged peptides at a neutral pH where the individual peptide molecules were soluble. The self-assembly was driven by an electrostatic attraction involving the charged peptides rather than by the simple hydrophobic collapse. The electrostatic attraction made the oppositely charged peptides contact with each other, providing a chance for the β-sheet like arrangement of the peptide backbones through hydrogen bonding interactions. The fluorenyl rings connected to the peptide backbones as hydrophobic tails were thus positioned so that they π-stacked with each other in an antiparallel fashion, resulting in the formation of nanofibres and ultimately supramolecular hydrogels. Debnath *et al.* designed a class of Fmoc amino acid/peptide functionalized cationic amphiphiles having pyridinium moiety at the C-terminal. This material exhibited excellent gelation ability (minimum gelation concentration (MGC) – 0.6-2.2%, w/v) in plain water over a wide range of pH at room temperature. [56]

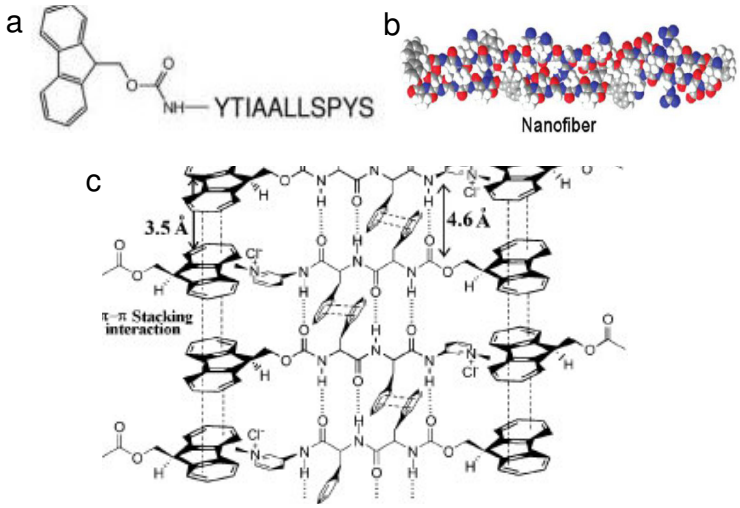

Figure 2.7 Fmoc-peptides nanostructures produced by various groups: a, Fmoc group shown conjugated to the amino acid sequence of $TTR_{105-106}$, b, Nanofibres with β-sheet like superstructure, c, Probable arrangement of the molecules the gel state. [a, b, c were taken from 54, 55, 58 separately].

2.3 CONTROL OF SELF-ASSEMBLY BY ENZYMES

2.3.1 Enzymes as selective catalysts

Enzymes are catalysts that accelerate a chemical reaction without undergoing any net changes. The activity of enzyme is affected by temperature, chemical environment (e.g. pH), and the concentration of the substrate. It is well-known that intramolecular reactions between groups held together in a single molecule are faster than the corresponding intermolecular reactions between two independent molecules. Therefore, enzymes can accelerate the speed of a reaction between two species simply by holding the two reactants close enough together in an appropriate orientation. The enzyme does not change the free energy of the substrate or product but rather lowers the free energy of the transition state.[57]

Subtilisin and thermolysin were used in the self-assembly routes in this thesis. Subtilisin is a serine protease consisting of three essential amino acids (histidine, serine and aspartic acid) which play an essential role in the cleaving of peptides.[58] Thermolysin contains a zinc ion and four calcium ions, which are essential for catalysis and thermal stability.[59]

2.3.1 Enzyme triggered assembly via hydrolysis

There are a number of ways of controlling self-assembly with externally applied stimulus, such as pH switches, temperature and the use of enzyme catalysis. Triggering of supramolecular events by enzymes is a valid method to control the self-assembly process under mild conditions. In principle, two modes of enzymatic controlled self-assembly are possible: 1) using kinetically controlled pathways where both enzyme reaction and self-assembly are thermodynamically favoured and are therefore uncoupled; 2) the self-assembly event driving a thermodynamically unfavoured enzymatic conversion. The former situation gives rise to largely irreversible systems, while the latter situation gives rise to reversible systems. Both systems have been described in the literature and will be described below.

The direction and nature of a chemical reaction is related to its chemical equilibrium. Since breaking bonds requires energy and forming bonds releases energy, the energy of a chemical reaction will depend on the sum of energy absorbed and generated. The system will also favour going towards a higher entropy where enthalpy allows. If the Gibbs free energy of the reactants is higher than the energy of the products, $G_{reactants} > G_{products}$, the reaction will occur spontaneously. Figure 2.8 shows a (hypothetical) thermodynamic pathway of a system in which the formation of the products (building blocks: Fmoc-peptide) are formed in a thermodynamically distinct process to the self-assembly. Therefore, the formation of building blocks via hydrolysis and the process of self-assembly are independent.

In 2004, Xu's group[60] described the first example of this type of supramolecular hydrogelation driven by enzymatically mediated self-assembly. They utilized an enzymatic (alkaline phosphatase) reaction to remove a charged, hydrophilic phosphate group from an amino acid derivative (PO_4^{3-} of N-fluorenylmethyloxycarbonyl (Fmoc) tyrosine phosphate) to produce a neutral group under basic conditions. This process created a small molecular hydrogelator (Fmoc-Y) and which subsequently assembled into a supramolecular hydrogel. In 2007, the same group[61], described the use of phosphatase to catalyze a bond-cleavage reaction to generate a supramolecular hydrogel. In 2009, the group reported the action of an enzyme to transform a

hydrogel precursor (5a) based on taxol (1) into a hydrogelator (5b), which self-assembled into nanofibres and a supramolecular hydrogel (Figure 2.9).[62]

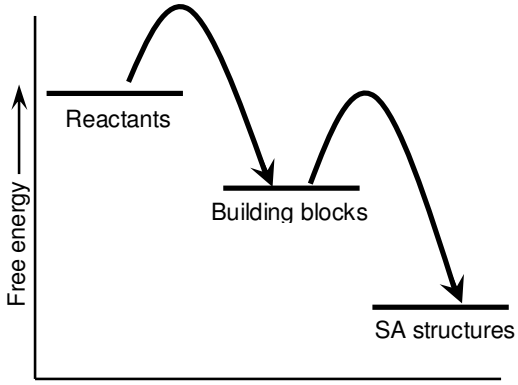

Figure 2.8 Free energy diagram for hydrolysis of Fmoc-peptide methyl esters by enzyme triggered self-assembly systems.

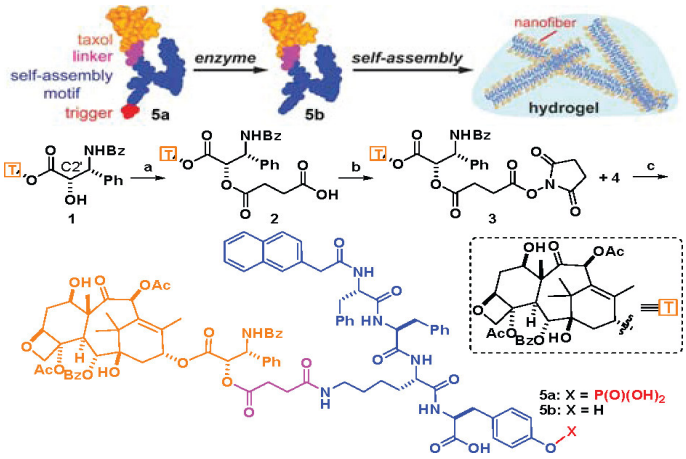

Figure 2.9 Scheme of synthetic route and the structure of 5a. (a) Succinic anhydride, DIEA, chloroform; (b) NHS, DCC, chloroform, (c) sodium carbonate, acetone, water [Adapted from 62].

In 2007, Ulijn's group demonstrated the conceptually novel approach of enzyme triggered peptide self-assembly for nanoparticle based sensing of proteases. In this work, protease-responsive peptide-functionalized nanoparticles (NPs) were modified with Fmoc-peptides. The Fmoc-peptides contain a cysteine group for anchoring onto the nanoparticles. A short, enzyme cleavable peptide sequence matched with the target protease was also included in the Fmoc-peptide chain. Upon enzymatic hydrolysis, the Fmoc groups were removed and charged amines

were revealed, resulting in a NP dispersion. Real-time monitoring of the protease action was found to be possible using this approach. [63]

In 2008, Ulijn's group explored enzymatic methods to prepare peptide nanomaterials. [64] They demonstrated that subtilisin can be used to selectively trigger the self-assembly of peptide hydrogels via the hydrolysis of Fmoc-peptide esters at physiological pH. The diameters of the nanotubular structures produced were found to vary with the Fmoc-peptide building blocks used. In 2009, they demonstrated further development of the Fmoc-Y-OH system by forming gels by enzymatic dephosphorylation under physiological conditions and providing evidence for the ability to control the elastic modulus of the gels. [65]

Mann and co-workers[66], in 2006, demonstrated that supramolecular hydrogels can be used as templates for calcium phosphate mineralization. The hydrogel was produced by enzymatic dephosphorylation of N-fluorenylmethyloxycarbonyl (Fmoc) -tyrosine (Y) -phosphate. The mineralization of the hydrogels was found to increase the stiffness, critical strain, thermal stability, and dynamic storage and loss moduli of the gels. In 2008, a novel reverse microemulsion self-assembly method for the fabrication of peptide nanoparticles was introduced by Wang and Chao *et al.* [67] Fmoc-FY phosphate dissolved in alkaline phosphatase was mixed with bis(2-ethylhexyl) sulfosuccinate sodium salt (AOT). The Fmoc-FY was found to self-assemble into peptide nanoparticles upon triggering by the enzyme which is encapsulated into micelles.

2.3.2 Enzyme assisted assembly by condensation

In contrast to the use of enzymes for hydrolysis, there are a few examples in which enzymes are used to produce gelators by making bonds, rather than breaking bonds, and in some cases to build polymers or biopolymers (i.e. to increase their molecular weight).[68] For example, in 1997, Sperinde *et al.* demonstrated the formation of a hydrogel network by cross-linking functionalized poly(ethylene glycol) (PEG) and a lysine-containing polypeptide through the action of a natural tissue enzyme, transglutaminase. [69]

It is possible to control the self-assembly of peptide hydrogelators by producing the gelators via condensation reactions (i.e. the direct reversal of hydrolysis). For example, this approach has been achieved by producing Fmoc-peptide-esters via amide bond formation from non-assembling Fmoc amino acid and amino acid esters.[70] This reversed hydrolysis system is under thermodynamic control; before reversed hydrolysis, the concentration of each non-assembling precursor depends on the relative free energy of each chemical component. Therefore, anything that can alter these free energies will change the distribution of the material in the network.[71] The amide hydrolysis reaction is close to equilibrium in dilute aqueous condition with a $\Delta G^0_{\text{amide hydrolysis}}$ of -4.0 KJ mole^{-1} at pH 7.5, 25 ºC. This equilibrium will be shifted towards amide formation by the removal of the amide component form solution by, for example, the formation of self-assembled structures ($\Delta G^0_{\text{self-assembly}} - \Delta G^0_{\text{amide hydrolysis}} < 0$). This approach for hydrolysis driven self-assembly is shown in Figure 2.10 and it should be compared to the condensation reaction shown in Figure 2.8. [72] This condensation approach also has the benefit in that the self-assembly process is reversible, allowing the annealing of high energy defect structures.

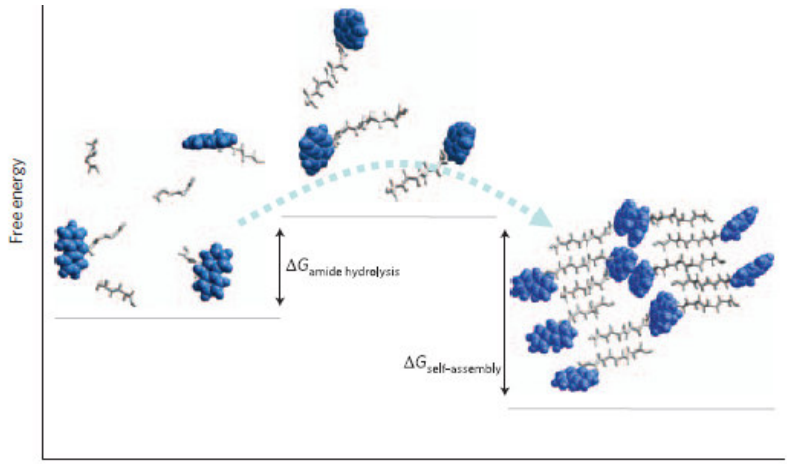

Figure 2.10 Diagram showing the free energy profile of enzyme-assisted self-assembly of peptide derivatives. [Adapted from 70].

Alternative approaches to achieve reversibility are based on the use of coupled reactions, for example phosphate ester hydrolysis can be reversed by a phosphorylation reaction which is driven by the hydrolysis of high energetic molecular fuel such as adenosine triphosphate (ATP). For example, in 2000, Kaplan and Winkler employed enzymatic phosphorylation and

dephosphorylation reactions to regulate the assembly of the β-sheet secondary structure in silk-like proteins.[73] The kDa protein was phosphorylated with cyclic AMP-dependent kinase and dephosphorylated with calf intestinal alkaline phosphatise. Phosphorylation inhibited the β-sheet assembly of the protein and enhanced the solubility of the protein to about 5 mg/mL in water, relative to ~ 1 mg/mL for the enzymatically dephosphorylated protein.

In 2006, the use of enzyme-triggered self-assembly via reversed hydrolysis to form peptide hydrogels was shown by Ulijn *et al*. They used the specificity of protease enzymes, which normally hydrolyze peptide bonds in aqueous medium, to perform the reverse reaction (i.e., peptide synthesis or reversed hydrolysis) instead of hydrolysing the bond to produce amphiphilic peptide hydrogelators.[74] They used proteases to link non-gelling Fmoc-amino acid (Fmoc-Phe) and dipeptide (Phe-Phe) starting materials to form amphiphilic Fmoc-tripeptides (Fmoc-Phe-Phe-Phe) that assembled into interwoven fibres approximately 10-20 nm in diameter.[74]

Xu *et al.* [75], in 2006, further refined the process of hydrolysis by enabling a degree of reversibility in a two-enzyme system. The kinase/phosphatase switch was used to control the phosphorylation and dephosphorylation of the hydrogelator and therefore regulate the formation of supramolecular hydrogels. They synthesized Nap–FFGEY that formed a supramolecular hydrogel by self-assembly. Kinase was added to the hydrogel. This process then induced a gel-sol phase transition due to the presence of adenosine triphosphates (ATP) as an energy source. The tyrosine residue was converted into tyrosine phosphate by the kinase to give a more hydrophilic molecular of Nap-FFGEY-phosphate. The resulting solution with a phosphatase transforms Nap-FFGEY- phosphate back to Nap-FFGEY by adding alkali phosphatase, and restores the hydrogel. (Figure 2.11)

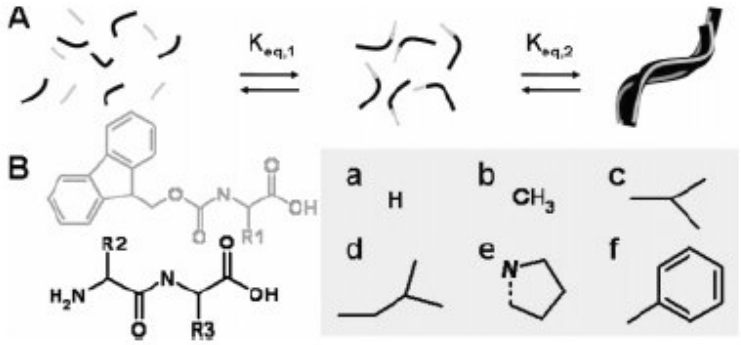

Figure 2.11 Proposed mechanism and chemical structures of Fmoc-amino acids: (A) Proposed mechanism: Fmoc amino acids (gray) are enzymatically coupled to dipeptides (black) by a protease to form Fmoc-tripeptides that self-assemble into higher-order aggregates, driven by π-π interactions between fluorenyl groups. $K_{eq,1}$ represents the equilibrium constant for peptide synthesis / hydrolysis, $K_{eq,2}$ for self-assembly. (B) Chemical structures of Fmoc-amino acids, dipeptide precursors and amino acid side chains: a Gly, b Ala, c Val, d Leu, e Pro, f Phe [Adapted from 75].

2.4 SUPRAMOLECULAR ELECTRONICS

2.4.1 π-electronic nanostructures from organic building block

Small molecule self-assembly allows for the creation of nanoscale structures with controlled size and shape, which could be used in electronic and biological applications.[76] These self-assembled supramolecular structures have various applications for nanotechnology, periodic porous materials, biomimetic materials and optoelectronic nanomaterials.[77] The well known π–π interaction is widely recognized as an important strategy in self-assembly. Recently, several new approaches have been reported to fix self-organized π-conjugated systems for ultimate use in electronics. The success of the self-assembly largely depends on the structure and, more specifically, on the positioning of aromatic groups for optimized π–π overlap. The self-assembled π-conjugated systems will be a starting point for the search for peptide candidate for supramolecular electronics. [78]

In this Chapter, supramolecular electronic systems are initially compared to single molecule and polymeric counterparts. Three kinds of electronics are shown in Figure 2.12.[79] Molecular

electronics are composed by molecular connection between two electrodes, which are separated on angstrom length scale. Plastic electronics are based on a polymeric film or network between two electrodes. Supramolecular electronics bridge the gap between molecular electronics and bulk plastic electronics and are concerned with molecules assembly into larger structures, such individual nanowires. Single molecule devices have some disadvantages, for example, orientational and conformational motion of the molecule (thermal noise) can cause defects and contact problems between the molecule and the electrode. These issues are reduced by some extent by stabilisation in a self-assembled nanostructure. Hence supramolecular electronics based upon π-conjugation is an attractive strategy for future applications.

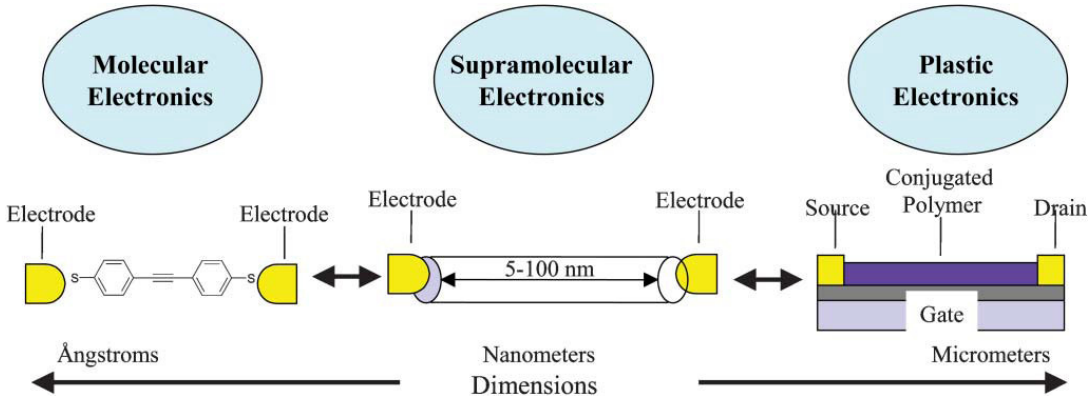

Figure 2.12 To show the gap between molecular electronics and plastic electronics. Supramolecular electronics is an unexplored field with the aim of constructing and investigating supramolecular optoelectronic and devices [Adapted from 79].

In 2004, Layachi showed that π-electron interaction in the vicinity of HOMO-LUMO gap region has a significant influence on the electronic properties of the materials. The intermolecular distance played a major role on the extent of the π-coupling and hence electron delocalisation. Consequently the electronic properties of molecular wires was found to be strongly influenced by the position of the aromatic motifs in its structure.[80]

For effective charge transport, it is imperative that precisely controlled, tunable geometries with limited defects can be produced. In 2004, Mansikkamaki *et al.* reported that noncovalently bound supramolecular structures, such as tubular structures, were well ordered due to π–π interactions

and hydrogen bonding.[81] They have shown that by using a weaker hydrogen bond acceptor (bromide instead of chloride) and appropriate conditions, the self-assembly process of C-methyl resorcinarene can be driven to favour weaker interactions such as π–π interactions instead of hydrogen bonding. Aida and Yamamoto *et al.*, in 2006, demonstrated the self-assembly of norbornene-appended hexabenzocoronene (HBC) amphiphiles resulting in the formation of either a coiled or a tubular structure, depending on the self-assembling conditions used (Figure 2.13). The electroconductive properties of both the nonpolymerized and polymerized nanocoils were investigated by using 3-μm-gap two-probe electrodes. Upon exposure to I_2, the former was readily disrupted with a loss of the coiled structure, while the latter was successfully doped with the retention of the coiled morphology and displayed a linear I-V profile, which allowed determination of conductivity as 1×10^{-4} S/cm.[82] Recently, Huang *et al.* made ultra-long microbelts with a length in the range of millimetres by polymerisation of (3,4,9,10-perylenetetracarboxylic acid potassium salt: PTCAPS). These microbelts induced self-assembly of small organic molecules and showed significant electrical conductivity along the belt axis.[83] In addition, the composite structure of the microbelts offered unique new possibilities such as targeted doping of the organic semiconductor microbelts and the associated significant alteration of their electronic properties.

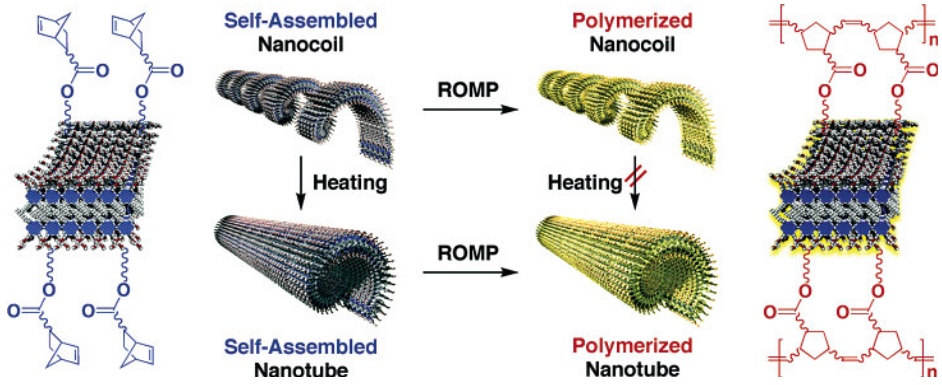

Figure 2.13 Schematic representation of the concept of post-ROMP stabilization of self-assembled nanocoils and nanotubes from 1 (HBC). ROMP: ring-opening metathesis polymerization. [Adapted from 82].

Recently, Sakai and Matile *et al.* reported the creation of the first supramolecular n-p heterojunctions by using oriented, multicoloured, antiparallel, redox gradients. They introduced a

zipper assembly mechanism, in which naphthalenediimide (NDI) chromophores attached to p-oligophenyl (POP) or p-oligophenylethynyl (OPE) chromophores are assembled step-by-step to build mutually interdigitating π-stacks along interdigitating rigid-rod scaffolds (Figure 2.14).[84] Molecular dynamics (MD) simulations confirmed that intrastack hydrogen-bonded chains, interstack ion pairing and hydrophobic domains were placed perfectly to stabilize the highly ordered π stacks along the oriented rigid-rod scaffolds. Because their HOMO-LUMO gap decreases with increasing LUMO energy, the NDIs are ideal for building redox gradients into the e^- transporting π stacks. OPE hole acceptors and POP donors should suffice for producing a minimalist gradient in the h^+ channel.

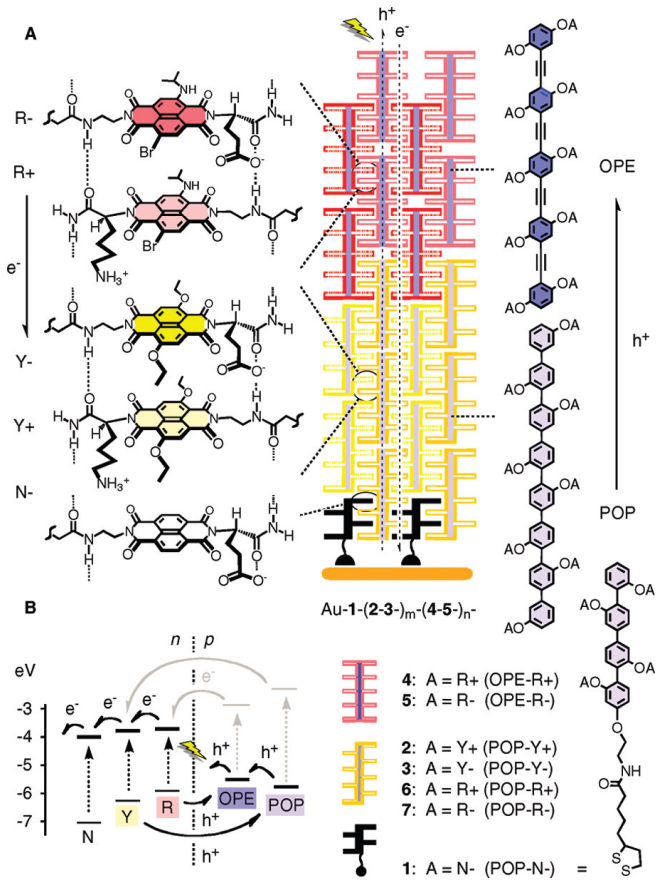

Figure 2.14 A. Molecular structures and hypothetical OMARG-SHJ architecture Au-1-(2-3-)m(4-5-)n of POP-N initiator: (1) and POP-Y (2,3) and OPE-R (4,5) propagators on gold (for 8 and the full structures). B. HOMO and LUMO levels show photoinduced (dashed arrow) e^- (gray) and h^+ (black) injection into e^- (n) and h^+ (p)-transporting pathways (bold) [Adapted from 84].

2.4.2 DNA based electronics

Nanobioelectronics is a new and fast-progressing discipline, which integrates the achievements of nanoelectronics and molecular biology. In the future, the biotechnology and electronic industries may merge together and push nanotechnology forward, which implies the use of charge transfer processes in bio-molecules and their assemblies at the nanometer size.[85] DNA is the code of life, which not only plays an important role in biology carrying genetic information in all living species, but also could be a one-dimensional molecule wire.[86] The DNA structure is ideal for electron transfer because the electron orbitals in the bases overlap reasonable well with each other along the axis of DNA. Understanding the principal mechanisms of electron transfer within the DNA molecule is a key threshold in the development of DNA as an electronic wire. Singh considered that the charge carriers are localized in the bases of the DNA nucleotides and nucleosides, which include H-bonds and $\pi-\pi$ bonds in these systems.[87] The localized carriers are responsible for charge conduction in DNA because of the variable range hopping mechanism. The common model for electron transfer through DNA is based on overlap between π orbitals in adjacent base pairs.[88]

Different experimental approaches have been used to study the electronic conductivity mechanism in DNA, such as AC impedance spectroscop[89], I-V curves measured by triple-probe atomic force microscopy (T-AFM) [90] and scanning tunnelling spectroscopy[91]. Direct measurement of electrical transport through DNA (10.4-nm-long (30 base pairs) poly(G) – poly(C) DNA oligomers) molecules were studied by Porath *et al.* in 2000.[92] The single DNA molecule (10.4 nm) was positioned between two closely spaced metal nanoelectrodes (8 nm) by electrostatic trapping from a dilute aqueous buffer (Figure 2.15). The device was dried after the DNA molecule was trapped from the solution. Based on experimental results, DNA has been categorized as anything from a semiconductor to an insulator. It was concluded that the system behaves as an insulator at low bias, while the current rises sharply beyond a threshold bias, with the charge carrier transport

being mediated by the molecular energy bands of DNA. In 2001, Watanabe and coworkers reported the measurement of the electronic properties of a single DNA strand by using a three-therminal single molecule DNA device with a Triple-Probe Atomic Force Microscope (T-AFM). It was found that the DNA double strand was semiconducting.[93]

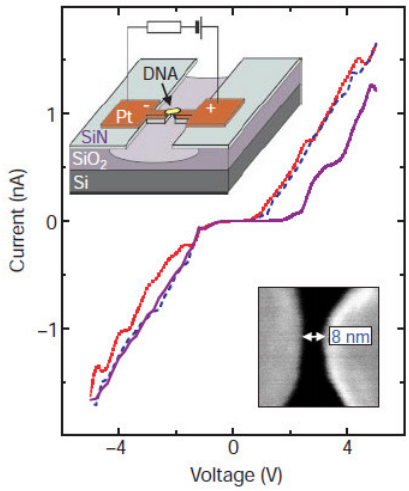

Figure 2.15 Current-voltage curves measured at room temperature on a DNA molecule trapped between two metal nanoelectrodes. [Taken from 92].

2.4.3 Peptides in supramolecular electronics

2.4.3.1 Designed peptide for electronics

Self-assembled, supramolecular objects with π-electron functionality have attracted much attention for applications in organic electronic devices. One dimensional (1D) bionanoelectronics is exciting and challenging route to such devices.[94] Peptides are especially attractive in this context due to the precisely controlled geometries that can be accessed. The electronic properties of a self-assembled eight-residue cyclic peptides with the sequence [-(L-Gly-D-Ala)$_4$-] was studied by Mintmire *et al.* in 1998. They calculated that the electronic band structure of such a peptide nanotube was an insulator with an energy gap of 4.7 eV.[95] Recently, Lewis *et al.* indicated that self-assembling cyclic D, L-peptide nanotubes (PNTs) are also electronic insulators with wide band gaps. The presence of aromatic rings in the side chain of peptide nanotubes significantly reduces the band gap.[96] However, such functionalised cyclic D, L-peptide nanotubes

are still poor-tunnelling, wide-gap, semiconductors, since the aromatic rings in the phenylalanine side chains are separated by a large distance of 4.73 Å.

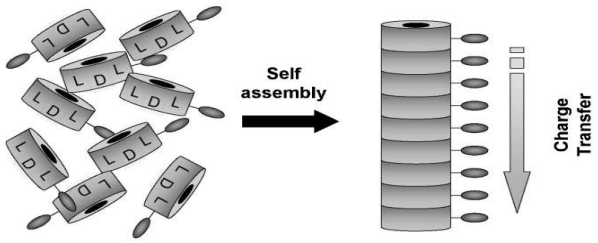

Figure 2.16 To show the first peptide nanotubes were developed in the 1990s by M. Reza Ghadiri. These tubes are made of the precise assembly of alternating D- and L-amino acid cyclic peptide, which form elongated and hollow nanotubes [Adapted from 98].

According to theory, the band gap of peptide nanotubes can be altered by modifying the cyclic peptide sequence. However, natural amino acid side chains are not sufficient to create electronically conductive assemblies.[97] Ghadiri and coworkers, in 2005, prepared D, L-α-peptides bearing 1, 4, 5, 8-naphthalenetetracarboxylic acid diimide (NDI) side chains. This material can form peptide nanotubes (Figure 2.16) [98], in which the charges can transfer[99]. The group also reported self-assembling peptide nanotubes from an eight-residue cyclic D, L -α-peptide bearing four NDI side chains. The inter-subunit distance between peptides rings was typically 4.7 Å (Figure 2.17), which is too large for efficient orbital overlap (3.6 Å). As a result, they enforced inter-subunit juxtaposition of four homochiral NDI residues in self-assembled nanotubular configuration to minimize the distance between the aromatic moieties.[100] The intermolecular distance could be reduced significantly when the exterior of the peptide nanotubes was decorated with pendant aromatic structures which tilt with respect to the peptide structures, thereby lowering the intermolecular distance and allowing electron delocalization.

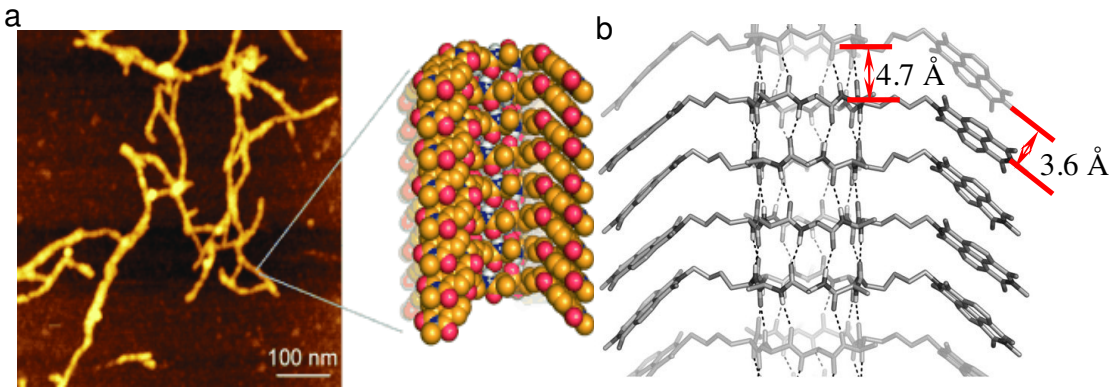

Figure 2.17 a) Atomic force microscopy (AFM) image of reduced cyclic peptide absorbed on mica;
b) A suggested model for the organization of the self-assembled cyclic peptide with a distance of 4.7 Å between two cyclic rings and 3.6 Å between NDI residues. [Adapted from 100].

2.4.3.2 Aliphatic peptide electronics

Redox-active supramolecular nanostructures constructed by the self-assembly of peptide amphiphiles (PAs) could serve as both biologically and electronically active matrices for the transduction of biological events. In 2007, Stupp's group presented the use of PAs to sequester precursors to conducting polymers during PA self-assembly. They generated polymerization confined conducting polymers insulated by bioactive shells upon oxidative.[101] Here the peptide-sequence N-acylated with a fatty acid tail enables assembly in aqueous environments into high-aspect-ration cylindrical nanostructures with poly(3,4-ethylenedioxy-thiophene) PEDOT, which obtained robust and stable electroactivity (Figure 2.18). In 2008, this group reported a set of diacetylene-derivatized PAs reacting to form conjugated polydiacetylene backbones while retaining the shape of the nanostructure with potential electronic properties. Diacetylene-derivatized PAs react to form conjugated polydiacetylene backbones which then self-assembly into cylindrical nanofibres. Polymerization of these systems with conjugated backbones may offer new possibilities for mechanical and optical properties.[102] They also studied the PAs conjugated with a terthiophene segment of potential electronic interest, which self-assembled into high-aspect-ratio, left-handed, helical nanofibres which possessed a regular diameter and pitch.[103] In 2008, Matmour and Schenning *et al.* also reported that peptide hybrid amphiphiles were

composed of a π-conjugated oligo(p-phenylenevinylene) trimer (OPV), which is coupled at either a (GAGAG) silk-inspired β-sheet or a (GANPNAAG) β-turn forming oligopeptide sequence.[104]

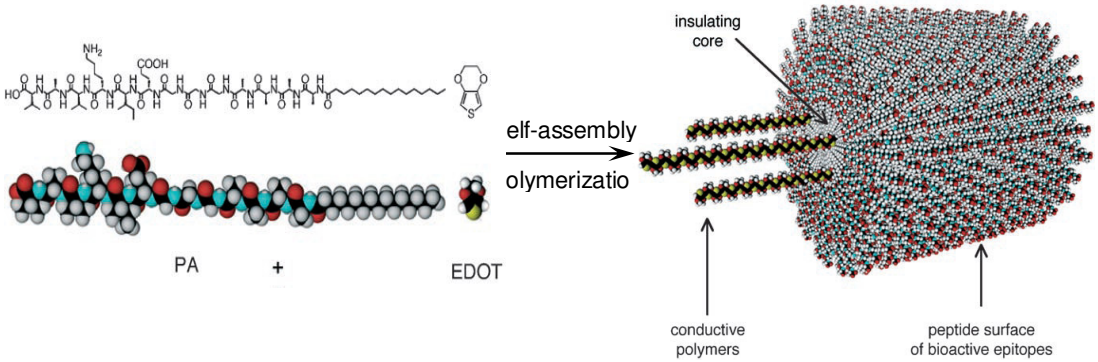

Figure 2.18 Depiction of PA self-assembly in the presence of EDOT monomer: Self-assembly yields nanostructures with hydrophobic cores that sequester the organic monomer from aqueous solution. Confined oxidative polymerization of EDOT once partitioned should occur predominately within these hydrophobic regions resulting in encapsulated conductive polymers. This computer-generated image is a suggested structure where a portion of the schematized PA nanostructure has been omitted to reveal idealized chains of conductive polymers encapsulated within [Adapted from 101].

2.4.3.3 Aromatic peptide electronics

The driving force for the self-assembly usually relies on several molecular recognition events that include the π-π stacking interactions which occur between aromatic units.[105] For example, in 2004, Gazit described the ability of self-assembled diphenylalanine peptide nanotubes to improve the electrochemical parameters of graphite electrodes. They proposed that electron transfer between spatially aligned aromatic systems could contribute to the electronic conductivity by the assemblies. Also, the enhancement of electrochemical activity and the selectivity of peptide nanotube based electrodes can be used for the development of sensors and biosensors.[106]

In 2009, Stone and Stupp *et al.* reported novel peptidic quinquethiophene bolaamphiphiles which form 1D nanostructures consisting of π–π stacked thiophene core with amino acids.[5] In the paper, quinquethiophene was chosen as the central segment in the molecule due to its π–π stacking and conductive properties. Hydrogen bonding occurs over longer length scales than π–π stacking. Therefore, a flexible linker is necessary to facilitate simultaneous formation of β-sheets and π–π

stacking within a supramolecular nanostructure. The addition of an alkyl spacer was necessary to allow both π–π stacking and β-sheet formation to coexist. Without an alkyl spacer, π–π stacking was found to dominate the aggregation and suppress β-sheet formation. Spectroscopy indicated the occurrence of face-to-face packing among oligothiophene moieties. This material has been of great interest, especially in electronic materials, due to the fact that self-assembly can improve functionality due to the enforcement of the π-orbital overlap.

In 2008, Diegelmann *et al.* proposed that small peptide sequences could be used to form 1-D nanostructures which contained strong π–π intermolecular delocalisation (Figure 2.19). The small peptide sequences were embedded by π-conjugated segments internally in the backbone[4,107] They used circular dichroism (CD) and fluorescence to follow the self-assembly process. Understanding this assembly, in terms of the π-conjugated amino acids and peptide sequences, will allow us to engineer and evaluate electronically functional nanostructures in a rapid manner.

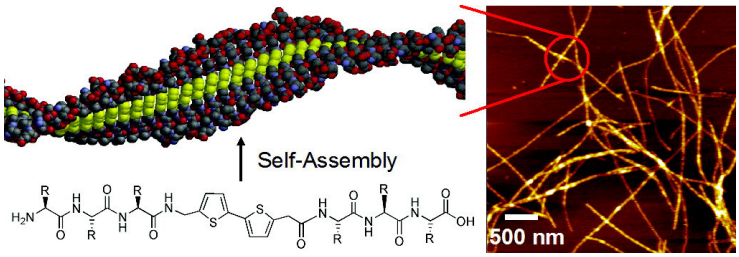

Figure 2.19 Energy-minimized illustration of b-sheets and -stacks as helical twist sense along a model aggregate. [Adapted from 107].

Recently, Parquette's group demonstrated self-assembled 1-D n-type nanostructures in which dopant atoms provided extra conduction electrons to the host material. These nanostructures were based on naphthalene diimide-appended dipeptides (dipeptide-NDI) and where the NDI acted as the dopant. They developed a strategy to produce π-electronic nanostructures from small, n-type organic building blocks in water. These n-type, 1D nanostructures were built by the β-sheet assembly of dipeptides bearing a 1,4,5,6-naphthalenetetracarboxylic acid diimide (NDI) side chain into either helical nanofibres or twisted nanoribbons. The hydrogen-bonding along the peptide backbone and π–π association of NDI chromophores strongly drives β-sheet assembly in

water. This assembly would be mitigated by the electrostatic repulsions of adjacent protonated lysines resulting in soluble, well-ordered nanostructures.[108] Furthermore, Parquette's group added Fmoc to dilysine peptide (Fmoc-KK(NDI)) which was functionalized at the ε-amino position with an NDI chromophore and an N-terminal fluorenylmethoxycarbonyl (Fmoc). The Fmoc-protecting group induced aqueous assembly into a self-supporting hydrogel composed of uniform 1D nanobelts. In this system, β-sheet self-assembly is driven by hydrophobic π–π association of both the NDI and Fmoc chromophores in aqueous media.[6] The arrangement of the structure sequesters the hydrophobic NDI chromophores within the interior of the assembly and projects the hydrophilic lysine side chains towards the aqueous interface as shown in Figure 2.20. The decreased absorption and emission intensities were observed indicating the presence of aggregates. The intermolecular π-delocalization between NDI and Fmoc should mediate long-range charge migration with potential application in optoelectronic and biomedical devices.

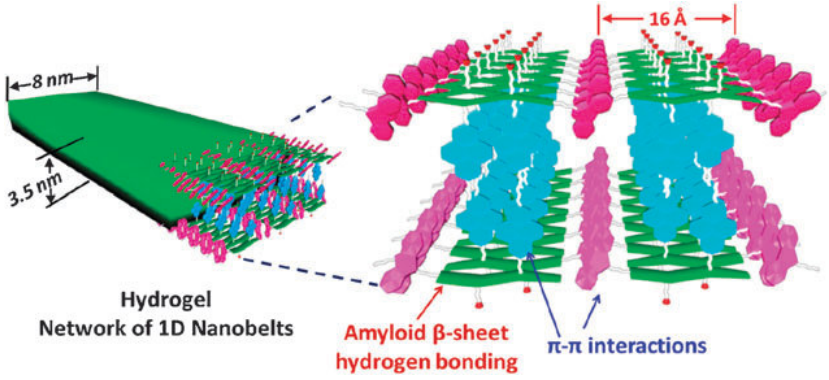

Figure 2.20 Schematic representation of the self-assembly of Fmoc-KK(NDI) into nanobelts [Adapted from 6].

2.5 ALIGNMENT OF SELF-ASSEMBLED PEPTIDE NANOSTRUCTURE

High-density and spatially-oriented arrays of nanostructures h are of relevance to many nanotechnological applications[109], such as molecular electronics, scaffolds for tissue engineering and patterned adhesives. Fabrication techniques for organized arrays of carbon[110] and inorganic nanostructures[111] are developing quickly. Some groups have already demonstrated the

application of aromatic peptide self-assembled nanostructures in the fabrication of metallic nanowires[9] and in the improvement of the sensitivity of electrochemical biosensors[112].

Gazit *et al.*[7] in 2006, was the first to report the alignment of self-assembled peptide nanotubes. They achieved the alignment by first dissolving the dipeptide monomeric building blocks in 1,1,1,3,3,3-hexafluoro-2-propanol (HFP) and then depositing the solution on a glass. A thin layer of peptide was formed on the glass as the HFP evaporated rapidly. This layer was found to contain aligned aromatic dipeptide nanoforests. Gazit also took a second approach of using attaching magnetic nanoparticles non-convalently to the walls of ADNTs via hydrophobic interactions. These magnetic-coated ADNTs horizontally aligned on exposure to a magnetic field, as illustrated in Figure 2.21. In 2009, the same group used a vapour deposition method to fabricate highly oriented, self-assembled aromatic dipeptide nanotubes (Cyclo-F-F). This vapour deposition approach allowed the nanotubes to be densely and homogeneously coated over a large area. The nanotubes arrays may be used in the future to develop high-surface-area electrodes for energy storage applications, highly hydrophobic self-cleaning surfaces and microfluidic chips.[113]

In 2007, Stupp *et al.* demonstrated the patterning of peptide amphiphile nanofibres self-assembled by soft lithography. By using this technique, the nanostructures self-assembled, oriented and patterned from solution via an elastomeric stamp with specific topographical features. The nanofibres oriented parallel to the channels and formed bundles of aligned nanofibres on the substrate after the stamp was removed.[114] In 2009, Stupp's group reported another large-area aligned patterning technique for self-assembled, supramolecular nanofibres of peptide amphiphiles (PA). These nanofibres were assembly within microchannels approximately 700 nm in width. Within these channels, the nanofibres were forced by steric repulsion to orient parallel to the channel direction.[115] This technique might be effective up to the micrometer length scale where patterned masters could be easily fabricated by photolithography.

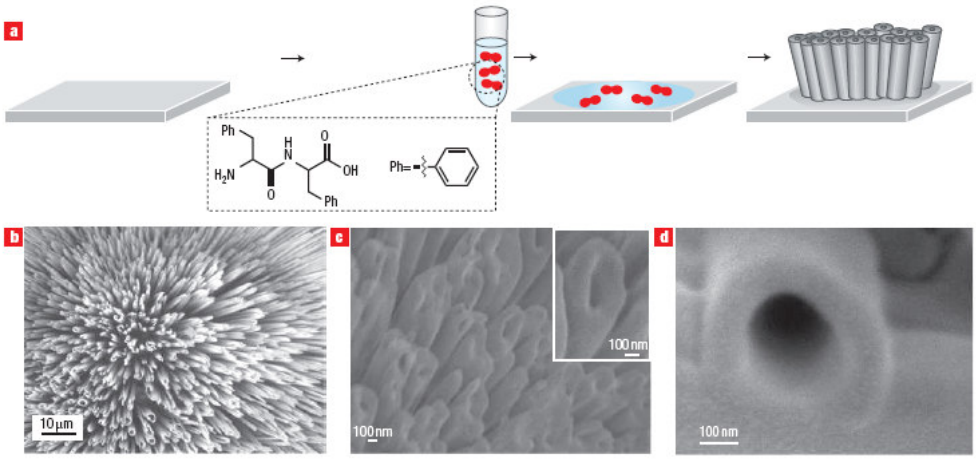

Figure 2.21 Vertically aligned diphenylalanine-based nanotubes self-assembled into a peptide nanoforest a, A possible model for the formation of the aligned peptide nanotubes array. Applying the dipeptide monomers dissolved in the organic solvent onto siliconized glass resulted in the formation of a vertically aligned array of peptide nanotubes. b, SEM analysis of the vertically aligned peptide nanotubes. c, Cold field-emission gun high-resolution scanning electron microscope (CFEG HRSEM) analysis of the nanotubes array. The inset represents higher magnification of the aligned nanotubes [Adapted from 7].

In 2008, Park and co-workers reported that amorphous peptide thin films could be aligned through vacuum desiccation. The initial amphorus films were prepared by drying a drop of peptide-1,1,1,3,3,3-hexafluoro-2-propanol (HFIP) solution on a Si substrate which was put in a vacuum desiccator due to the fact that water vapour could have affected the final surface structure of the peptide thin film. The vertically well-aligned peptide nanowires were grown by aging the film at temperatures of 150 ℃ within aniline vapour as shown in Figure 2.22. Furthermore, they simultaneously fabricated a micro-pattern of peptide nanowires by combining a simple soft-lithographic technique and the high-temperature aniline vapour-aging process. [116]

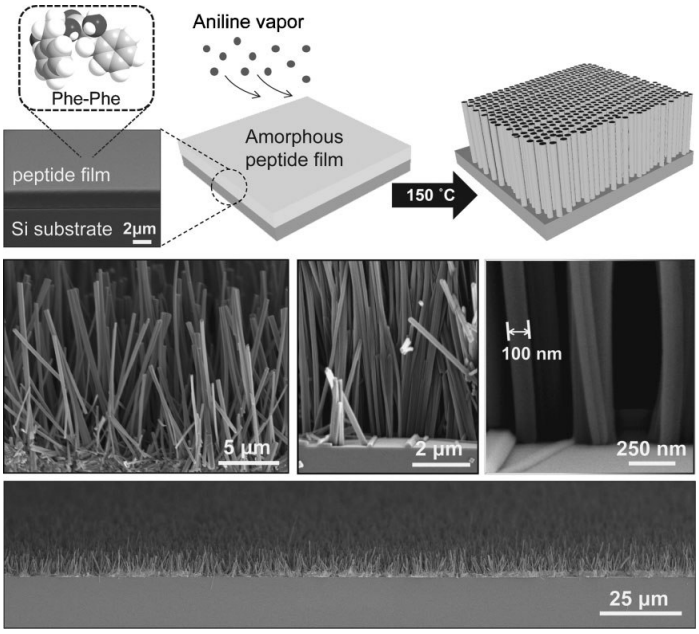

Figure 2.22 Experimental scheme and cross-sectional electron micrographs showing the growth of vertically well-aligned nanowires from amorphous peptide thin film by high-temperature aniline vapour aging [Adapted from 116].

Magnetic-field-induced alignment has been observed for amyloid fibrils, [117] and self-assembled anthracene organogel fibres. [118] Hest *et al*., in 2007, explored this kind of method to form aligned peptide amphiphile nanofibre assemblies. They organized low-molecular-weight peptide amphiphile-based nanoribbons under a high magnetic field. The fibrous structures were disassembled by heating, and then cooled down in a high magnetic field, which resulted in the alignment of the polymerizable peptide amphiphile assemblies. UV light irradiation was used to polymerize the diacetylenes in the alkyl chain of the peptide amphiphiles, which transferred the alignment of the monomeric amphiphiles into the chromophores, Figure 2.23. [119] In the same year, Tendler *et al.* also described aligning aromatic peptide tubes in magnetic fields of 12 T. [120] The magnetic alignment of prepared diphenylalanine (Phe-Phe peptide) tubes was investigated. The evaporated 1,1,1,3,3,3-hexafluoro-2-propanol (HFIP)-water solution was suspended with F-F peptide tubes in magnetic fields up to 12T (Figure 2.24). The F-F peptide tubes were found to align under a strong magnetic field (12 T) without any additional treatment. This alignment was due to the effect of the magnetic torque is associated with the diamagnetic anisotropy of the aromatic rings of phenylalanine.

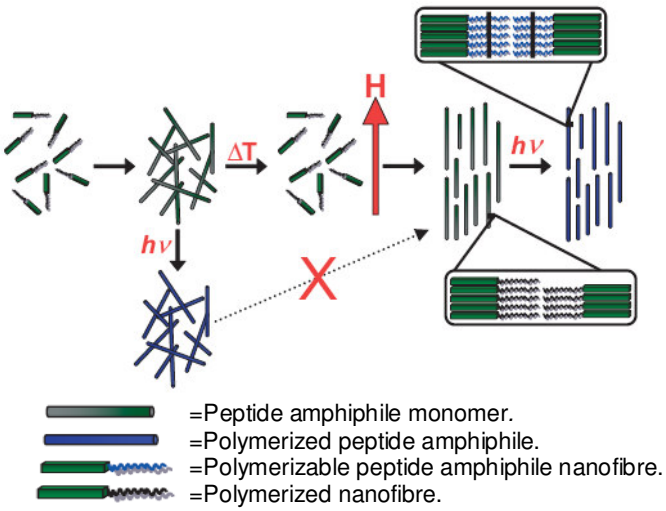

Figure 2.23 Schema of the process to obtain alignment peptide nanofibres at magnetic field and polymerization of peptide amphiphile assemblies. The red arrow indicates the direction of the magnetic field. [Adapted from 119].

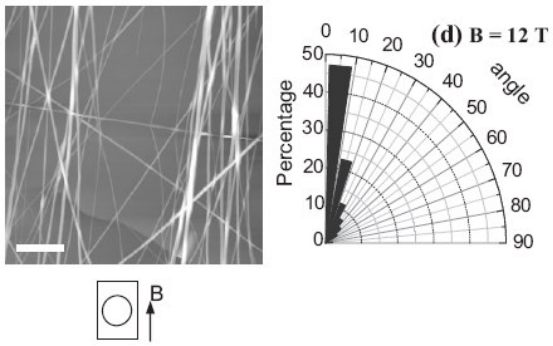

Figure 2.24 AFM topography images of the residues of droplets of HFIP water solution containing FF tubes, allowed to evaporate in applied magnetic fields at 12 T. The number of tubes falling into a particular bin is expressed as a percentage of the number of tubes counted [Adapted from 120].

Furthermore, other methods were applied in the alignment of nanostructures. For example, in 2007, Han and Kim introduced liquid crystalline peptide (NH_2-F-F dipeptide) nanowires obtained by the sonication of the dipeptide in carbon disulfide (CS_2) at ambient temperature. This lyotropic, nematic liquid crystalline phase allowed the rapid alignment of nanowires. Furthermore, immediate drying under an electric field yielded a well-aligned morphology of nanowires over a broad area.[8] Singh *et al.*, in 2008, obtained dipeptide (F-F) fibres by electrospinning from a highly

concentrated solution. The fibres were aligned simply by employing conductive substrates with sub-millimetre gaps.[121]

2.6 SUMMARY

There are three broad strategies for achieving organic electronic devices, depending on the size scale of the active element; molecular, supramolecule and plastic. The supramolecule approach relies on the assembly of molecular subunits into highly defined, relatively defect free structures. One approach to achieve such control is to build upon the extensive knowledge of self-assembly in peptide systems. The self-assembly of peptides and their derivatives is driven by weak intermolecular forces, such as hydrogen bonding, π-π interactions, and hydrophobic / hydrophilic interactions. A variety of different supramolecular structures, including nanotubes, nanofibrils, nanoribbons and nanowires, have been generated in both nature and in the laboratory. For example, the medical community have found that the self-assembly of mis-folded peptides into amyloid fibrils is a common characteristic of many neurodegenerative diseases. In each of these cases, cellular proteins undergo a self-assembly process to form large scale, ordered structures demonstrating predominantly β-sheet secondary structure. These same structures, though, are now being mimicked in the laboratory for a new generation of biomaterials to help cure disease.

Several methods have been used to control the self assembly process of peptides. In particular, the use of enzymes to initiate the self-assembly of small molecules under mild conditions has emerged as a powerful tool and discovery of peptide nanomaterials. Xu discovered a relatively new class of self-assembled systems, aromatic short peptide derivatives comprising of Fmoc-capped short chain peptide. These building blocks are amphiphiles, consisting of a highly hydrophobic Fmoc group and the polar peptides. They are believed to assemble via π–π interactions of the aromatic capping group resulting in self-assembled fibres. Fmoc-peptide self-assembly under kinetic control can be initiated by the enzymatic hydrolysis of methyl esters to produce gelators. However, such an approach may suffer from kinetically trapped defects. Therefore, an alternate approach under thermodynamic control has been developed in which an

enzyme catalyses amide bond formations (condensation). This condensation system is essentially irreversible, does not require heating and can form hydrogelators on a surface directly.

Despite the advantages of using biomolecular self-assembly approaches for the supramolecular electronics, the area is still relatively poorly studied. A key approach that has been taken in the field is to assembly peptides with aromatic motifs into fibres with the aim of overlapping the π-orbitals to achieve a delocalised electron system along the length of the fibre. In order for delocalisation to be successful, the aromatically groups need to be stacked with little defects and at a spacing of less than ~ 3.9 Å. In 1998, Mintmire *et al.* reported insulator cyclic peptide nanotubes which had a large distance of 4.73 Å between the aromatic rings. Redesigning the molecules, though, can improve this conductivity by enforcing the π-orbital overlap. For example, 1, 4, 5, 8-naphthalenetetracarboxylic acid diimide (NDI) side chain was added to cyclic peptide nanotubes to decrease the π–π stacking distance (~3.8 Å) and increase π-π intermolecular electronic communication. Furthermore, aromatic peptides amphiphile hydrogels, which coupled a variety of aromatic groups including phenyl and Fmoc to short peptides, have been studied for electronics applications. Hydrogelators consisting of aromatic moieties can also rely on aromatic-aromatic interaction to promote hydrogelation.

Highly ordered peptide supramolecular nanostructures formed by self-assembly have attracted significant interest because the alignment of the nanostructure could improve various properties including electronic and mechanical properties. Self-assembled peptide nanostructures have been aligned in special evaporated environments (such as HFP). Soft lithography, magnetic field, electronic field and electrospinning approaches have also been used to align the peptide nanostructures.

From the observations above, the conductivity of the self-assembled peptide supramolecular has to-date been studied only by modelling and spectroscopy techniques including fluorescence spectroscopy, circular dichroism (CD) and ultraviolet-visible spectroscopy (UV-Vis). Although charge transfer within an aromatic group will be monitored by fluorescence spectroscopy, peptide nanotubes are an insulator with large electronic band gap (4.7 eV) as calculated by using a first

principles. In order to explore new biomaterials for organic electronics, three main tasks should be solved: i) seek self-assembled peptide nanostructures based upon delocalised π electron systems formed by the efficient orbital overlap of aromatic groups within the material; ii) study the nanostructure/microstructure and conductivity of peptide nanostructures by using microscopy and proper electrical equipments and methods instead of only spectroscopy and calculations; iii) improve the conductivity of the nanostructure networks. These studies could move the biomaterials towards more conductive systems and devices applications.

The main focus of this work is to characterise the structure and conductivity of self-assembled Fmoc-peptides nanostructures. The nanostructure contains either aromatic or non-aromatic hydrophobic residues produced via the enzymatic (subtilisin or thermolysin) hydrolysis or condensation of precursors. Fluorescence spectroscopy, FT-IR and WAXS were used to characterise the resultant nanostructures. The morphology of the peptide nanostructures was also studied by using TEM, SEM and AFM. Impedance spectroscopy and I-V methods were used to evaluate the conductivity of the nanostructures. Finally, the conductivity of peptide nanotubes was improved further after peptide nanotubes were aligned in electronic field.

2.7 REFERENCES:

1. Y. Yamamoto, T. Fukushina, N. Ishii, A. Saeki, S. Seki, S. Tagawa, M. Taniguchi, T. Kawai, T. Aida, Photoconductive coaxial nanotubes of molecularly connected electron donor and acceptor layers, Science, 2006, 314, 1761-1764.
2. F. Fujimura, S. Kimura, Columnar assembly formation and metal binding of cyclic Tri-β-peptides having terpyridine ligands, Org. Lett., 2007, 793-796.
3. C. Daniel, F. Makereel, L. M. Herz, F. J. M. Hoeben, P. Jonkheijm, P. H. J. Schenning, E. W. Meijer, R. H. Friend, C. Silva, J. Chem. Phys., The effects of supramolecular assembly on exciation decay rates in organic semiconductors, 2005, 123, 084902.
4. S. R. Diegelmann, J. M. Gorham, J. D. Tovar, One-dimensional optoelectronic nanostructures derived from the aqueous self-assembly of π-conjugated oligopeptides, J. AM. CHEM. SOC., 2008, Vol. 130, No. 42, 13840-13841.
5. D. A. Stone, L. Hsu, S. I. Stupp, Self-assembling quinquethiophene-oligopeptide

hydrogelators, Soft Matter, 2009, 5, 1990-1993.

6. H. Shao, J. R. Parquette, A π-conjugated hydrogel based on an Fmoc-dipeptide naphthalene diimide semiconductor, Chem. Commun., 2010, 46, 4285-4287.
7. M. Reches, E. Gazit, Controlled patterning of aligned self-assembled peptide nanotubes, Nature Nanotechnology, 2006, Vol. 1, 195-200.
8. T. H. Han, J. Kim, J. S. Park, C. B. Park, h. Ihee, S. O. Kim, Liquid crystalline peptide nanowires, Adv. Mater. 2007, 19, 3924-3927.
9. M. Reches, E. Gazit, Casting metal nanowires within discrete self-assembled peptide nanotubes, Science, Vol. 300, 2003, 625-627.
10. M. Reches, E. Gazit, Designed aromatic homo-dipeptides: formation of ordered nanostructures and potential nanotechnological applications. Physical Biology, 2006, 3, S10-S19.
11. S. G. Zhang, X. J. Shao, Design of molecular biological materials using peptide motifs, Journal of materials chemistry, 2004, 4, 2082-2086.
12. R. J. Mart, R. D. Osborne, M. Stevens, R. V. Ulijn, Peptide-based stimuli-responsive biomaterials, Soft matter, 2006, 2, 822-835.
13. M. Swart, T. van der Wijst, C. F. Guerra, F. M. Bickelhaupt, π-π stacking tackled with density functional theory, J Mol Modle, 2007, 13, 1245-1257.
14. D. L. Nelson, M. M. Cox, Lehninger principles of biochemistry, 2rd ed. 2000, New York, Worth.
15. A. M. Smith, R. J. Willams, C. Tang, P. Coppo, R. F. Collins, M. L. Turner, A. Saiani, R. V. Ulijn, Fmoc-diphenylalanine self-assembles to a hydrogel via a novel architecture based on π-π interlocked β-sheets, 2008, Vol. 20, 37-41.
16. R. E. Dickerson, I. Geis, The structure and Action of Proteins, Harper & Row, New York, 1969.
17. M. Hashimoto, E. Masliah, Alpha-synuclein in Lewy body disease and Alzheimer's disease, *Brain Pathology*, 2004, 707-720.
18. Role of protein aggregation in mitochondrial dysfunction and neurodegeneration in Alzheimer's and Parkinson's diseases, *Neuromolecular Medicine*, 2003, 21-35.
19. Protein aggregation and neurodegenerative disease, C. A. Ross, M. A. Poirier, Neurodegeneration, 2004, S10-S16.
20. M. R. Ghadiri, J. R. Granja, R. A. Milligan, D. E. McRee, N. Khazanovich, Self-assembling organic nanotubes based on a cyclic peptide architecture, Nature, 1993, Vol. 366, 324-327.
21. Z. Yang, G. Liang, B. Xu, Supramolecular hydrogels based on b-amino acid derivatives, Chem. Common., 2006, 738-740.
22. P. De Santis, S. Morosetti, R. Rizzo, Conformational-analysis of regular enantiomeric sequences, Macromolecules, 1974, Vol. 7, 52-58.

23. M. R. Ghadiri, J. R. Granja, L. K. Buehler, Artificial transmembrane ion channels from self-assembling peptide nanotubes, Nature, 1994, Vol. 369, 301-304.
24. W. S. Horne, C. D. Stout, M. R. Ghadiri, A heterocyclic peptide nanotube, J. AM. CHEM. SOC., 2003, 125, 9372-9376.
25. J. Zhu, J. Cheng, Z. Liao, Z. Lai, B. Liu, Investigation of structures and properties of cyclic peptide nanotubes by experiment and molecular dynamics, J Comput Aided Mol Des, 2008, 22, 773-781.
26. E. Gazit, Self-assembly of short peptides for nanotechnological applications, NanoBioTechnology: BioInspired Devices and Materials of the Future, 385-395.
27. M. Reches, E. Gazit, Casting metal nanowires within discrete self-assembled peptide nanotubes, Science, 2003, 300, 625-627.
28. Y. Song, S. R. Challa, C. J. Medforth, Y. Qiu, R. K. Watt, D. Pena, J. E. Miller, F. V. Swol, J. A. Shelnutt, Synthesis of peptide-nanotube platinum-nanoparticle composites, 2004, Chem. Commun., 2004, 1044-1045.
29. P. Tamamis, L. Adler-Abramovich, M. Reches, K. Marshall, P. Sikorski, L. Serpell, E. Gazit, G. Archonits, Self-assembly of phenylalanine oligopeptides: insights from experiments and simulations, Biophysical Journal, Vol. 96, 2009, 5020-5029.
30. X. Yan, P. Zhu, J. Li, Self-assembly and application of diphenylalanine-based nanostructures, Chemical Society Review, 2010, Vol. 39, No. 6, 1861-2336.
31. J. D. Hartgerink, E. Beniash, S. I. Stupp, Self-assembly and mineralization of peptide-amphiphile nanofibres, Science, 2001, Vol. 294, 1684-1688.
32. J. C. Stendahl, M. S. Rao, M. O. Guler, S. I. Stupp, Intermolecular forces in the self-assembly of peptide amphiphile nanofibres, Adv. Funct. Mater., 2006, 16, 499-508.
33. S. Ghanaati, M. J. Webber, R. E. Unger, C. Orth, J. F. Hulvat, S. E. Kiehna, M. Barbeck, A. Rasic, S. I. Stupp, C. J. Kirkpatrick, Dynamic in vivo biocompatibility of angiogenic peptide amphiphile nanofibres, Biomaterials 2009, 30, 6202-6212.
34. H. Cui, T. Muraoka, A. G. Cheetham, S. I. Stupp, Self-assembly of giant peptide nanobelts, Nanoletters, 2009, Vol. 9, No.3, 945-951.
35. M. A. Greenfield, J. R. Hoffman, M. O. de la Cruz, S. I. Stupp, Tunable mechanics of peptide nanofibres gels, Langmuir, 2010, 26, 3641-3647.
36. E. T. Pashuck, H. Cui, S. I. Stupp, Tuning supramolecular rigidity of peptide fibres through molecular structure, J. AM. CHEM. SOC. 2010, 132, 6041-6046.
37. H. Cui, M. J. Webber, S. I. Stupp, Invited reveiew self-assembly of peptide amphiphiles: from molecules to nanostructures to biomaterials, PeptideScience, Vol. 94, 2009, 1-18.
38. A. P. Nowak, V. Breedveld, L. Pakstis, B. Ozbas, D. J. Pine, D. Pochan, T. J. Deming, Rapidly recovering hydrogel scaffolds from self-assembling diblock copolypeptide amphiphiles, Nature, 2002, Vol. 417, 424-428.

39. E. K. Elliott, M. M. Daschbach, G. W. Gokel, Aggregation behavior and dynamics of synthetic amphiphiles that self-assemble to anion transporters, Chem. Eur. J. 2008, 14, 5871-5879.
40. E. L. Rexeisen, W. Fan, T. O. Pangburn, R. R. Taribagil, F. S. Bates, T. P. Lodge, M. Tsapatsis, E. K.okkoli, Self-assembly of fibronectin mimetic peptide-amphiphile nanofibres, Langmuir, 2010, 26(3), 1953-1959.
41. R. Vegners, I. Shestakova, I. Kalvinsh, R. M. Ezzell, P. A. Janmey, Use of a gel-forming dipeptide derivative as a carrier for antigen presentation, Journal of Peptide Science, 1995, Vol. 1, 371-378.
42. Y. Zhang, H. Gu, Z. Yang, B. Xu, Supramolecular hydrogels respond to ligand – receptor interaction, J. AM. CHEM. SOC. 2003, 125, 13680-13681.
43. Z. Yang, K. Xu, L. Wang, H. Gu, H. Wei, M. Zhang, B. Xu, Self-assembly of small molecules affords multifunctional supramolecular hydrogels for topically treating simulated uranium wounds, Chem. Commun., 2005, 4414-4416.
44. Z. Yang, H. Gu, D. Fu, P. Gao, J. K. Lam, B. Xu, Enzymatic formation of supramolecular hydrogels, Advanced Materials, 2004, 16, 1440-1444.
45. V. Jayawarna, M. Ali, T. A. Jowitt, A. F. Miller, A. Saiani, J. E. Gough, R. V. Ulijn, Nanostructured hydrogels for three-dimensional cell culture through self-assembly of fluorenylmethoxycarbonyl-dipeptides, Adv. Mater, 2006, 18, 611-614.
46. A. M. Smith, R. J. WIliams, C. Tang, P. Coppo, R. F. Collins, M. L. Turner, A. Saiani, R. V. Ulijn, Fmoc-Diphenylalanine self assembles to a hydrogel via a novel architecture based on π-π interlocked β-sheets, Advance Materials, 2007, 1-5.
47. V. Jayawarna, S. M. Richardson, A. R. Hirst, N. W. Hodson, A. Saiani, J. E. Gough, R. V. Ulijn, Introducing chemical functionality in Fmoc-peptide gels for cell culture, Acta Biomaterialia, 2009, 5, 934-943.
48. C. Tang, A. M. Smith, R. F. Collins, R. V. Ulijn, A. Saiani, Fmoc-diphenylalanine self-assembly mechanism induces apparent pK_a shifts, Langmuir, 2009, 25, 9447-9453.
49. L. Chen, K. Morris, A. Laybourn, D. Elias, M. R. Hicks, A. Rodger, L. Serpell, D. J. Adams, Self-assembly mechanism for a naphthalene-dipeptide leading to hydrogelation, Langmuir, 2010, 26, 7, 5232-5242.
50. E. K. Johnson, D. J. Adams, P. J. Cameron, Directed self-assembly of dipeptides to form ultrathin hydrogel membranes, J. AM. CHEM. SOC., 2010, 132, 5130-5136.
51. A. Mahler, M. Reches, M. Rechter, S. Cohen, E. Gazit, Rigid, self-assembled hydrogel composed of a modified aromatic dipeptide, Adv. Mater. 2006, 18, 1365-1370.
52. R. Orbach, L. Adler-Abramovich, S. Zigerson, I. Mironi-Harpaz, D. Seliktar, E. Gazit, Self-assembled Fmoc-peptides as a platform for the formation of nanostructures and hydrogels, Biomacromolecules, 2009, 10, 2646-2651.

53. D. Bardelang, F. Camerel, J. C. Margeson, D. M. Leek, M. Schnutz, M. B. Zaman, K. Yu, D. V. Soldatov, R. Ziessel, C. I. Ratcliffe, J. A. Ripmeester, Unusual sculpting of dipeptide particles by ultrasound induces gelation, 10.1021/ja711342y
54. K. J. Channon, G. L. Devlin, S. W. Magennis, C. E. Finlayson, A. K. Tickler, C. Silva, C. E. Macphee, Modification of fluorophore photophysics through peptide-driven self-assembly, J. Am. Chem. Soc., 2008, 130, 16, 5487-5491.
55. X. Xu, C. Chen, B. Lu, S. Cheng, X. Zhang, R. Zhuo, Coassembly of oppositely charged short peptides into well-defined supramolecular hydrogels, J. Phys. Chem. B 2010, 114, 2365-2372.
56. S. Debnath, A. Shome, D. Das, P. K. Das, Hydrogelation through self-assembly of Fmoc-peptide functionalized cationic amphiphiles: potent antibacterial agent, J. Phys. Chem. B 2010, 114, 4407-4415.
57. Geoffrey L. Zubay, Biochemistry, 4th edition (1998), 177.
58. http://biochem.wustl.edu/~protease/ser_pro_overview.html
59. http://swift.cmbi.ru.nl/teach/B2/tln/chapter31.html
60. Z. Yang, H. Gu, D. Fu, P. Gao, J. K. Lam, B. Xu. Enzymatic formation of supramolecular hydrogels, Advanced Materials. 2004, 16, 1440-1444.
61. Z. Yang, G. Liang, M. Ma, Y. Gao, B. Xu, In vitro and in vivo enzymatic formation of supramolecular hydrogels based on self-assembled nanofibres of β-amino acid derivative, Small 2007, 3, 558-562.
62. Y. Gao, Y. Kuang, Z. Guo, Z. Guo, I. J. Krauss, B. Xu, Enzyme-instructed molecular self-assembly confers nanofibres and a supramolecular hydrogel of taxol derivative, J. AM. CHEM. SOC. 2009, 131, 13576-13577.
63. A. Laromaine, L. koh, M. Murugesan, R. V. Ulijn, M. M. Stevens, Protease-triggered dispersion of nanoparticle assemblies, J. AM. CHEM. SOC. 2007, 129, 4156-4157.
64. A. K. Das, R. Collins and R. V. Ulijn, Exploiting enzymatic (reversed) hydrolysis in directed self-assembly of peptide Nanostructures. Small, 2007, 4, 2, 279-287.
65. K. Thornton, A. M. Smith, C. L. R. merry, R. V. Ulijn, Controlling stiffness in nanostructured hydrogels produced by enzymatic dephosphorylation, Biochem. Soc. Trans. 2009, 37, 660-884.
66. Z. A. C. Schnepp, R. Gonzalez-McQuire, S. Mann, Hybrid Biocomposites based on calcium phosphate mineralization of self-assembled supramolecular hydrogels. Advanced Materials, 2006, 18, 1869-1872.
67. W. Wang, Z. Yang, S. Patanavanich, B. Xu, Y. Chau, Controlling self-assembly within nanospace for peptide nanoparticle fabrication, Soft Matter, 2008, 4, 1617-1620.
68. L. Wu, G. F. Payne, Biofabrication: using biological materials and biocatalysts to construct nanostructured assemblies, Trends in Biotechnology, 2004, Vol. 22, No. 11, 593-599.

69. J. J. Sperinde, L. G. Griffith, Synthesis and characterization of enzymatically-cross –linked poly(ethylene glycol) hydrogels, Macromolecules, 1997, Vol. 30, No. 18, 5255-5264.
70. A. K. Das, R. Collins, R. V. Ulijn, Exploiting enzymatic (reversed) hydrolysis in directed self-assembly of peptide nanostructures, Small, 2008, 4, 279-287.
71. R. F. Ludlow, S. Otto, Systems chemistry, Chem. Soc. Rev., 2008, Vol. 37, 101-108.
72. R. J. Williams, A. M. Smith, R. Collins, N. Hodson, A. K. Das and R. V. Ulijn, Enzyme-assisted self-assembly under thermodynamic control, Nature nanotechnology, 4, 2009, 19-24.
73. S. Winkler, D. Wilson, D. L. Kaplan, Controlling β-sheet assembly in genetically engineered silk by enzymatic phosphorylation/dephosphorylation, Biochemistry, 2000, 39, 12739-12746.
74. S. Toledano, R. J. Willams, V. Jayawama, R. V. Ulijn, Enzyme-triggered self-assembly of peptide hydrogels via reversed hydrolysis. J. Am. Chem. Soc. 2006, 128, 1070-1071.
75. Z. Yang, G. Liang, L. Wang, B. Xu, Using a kinase/phosphatase switch to regulate a supramolecular hydrogel and forming the supramolecular hydrogel in vivo. J. Am, Chem. Soc. 2006, 128, 3038-3043.
76. L. C Palmer, Y. S Velichko, M. O. De la Cruz, S. I. Stupp, Supramolecular self-assembly codes for functional structures, R. Soc. A, 2007, 365, 1417-1433.
77. J. Ryu, D. Hong, M. Lee, Aqueous self-assembly of aromatic rod building blocks, Chem. Commun., 2008, 1043-1054.
78. F. J. M. Hoeben, P. Jonkheijm, E. W. Meijer, A. P. H. J. Schenning, About supramolecular assemblies of pi-conjugated systems, Chem. Rev. 2005, 105, 1491-1546.
79. A. P. H. J. Schenning E. W. Meijer, Supramolecular electronics; nanowires from self-assembled π-conjugated systems, Chem. Commun, 2005, 3245.
80. M. Layachi, Y. Savaria, The effect of pi-coupling on the electronic properties of 1,4-Dithiol benzene stacking, Proceeding of the 2004 international conference on MEMS, NANO and Smart Systems (ICMENS'04).
81. H. Mansikkamaki, M. Nissinen, K. Rissanen, Noncovalent pi-pi stacked exo-functional nanotubes: subtle control of resorcinarene self-assembly, Angew, Chem. Int. Ed., 2004, 43, 1243-1246.
82. T. Yamamoto, T. Fukushima, Y. Yamamoto, A. Kosaka, W. Jin, N. Ishii, T. Aida, Stabilization of a kinetically favored nanostructure: surface romp of self-assembled conductive nanocoils from a norbornene-appended hexa-peri-hexabenzocoronene, J. AM. CHEM. SOC. 2006, 128, 14337-14340.
83. M. Huang, U. Schilde, M. Kumke, M. Antonietti, H. Colfen, Polymer-induced self-assembly of small organic molecules into ultralong microbelts with electronic conductivity, J. AM.CHEM. SOC. 2010, 132, 3700-3707.

84. N. Sakai, R. Bhosale, D. Emery, J. mareda, S. Matile, Supramolecular n/p-heterojunction photosystems with antiparallel redox gradients in electron- and hole- transporting pathways, J. AM. CHEM. SOC., 2010, 132, 6923-6925.
85. V. D. Lakhno, DNA Nanobioelectronics, International Journal of Quantum Chemistry, 2008, Vol 108, 1970-1981.
86. H. Watanabe, K. Shimotani, T. Shigematu, C. Manabe, Electric measurements of nano-scaled devices, Thin Solid Films, 2003, 462-466.
87. M. R. Singh, Charge conduction in biomaterials: Application to DNA structures, Photonics North, 2007, Proc. Of SPIE Vol. 6796, 67960s-1-12.
88. D. D. Ellley, D. I. Spivey, Semiconductivity of organic substance, Trans Faraday Soc. 1962, 58, 411-415.
89. Y. Long, C. Li, H. Kraatz, J. S. Lee, AC impedance spectroscopy of native DNA and M-DNA, Biophysical journal 84 (5) 3218-3225.
90. H. Watanabe, K. Shimotani, T. Shigematu, C. Manabe, Thin Solid Films, 2003, 462-466.
91. I. Kratochvilova, K. Kral, M. Buncek, S. Nespurek, T. Todorcluc, M. Welter, J. navratil, B. Schnelder, J. Pavluch, Scanning Tunneling spectroscopy study of DNA conductivity, Cent. Eur. J. Phys. 6(3), 2008, 422-426.
92. D. Porath, A. Bezryadln, S. De Vrles, C. Dekker, Direct measurement of electrical transport through DNA molecules, Nature, 2000, Vol. 403, 635-638.
93. H. Watanabe, C. Manabe, T. Shigematsu, K. Shimotani, M. Shimizu, Single molecule DNA device measured with triple-probe atomic force microscope, Appl. Phys. Lett., Vol. 79, No. 15, 2001, 2642-2644.
94. A. Noy, A. B. Artyukhin, N. Misra, Bionanoelectronics with 1D materials, Materials Today, 2009, Vol. 12, 22-3.
95. R. A. Jishi, N. C. Braier, C. T. White, and J. W. Mintmire, Peptide nanotubes: An inert environment, The American Physical Society, 1998, 58, R16009-R16011.
96. R. Takahashi, H. Wang, and J. P. Lewis, Electronic structures and conductivity in peptide nnaotubes, J. Phys. Chem. B 2007, 111, 9093-9098.
97. H. Okamoto, T. Nakanishi, Y. Nagai, M. Kasahara, K. Takeda, Variety of the molecular conformation in peptide nanorings and nanotubes, J. Am. Chem. Soc. 2003, 125, 2756-2769.
98. E. Gazit, Self-assembled peptide nanostructures: the design of molecular building blocks and their technological utilization, Chem. Soc. Rev., 2007, 36, 1263-1269.
99. W. S. Horne, N. Ashkenasy, and M. R. Ghadiri, Modulating charge transfer through cyclic D,L- -peptide self-assembly, Chem, Eur, J. 2005, 11, 1137-1144.
100. N. Ashkenasy, W. S. Horne, and M. R. Ghadiri, Design of self-assembling peptide nanotubes with delocalized electronic states, Small, 2006, 2, 99-102.

101. J. D. Tovar, B. M. Rabatic, S. I. Stupp, Conducting polymers confined within bioactive peptide amphiphile nanostructures, Small, 2007, 3, No. 12, 2024-2028.
102. L. Hsu, G. L. Cvetanovich, S. I. Stupp, Peptide amphiphile nanofibres with conjugated polydiacetylene backbones in their core, J. AM. CHEM. SOC. 2008, 130, 3892-3899.
103. W. Tsai, L. Li, H. Cui, H. Jiang, S. I. Stupp, Self-assembly of amphiphiles with terthiophene and tripeptide segments into helical nanostructures, Tetrahedron, 2008, 64, 8504-8514.
104. R. Matmour, I. De Cat, S. J. George, W. Adriaens, P. Leclere, P. H. H. Bomans, N. A. J. M. Sommerdijk, J. C. Gielen, P. C. M. Christianen, J. T. Heldens, J. C. M. V. Hest, D. W. P. M. Lowik, S. De Feyter, E. W. Meijer, A. P. H. J. Schenning, Oligo(p-phenylenevinylene)-peptide conjugates : synthesis and self-assembly in solution and at solid-liquid interface, J. AM. CHEM. SOC., 2008, 130, 14576-14583.
105. C. G. Claessens, J. F. Stoddart, Reveiw commentary π-π interactions in self-assembly, Journal of Physical organic chemistry, 1997, Vol. 10, 254-272.
106. M. Yemini, M. Reches, J. Rishpon, D. Gazit, Novel electrochemical biosensing plattorm using self-assemble peptide nanotubes, Nanoletters, 2005, 5, 183-186.
107. G. S. Vadehra, B. D. Wall, S. R. Diegelmann, J. D. Rovar, On-resin dimerization incorporates a diverse array of pi-conjugated functionality within aqueous self-assembling peptide backbones, Chem. Commun., 2010, 46, 3947-3949.
108. H. Shao, T. Nguyen, N. C. Romano, D. A. Modarelli, J. R. Parquette, Self-assembly of 1-D n-type nanostructures based on naphthalene diimide-appended dipeptides, J. AM. CHEM. SOC. 2009, 131, 16374-16376.
109. Z. H. Zhong, D. L. Wang, Y. Cui, M. W. Bockrath, C. M. Lieber, Nanowire crossbar arrays as address decoders for integrated nanosystems. Science, 2003 302, 1377-1379.
110. W. Z. Li, S. S. Xie, L. X. Qian, B. H. Chang, B. S. Zou, W. Y. Zhou, R. A. Zhao, G. Wang, Large-scale synthesis of aligned carbon nanotubes, Science, 1996, Vol. 274, 1701-1703.
111. T. Thurn- Albrecht, J. Schotter, C. A. Kastle, N. Emley, T. Shibauchi, L. Krusin-Eibaum, C. T. Black, M. T. Tuominen, T. P. Russell, Ultrahigh-density nanowire arrays grown in self-assembled diblock copolymer templates, Science, 2000, Vol. 290, 2126-2129.
112. M. Yemini, M. Reches, J. Rishpon, E. Gazit, Novel electrochemical biosensing platform using self-assembled peptide nanotubes. Nano Lett., 2005, 5, 183-186.
113. L. Adler-Abramovich, D. Aronov, P. Beker, M. Yevnin, S. Stempler, L. Buzhansky, G. Rosenman, E. Gazit, Self-assembled arrays of peptide nanotubes by vapour deposition, Nature Nanotechnology, 2009, Vol. 4, 849-854.
114. A. M. Hung, S. I. Stupp, Simultaneous Self-Assembly, Orientation, and Patterning of Peptide-Amphiphile Nanofibres by Soft Lithography, NanoLetters, 2007, 7, 1165-1171.
115. A. M. Hung, S. I. Stupp, Understanding factors affecting alignment of self-assembling nanofibres patterned by sonication-assisted solution embossing, Langmuir, 2009, 25 (12),

7084-7089.

116. J. Ryu, C. B. Park, High-temperature self-assembly of peptides into vertically well-aligned nanowires by aniline vapor, Adv. Mater., 2008, 20, 3754-3758.
117. H. Inouye, P. E. Fraser, D. A. Kirschner, Structure of β-crystallite assemblies by Alzheimer β-amyloid protein analogues: analysis by X-ray diffraction, Biophys. J. 1993, 502-519.
118. I. O. Shklyarevsky, P. Jonkheijm, P. C. M. Christianen, A. P. H. J. Schenning, A. D. Guerzo, J. Desvergne, E. W. Meijer, J. C. Maan, Magnetic alignment of self-assembled anthracene organogel fibres, Langmuir, 2005, 21, 2108-2112.
119. D. W. P. M. Lowik, I. O. Shklyarevskiy, L. Ruizendaal, P. C. M. Christianen, J. C. Maan, J. C. M. Van Hest, A highly ordered material from magnetically aligned peptide amphiphile nanofibre assemblies, Advanced Materials, 2007, 19, 1191-1195.
120. R. J. A. Hill, V. L. Sedman, S. Allen, P. M. Willians, M. Paoli, L. Adler-Abramovich, E. Gazit, L. Eaves, S. J. B. Tendler, Alignment of aromatic peptide tubes in strong magnetic fields, Advanced Materials, 2007, 19, 4474-4479.
121. G. Singh, A. M. Bittner, S. Loscher, N. Malinowski, K. Kern, Electrospinning of diphenylalanine nanotubes, Adv. Mater., 2008, 20, 2332-2336.

CHAPTER 3 EXPERIMENTAL METHODS

3.1 MATERIALS AND METHODS

3.1.1 Suppliers

The majority of reagents used were purchased from commercial sources (Sigma-Aldrich, UK and Bachem, Germany) at the highest purity available (≥ 98 %) and were used as supplied, unless stated otherwise in the experimental procedures. Fmoc-amino acids (Fmoc-L, Fmoc-W, Fmoc-Y, Fmoc-T, Fmoc-S) and amino acid methyl esters (L-OMe, F-OMe) were supplied by Sigma-Aldrich and Bachem. Alcalase 2.4 L (10 µL/mL) (subtilisin) from Bacillus licheniformis was supplied by Sigma Aldrich. Thermolysin was supplied by Sigma Aldrich in the form of a lyophilized powder from Bacillus thermoproteolyticus rokko at 40 units per mg. Fmoc-L_3-OMe was purchased from C S Bio Co., USA and its purity was verified as > 99 % by using high performance liquid chromatography (HPLC) and mass spectroscopy (MS). HPLC grade water, deuterium and acetonitrile were supplied by Sigma Aldrich.

The Fmoc group was used for N-terminal protection and the C-terminus was protected by a methyl ester. Couplings were mediated by N,N,N',N'-O-(1H-benzotriazol-1-yl)uroniumhexafluorophosphate (HBTU) that was supplied by Sigma Aldrich. The final products were purified by column chromatography using silica gel (60 mesh size) as the stationary phase and chloroform-methanol (9:1) mixture as the eluent.

3.1.2 Synthesis

Fmoc-LL-OMe:

The synthesis method followed that of Das et al. Fmoc-L-OH (0.706 g, 2 mmol) was dissolved in dichloromethane (DCM) (15 mL) in an ice-water bath. Leucine methyl ester hydrochloride (0.726 g, 4 mmol) was added to the reaction mixture, followed immediately by N,N-disopropylethylmine (DIPEA) (0.697 mL, 4 mmol) and HBTU (0.758 g, 2 mmol). The reaction mixture was allowed to warm to room temperature and then stirred for twenty four hours. The DCM was evaporated by

rotary evaporation, the residue was taken up in ethyl acetate (60 mL) and the precipitate was filtered out. The organic layer was washed first with 1 M HCl (2 × 50 mL), and 1 M sodium bicarbonate (2 × 50 mL), and then brine (1 × 50 mL) and dried over anhydrous magnesium sulphate. Finally, the solution was evaporated in a vacuum to yield Fmoc-LL-OMe as white powder. The product was purified using a silica gel column (60 mesh) and chloroform-methanol (9:1) as the eluent. The synthesis of the Fmoc-WL-OMe and Fmoc-YL-OMe followed the same procedure as for Fmoc-WL-OMe.

3.2 METHODS

3.2.1 Formation of the hydrogels

3.2.1.1 Hydrogels via ester hydrolysis

Hydrogels of Fmoc-LL, Fmoc-WL, and Fmoc-YL were prepared via the hydrolysis of the corresponding methyl ester (Fmoc-LL-OMe, Fmoc-WL-OMe, and Fmoc-YL-OMe) using the enzyme alcalase 2.4 L from Bacillus licheniformis (Scheme 3.1).

20 mmol of Fmoc-peptide ester was suspended in 2 ml of 0.1 M phosphate buffer at pH 8 in a glass vial. Alcalase 2.4 L (10 µL/mL) (subtilisin) was added to the suspension of the Fmoc-peptide esters in phosphate buffer. The resulting solution was heated at 55 ºC to produce a homogenous solution. Stable gels were found to form upon cooling.

Fmoc-L_3 hydrogels were also prepared via the hydrolysis of methyl ester using alcalase 2.4 L from *Bacillus licheniformis*. 40 µmol of Fmoc-L_3-OMe was suspended in 2 ml of 0.1 M phosphate buffer at pH 8 in a glass vial. Alcalase 2.4 L (10 µl/mL) (subtilisin ≥ 2.4 U/g, Sigma P4860) was added to the suspension of Fmoc-peptide esters in a phosphate buffer. The resulting solution was heated at 55 ℃ for two hours to produce gel-phase structures. The resultant Fmoc-peptide hydrogels were then characterized by measuring the concentration of the constituent molecular components via HPLC to confirm the gelators involved. The HPLC methodology is described in section 3.2.2.5.

3.2.1.2 Hydrogels via reversed hydrolysis

The "reversed hydrolysis" hydrogels were prepared via reverse hydrolysis using thermolysin as a catalyst. 20 mmol/L of Fmoc-amino acid and 80 mmol/L of amino acid methyl ester hydrochloride were solubilised in 2 mL of 0.1 mol sodium phosphate buffer at pH 8. No hydrogel formation was observed prior to the addition of the enzyme. Upon addition of 1 mg of thermolysin, a hydrogel was observed around five hours after the formation of Fmoc-dipeptide-methyl ester at room temperature (25 ℃).

3.2.2 Characterization techniques

3.2.2.1 Atomic Force Microscopy (AFM)

Atomic force microscopic images were obtained using a VEECO Multimode Atomic force Microscope (AFM) with a Nanoscope IIIa controller and an 'E' scanner. Olympus high aspect ratio, etched silicon probes with a spring constant of 42 N/m were used. The cantilever oscillation was varied between 300 and 350 kHz. The peptide hydrogels were diluted to a final concentration of 1 mg/mL in deionized, double-distilled water. The nanostructures were found not to be damaged by the AFM imaging. The AFM samples were prepared by dropping 100 μL of 1.25 mg/mL peptide hydrogel solution onto a freshly cleaved mica substrate and then 60 s later blotting the drop using filter paper. (The cleaved mica surfaces were prepared by peeling off the top layer of mica with adhesive tape immediately prior to sample deposition.) The peptide nanostructures were imaged in air by tapping mode.

3.2.2.2 Cryogenic temperature Transmission Electron Microscopy (Cryo-TEM)

3 μL of 20 mmol/L hydrogel was deposited onto a holey carbon grid that was held by forceps in the humidity chamber of a GATAN cryo-plunge unit. The grid was then blotted for around 20 seconds to give a thin film with a thickness of between 100-200 nm. The grid was then plunged into liquid ethane which was at a temperature of < -170 ^{o}C and the grid transferred to a GATAN 626 cryo-holder for examination. (The temperature of the holder was also kept below -170 ^{o}C.) The sample was analyzed using a JEOL 2100 TEM operating at 100 kV. Representative areas

were recorded using a GATAN 4 K Ultrascan camera and analysed using the Digital Micrograph software.

3.2.2.3 Fourier transform infrared spectroscopy (FT-IR spectra)

FT-IR spectra were collected on a Nicolet 5700 FT-IR spectrophotometer and analyzed using the Omnic software. The hydrogel samples were measured at a concentration of 20 mmol/L by placing them between crystal zinc selenium plates. Spectra were collected between the wave numbers of 4000 and 400 cm^{-1} over 128 scans at a resolution of 4 cm^{-1} and an interval of 1.9285 cm^{-1}.

3.2.2.4 Fluorescence Spectroscopy

The fluorescence emission spectra of the dried films and hydrogels were measured on a Jasco FP-6500 spectrofluorometer with the light measured orthogonally to the excitation light at a scanning speed of 100 nm min^{-1} and a response of 1 second, with excitation at 280 nm and an emission data range of between 300 and 500 nm. The spectra were measured using a bandwidth of 5 nm with a medium response and a 1 nm data pitch. The hydrogel samples were prepared as described above and placed in a 5 mL UV quartz curvette. Dried films were prepared by spreading the hydrogels onto a quartz slide and leaving them to dry. The quartz slide was then put onto the slide holder for measurement.

3.2.2.5 High-performance liquid chromatography (or High pressure liquid chromatography, HPLC)

A Dionex P680 pump with a Macherey-Nagel C18 column (length: 250 mm, internal diameter: 4.6 mm, fused silica particles: 5 µm) was used to verify the purity of the Fmoc-peptides and their reactions. 50 µL of a hydrogel or peptide solution was dissolved into an acetronitrile/water mixture (950 µL, 50:50 mixture) containing 0.1% trifluoroacetic acid. The samples were filtered through a 0.45 µm syringe filter (Whatman, 150 units, 13 mm diameter, 2.7 µm pore size) and then 100 µL of the sample was injected into the column at a flow rate of 1 mL/minute. The gradient was linear to 20 %(v/v) acetonitrile in water at 4 minutes; gradually rising to 80 %(v/v) actonitrile in water at

35 minutes. This concentration was kept constant until 40 min, at which time the gradient was decreased to 20 %(v/v) acetonitrile in water at 42 min. The purity of each identified peak was determined by UV spectroscopy at 280 nm. The peak retention times and peak areas were compared with known standards. The absorbance of Fmoc group was measured at a wavelength of 310 nm. The data was recorded by Solvent Rack SOR-100.

3.2.2.6 Impedance Spectroscopy

The complex impedance of the dried networks were measured by using a Solartron 1255 frequency response analyser over a frequency range of 0.1 to 10^7 Hz. The measurement was carried out with a two terminal set-up. The formation of the networks could be controlled by a combination of random percolation. The deposition and drying conditions were used to prepare the sample.

In the experiments where the electrical conductivity of different network gelators were studied, 100 µL of the Fmoc-LL, Fmoc-L_3, Fmoc-WL, Fmoc-YL (20 mmol/L) hydrogels were deposited onto a glass slide. The hydrogels were then spread out to cover the entire slide in order to create a uniform coating on the glass. The peptide films were then dried in a dry box at room temperature for two days. The repeatability in this sample preparation procedure was studied by measuring the properties of three different samples and an error on the mean of 33 % was found in their resistance. The effect of network density, i.e. mass deposited per unit area, was studied by depositing 100 µL of Fmoc-L_3 hydrogel with concentrations between 20 and 400 nmol and then drying the sample as described above.

Gold electrodes were thermally evaporated directly on top of the dried film through a shadow mask. The electrode spacing ranged from 1 mm to 3 mm. The length of the electrodes was 12 mm as shown in Figures 3.1 and 3.2 a. Platinum film was then used to connect the electrodes to the impedance spectrometer using crocodile clips (Figure 3.2 b).

As discussed in section 4.3, the resistance of a given network is the resistance measured for that sample. The resistivity is the intrinsic property and is independent of the geometry. The cross-

sectional area of the sample needs to be known in order to calculate the resistivity. However, as the peptide networks were very porous, it was hard to relate their thickness to their cross-sectional area. Therefore, the sheet resistance of the networks was measured. The sheet resistance is explained in more detail in section 3.2.4.3. Briefly, it is the resistance of a thin film where the thickness of the film is not considered. Sheet resistance is a standard measurement in the semiconducting industry where a film of a certain resistance is needed, regardless of the film's thickness. Sheet resistance does clearly vary with sample thickness. Therefore, the preparation procedures described above were chosen to minimise variation in the film thickness between samples. It is possible to convert from sheet resistance to the resistivity if the film thickness is known. For particular samples, where the thickness was measured directly (Section 3.2.2.9), this conversion to resistivity was performed and tabulated.

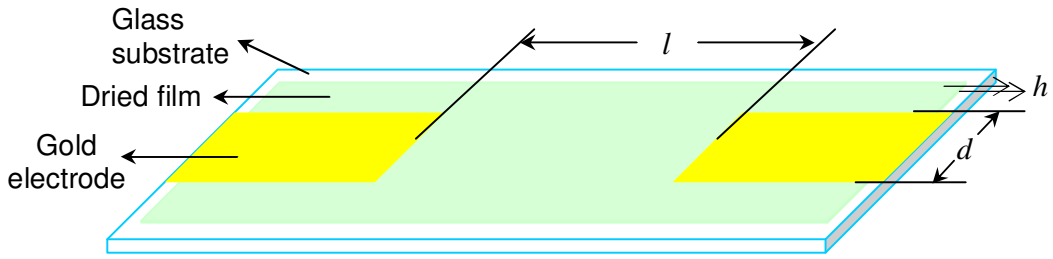

Figure 3.1 Schematic representation of the sample used to measure electrical resistivity. l -- electrode distance, d -- electrode width, h --thickness of the film.

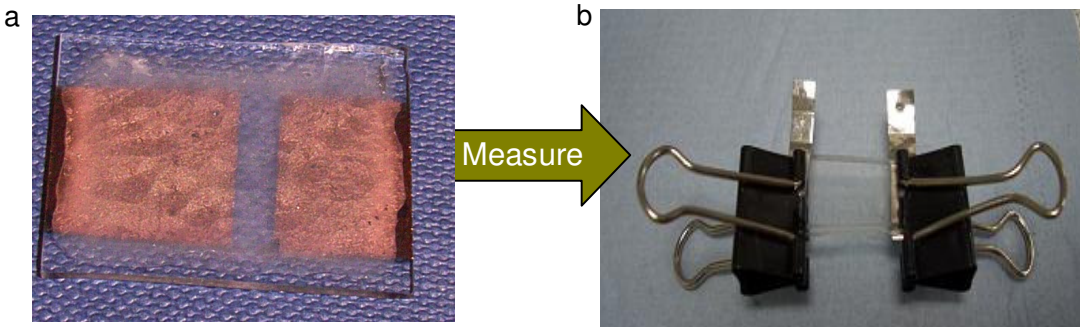

Figure 3.2 Sample preparation for conductivity measurement: a) A dried peptide film with gold electrodes. b) The platinum wire contacts on the electrodes.

3.2.2.7 I-V curve

The I-V response of the samples was measured on a BASI Epsilon electrochemical workstation at a scan rate of 1000 mV/s under different conditions, including at room temperature and under vacuum (a vacuum of 1.03 mbar pressure was achieved using a diaphragm oil free vacuum pump).

3.2.2.8 Scanning Electron Microscopy (SEM)

The measurements were conducted on a Philips FEG-SEM XL30 instrument using a typical voltage of 5 kV. SEM samples were prepared by dropping 20 µL of 20 mM peptide hydrogel onto silicon substrates. The dried samples were sputter-coated with gold.

3.2.2.9 Thickness measurement

Surface mapping microscopy was performed to determine the thickness of the films. The samples were prepared as described in the impedance section. The thickness of the films was measured by first making a scratch across the dried films so that the relative height between the substrate and the top of the film could be measured (Figure 3.3). This scratch was ~ 50 µm wide and 1 cm long. The thickness of the films was found to be 5 -15 µm depending on the gel used. The film thickness of a given sample was found to be similar under air and vacuum.

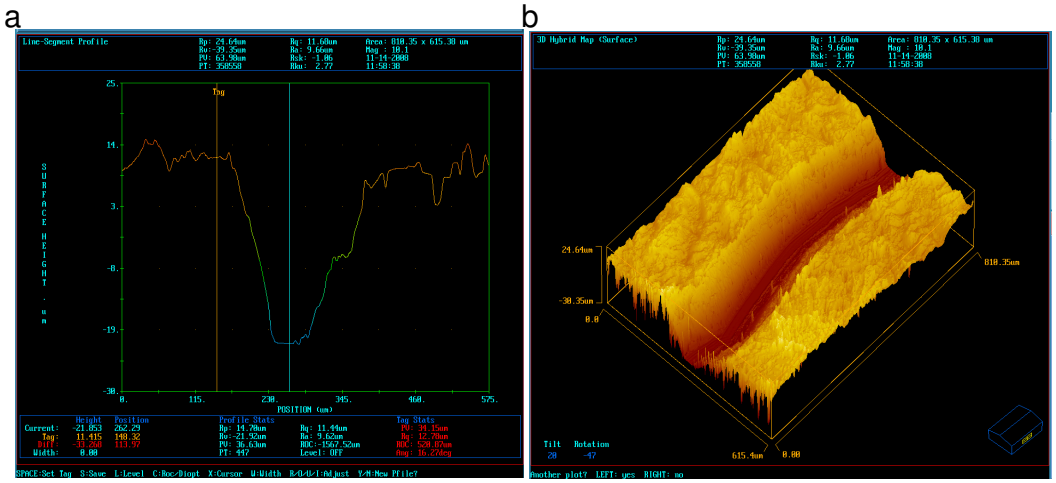

Figure 3.3 a, Surface mapping curve of the scratched film, b, 3D micrograph of scratched film

3.2.2.10 Transmission Electron Microscopy (TEM)

Carbon-coated copper grids (400 mesh) were functionalized by glow discharge for 30 s and then placed shiny-side down on the surface of 10 µL hydrogel (20 mmol/L) for 10 s and blotted. Excess gel was removed by placing a 10 µL droplet of HPLC water onto the samples for 60 seconds and then blotted again. Finally, the washed grids were stained by placing on a 10 µL droplet of freshly prepared and filtered 2% (w/v) uranyl acetate on to the sample for 60 s following by blotting by Whatman 50 filter paper. The samples were studied in a Tecnai 10 TEM operating at 100 kV (calibrated magnification of × 43,600) with images recorded on a Kodak SO-163 film. Images recorded on the microscopy were subsequently scanned using a UMAX2000 transmission scanner at a resolution of 3.66 Å/pixel.

3.2.2.11 Ultraviolet (UV) and visible (Vis) spectroscopy (UV-Vis)

50 µL of hydrogel was deposited on a quartz slide and dried. UV-Vis-NIR absorption spectra of the dried films were recorded on a Varian Cary 5000 UV-Vis-NIR spectrophotometer at a scanning speed of 600 nm/min between the wavelengths of 300 and 3000 nm.

3.2.2.12 Wide Angle X-ray Scattering (WAXS)

WAXS analysis was performed using a Philips X'Pert diffractometer with a wavelength of 1.5406 Å. Hydrogels and buffer solution were spread onto silica substrates as films and allowed to dry under ambient conditions prior to data collection.

3.2.3 Background of electrical conductivity

3.2.3.1 Ohm's law

Ohm's law states that:

$$V = IR \tag{3.1}$$

where, *R* is the resistance of the material through which the current is passing, *V* is the potential across the sample and *I* is the current. *R* is related to the geometry of the sample, whereas the resistivity of the sample, ρ , is the intrinsic physical property of the material:

$$\rho = \frac{RA}{l} \tag{3.2}$$

where l is the distance between the two points at which the voltage is measured, and *A* is the cross-sectional area perpendicular to the direction of the current, as shown in Figure 3.4. Electrical conductivity, σ **,** is then given by:

$$\sigma = \frac{1}{\rho} \tag{3.3}$$

Thus Ohm's law can be expressed in turns of geometry independent parameters:

$$J = \sigma\varepsilon \tag{3.4}$$

where, *J* is the current density, the current per unit of specimen area *I/A*; and ε is the electric field intensity, or the voltage difference between two points divided by the distance separating them,[1] reading as,

$$\varepsilon = \frac{V}{l}. \tag{3.5}$$

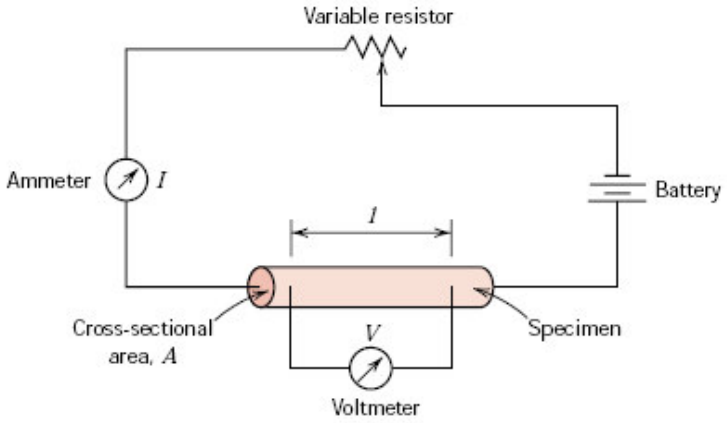

Figure 3.4 Schematic representation of the apparatus of the apparatus used to measure electrical resistivity. [Adapted from 1]

3.2.3.2 Electric and ionic conduction

The motion of electrically charged particles in an applied electric field results in an electric current. Positively charged particles are accelerated in the direction of the field whilst negatively charged particles accelerate in the opposite direction. For most solid materials, current comes from the flow of electrons, which is called electronic conduction. Whereas in some materials, there is a migration or diffusion of cations or anions under the applied electric field, this phenomenon is known as ionic conduction.

3.2.3.3 Energy band structures in solids

The magnitude of the electrical conductivity of a material depends strongly on the number of electrons that can participate in the conduction process. Not all electrons in every atom will be accelerated under an electric field. The arrangement of the electron states will determine the available number of electrons for electrical conduction. These states can be split into either (i) valence states; where the electrons are involved in inter-atomic bonding and hence cannot move and (ii) conduction bands; in which there are empty states for the electrons to move into. The electrical properties of a solid material therefore depend on the outermost electron band structure and the way in which these bands are filled with electrons. There are four different types of band structures at a temperature of 0 K: (i) one outermost band that is only partially filled with

electrons, (i.e. some metals such as copper); (ii) there is an overlap of an empty band and a filled band,(i.e. metals such as magnesium); structures (iii) and (iv) are similar in that one band (the valence band) is completely filled with electrons and there is a separate empty conduction band with an energy band gap between the two bands. Insulators have a large band gap, while the band gap of semiconductor is relatively narrow (1-3 eV) (Figure 3.5)[1]. This band gap energy can fall within the optical range and thus can be measured from the UV absorption measurements. An alternate method for understanding the conductivity of semiconductors as function of temperature is plot an Arrhenius plot of temperature versus conductivity, so that the band gap is in effect defined by an activation energy. For an intrinsic semiconductor, the activation energy is half of the band gap. For example, a doped CdSe thin film can have a band gap of 1.67 eV and an activation energy 0.34 eV.[2]

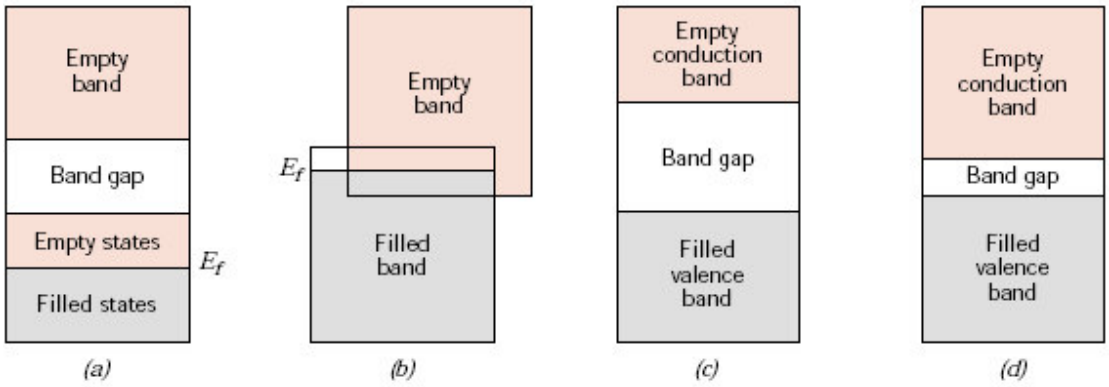

Figure 3.5 The various possible electron band structures in solids at 0 K: (a) The electron band structure found in metals, in which there are available electron states above and adjacent to filled states, in the same band. (b) The electron band structure of metals, wherein there is an overlap of filled and empty outer bands. (c) The electron band structure of insulators; the filled valence band is separated from the empty conduction band by a relatively large band gap. (d) The electron band structure found in the semiconductors, which is the same as for insulators except that the band gap is relatively narrow [adapted from 1].

These four different band structures led to three general classes of solid-state materials with respect to their conductivity: insulators, semiconductors, and conductors (Figure 3.6)[3]. The conductivities of insulators are very low: 10^{-16}-10^{-6} S/m, such as fused quartz and glass. Conductors such as aluminium and silver have high conductivities of the order of 10^{6}-10^{8} S/m. On the other hand, semiconductors have conductivities between those of insulators and those of

conductors, which is from 10^{-6}-10^{2} S/m. The conductivity of a semiconductor is generally sensitive to temperature, illumination, magnetic field, and minute amounts of impurity atoms. This sensitivity in conductivity makes the semiconductor one of the most important materials for electronic applications.

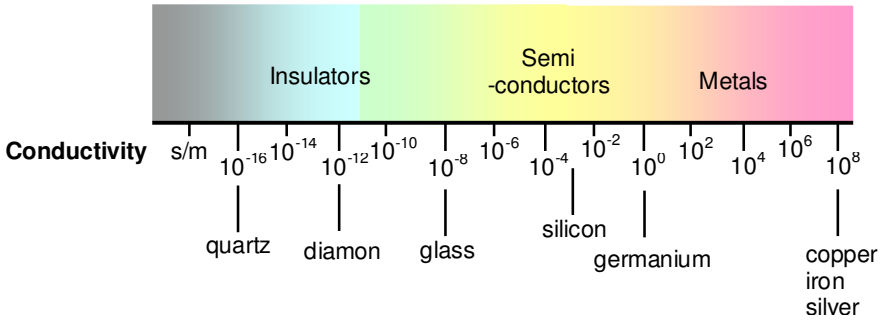

Figure 3.6 Conductivity of three kinds of materials: conductor, semiconductor and insulator. [Adapted from 3].

3.2.3.4 Sheet resistance

Sheet resistance is commonly used to characterize films in the electronics industry where the thickness of the material is either not relevant or known. The resistance (*R*) of a conductor of uniform cross section is given by:

$$R = \rho \frac{L}{A} \tag{3.6}$$

where, *L* is the length of the conductor, A is the cross-sectional area of the current flow on the material and ρ is the electrical resistivity of the material. The width and the thickness of a thin film are denoted by *d* and *h*, respectively (Figure 3.7). Therefore:

$$R = \rho \frac{L}{A} = \rho \frac{L}{dh} \tag{3.7}$$

$$R = \frac{\rho}{h} \frac{L}{d} = R_s \frac{L}{d} \tag{3.8}$$

where R_s is defined as the sheet resistance. Thus, sheet resistance is a function of the bulk resistivity of the film and has units of Ohms per square, where square is a unitless dimension of width divided by length. As equation 3.14 shows, R_s is the resistance measured of a square of film (L=d) regardless of the lengths of the side of that square.

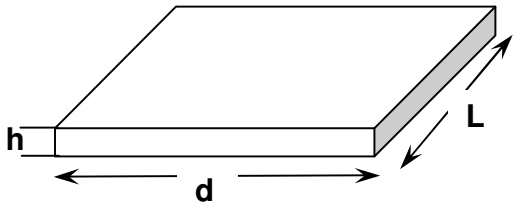

Figure 3.7 Diagrammatic sketch of the thin film.

Sheet resistance was used to characterise the peptide networks in this thesis since the porosity of the networks made it difficult to measure the effective thickness of the film. The resistance, R, of the networks was taken from the intercept of the x-axis on a Z'-Z'' plot, L was the distance between the electrodes and d was the width of the electrodes. The variation in the conductivity between samples was found to be much greater than the measurement accuracy of R, L and d, due to the random nature of the network formation. The error in the mean conductivities was calculated by measuring the R_s of three samples which had been prepared identically and taking the percentage error as the standard deviation in the R_s, divided by the mean R_s (i.e. in the error on the mean). This percentage error of 33 % at ambient conditions and 41 % under vacuum was then applied to all the other measurements. Ten separate samples in total were measured to obtain the percolation data.

3.2.3.5 Introduction to Impedance spectra

Electrical impedance is the general case for resistivity, where the response of a material, or circuit, to an alternating voltage is considered. Hence the impedance of a material includes its resistivity, inductance and capacitance and is a function of the angular frequency of the applied alternating voltage. Impedance, Z, is defined as:

$$Z(\omega) = \frac{V(\omega)}{I(\omega)} \tag{3.9}$$

If the applied alternating voltage is consider as a complex wave then the impedance of the material can be stated as[5] :

$$Z(\omega) = Z' - jZ'' \tag{3.10}$$

where $V(\omega) = V_m \sin(\omega t)$, $I(\omega) = I_m \sin(\omega t + \theta)$, $\omega = 2\pi f$, and θ (phase angle) is the phase difference between the current and the voltage. The phase angle of this expression relates to the balance between capacitive (out-of-phase) and resistive (in-phase) components in the material. For a pure resistance, θ=0 and for a pure capacitance θ=π/2. For systems that have a mixture of the two properties, intermediate phase angles are observed (Figure 3.8). Nyquist and Bode plots are the most frequently used graphs to show these components as a function of frequency. In a Nyquist (or *Cole-Cole*) plot, the imaginary part (*Z*") is plotted versus the real part of impedance (*Z*') in a complex plane

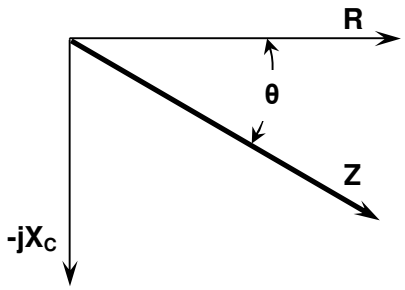

Figure 3.8 An impedance vector diagram.

Whereas, Bode plots comprise of a combination of the phase angle (θ), real (Z') impedance and imaginary impedance (Z") plotted versus frequency. Usually, the Nyquist plot is used to determine the main parameters, such as resistance and capacitance, of an electrical or an electrochemical system by fitting the measured spectra to an equivalent circuit. The Bode plot, however, reflects the physical characteristics of the material and the chemical activity at the electrolyte/electrode interface.

The impedance of ideal circuit elements and their representation as both Bode and Nyquist plots will now be considered. An ideal metallic conductor possesses only resistance and thus its impedance is:

$$Z_{metal} = R \tag{3.11}$$

which is independent of frequency and the phase angle is 0° (Figure 3.9). A perfect capacitor shows only capacitance and has a phase angle of 90°:

$$Z = \frac{1}{j\omega C} \tag{3.12}$$

. The Nyquist and Bode plots for the capacitor are shown in Figure 3.10.

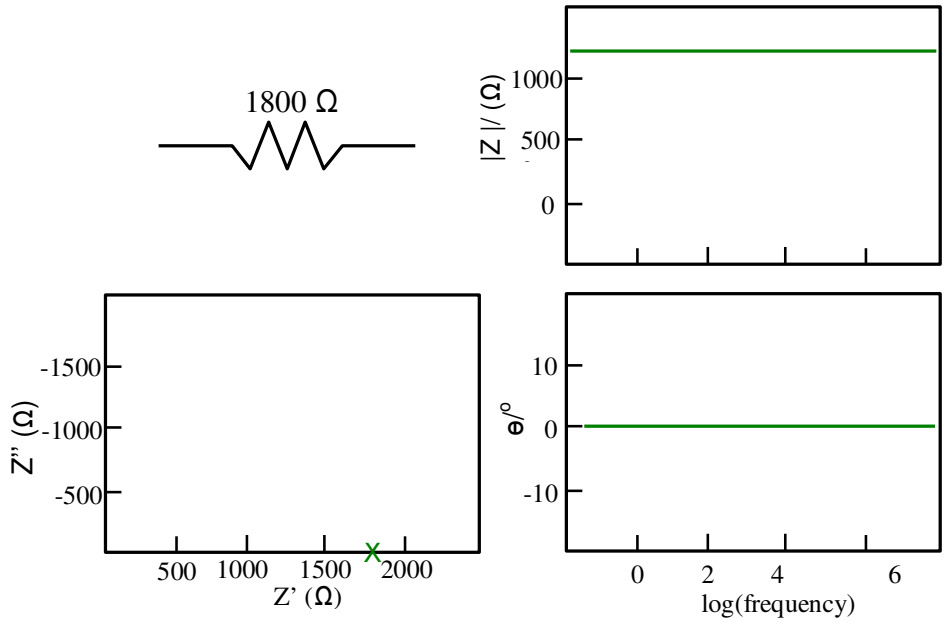

Figure 3.9 Nyquist and Bode plots for the impedance of ideal conductor.

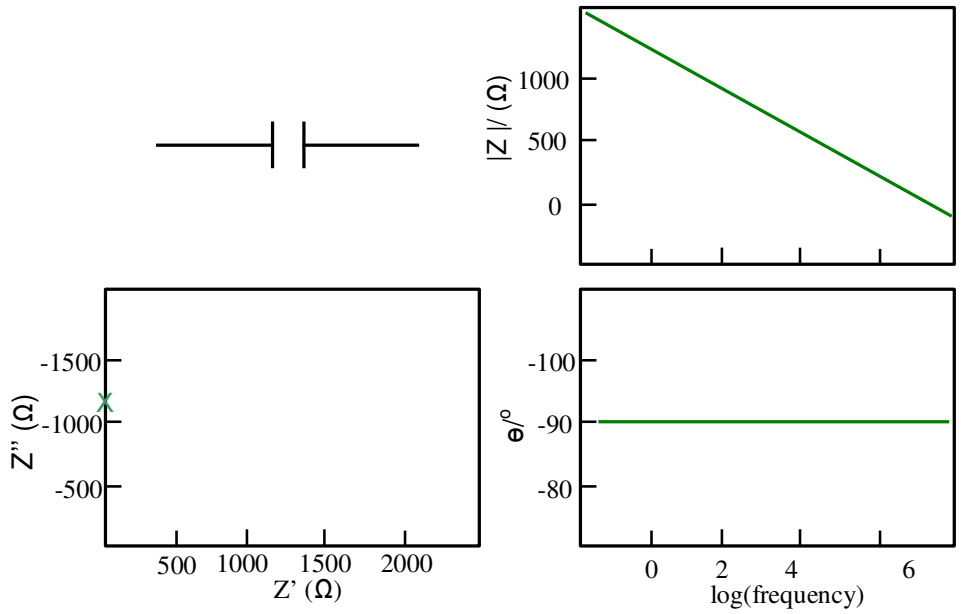

Figure 3.10 Nyquist and Bode plots for the impedance of a perfect capacitor.

The impedance of an R (resistor) and C (capacitor) in parallel (Figure 3.11[6]), is given by:

$$\frac{1}{Z} = \frac{1}{R} + j\omega C \tag{3.13}$$

$$\Rightarrow Z = \frac{1}{\frac{1}{R} + j\omega C} \tag{3.14}$$

where $\omega = 2\pi f$, R is resistance; C is capacitance; f is frequency.

For a sample containing electrolyte, there is a concentration of ions through the sample due to diffusion. The Warburg impedance, *W*, is from mass transfer at the electrode-electrolyte interface, and results in a line at 45° on the semicircle in the Nyquist plot. This line is often referred to as the '*mass transport tail*'. Therefore, diffusion can be represented by using the complete equivalent circuit given in Figure 3.12 for a single-step charge transfer reaction in the presence of diffusion[7].

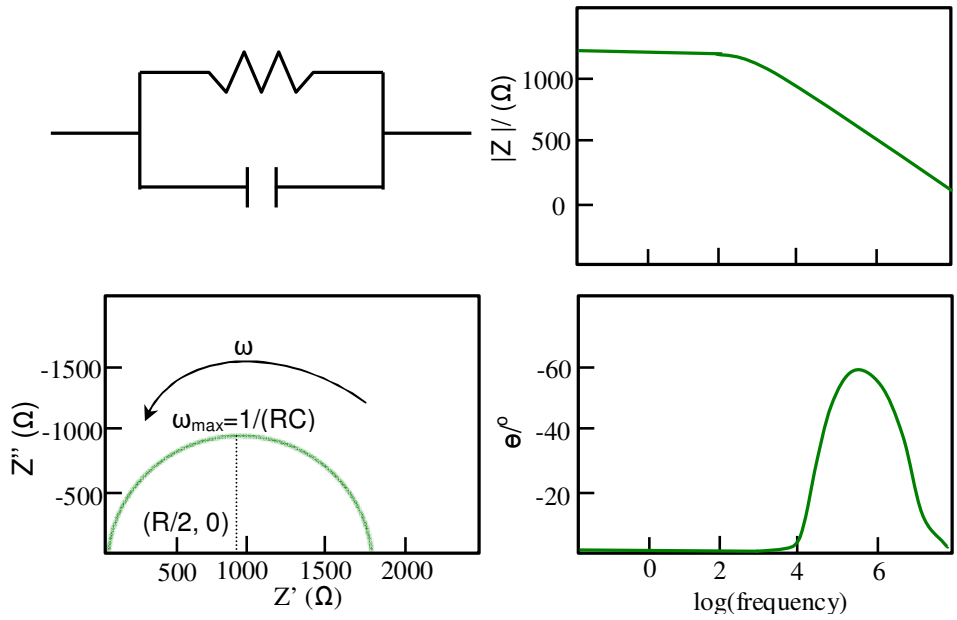

Figure 3.11 Schematic of (a) equivalent circuit, (b) Nyquist plot for a parallel RC circuit.

For an electrolyte,[8] there will also be a capacitance of the solution, C_{DL}, which is due to the charge separation double layer which develops at the electrodes' surfaces. In parallel with this capacitance there will be a resistance due to the solution polarization which is related to the transport of the ions in solution, R_p. The solution resistance due to the charge of the ions in solution is R_{sol}. The Nyquist and Bode plots of such an ion-containing solution are shown in Figure 3.13.

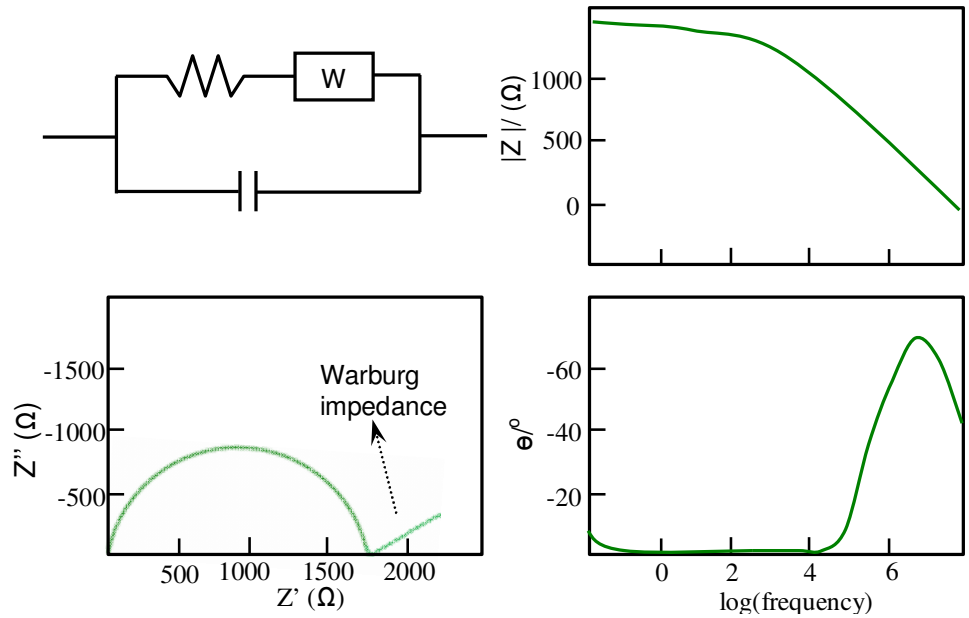

Figure 3.12 Nyquist and Bode plots for the impedance with a diffusion gradient between the electrodes

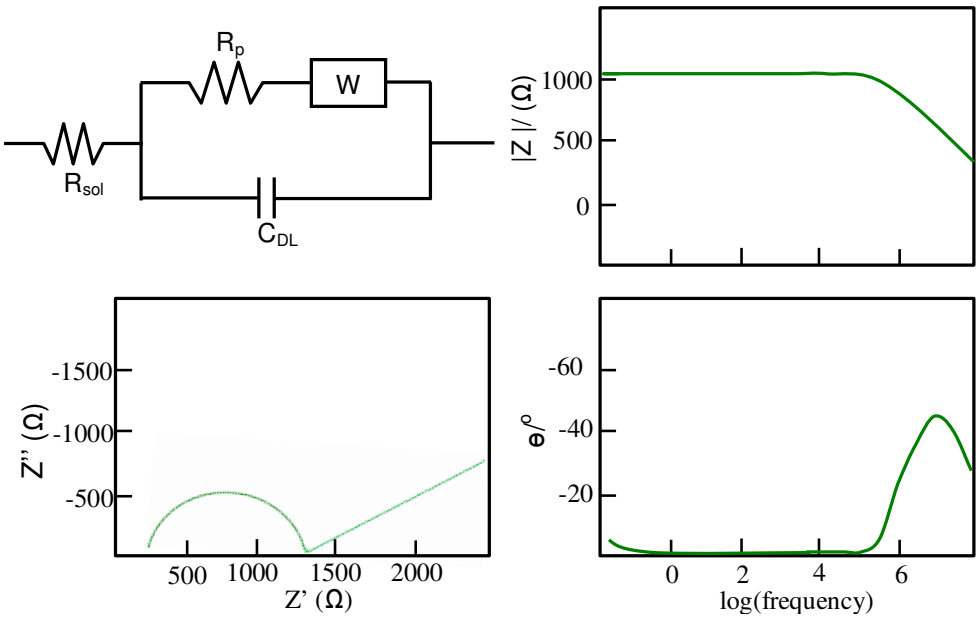

Figure 3.13 Nyquist and Bode plots for the impedance of an electrolyte measured with two electrodes.

3.3 REFERENCES:

1. William D. Callister. Jr. Fundamentals of materials science and engineering, 366-367.

2. D. Patidar, K. S. Rathore, N. S. Saxena, K. Sharma, T. P. Sharma, Energy band gap and conductivity measurement of CdSe thin films, Chalcogenide Letters, 2008, Vol. 5, No. 2, 21-25.
3. Bengt Nordén, Eva Krutmeijer, The Nobel Prize in Chemistry, 2000: Conductive polymers.
4. S. M. SZE, Semiconductor Devices, Physics and technology, 2nd edition, 17-18.
5. A. J. Bard, L. R. Faulkner, Electrochemical methods fundamentals and applications, Second edition, John Wiley & Sons, INC., 368-416.
6. F. Yang, P. Xiao, Nondestructive evaluation of thermal barrier coatings using impedance spectroscopy, Int. J. Appl. Ceram. Technol., 2009, 6, 381-399.
7. E. Barsoukov, J. R. Macdonald, Impedance spectroscopy theory, experiment, and applications, 70-71.

CHAPTER 4 STRUCTURE AND CONDUCTIVE PROPERTIES OF FIBROUS NETWORKS PRODUCED BY ENZYME TRIGGERED SELF-ASSEMBLY

4.1 INTRODUCTION

Nanoscale conductive wires with stacked aromatic rings prepared by the self-assembly of organic molecules may have applications in the next generation of optical and (bio-) electronic devices.[1-4] For effective charge transport in these wires, the aromatic moieties should be positioned close enough, and at a suitable orientation, to ensure that there is an effective π-orbital overlap. To achieve this, researchers have looked at biomolecular self-assembly, using DNA,[5, 6] porphyrins,[7, 8] engineered viruses and peptides,[9-14] for inspiration. In a separate development, it has been shown that the spectroscopic nature of a fluorenylmethoxycarbonyl (Fmoc) significantly altered within a self assembled fibrillar environment of β-sheet forming oligo-peptides suggesting that such peptide systems could lead to conductive wires.[14] It should be noted that the conductivity of none of these examples of peptide based electronic materials in the literature have been measured directly, but rather inferred from spectroscopy.

A relatively new class of peptide-based nanomaterials, aromatic peptide amphiphiles composed of short (between two and five amino acids) peptides with N-terminal aromatic groups[15-19] (such as fluorenylmethoxycarbonyl, Fmoc) have not yet been explored as supramolecular wires. A supramolecular structure for this class of peptide was proposed in 2008 from the models such as Smith's Fmoc-FF[18], Parquette's Fmoc-KK(NDI)[20] and Adam's Br-naphthalene-AV systems[21]. These models stated that the structure consisted of π-π interlocked β-sheets. In this *π-β* peptide configuration, H-bonding and aromatic interactions both contribute significantly, and, depending on the nature of the peptide, may inherently position N-linked aromatic fluorene ligands into a suitable position for close π cloud overlap as proposed previously for Fmoc-diphenylalanine[18].

This observation prompted me to investigate the conductive properties of the surface dried films (xerogels) of these materials as possible conductive networks. It is known that the chemical composition and the conditions used during self-assembly (*e.g.* concentration of self-assembly

building blocks, solvent, temperature and pH) can significantly affect the nanostructure morphology and hence the conductivity of supramolecular structures.[1,7,8,15,22,23] Enzyme-triggered self-assembly[18,22,23] is a mild method that converts non-assembling precursors into self-assembly building blocks under constant conditions, and may allow for better control and reproducibility of the self-assembly process. In this chapter, the electronic properties and nanostructures of Fmoc-LL, Fmoc-L_3, Fmoc-WL and Fmoc-YL are studied. Fmoc-L_3 is then studied in more detail as its conductivity was found to be much higher than the other sequences studied.

Overall, the aims of this chapter are:

(i) Characterization of the nanostructures of the hydrogels and dried films (Fmoc-LL, Fmoc-WL, Fmoc-YL and Fmoc-L_3).

(ii) Comparison of the conductivity between the four xero-hydrogels (Fmoc-LL, Fmoc-L_3, Fmoc-WL and Fmoc-YL) and assessment of the electronic properties.

(iii) Characterisation of xerogel networks formed via the enzyme-triggered self-assembly of fluorenylmethoxycarbonyl-tri-leucine, Fmoc-L_3, with an emphasis on the π-π stacking distance using molecular dynamics simulations and wide angle X-ray scattering (WAXS);

(iv) Demonstrate conductivity of the networks and its relationship to network properties using impedance spectroscopy at ambient and vacuum conditions.

4.2 HYDROGELS

4.2.1 Formation of self assembled hydrogel via ester hydrolysis

Figure 4.1 shows schematically the formation of Fmoc-peptide building blocks using subtilisin. The enzyme (subtilisin) performs a hydrolysis reaction (under aqueous conditions) in which the Fmoc-peptide is formed from Fmoc-peptide methyl ester. The proposed mechanism of Fmoc-peptide self-assembly is shown in Figure 4.2. First, precursor self-assembling building blocks (gelators) are formed after adding the enzyme (subtilisin). Second, the building blocks self-

assemble to high-order aggregates via π–π interactions between fluorenyl groups and hydrogen bonding to form anti-parallel β-sheets peptide layers. Third, these layers can form nanostructures such as nanotubes and nanofibres. As more nanostructures are formed, a network is formed which immobilizes the solvent and leads to gel formation (Figure 4.3)[19]. Gel formation was checked by the inversion test tube method (Figure 4.3b). A sample was deemed to have gelled when it remained at the same level in an inverted test tube for at least 30 seconds. The resulting hydrogels were characterized by HPLC and it was confirmed that the main product was Fmoc-L_3 (Figure 4.4d).

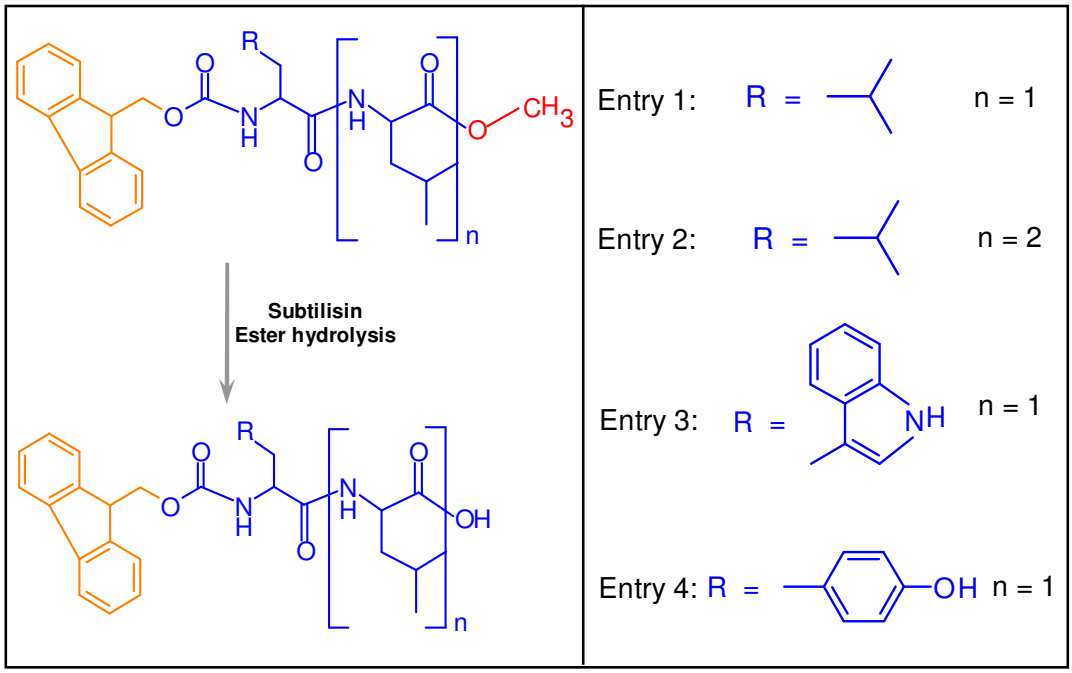

Figure 4.1 Fluorenylmethoxycarbonyl (Fmoc) -peptide building blocks, supramolecular structures: Entry 1: Fmoc-Leu-Leu (Fmoc-LL) formation; Entry 2: Fmoc-Leu-Leu-Leu (Fmoc-L_3) formation; Entry 3: Fmoc-Tyr-Leu (Fmoc-YL) formation; Entry 4: Fmoc-Trp-Leu (Fmoc-WL) formation. Aromatic Fmoc ligand : yellow; methyl ester : red; amino acid: blue.

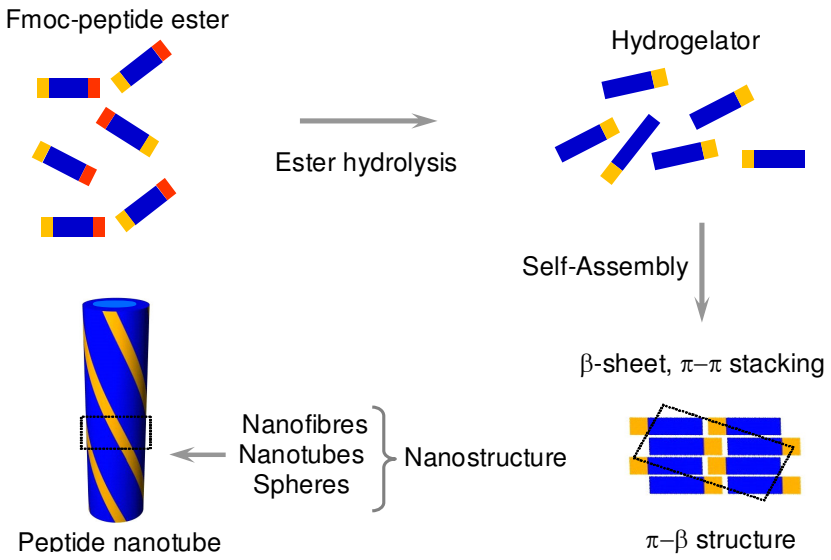

Figure 4.2 Schematic diagram of the proposed mechanism for Fmoc-peptide ester hydrolysis. The gelators self-assembly to form higher-order aggregate anti-parallel β-sheets driven by π–π stacking between fluorenyl groups. Self-assembled nanostructure showing *π-β structure* such as nanotubes.

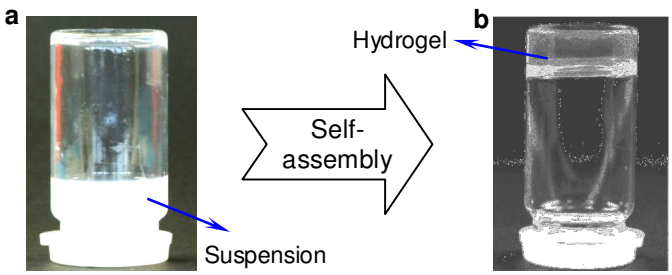

Figure 4.3 Formation of hydrogels by hydrolysis:(a) Suspension of Fmoc-peptide ester, subtilisin and buffer, (b) Hydrogel (Note that the colours in (a) are an artefact of the lighting).

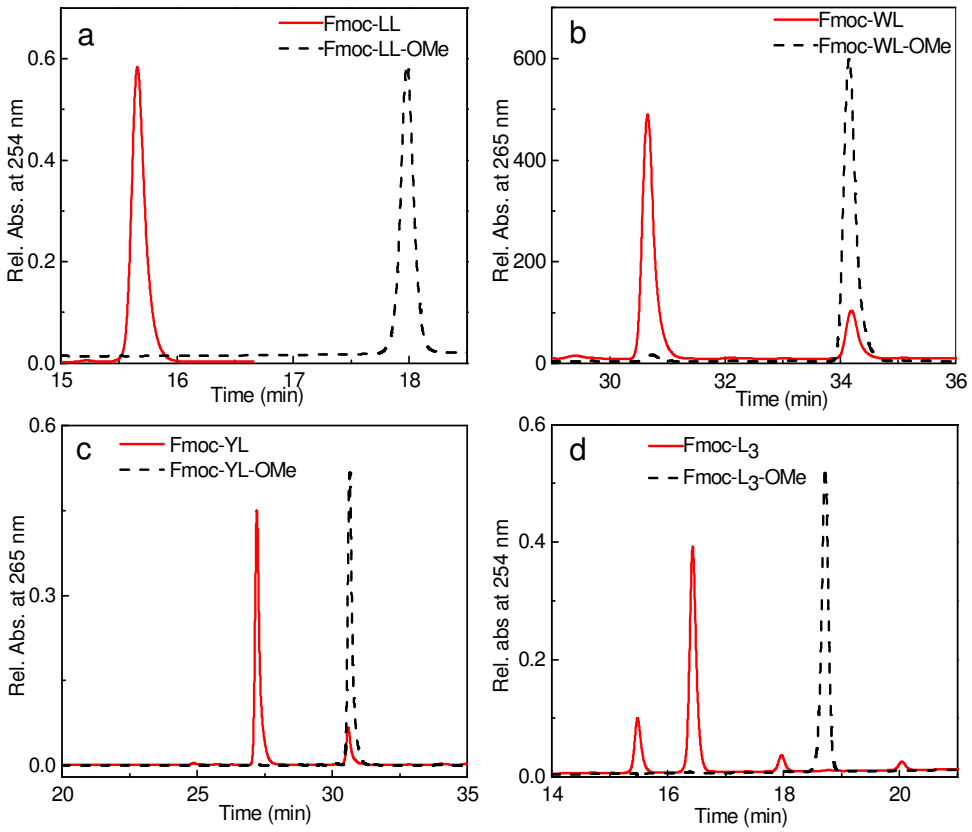

Figure 4.4 HPLC Chromatograms: a, Fmoc-LL-OMe and corresponding ester hydrolysed peptide Fmoc-LL; b, Fmoc-WL-OMe and corresponding hydrolysed peptide Fmoc-WL; c, Fmoc-YL-OMe and corresponding enzyme ester hydrolysed peptide Fmoc-YL; d, Fmoc-L_3-OMe and corresponding hydrolysed peptide Fmoc-L_3 (Note: the small peaks are from Fmoc-L_2, Fmoc-L_4 and Fmoc-L_5).

4.2.2 Fmoc-XY

4.2.2.1 Characterisation of Fmoc-XL hydrogels

Fluorescence spectroscopy measurements were performed to monitor the environment of the fluorenyl moiety in the hydrogels and π-stacking interactions (Figure 4.5). The emission maxima of Fmoc-LL was found to shift from 317 nm to 332 nm upon gelation by the removal of the methyl motif. Similarly, the emission maxima at 349 nm was observed from Fmoc-WL-OMe suspension (λ_{ex} = 280 nm) with the same concentration, comparing with the emission maxima at 376 nm from Fmoc-WL hydrogel. The red shift is probably related to the presence of a fluorenyl excimer species. The emission at 349 nm from Fmoc-WL-OMe is due to aromatic indole moieties of

tryptophan. The pronounced emission at around 450 nm from Fmoc-LL, Fmoc-WL and Fmoc-YL indicates that multiple fluorenyl moieties locked together through π–π stacking (2004, Xu's paper)[24]. Overall, these data provide evidence that Fmoc-LL, Fmoc-YL and Fmoc-WL self-assemble via π–π interaction.

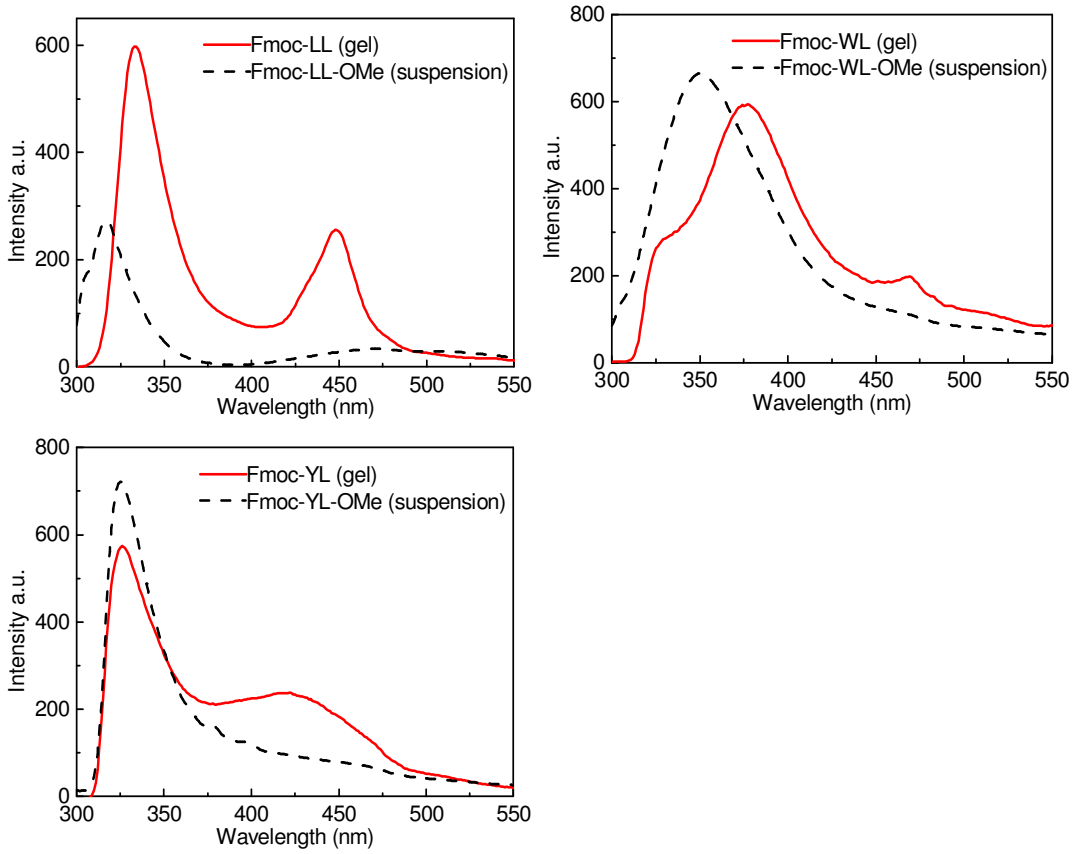

Figure 4.5 Fluorescence emission spectra of gels (20 mM) and suspension (20 mM). The appearance of new broad peaks at 450 nm indicated the formation of higher-order aggregates. Fluorescence emission spectra (λ_{ex} = 280 nm).

FT-IR spectra of the hydrogelators are shown in Figure 4.6, with a H_2O background having been removed from the spectra (hence the weak O-H bands despite being taken from hydrated films.) Fmoc-LL and Fmoc-YL were found to contain well-defined CO-stretching bands (amid I band) at around 1635-1646 cm^{-1} which is consistent with the formation of β-sheets structures. Moreover, these gelators displayed a medium intensity band at 1685-1691 cm^{-1}. These observations

indicated the formation of an anti parallel β-sheet structure. Taken together, the results suggest that the peptide gelators self assemble into a π–β conformation.[25, 26] Interestingly, there is not a distinct band at 1691 cm^{-1} from the Fmoc-WL film, suggesting that this hydrogel had a different structure to the other hydrogels. The lack of the anti parallel β-sheet peak for Fomc-WL gel indicates that its structure is dominated by hydrophobic effect (π–π interactions). This difference in the Fmoc-WL gel is also apparent in the AFM studies which are discussed later in this chapter.

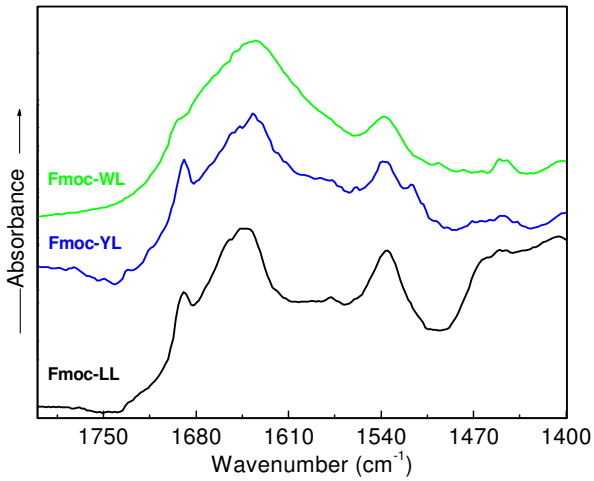

Figure 4.6 FT-IR spectra of Fmoc-LL, Fmoc-WL, Fmoc-YL showing a broad peak at around 1635–1646 cm-^{1} and a medium intensity band at 1685–1691 cm-^{1} (amide band), consistent with the antiparallel -sheet structure. A H_2O background was subtracted.

4.2.2.2 Characterization of xero-gels (films)

Xero-gel films and films of Fmoc-peptide-ester dissolved with buffer solution were prepared by depositing the hydrogel onto glass slides and then drying them at 37 °C. FT-IR spectra of dried hydrogel films of Fmoc-LL, Fmoc-WL and Fmoc-YL and films of Fmoc-LL-OMe, Fmoc-WL-OMe, and Fmoc-YL-OMe were also performed to investigate the CO-stretching bands (Figure 4.7). These spectra were found to be similar to the spectra obtained from original, hydrated hydrogels with two bands at ~ 1691 cm^{-1} and ~1636 cm^{-1}. The dried Fmoc-WL film, however, did not have a distinct band at 1691 cm^{-1}, as obtained from the Fmoc-WL hydrogel film, further confirming that this hydrogel was different in structure to the other films and was dominated by hydrophobic effects (π–π affection). Figure 4.8 shows the fluorescence spectra obtained from the xero-gel films

(Fmoc-LL, Fmoc-WL and Fmoc-YL) and dried films from precursors (Fmoc-LL-OMe, Fmoc-WL-OMe and Fmoc-YL-OMe). These fluorescence spectra had similar peaks to the original hydrogels except Fmoc-WL (Figure 4.5). Red shift emerged between peptide molecular and hydrogel film. The peak at around 450 nm has been proposed both from anti-parallel and parallel dimerization of the fluorenyl group.[27] However, the intensity of the peak from the films is lower than that from the hydrogels due to the film thickness. This is because the thin films contain a small amount of networks. It should also be noted that the peak of Fmoc-WL film at around 450 nm is broader than Fmoc-WL hydrogel.

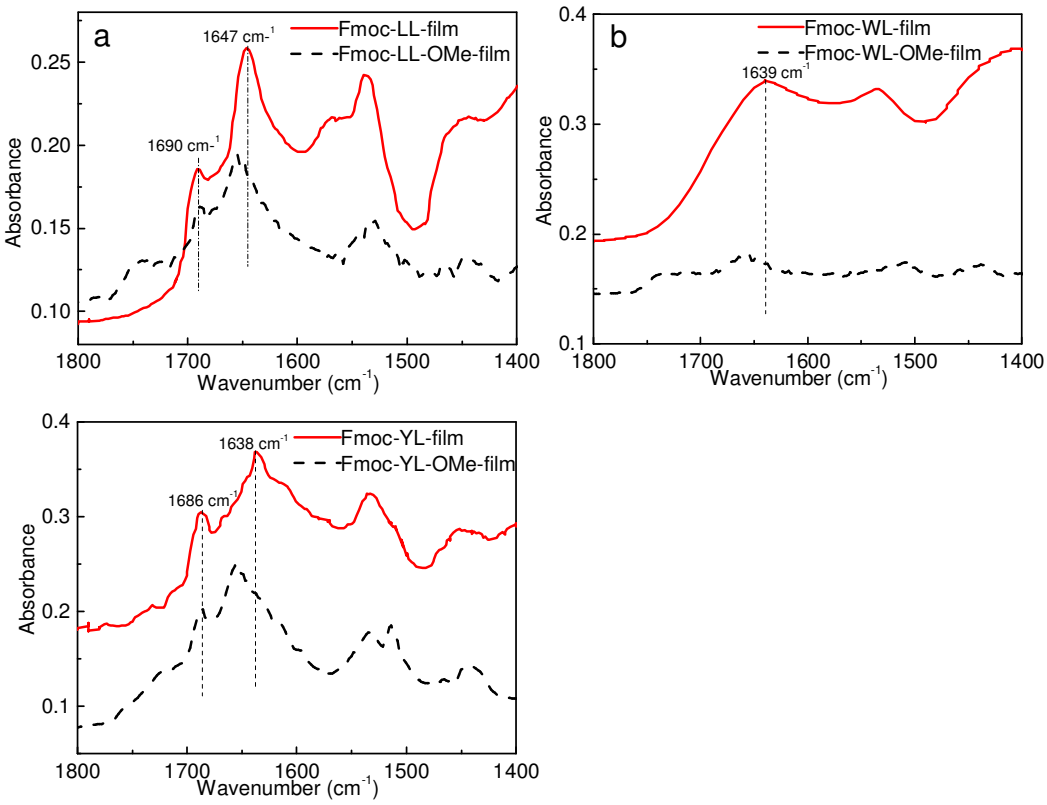

Figure 4.7 FT-IR spectra of dried films of Fmoc-peptides gels prepared enzymatically and precursor Fmoc-peptides-ester dissolved in 0.1 M phosphate buffer solution: a, Fmoc-LL gel and Fmoc-LL-OMe, b, Fmoc-WL gel and Fmoc-WL-OMe, c, Fmoc-YL gel and Fmoc-YL-OMe.

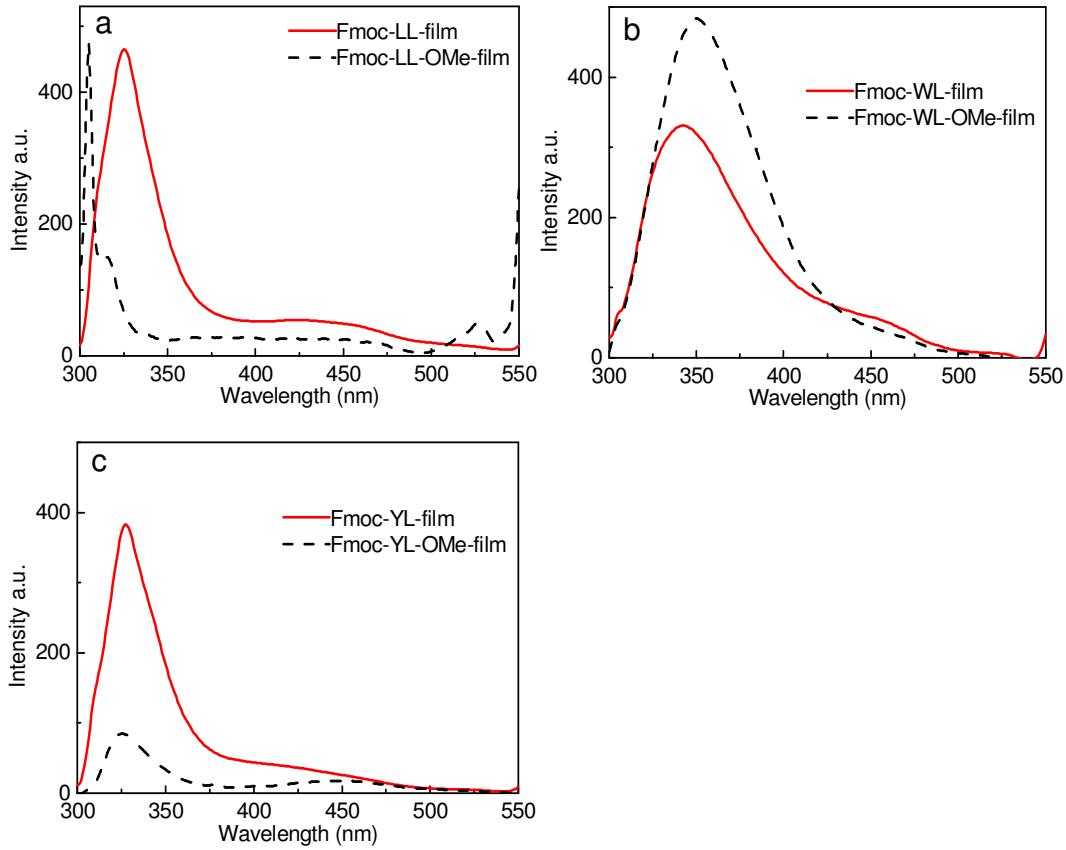

Figure 4.8 Fluorescence spectra of dried films prepared by enzymatic hydrolysis and Fmoc-peptide-ester solution (Fmoc-peptide-ester dissolved in 0.1 M phosphate buffer solution): a, Fmoc-LL gel and Fmoc-LL-OMe, b, Fmoc-WL gel and Fmoc-WL-OMe, c, Fmoc-YL gel and Fmoc-YL-OMe.

Atomic Force Microscopy (AFM) was used to investigate the morphology of the self-assembled peptide nanostructures. These nanostructures were absorbed onto mica substrates and imaged in air by tapping mode (Figure 4.9). The diameters of the nanofibres were determined by the heights of peaks from the cross section of the nanostructures. AFM visualization revealed well-defined nanofibres with the diameter varying with the gelator used. The diameters were found to be 4-6 nm and 6-8 nm for Fmoc-LL and Fmoc-YL nanofibres, respectively (Figure 4.9a, b). The nanostructure of Fmoc-WL was found to be different from the other xero-gels and consisted of a mixture of fibres of 4-8 nm in diameter (Figure 4.9c) and spherical nanostructures with a height of around 40 nm. These results suggest that Fmoc-WL had a tendency to form spherical nanostructures which may be large disorder aggregates. The peaks of Fmoc-WL film were red

shifted, compared to the hydrated Fmoc-WL hydrogel (Figure 4.5b and Figure 4.8b), possibly due to the large disorder aggregates structures (Figure 4.9c).[28] These large disorder aggregate structures also explain the absence of the β-sheet peak in the FT-IR spectra (Figure 4.7b).

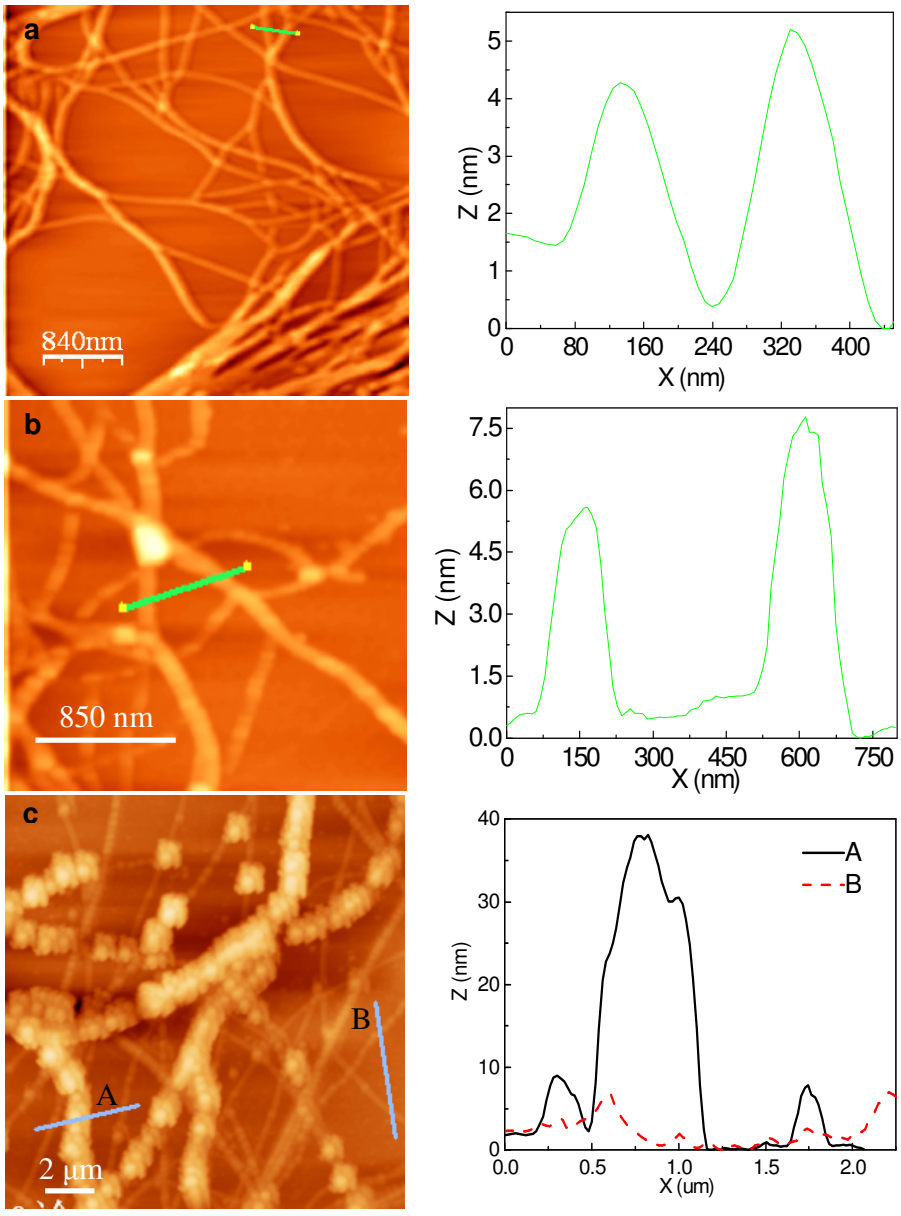

Figure 4.9 Atomic force microscopy (AFM) images Fmoc-peptide hydrogel film and the cross section of the nanostructures: a, Fmoc-LL; b, Fmoc-YL; c, Fmoc-WL.

The structure of the films were studied in more detail using X-ray scattering (WAXS) (Figure 4.10). It is widely reported in the literature that the spacing of the β-sheet from the WAXS is around 4.6 Å.[29] Therefore, the WAXS was studied in this region. A moderately intense reflection at a position corresponding to d =4.6 Å was observed for Fmoc-LL and Fmoc-YL. It should be noted that there was a peak in a similar position for the buffer salt. However, this peak was much less intense. This 4.6 Å reflection combined with the FT-IR spectra suggests the presence of β-sheets in the Fmoc-LL and Fmoc-YL samples. The reflection at 4.6 Å from Fmoc-WL is similar in intensity to that expected from the buffer salts present in the sample, based upon the relative heights of the other salt reflections. Therefore, the weak 4.6 Å reflection in the Fmoc-WL sample is probably due to the salt impurities. Thus the WAXS data combined with the FT-IR spectra suggest strongly that the Fmoc-WL samples contained no β-sheets. The peak from Fmoc-WL and Fmoc-YL at ~ 15 Å possibly corresponds to the length of the gelator.

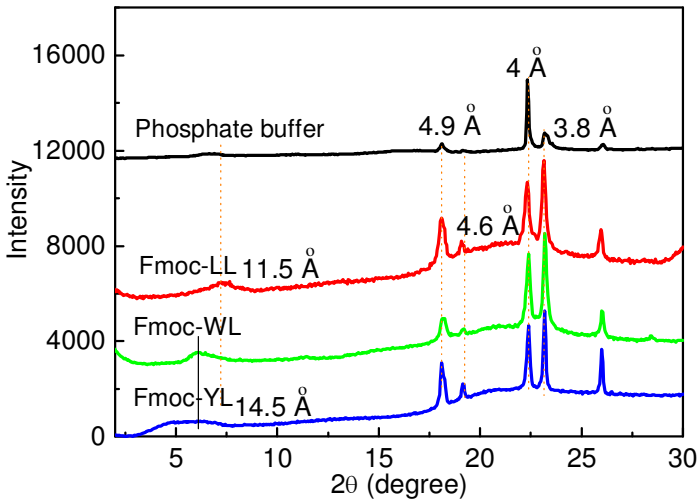

Figure 4.10 Analysis of X-ray Scattering of Fmoc-LL, Fmoc-YL and Fmoc-WL film on a silica surface. Peaks corresponding to the spacing of peptides within a -sheet structure and the spacing between π–πstacking.

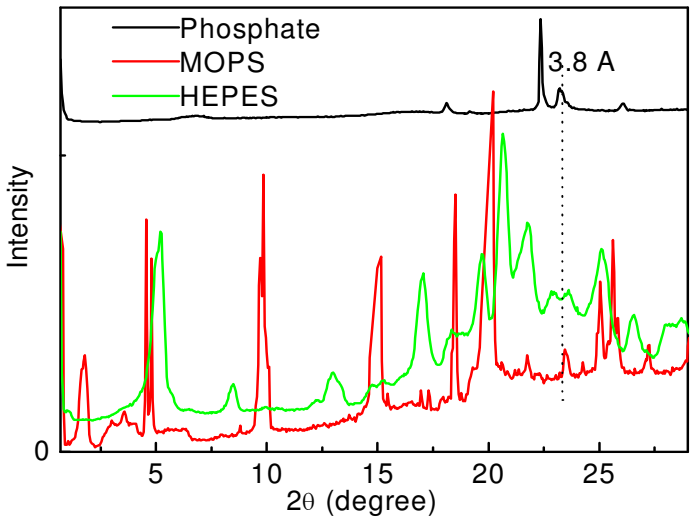

Figure 4.11 Analysis of X-ray scattering of the dried phosphate, MOPS and HEPES buffer.

X-ray diffraction patterns were also taken from dried 0.1 mol/L HEPES buffer and 0.1 mol/L MOPS buffer in order to try to find a buffer which had no peaks that overlapped the π–π stacking reflection. Unfortunately, both of these buffers had peaks at ~ 3.8 Å (Figure 4.11). Furthermore these buffers had even more reflections than the phosphate buffer (Appendix: Table A.1).

4.2.3 Fmoc-L_3

4.2.3.1 Characterization of Fmoc-L_3

The hydrogel was deposited onto a glass slide and dried to leave a xerogel consisting of a network of interwoven fibres (Figure 4.12). FT-IR spectra of the Fmoc-L_3 xerogel (Figure 4.13 a) showed two bands centered around 1636 cm^{-1} and 1690 cm^{-1}. These bands indicate that anti-parallel β-sheet structures were retained in the dried state. Fluorescence spectroscopy of the Fmoc-L_3 gels suggested that electron delocalization was significant (Figure 4.13b).[23,30] The self-assembly route used in this thesis involved a shorter exposure to enzyme at 55 ℃ (2 hr instead of 4hrs), giving rise to more pronounced emissions in the 420-460 nm range (Figure 4.13b).

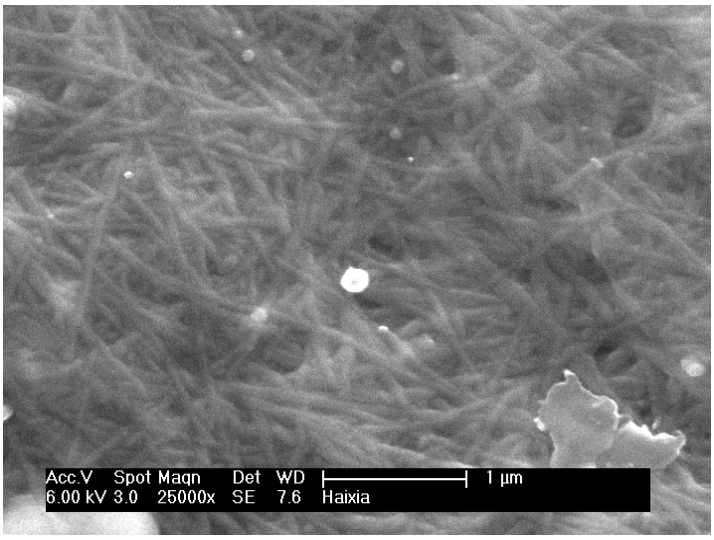

Figure 4.12 Scanning Electro Microscopy (SEM) image of dried Fmoc-L_3 film on the glass slide prepared for electronic properties measurements.

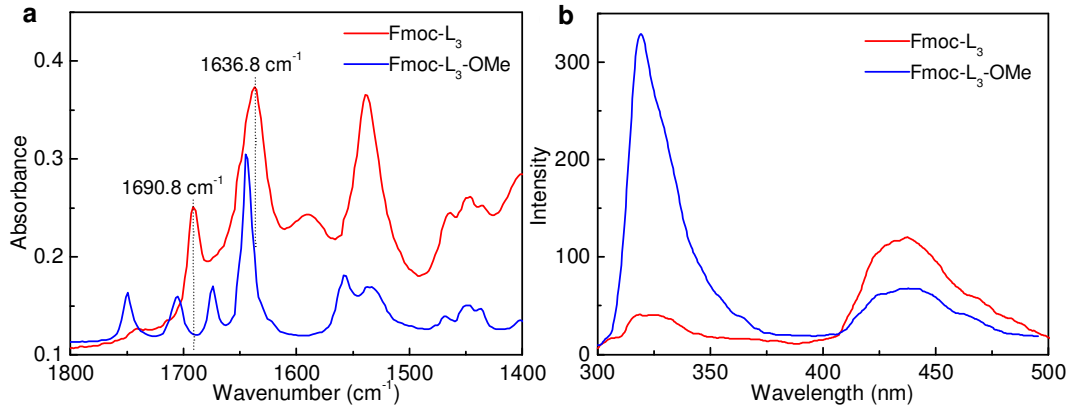

Figure 4.13 FT-IR spectra and Fluorescence emission spectra of Fmoc-L_3 dried films: (a) FT-IR spectra of dried films of Fmoc-L_3 gel prepared enzymatically and precursor Fmoc-L_3-OMe dissolved in 5% acetone and 0.1 M phosphate buffer solution. The Fmoc-L_3 dried film (top spectrum) shows a broad peak at around 1635-1646 cm^{-1} and a medium intensity band at 1685-1691 cm^{-1} which are consistent with the anti-parallel β-sheet structure. The spectrum obtained from the Fmoc-L_3-OMe precursor suggests that peptides interact in a number of orientations with less molecular order. (b) Fluorescence emission spectra of Fmoc-L_3 gel prepared by enzymatic hydrolysis and Fmoc-L_3-OMe solution. (50µL acetone was used to dissolve Fmoc-L_3-OMe, and then mixed with 0.1 M phosphate buffer at pH 8 to prepare 20 mM Fmoc-L_3-OMe solution).

4.2.3.2 Structure of Fmoc-L_3 nanotube

Fmoc-L_3 nanostructures were analyzed by transmission electron microscopy (TEM) using 2% uranyl acetate as a negative stain, confirming the formation of peptide nanotubes[23] with inner

diameters of around 9 nm and external diameters of around 24 nm (Figure 4.14a). Cryogenic TEM analysis confirmed the presence of the hollow core in the hydrogel with an inner diameter of ~7 nm and external diameter of ~16 nm (Figure 4.14b). AFM analysis (Figure 4.14c) showed that the peptide nanotubes were straight and had diameters of between 15-16 nm (Figure 4.14d). The AFM observations closely resembled the dimensions observed by Cryo-TEM. The cross-section profiles from AFM had sharp peaks, indicating that the discrepancy between height (by AFM) and width (TEM) is most likely due to the flattening of the tubes onto the surface during drying, giving rise to the larger diameters measured in TEM when compared to Cryo-TEM.

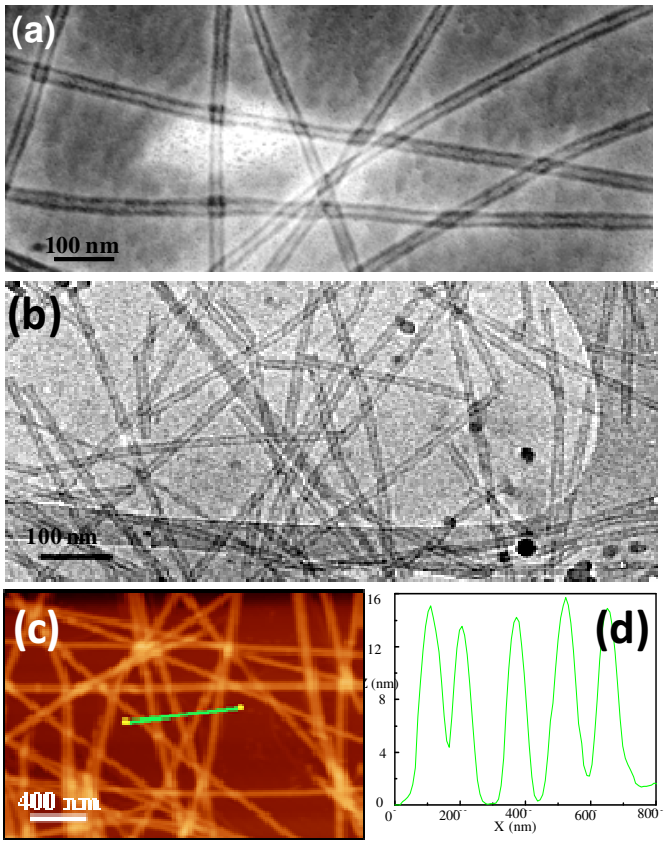

Figure 4.14 Transmission electron micrographs of the tubular structures formed and tapping-mode AFM analysis of peptide nanotubes on mica: (a) TEM image of Fmoc-L_3. Sample was negatively stained with 2% uranyl acetate, (b) Cryo-TEM micrograph of Fmoc-L_3 hydrogel. (c) AFM image of Fmoc-L_3, (d) Height profile of the line shown in (b).

Structural features of the Fmoc-L_3 system in TIP3P water were analyzed by a MD simulation over 7 ns performed by Dr. Majeed S. Shaik. The Fmoc-L_3 16-mer, after initial minimisation and equilibration, is shown in Figure 4.15 and Figure 4.16. It may seem counterintuitive that these molecules assemble in this way, as the proposed model leads to the positioning of the polar COOH group in the unpolar environment where π-stacking takes place. However, the two key components of this structural model, the β-sheet and π-stacking have both been observed experimentally. The anti-parallel β-sheet structures were confirmed by FT-IR (Figure 4.13a). It is widely reported in the literature that the spacing of the β-sheet from the WAXS is around 4.6 Å.[29] Therefore, the WAXS was studied in this region to confirm that the distance between β-sheets is around 4.7 Å (Figure 4.17). The chemical structure of β-sheet is shown in Figure 4.18. The π–π stacking has also been observed experimentally in the fluorescence measurements in Figure 4.13, where there was a broad peak at 450 nm which is due to delocalisation between aromatic groups, as observed in other systems by Ghadiri *et al*.[30]

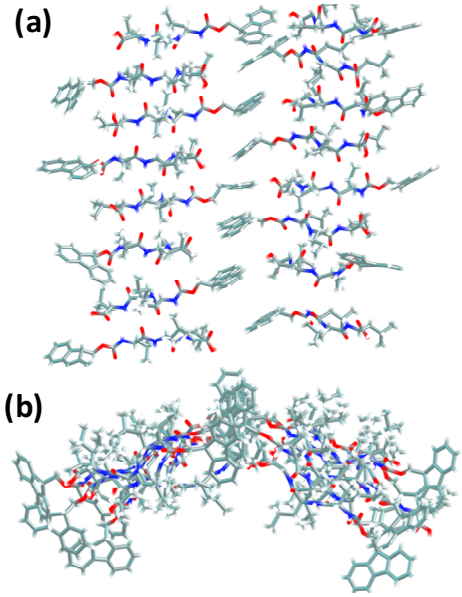

Figure 4.15 Structure of Fmoc-L_3 16-mer in TIP3P water after initial minimisation and equilibration. The water molecules are not shown for clarity in the above figure: (a) Front view, (b) Top view schematic (not to scale) of a single molecular layer. This simulation was done by Dr. Majeed S. Shaik.

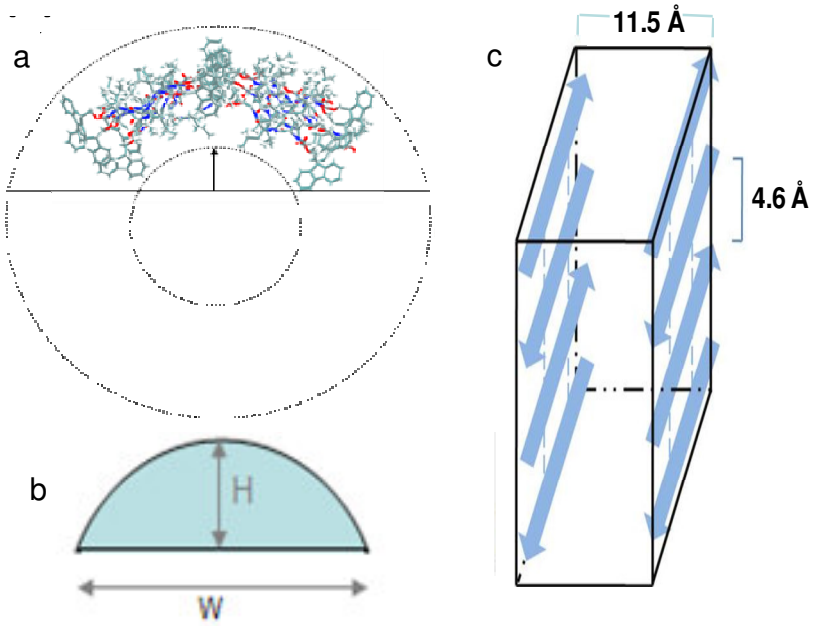

Figure 4.16 schematic of a single Fmoc-L_3 molecular layer nanotubes: a, Top view schematic of a single Fmoc-L_3 molecular layer nanotube, which was inferred from the part arc to a whole tube, b, Schematic of calculation method of nanotube radius, c, Schematic of layer inter-sheet model. This simulation was done by Dr. Majeed S. Shaik.

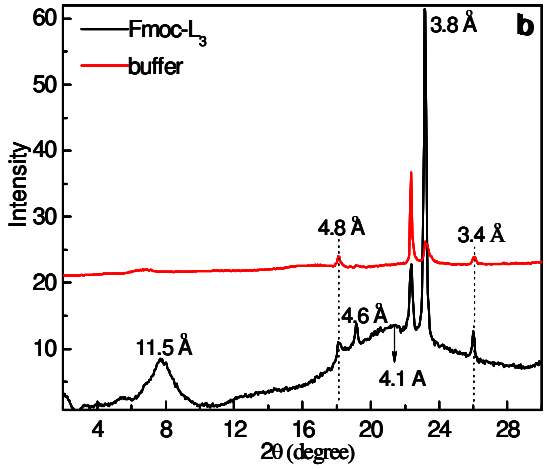

Figure 4.17 Wide angle X-ray scattering (WAXS) data of dried Fmoc-L_3 (bottom line) and buffer (top line) on a silica surface. Peaks corresponding to the spacing of peptides within a β-sheet structure, pairs of fluorenyl groups, the spacing between π-π stacking and the intersheet distance between layers. The spectrum of the buffer is included for comparison.

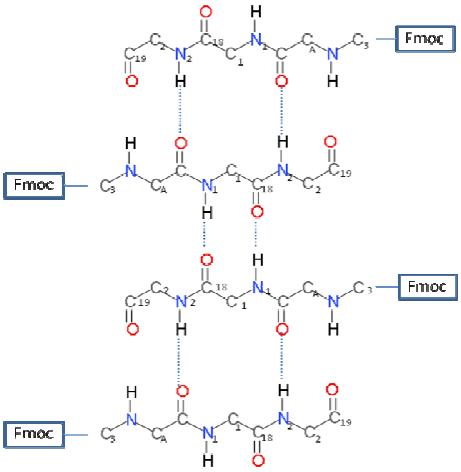

Figure 4.18 Chemical structure of Fmoc-L_3 molecules with β-sheet and hydrogen bonding.

One final question on the model is why the apparent β-sheet spacing is larger than that for the π–π stacking (spacing between Fmoc groups) when the Fmoc groups are at the end of each β-sheet. This issue is explained by considering the relative bond energies and hence the bond orientations to each other. As discussed below, the inter-Fmoc forces are strong than those in the β-sheets, meaning that the Fmoc groups twist significantly out of the β-sheet plane as the nanotubes is formed (see Figure 4.15).

The individual N-H…O=C dipole-dipole and C-H…O=C attractive interaction in the antiparallel β-sheet models are predicted to be -6.2±0.2 kcal/mol and -1.2±-0.2 kcal/mol, respectively.[31] The binding energy of π–π stacking is around 48±10 kcal/mol, taking the porphyrin-porphyrin interaction in chloroform as an example.[2] The presence of π-stacks may often be inferred from X-ray diffraction patterns. The π-stacking distance is typically 3.4-3.6 Å, representing the shortest interplanar distance.[32] Fmoc molecules are self-assembled through π-stacking strands. The extent of Fmoc molecules was determined by monitoring the distances and angles between the planes of the Fmoc rings from simulation. The criteria for the π–π stacking between the Fmoc groups was obtained from molecular mechanics calculations (The simulation work was provided by Dr Shaik). From the MD simulation, Figure 4.19 shows the distribution of the β-sheet distances

between the Fmoc-L_3 molecules and π-π stacking distances between Fmoc residues. It is observed from Figure 4.19 that there is a strong possibility of β-sheet formation at around 4.7 Å between the Fmoc-L_3 molecules and a great potential of π-π stacking at around 3.6 Å between Fmoc residues. The predicted distances are in good agreement with those measured experimentally using wide angle X-rays scattering (WAXS). Figure 4.17 shows the distances obtained from the WAXS. WAXS analysis suggests that the β-sheet was formed at 4.6 Å [33] and π-π stacking at 3.8 Å. The distances obtained from the MD simulations are close to these experimental values. The breadth of the experimental reflections compared to the di-peptide system (Figure 4.10) should be noted. This breadth indicates that the Fmoc-L_3 nanostructures were poorly annealed. The experimental relative intensities of the β-sheet, inter-sheet and π–π reflections are also unexpected and would require further modelling to explain.

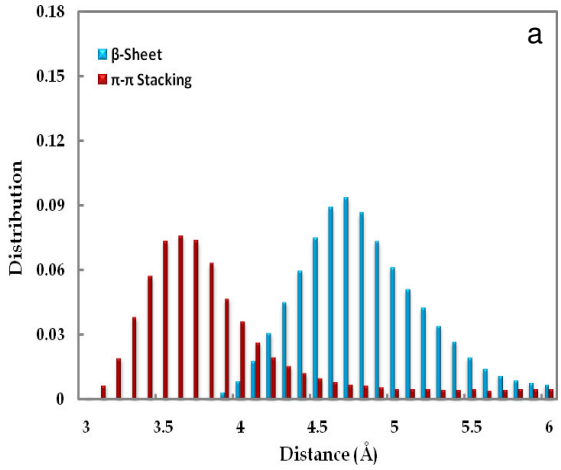

Figure 4.19 Distribution of β-sheet distances between the Fmoc-L_3 molecules and π-π stacking distances between Fmoc residues.

However, it was previously demonstrated for a closely related aromatic peptide amphiphile Fmoc-FF[34], that very large pK_a shifts (of up to 6 pH units) are observed upon self-assembly which provides direct evidence that the polar group is indeed in a highly hydrophobic environment. The reflection at d=11.5 Å is thought to correspond to the intersheet distance between two single layers of Fmoc-L_3 molecules (Figure 4.16a, c).[35] It should be noted that this pronounced WAXS reflection suggests long range order and may suggest that additional interactions are important here.

The wall thicknesses observed in the TEM micrographs (Figure 4.14 a, b) suggests that multi-layers were formed. A single molecular layer nanotube was inferred from the small arc (Figure 4.16 b). The radius of this monolayer nanotube can be calculated using:

$$Radius = \frac{H}{2} + \frac{w^2}{8H} \qquad (4.1)$$

Here, *w* is the width of the arc and H is the height of the arc (Figure. 4.16b). The estimated inner diameter for the Fmoc-L_3 model is 7.8 nm, which is in good agreement with the experimental value (6 - 9 nm) from TEM and Cryo-TEM images (Figure 4.14a, b). The calculated outer diameter is 9.8 nm, giving the thickness of one layer as (9.8-7.8)/2=1 nm. The nanotubes were found experimentally, however, to be much larger with diameters of 16-20 nm, corresponding to an average radius of 18/2=9 nm. Figure 4.19 suggests an inter-layer spacing of 11.5 Å or approximately 1 nm. Thus, the experiment nanotubes are expected to consist of three layers, i.e. outer radius = inner radius + 3 layers + 2 inter-layers = 3.9+ 3 + 2 = ~ 9 nm.

4.3 CONDUCTIVITY OF THE HYDROGEL FILMS

4.3.1 Current-Voltage (I-V) and impedance characterization

The current-voltage (I-V) curves of the dried films were obtained by using a BASI Epsilon electrochemical workstation. Electrodes were made by the evaporating gold on top of the dried coated networks as described in the methods section. The spacings between the deposited electrodes ranged from 1 mm to 3 mm, and the length of the electrodes was 12 mm.

Figure 4.20a shows the I-V curves of the network films, which were carried out in air. The curves in Figure 4.20b were obtained under vacuum. When the applied voltage was between +/-3 V, the I-V curves were linear, indicating Ohmic contact between electrodes and peptide films. It was found that the I-V curves of the films in air did not pass through the origin (Figure 4.20a) whilst the I-V curves of the films under vacuum did. It is believed that the response in the air was due to

ionic conduction as the mass of an ion is larger than that of an electron. Thus, at the high scan rate used (500 mV/s), the ion current was still flowing at V=0 due to inertia.

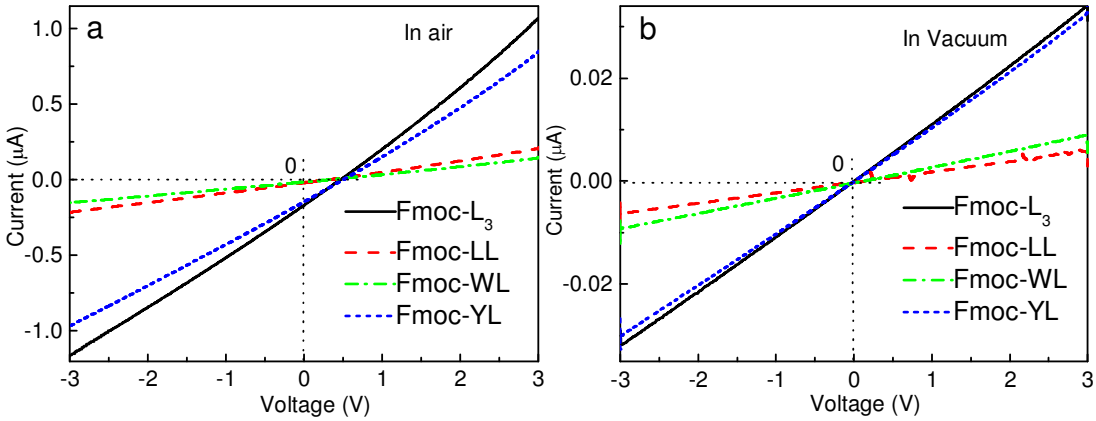

Figure 4.20 Current versus voltage characteristics of the peptide films at a scan rate of 500 mV/s at room temperature at the voltage between -3 V to 3 V for each measurement: a) at ambient condition; b) at vacuum environment (0.1 mba)

Impedance spectroscopy measurements were also carried out to evaluate the conductive behavior at the interface between the sample and electrode, which is a method for characterizing electronic properties of materials. The measurements covered the frequency range from millihertz to megahertz. It should be noted that all these resistances obtained from I-V curve and impedance spectra throughout the thesis are sheet resistances, unless otherwise stated. Impedance spectroscopy can give information on the nature of the conducting species within the sample, particularly, whether the conduction is caused by ion or electrons. Impedance data are presented in the form of real impedance, Z' (resistive), against imaginary, Z'' (capacitive), as shown in Figure 4.21. One phase region gives rise to ideally a semicircle (or arc). The samples' resistance (R) values are obtained from the intercepts of this semicircle on the Z' axis,[36] which were analysed with the Zview software, using the 'FitCircle' commands to estimate the resistance for each sample.

The impedance experimental data (labelled 'Exp') were also simulated by software (Zsimpwin) using an equivalent circuit models (Figure 4.23). (The calculated data was labelled as 'Cal'.) In air,

the conductivity of the Fmoc-peptides networks is labelled 'networks'. The conductivity of buffer salts absorbed with water from air is labelled 'ion' (Figure 4.23a). The resistance of the film in air was modelled with a bulk resistance of networks ($R_{networks}$) and Warburg impedance (W_{ion}), in parallel with a capacitance $C_{networks}$. W_{ion} is from mass transfer because the buffer salt ions moved in the water adsorbed from the air. $C_{networks}$ is representing the capacitance of the networks. In the vacuum system (Figure 4.23b), the resistance of film is from Fmoc-peptides nanostructure networks (labelled 'networks') and dried buffer salts (Figures 4.24 and 4.25). The later was not considered due to very high resistance. The resistance of the film obtained from impedance spectra in air included $R_{networks}$ and Warburg impedance W_{ion}, which could not be separated. However, in vacuum, the resistance of the film was $R_{networks}$.

Figures 4.21 and 4.22 show a complex impedance plot (so called Cole-Cole plot) for the xero-gel films and Fmoc-peptide-ester films, in which the experimental data were modelled by using the equivalent circuits in Figure 4.23a (model in Figure 3.11). The resistances of the Fmoc-peptide-ester films were found to be at least two to three orders of magnitude higher than those found for the hydrogel film both in air and under vacuum (Figure 4.21, Figure 4.22, Figure 4.24 and Figure 4.25). In vacuum, the experimental data were simulated according to the equivalent circuits in Figure 4.23b (model in Figure 3.10). Good agreement has been obtained between the experimental data curves and the calculated data curve (Figure 4.21, Figure 4.22, Figure 4.24, and 4.25), indicating that the equivalent circuits models applied are valid. The resistance of the blank glass substrate is shown in Figure 4.26 with its full impedance spectra. The glass substrate had a high resistance of 4.8×10^{11} Ω/sq in air and 28.4×10^{11} Ω/sq in vacuum. It should be noted that the resistances of both the blank glass and Fmoc-peptide-ester films are much higher than the hydrogel films and therefore, the relatively low resistances of hydrogel films must arise from the nanostructure networks.

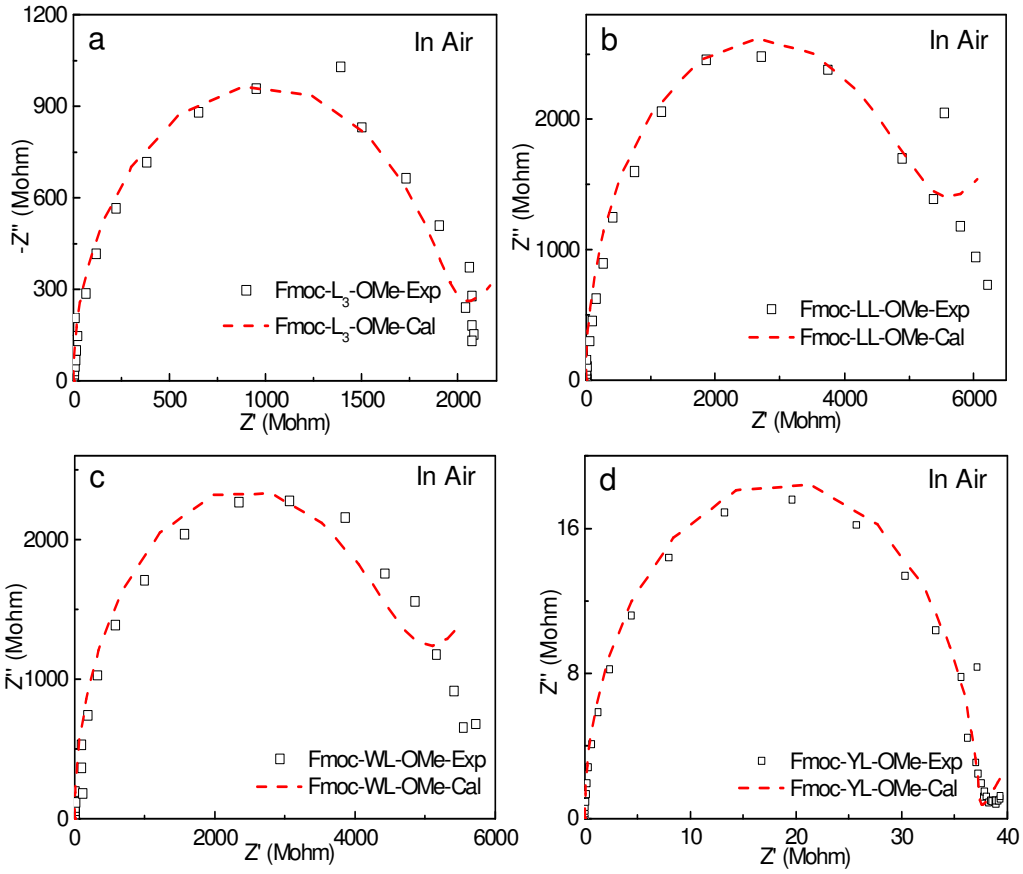

Figure 4.21 Impedance spectroscopy and fitted curves of the Fmoc-peptide-ester films in air. These films consisted of the precursor molecules before hydrolysis reaction deposited as a dried film.:a, Fmoc-L_3-OMe, b, Fmoc-LL-OMe, c, Fmoc-WL-OMe, d, Fmoc-YL-OMe. Dried films of Fmoc-peptide-ester were prepared by mixing Fmoc-peptide-ester molecular with 0.1 M phosphate buffer at pH 8 to prepare 20 mM Fmoc-peptide-ester solution. Exp: experimental data; Cal: calculated data by software Zsimpwin. $R_{Fmoc\text{-}L3\text{-}OMe}=7.6\times10^{9}$ Ω/sq, $C_{Fmoc\text{-}L3\text{-}OMe}=1.30\times10^{-5}$ μF, $R_{Fmoc\text{-}LL\text{-}OMe}=2.0\times10^{10}$ Ω/sq, $C_{Fmoc\text{-}LL\text{-}OMe}=1.31\times10^{-5}$ μF, $R_{Fmoc\text{-}WL\text{-}OMe}=1.8\times10^{8}$ Ω/sq, $C_{Fmoc\text{-}WL\text{-}OMe}=1.21\times10^{-5}$ μF, $R_{Fmoc\text{-}YL\text{-}OMe}=1.5\times10^{8}$ Ω/sq, $C_{Fmoc\text{-}YL\text{-}OMe}=1.16\times10^{-5}$ μF.

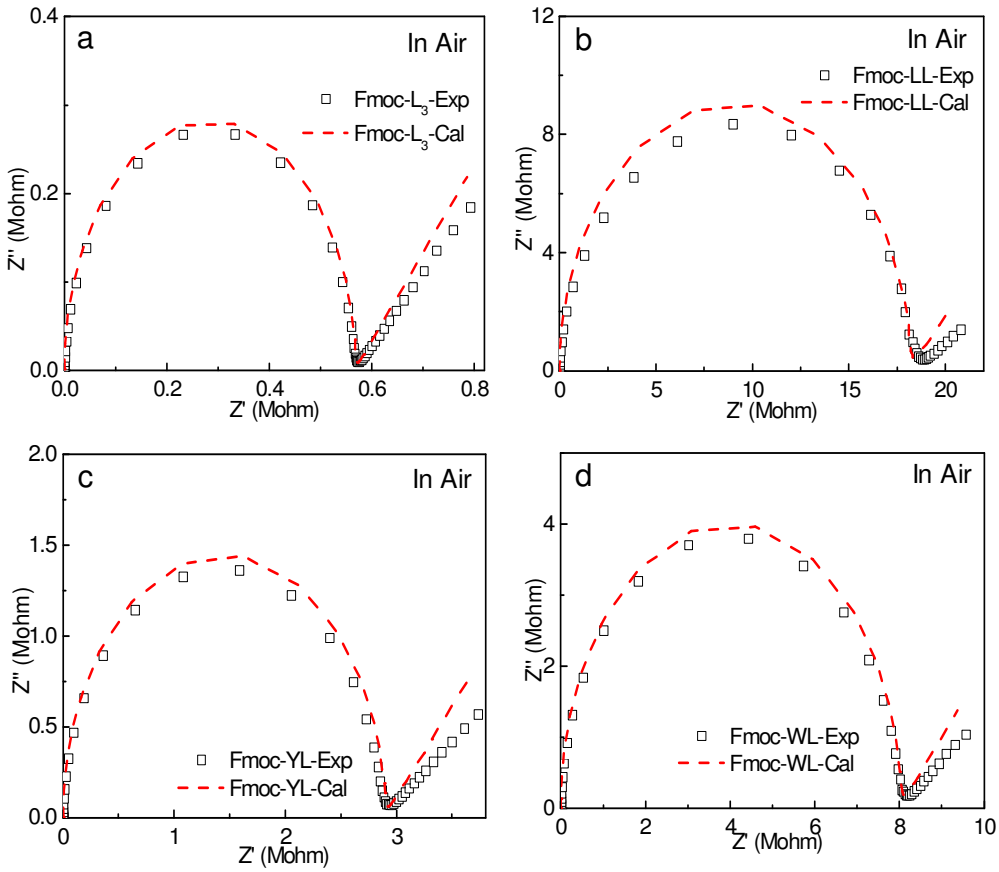

Figure 4.22 Impedance spectroscopy and fitted curves of the hydrogels films in air: a, Fmoc-L_3, b, Fmoc-LL, c, Fmoc-WL, d, Fmoc-YL. Exp: experimental data; Cal: calculated data by software Zsimpwin. $R_{Fmoc\text{-}L3}=2.3\times10^{6}$ Ω/sq, $C_{Fmoc\text{-}L3}=1.09\times10^{-5}$ μF, $R_{Fmoc\text{-}LL}=7.2\times10^{7}$ Ω/sq, $C_{Fmoc\text{-}LL}=1.11\times10^{-5}$ μF, $R_{Fmoc\text{-}WL}=3.2\times10^{7}$ Ω/sq, $C_{Fmoc\text{-}WL}=1.16\times10^{-5}$ μF, $R_{Fmoc\text{-}YL}=1.2\times10^{7}$ Ω/sq, $C_{Fmoc\text{-}YL}=1.05\times10^{-5}$ μF.

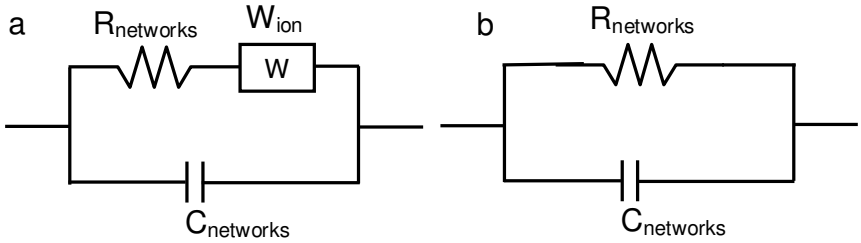

Figure 4.23 Equivalent circuits for Fmoc-L_3 film and Fmoc-L_3-OMe (a) in air; (b) in vacuum

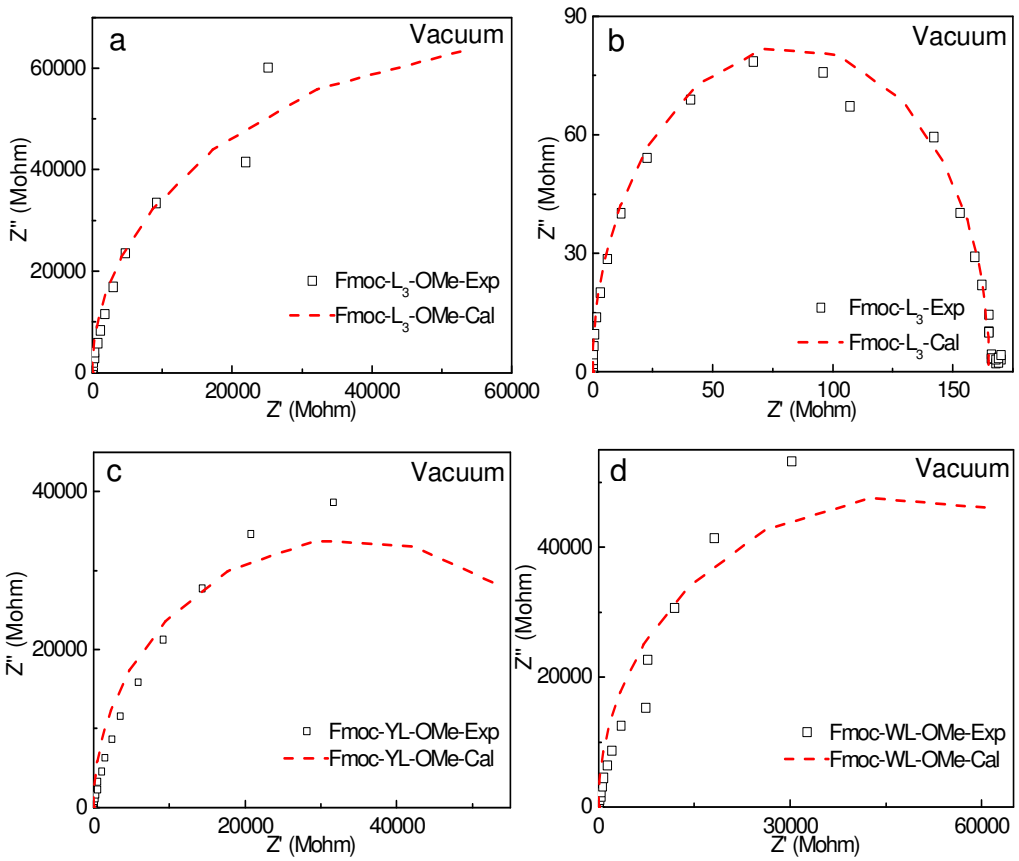

Figure 4.24 Impedance spectroscopy and fitted curves of Fmoc-peptide-ester films under vacuum condition a, Fmoc-L_3-OMe, b, Fmoc-LL-OMe, c, Fmoc-WL-OMe, d, Fmoc-YL-OMe. Dried films of Fmoc-peptide-ester were prepared by mixing Fmoc-peptide-ester molecular with 0.1 M phosphate buffer at pH 8 to prepare 20 mM Fmoc-peptide-ester solution. Exp: experimental data; Cal: calculated data by software Zsimpwin. Inset: equivalent circuits. $R_{Fmoc\text{-}L3\text{-}OMe}=5.2\times10^{11}$ Ω/sq, $C_{Fmoc\text{-}L3\text{-}OMe}=1.46\times10^{-5}$ μF, $R_{Fmoc\text{-}LL\text{-}OMe}=3.9\times10^{11}$ Ω/sq, $C_{Fmoc\text{-}LL\text{-}OMe}=1.38\times10^{-5}$ μF, $R_{Fmoc\text{-}WL\text{-}OMe}=3.8\times10^{11}$ Ω/sq, $C_{Fmoc\text{-}WL\text{-}OMe}=1.27\times10^{-5}$ μF, $R_{Fmoc\text{-}YL\text{-}OMe}=2.7\times10^{11}$ Ω/sq, $C_{Fmoc\text{-}YL\text{-}OMe}=1.25\times10^{-5}$ μF. (Fmoc-peptide-ester: molecular species before hydrolysis reaction)

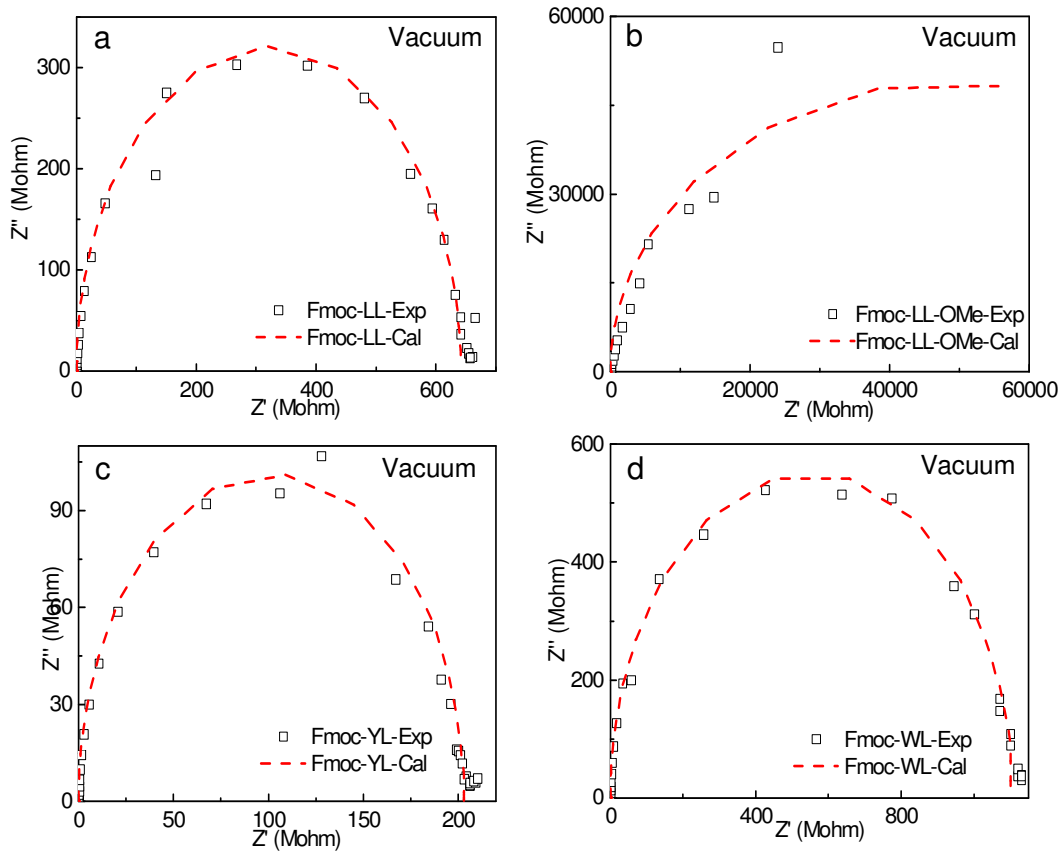

Figure 4.25 Impedance spectroscopy and fitted curves of the hydrogels films under vacuum condition a, Fmoc-L_3, b, Fmoc-LL, c, Fmoc-WL, d, Fmoc-YL. Exp: experimental data; Cal: calculated data by software Zsimpwin. Inset: equivalent circuits. $R_{Fmoc\text{-}L3}=6.4\times10^{8}$ Ω/sq, $C_{Fmoc\text{-}L3}=1.11\times10^{-5}$ μF, $R_{Fmoc\text{-}LL}=2.6\times10^{9}$ Ω/sq, $C_{Fmoc\text{-}LL}=1.16\times10^{-5}$ μF, $R_{Fmoc\text{-}WL}=4.4\times10^{9}$ Ω/sq, $C_{Fmoc\text{-}WL}=1.19\times10^{-5}$ μF, $R_{Fmoc\text{-}YL}=8.0\times10^{8}$ Ω/sq, $C_{Fmoc\text{-}YL}=1.07\times10^{-5}$ μF.

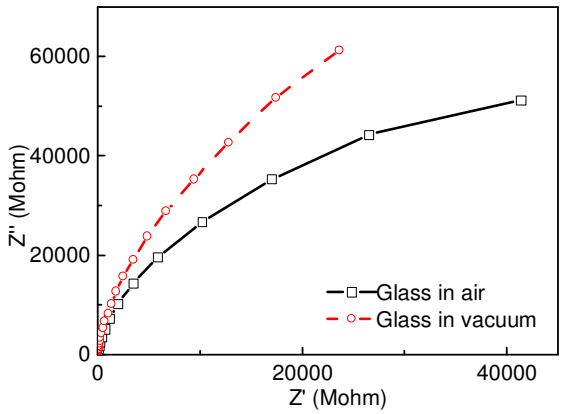

Figure 4.26 Complex impedance plot data of blank glass. The frequency ranged from 0.1 to 10^7 HZ): Blank glass by using evaporated gold as electrode with R=4.8×10^{11} Ω/sq in air and R=8.4×10^{11} Ω/sq in vacuum.

Figure 4.27a show four similar semicircles (arc) connected with the slopes at the end of arcs from films of Fmoc-LL, Fmoc-WL and Fmoc-YL measured in air. These slopes are known to be caused by mass transfer, i.e. ionic conductivity. Figure 4.27b shows the response of the same films under vacuum and there is no sign of a low-frequency ion transport. Therefore, there is no impedance barrier for charge transfer between the electrode and film and the conducting species are likely to be electrons in this system.[37] The electronic conductivity presumably arises from the delocalized electrons in the $\pi-\pi$ interactions that were observed in the fluorescence spectroscopy (Figure 4.8). The ionic conductivity is probably due to the hydroscopic nature of the samples meaning that they absorb water in air, leading to the formation of an electrolyte due to the dissolution of the buffer salts. This ionic conductivity will increase with humidity and is studied in more detail in the next section of the thesis.

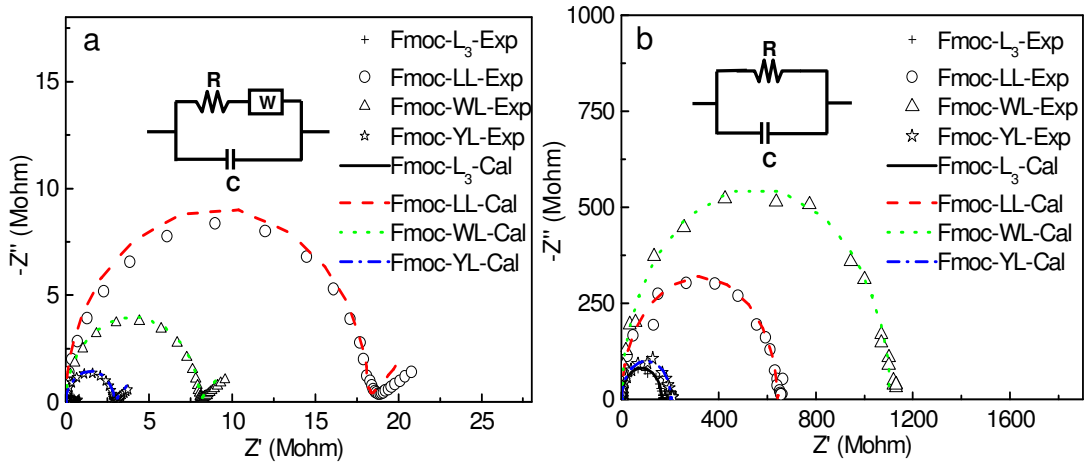

Figure 4.27 Impedance spectra and fitted data of peptide films (Fmoc-LL, Fmoc-L3, Fmoc-WL and Fmoc-YL) a, In air; b, In vacuum. Exp: experimental data; Cal: calculated data from software Zsimpwin by using the equivalent circuits inset. $R_{Fmoc\text{-}L3\ air}=2.3\times10^{6}$ Ω/sq, $C_{Fmoc\text{-}L3\ air}=1.09\times10^{-5}$ μF, $R_{Fmoc\text{-}LL\ air}=7.2\times10^{7}$ Ω/sq, $C_{Fmoc\text{-}LL\ air}=1.11\times10^{-5}$ μF, $R_{Fmoc\text{-}WL\ air}=3.2\times10^{7}$ Ω/sq, $C_{Fmoc\text{-}WL\ air}=1.16\times10^{-5}$ μF, $R_{Fmoc\text{-}YL\ air}=1.2\times10^{7}$ Ω/sq, $C_{Fmoc\text{-}YL\ air}=1.05\times10^{-5}$ μF; $R_{Fmoc\text{-}L3\ vacuum}=6.6\times10^{8}$ Ω/sq, $C_{Fmoc\text{-}L3\ vacuum}=1.11\times10^{-5}$ μF, $R_{Fmoc\text{-}LL\ vacuum}=2.6\times10^{9}$ Ω/sq, $C_{Fmoc\text{-}LL\ vacuum}=1.16\times10^{-5}$ μF, $R_{Fmoc\text{-}WL\ vacuum}=4.4\times10^{9}$ Ω/sq, $C_{Fmoc\text{-}WL\ vacuum}=1.19\times10^{-5}$ μF, $R_{Fmoc\text{-}YL\ vacuum}=8.1\times10^{8}$ Ω/sq, $C_{Fmoc\text{-}YL\ vacuum}=1.07\times10^{-5}$ μF.

From the complex impedance plot, the distance across the arc, which is obtained under AC bias conditions, is considered to correspond to the resistance of the xero-gel film. The conductivity of xero-gel films was measured under both AC mode and DC mode by using different equipment in different rooms and at different times (Table 4.1). The DC resistances are within experimental error of the AC resistances, indicating that there were no adsorption or reaction resistances between the film and electrode and the connection is Ohmic.[38] This observation is confirmed by the fact that the impedance plots intercepted the x-axis at high frequency at the origin due to no significant resistance between the film and electrodes. The thickness of each film was determined by surface profiling. From this value, the electrode spacing and electrode length, the conductivity of the peptide thin film was estimated as ~ 10^{-2} S/m under ambient conditions and 10^{-4} S/m hydroscopic under vacuum, which is in the conductivity range for semiconductors.

Table 4.1 Comparison of resistance of different films between DC and AC both in air and vacuum

Films	Electrode Length / Space (mm)	Thickness (μm)	In air				In vacuum
			DC R (Ω/sq)		Conductivity (S/cm)	DC R (Ω/sq)	Conductivity (S/cm)
Fmoc-LL	12 / 3	15.7±2	DC	$6.0\pm0.5\times10^{7}$	$4.2\pm0.5\times10^{-5}$	$2.0\pm0.6\times10^{9}$	$1.3\pm0.6\times10^{-6}$
			RC	$7.2\pm1.2\times10^{7}$		$2.6\pm0.5\times10^{9}$	
Fmoc-L_3	12 / 3	8.2±3	DC	$1.1\pm0.2\times10^{7}$	$4.4\pm0.3\times10^{-4}$	$4.0\pm0.5\times10^{9}$	$7.0\pm0.5\times10^{-6}$
			RC	$2.4\pm0.9\times10^{6}$		$6.8\pm0.1\times10^{8}$	
Fmoc-YL	12 / 3	11.5±5	DC	$1.6\pm1.4\times10^{7}$	$2.2\pm0.9\times10^{-4}$	$4.0\pm0.8\times10^{8}$	$4.3\pm0.4\times10^{-6}$
			RC	$1.2\pm0.5\times10^{7}$		$8.0\pm1.0\times10^{8}$	
Fmoc-WL	12 / 3	12.6±7	DC	$8.0\pm1.1\times10^{7}$	$4.0\pm1\times10^{-5}$	$2.2\pm2.0\times10^{9}$	$7.2\pm0.8\times10^{-7}$
			RC	$1.6\pm2.0\times10^{7}$		$4.4\pm0.8\times10^{9}$	

Table 4.2 Comparison of resistance of organic and inorganic conductive nano-networks from the literature

Materials	Measurement method	Conductivity in air (S/cm)	References
Polyaniline nanotubes networks	Four-probe method, in air, room temperature	3.5×10^{-5}	Y. Long et al. 2003[39]
Polyaniline microtube blends	Four-probe method, in air, room temperature	0.01 – 1.2	A. R. Hopkins et al. 2004[40]
Self-assembled nanocoils from a norbornene-appended hexabenzocoronene	Two-probe method, in air, room temperature	1×10^{-4}	T. Yamamoto et al. 2006[41]
Self-assembled $(NH_4)_{0.5}V_2O_5$ nanowires	Four-probe method, in air, room temperature	1×10^{-3}	X. Wu et al. 2004[42]

Fmoc-L_3 was found to have the lowest resistance out of all of the peptides studied. However, it still had a higher resistance than the conductivities of the organic and inorganic conductive nano-

networks reported in the literature, as shown in Table 4.2. It should be noted, though, that some of these networks are made from conductive polymers and were doped.

4.3.2 Conductivity of Fmoc-L_3 xerogel

4.3.2.1 Conductivity of Fmoc-L_3 (enzyme)

Nyquist plots were obtained to investigate the charge transport properties of the dried networks of the peptide nanostructures. Figure 4.28a, c shows the impedance characteristics of the Fmoc-L_3 networks with varying network density. (The network density is related to the total mass of peptide used to make the network.) In the complex impedance plot, the distance across the arc, which is obtained under AC bias conditions, corresponds to the electric resistance of the sample.[43] The slope observed at the low frequency end of the arc relates to mass transfer (Figure 4.28a) and this slope almost disappears under vacuum conditions (Figure 4.28c). These results imply that the films show both electronic and ionic conductivity when impedance measurements were made in air. The ionic conduction was probably caused by the presence of ion containing water absorbed to the hydrophilic nanostructures. In vacuum, the low frequency ionic part of the curve is absent which suggests predominately electronic conductivity in the dried films under vacuum [35]. Figures 4.28b, d show the Bode plots of an Fmoc-L_3 xerogel in air and under vacuum. Three relaxation processes appear in the spectra (Figure 4.28b) in air, which are attributed to peptide nanotubes (approximately 10^5 Hz), peptide nanotubes networks (approximately 10^4 Hz), and electrode response (approximately 10^{-1} Hz), as described by the Warburg model in Figure 3.11.[44] Two relaxation processes appear in the spectra in vacuum, which are attributed to peptide nanotubes and peptide nanotubes networks. These match the model as shown in Figure 3.10. The calculated data were modelled by software (ZSimpWin) based on the inset equivalent circuits (Figure 4.28 a, c).

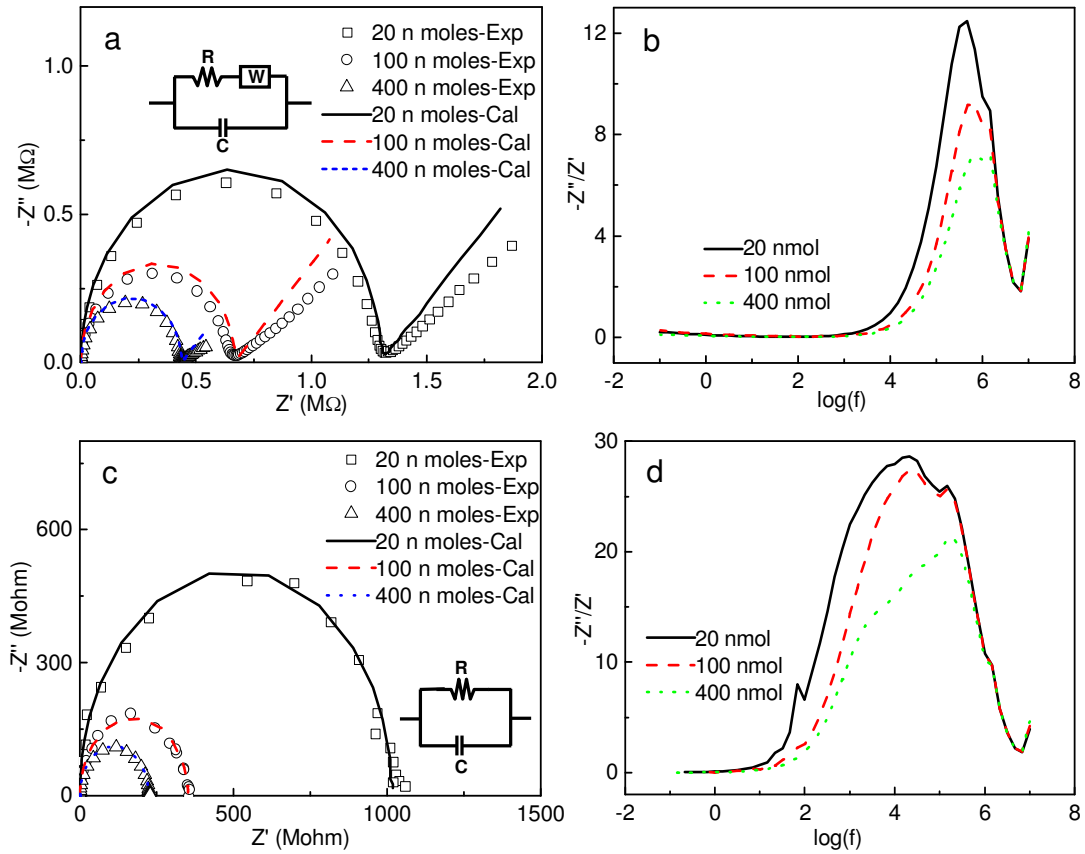

Figure 4.28 Impedance spectroscopy measurements and fitted data of the peptide networks as a function of amount of Fmoc-L_3-OMe used to make the network under ambient conditions in air (a and b) and under vacuum (c and d). Nyquist plots: a, c; Bode plots: b, d. Exp: experimental data; Cal: calculated data from software Zsimpwin. Inset: equivalent circuits. $R_{20\ n\ moles\ air}=5.2\times10^{6}$ Ω/sq, $R_{100\ n\ moles\ air}=2.7\times10^{6}$ Ω/sq, $R_{400\ n\ moles\ air}=1.8\times10^{6}$ Ω/sq, $C_{20\ n\ moles\ air}=1.25\times10^{-5}$ μF, $C_{100\ n\ moles\ air}=1.20\times10^{-5}$ μF, $C_{4000\ n\ moles\ air}=1.28\times10^{-5}$ μF, $R_{20\ n\ moles\ vacuum}=4.0\times10^{9}$ Ω/sq, $R_{100\ n\ moles\ vacuum}=1.4\times10^{9}$ Ω/sq, $R_{400\ n\ moles\ vacuum}=8.8\times10^{8}$ Ω/sq, $C_{20\ n\ moles\ vacuum}=1.27\times10^{-5}$ μF, $C_{100\ n\ moles\ vacuum}=1.23\times10^{-5}$ μF, $C_{400\ n\ moles\ vacuum}=1.30\times10^{-5}$ μF.

Figure 4.29 shows how the sheet resistance of the samples increased as the vacuum was applied and the water was removed. The resistance of the networks was found to equilibrate after 2 hours under vacuum. Therefore, all the samples studied in vacuum system were left to equilibrate for 2 hours prior to measurement. The resistance of the network showed little deviation over a time period of 4 days under vacuum conditions, with it increasing by 12 % as shown in Figure 4.30. Figure 4.31 shows the network resistance as a function of the amount of Fmoc-L_3 present for both ambient and under vacuum conditions, respectively. The sheet resistance is

used since it is difficult to accurately establish the sample thickness due to the porosity of the network. (Surface mapping meter analysis suggests that the thickest of the films were around 1 µm in height). The variation in the sheet resistance for the films at 400 n moles should be noted. This variation is due to the random, statistical nature of the drying process and subsequent percolation, which leads to some variation from sample to sample.

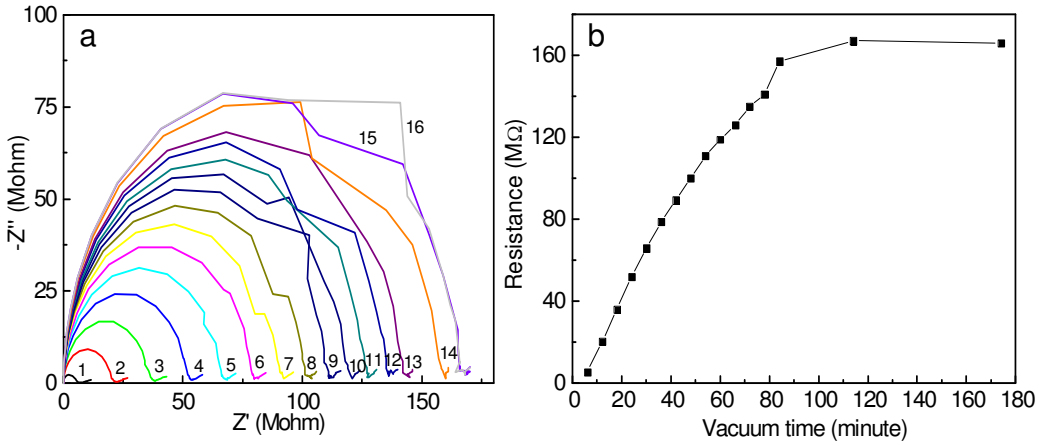

Figure 4.29 a, Impedance spectra of Fmoc-L_3 film at different vacuum time from 1 to 15 following vacuum time increasing, b, the resistance of a peptide network from impedance spectra (a) as a function of time spent under 1 mbar vacuum.

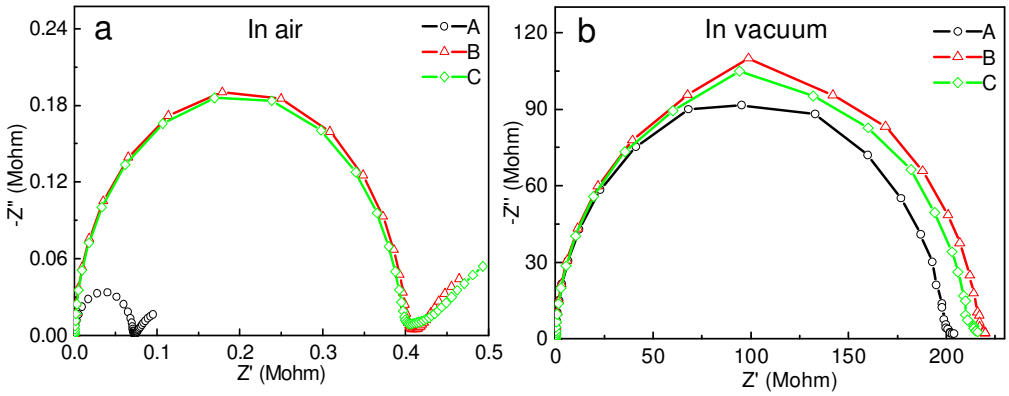

Figure 4.30 Complex impedance plot data (frequency ranged from 0.1 to 107 HZ) for Fmoc-L3 film at different times in vacuum. A—day 0, B—day 2, C—day 4 : a, in air, b, in vacuum.

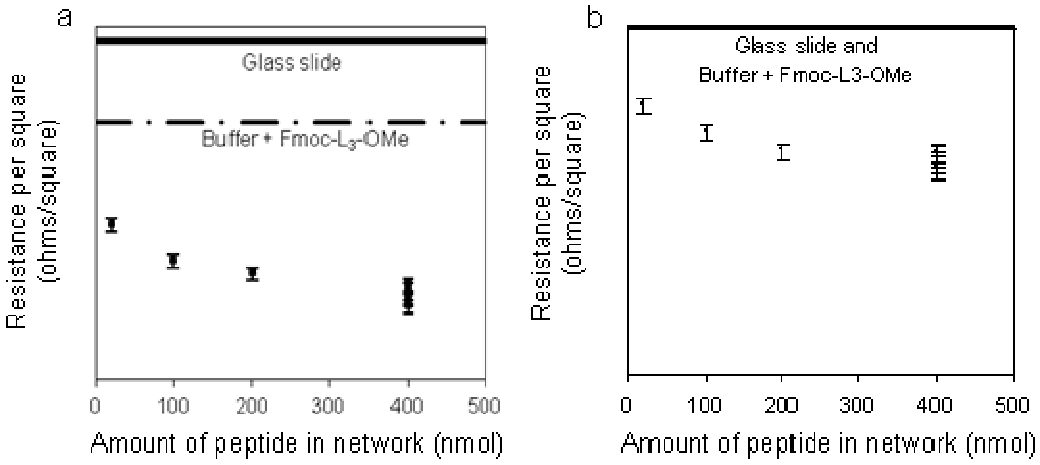

Figure 4.31 Sheet resistance of the peptide networks as a function of amount of Fmoc-L_3-OMe used to make the network under ambient conditions in air (a) and under vacuum (b).

The resistance of the blank glass substrate and dried Fmoc-L_3-OMe buffer solution are also shown in Figure 4.31a, b with their full impedance spectra shown in Figure 4.26. These resistances were at least two orders of magnitude higher than those found for the peptide nanotube networks. It is interesting to note that the conductivity of the Fmoc-L_3-OMe sample drops to that of the blank slide upon drying in the vacuum suggesting that its conductivity in air was largely due to the ions in the buffer solution diffusing through the absorbed water. Furthermore, the Fmoc-L_3-OMe film had significantly reduced conductivity compared to the Fmoc-L_3 network, showing the importance of forming the supramolecular π-β nanotubular structure.

In order to study the reproducibility of Fmoc-L_3 networks, a series of experiments were carried out to check the conductivity by impedance measurements. Figure 4.32 shows impedance spectra of a range of Fmoc-L_3 films (exo-gels) which were produced by the same methods, but on different dates. Samples 1, 2 and 3 were prepared at the same time, whilst samples 4 and 5 were made 4 months and 1 month beforehand, respectively. The resistance of samples varied by 75% in air, as shown in Figure 4.32, whereas the resistance of samples varied by 50% in vacuum, as shown in Figure 4.32b. Furthermore, 300 µL of hydrogel were dropped onto a large glass slide to make three samples on the same substrate. These were used to detect the uniformity of Fmoc-L_3 networks. Figure 4.33 shows the impedance measurements of these films. In vacuum, the resistances of the samples were of the same order, which indicated that the large area film from

Fmoc-L_3 hydrogel has high uniformity such as thickness and density, whilst there could be variation from substrate to substrate.

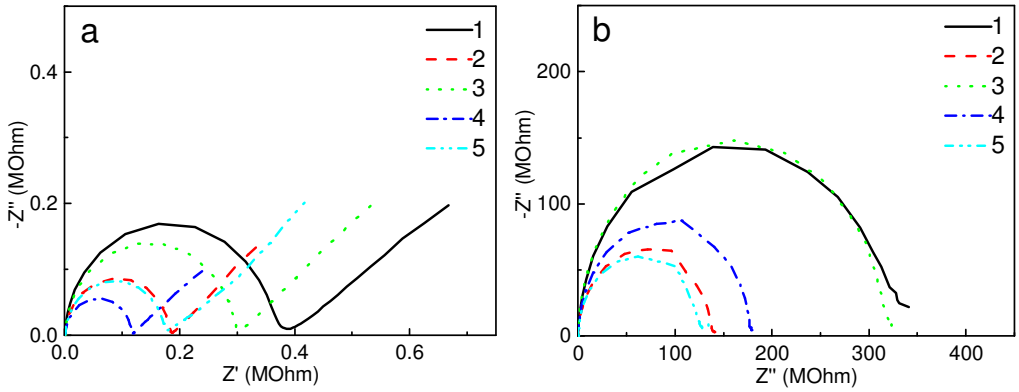

Figure 4.32 Impedance spectra of Fmoc-L_3 samples prepared by the same methods in air and vacuum. (a) in air, (b), in vacuum. Sample 1, 2 and 3 were prepared at the same time; Sample 4 was prepared for 5 months, sample 5 was prepared for 1 month.

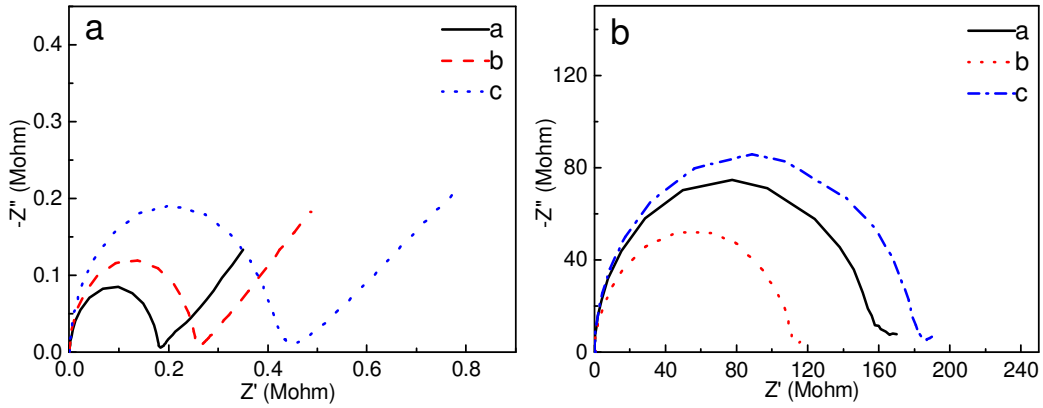

Figure 4.33 Impedance spectra of Fmoc-L_3 samples prepared on a big glass slide in air and vacuum.

4.3.2.2 Affection of relative humidity (RH) on conductivity of Fmoc-L_3 (enzyme)

The conductivity of Fmoc-L_3 dried films was different from air to vacuum, as discussed in the last section. Therefore, the impedance of a dried film was measured under different relative humidities (RH) in order to understand the relative contribution of electronic and ionic conductivity

of the dried film (Figure 4.34). A convenient method to produce controlled RH humidities is the use of saturated salt solutions. At any given temperature, the concentration of a saturated solution is fixed.[45] By providing excess solute, the solution will remain saturated. The sample was put in sealed glass chamber with a vial, which had the saturated salt solution prepared by a mixture of excess chemically pure salt with distilled water, for around 12 hours. The electrical measurements were carried out in the same environment. The saturated salt solution used were: lithium chloride (LiCl), magnesium chloride ($MgCl_2$), sodium chloride (NaCl), potassium chloride (KCl) and potassium nitrate (KNO_3) with relative humidity: 28.7%, 43.3%, 78.6%, 87.4% and 96.3% respectively. The slope appears at the end of the arc in a high relative humidity environment.

The impedance data of Fmoc-L_3 dried films at varied RH were simulated according to equivalent circuits. Equivalent circuits in Figure 4.23a and b were applied in vacuum, low RH (28.7%), and RH 43.3% (similar with in air), respectively (Figure 4.34 a, b, c). The equivalent circuit in Figure 4.35 was used to model the Fmoc-L_3 film at high RH (over 78.6%), which is the model shown in Figure 3.12. In this equivalent circuit, R_{wet} is from the resistance of the ions moving amongst the wet film due to very high RH. The resistance of film in high RH is the same as the film in air including $R_{networks}$ and Warburg impedance W_{ion}.

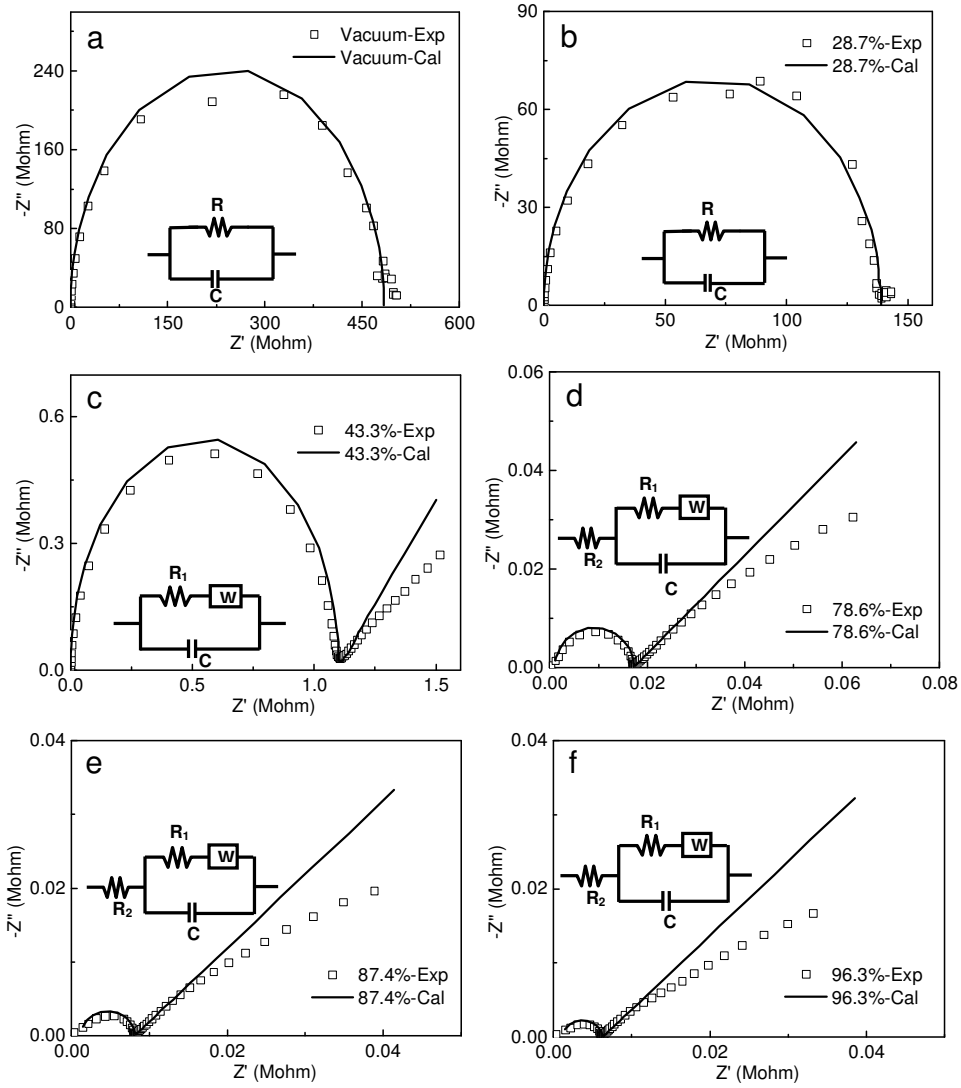

Figure 4.34 Impedance spectra of Fmoc-L_3 film at different relative humidity, fitted data and equivalent circuits (inset). a, in vacuum; b, LiCl, 28.7%; c, $MgCl_2$, 43.3%; d, NaCl, 78.6%; e, KCl 87.4%; f, KNO_3, 96.3%. Exp: experimental data; Cal: calculated data. $R_{vacuum}=1.9\times10^{9}$ Ω/sq, $C_{vacuum}=9.10\times10^{-6}$ μF, $R_{28.7\%}=5.6\times10^{8}$ Ω/sq, $C_{28.7\%}=9.17\times10^{-6}$ μF, $R_{43.3\%}=4.4\times10^{6}$ Ω/sq, $C_{43.3\%}=8.87\times10^{-5}$ μF, $R_{78.6\%}=6.4\times10^{4}$ Ω/sq, $C_{78.6\%}=1.16\times10^{-5}$ μF, $R_{87.4\%}=27808$ Ω/sq, $C_{87.4\%}=1.41\times10^{-5}$ μF, $R_{96.3\%}=20628$ Ω/sq, $C_{96.3\%}=1.59\times10^{-5}$ μF

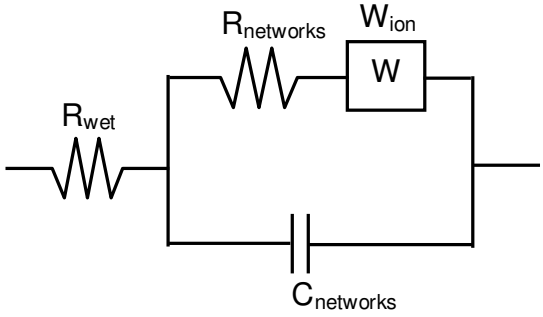

Figure 4.35 Equivalent circuits for Fmoc-L_3 film at high relative humidity (over 78.6%).

Nyquist and Bode plots of Fmoc-L_3 hydrogel was shown in Figure 4.36a, b, which was simulated by the equivalent circuit in Figure 4.36c which was developed by Armstrong *et al.*[46] The hydrogel contains two main phases: (i) Fmoc-L_3 nanotube networks, surrounded by structured or bound water (labelled 'gel-networks') and (ii) unbound water (or other aqueous solution contained buffer salts) which is free to solvate ions (labelled 'sol'). Fmoc-L_3 hydrogel (R_{gel}) was modelled with a resistance of hydrogel $R_{gel\text{-}networks}$ in parallel with a gel capacitance $C_{gel\text{-}networks}$. R_{ct} represents the charge transfer resistance at the metal interface due to corrosion, in parallel with a capacitance C_{DL} representing the interfacial capacitance between the electrode and the electrolyte. Warburg impedance W_{ion} is from mass transfer at the electrode-electrolyte interface. R_{sol} represents the charge transfer resistance in the solution (Figure 4.36c). Resistance of Fmoc-L_3 dried film was measured at different relative humidity, as shown in Figure 4.37. The resistance decreased from vacuum with 0% relative humidity to high relative humidity at around 96.3%. The hydrogel has the highest conductivity due to the ionic conductivity.

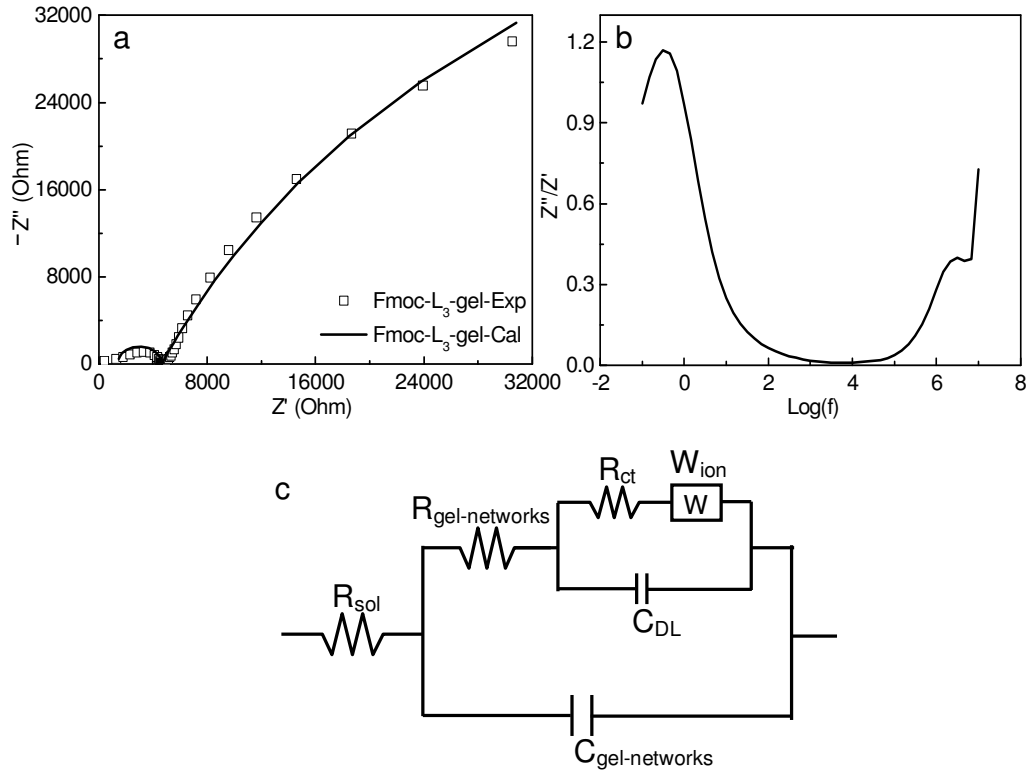

Figure 4.36 Impedance spectra of Fmoc-L_3 hydrogel: a, Nyquist plots, b, Bode plots; c, equivalent circuits for Fmoc-L_3 hydrogel. Exp: experimental data; Cal: calculated data. R_{gel}=13008 Ω/sq, C_{gel}=3.08 ×10^{-5} μF, C_{DL}=47.1 μF.

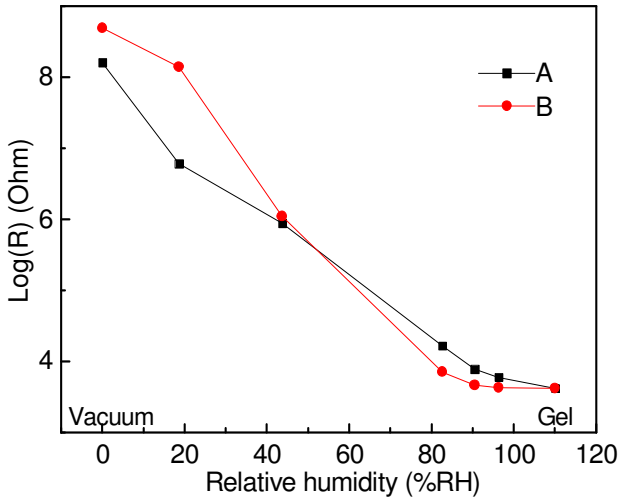

Figure 4.37 Resistance of Fmoc-L_3 dried film in varied relative humidity that was controlled by saturated salt solutions and resistance of Fmoc-L_3 hydrogel.

4.3.2.3 Fmoc-L_3 (pH)

To exclude the role of enzyme in the conduction mechanism, Fmoc-peptide networks were also prepared by using pH induced self-assembly of Fmoc-L_3. Figure 4.38 show the TEM images of resultant networks which consisted of hollow nanotubes with a diameter of around 15 nm, which is similar to that found for the enzyme triggered networks (Figure 4.14a). The AFM image from Figure 4.39 shows that the Fmoc-L_3 pH nanotubes had diameters of ~10 nm (Figure 4.39b), which is smaller than the diameter obtained from TEM due to the flattening of the nanotubes upon drying. As a result, the nanotube height is smaller than the width obtained from the AFM image. However, Fmoc-L_3 (enzyme) nanotubes are straighter than Fmoc-L_3 (pH) (Figure 4.14a, c, 4.38 and 4.39). The resistance of Fmoc-L_3 pH film was measured by impedance spectroscopy (Figure 4.40). It was found that the pH induced networks had a sheet resistance of 100 MΩ/sq in air and 810 MΩ/sq in vacuum, which was within error of the values found for the networks produced by enzyme induced self-assembly.

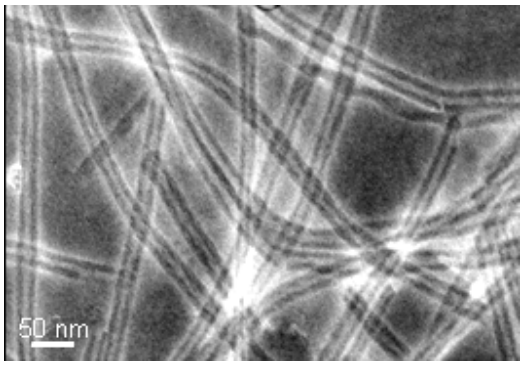

Figure 4.38 Transmission electron micrographs (TEM) image of peptide Fmoc-L_3 based on pH with a width of around 22 nm and inner diameter of around 6 nm, sample was negatively stained with 2% uranyl acetate.

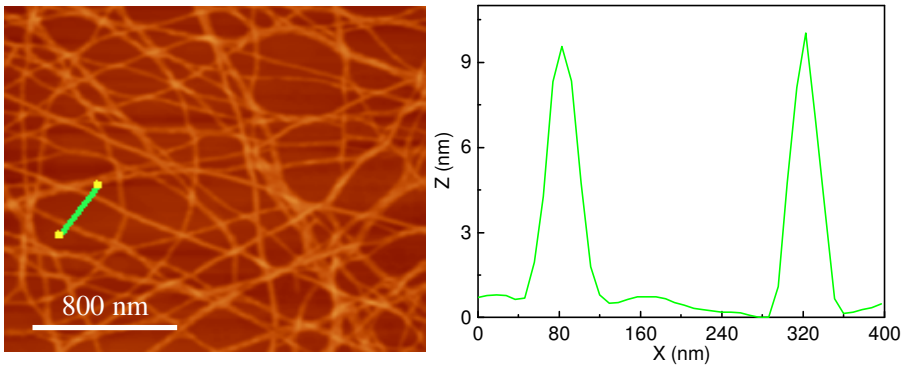

Figure 4.39 Tapping mode AFM analysis of Fmoc-L_3 network which based on pH: a, AFM image of the nanotubes, b, cross-section from the nanotubes. The tip had a diameter of approximately 30 nm, explaining the wider thickness that is observed compared to the height.

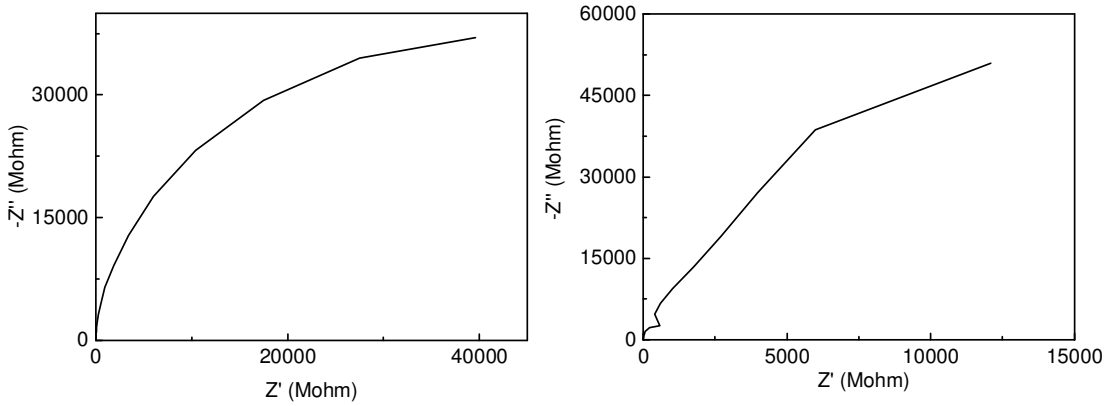

Figure 4.40 Complex impedance plot data (frequency ranged from 0.1 to 107 HZ) for Fmoc-L_3 pH film: a, in air, b, in vacuum

If the peptide networks acted as percolated films, then the conductivity of the networks should scale with a power law to the amount of peptide present in the films, above the percolation threshold concentration at which the peptide nanotubes form a coherent network. It was found however, that the conductivity of the networks scaled linearly with amount of peptide, suggesting that, at the concentrations used, the nanotubes formed a coherent film.

4.4 CONDUCTIVITY ANALYSIS AND COMPARISON

UV-Vis spectroscopy measures the energy to activate a molecule from its ground electronic state to an electronically excited state (promoting an electron from an occupied to an unoccupied

molecular orbital). Although electronic transitions arise between ground and excited states of the entire molecule, in UV-Vis absorption most of the excitation can be assigned to parts of the molecule (chromophores) where the valence electrons are found, such as the nonbonding (n) or π electrons. λ_{max} is the wavelength at which light absorption reaches a maximum. λ_{onset} is the onset of light absorbance depending on the molecule of interest. UV-Vis absorption spectrum may exhibit many absorption bands, with λ_{max} of each band corresponding roughly to the energy associated with the formation of a particular excited state. λ_{onset} corresponds to the excitation energy and the intensity of λ_{onset} is related to the probability of promoting an electron into that energy level. Electronic transitions may be classed as intense or weak according to their magnitude, roughly measured at λ_{onset}. According to Planck's equation, frequency is directly proportional to energy,

$$\Delta E = h\nu , \qquad (4.2)$$

$$\text{as } c = \lambda\nu \qquad (4.3)$$

$$\text{so } \Delta E = \frac{hc}{\lambda} , \qquad (4.4)$$

where, ν is the frequency of the wave, c is speed of light, which is 299792458 m/s, h is Planck constant, which is 6.62606896(33) × 10^{-34} J s = 4.13566733(10) × 10^{-15} eV s. Band gap values (Table 4.3) were evaluated in terms of UV-Vis-NIR Spectrum (Figure 4.41). These values are about 4 eV which is in the range typically associated with semiconductors [R. Takahashi 2007][47]. UV-Vis-NIR spectra of Fmoc-peptide-ester and hydrogel films were measured as shown in Figure 4.41. In the comparative curves between Fmoc-peptide-ester and hydrogel gel film, the maximum peak in the absorption spectra clearly showed a red shift from around λ=242 nm to 262 nm between the molecule and the self-assembled larger aggregates composed of π–π stacking. The peak at 242 nm and 261 nm from Fmoc-L_3 and Fmoc-LL is due to the aromatic fluorene electronic transitions.[48] The peak at about 305 nm is from fluorenyl group. Tryptophan has an indole chromophore which gives a peak at 280 nm. Tryrosine has a phenol residue which exhibits bands

at 290 nm. Also, the amide or peptide bond, -CO-NH- has bands at 225 nm.[49] So Fmoc-WL and Fmoc-YL have a broad peak from 260-275 nm.

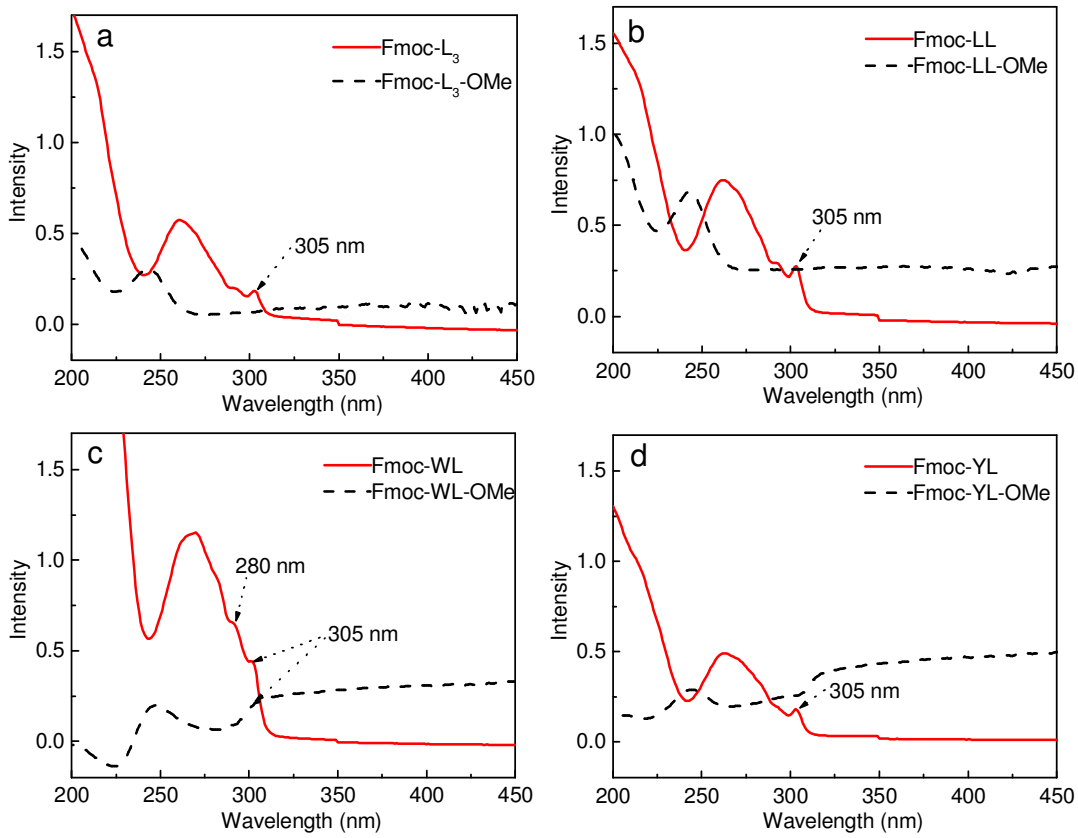

Figure 4.41 UV-Vis-NIR spectrum curves of films: Fmoc-LL, Fmoc-L_3, Fmoc-WL and Fmoc-YL

Table 4.3 The λ_{onset}, and band gap (E_g) of hydrogel films from UV-Vis spectra

Samples	UV-Vis	
	λ_{onset} (nm)	E_g (eV)
Fmoc-LL	309±2	3.99±0.02
Fmoc-L_3	309±2	4.01±0.02
Fmoc-WL	309±2	4.00±0.02
Fmoc-YL	309±2	4.00±0.02

The electronic properties of peptide films were also examined by cyclic voltammetry (CV). In CV, the material is put in a solvent containing an electrolyte, a reference solute, and the working, counter and reference electrodes. Voltage is swept across the electrodes, inducing a current. To avoid resistive drops and internal polarization, the voltage measured is that of the working electrode relative to the reference electrode. Here, the thin films of the peptide hydrogels were deposited onto a platinum working electrode. The electrolyte is an acetonitrile solution of $[(C_4H_9)_4N]PF_6$ (0.10 M).[50] The reference and counter electrode are $Ag/AgNO_3$ and platinum wire, respectively. The oxidation and reduction processes were found to irreversible and they destroyed the peptide network. Therefore, the oxidation and reduction processes were measured on separate samples and the resultant two CVs were stitched together to give a master CV in Figure 4.42. The energy levels of the highest occupied molecular orbital (HOMO) and the lowest unoccupied molecular orbital (LUMO) for these peptide films were estimated from the onset potential of oxidation and reduction peaks of CV, respectively (see Table 4.4). The electrochemical band gap ($E_{g\text{-}ec}$) was calculated from the difference between these values for the HOMO and LUMO. HOMO and LUMO are calculated as shown in Table 4.4.

$$HOMO = -(4.8 + E_{pa\text{-}onset} - E_{Fc}) \quad (4.5)$$

$$LUMO = -(4.8 + E_{pc\text{-}onset} - E_{Fc}) \quad (4.6)$$

Where E_{Fc} (= 0.105 V vs. $Ag/AgNO_3$) is half wave potential of ferrocence.,

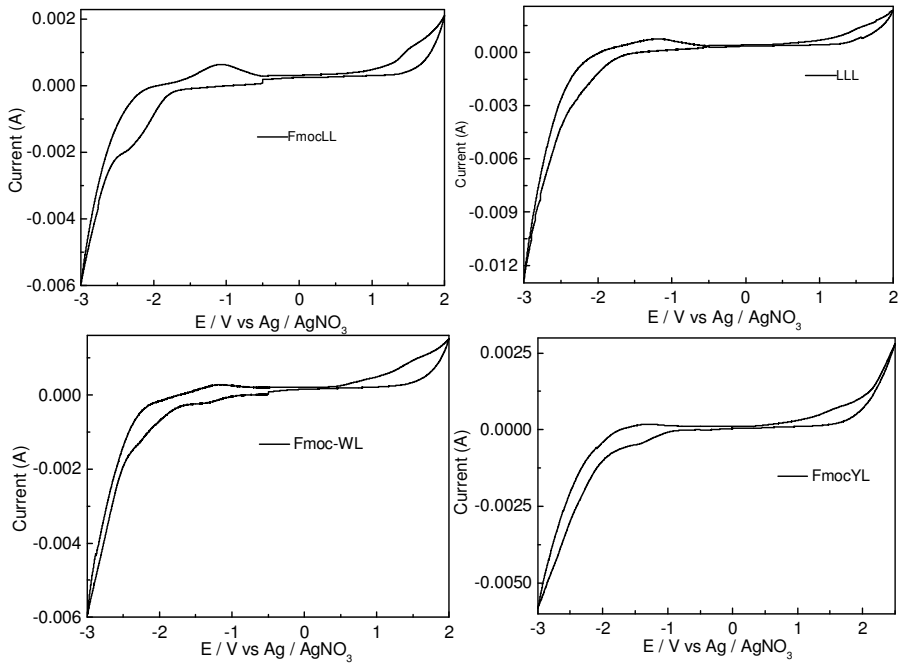

Figure 4.42 Cyclic voltammograms of on platinum plate electrodes in acetonitrile containing 0.1 M n-Bu_4NPH_6. Note that the oxidation and reduction peaks are irreversible and hence were measured on separate samples. Counter electrode: platinum wire. Reference electrode: $Ag/AgNO_3$ (0.1 M in acetonitrile). Scan rate: 50 mV/s. a: Fmoc-LL gel film: HOMO=-5.71 eV, LUMO=-3.00 eV, Eg-cv=2.71 eV. b: Fmoc-L_3 gel film: HOMO=-5.63 eV, LUMO=-3.145 eV, Eg-cv=2.48 eV. c: Fmoc-WL gel film: HOMO=-5.242 eV, LUMO=-3.88 eV, Eg-cv=1.326 eV. d: Fmoc-YL gel film: HOMO=-5.53 eV, LUMO=-3.82 eV, Eg-cv=1.711 eV.

It is noted that the electrochemical band gap observed from CV is similar to that for the optical band gap.

Table 4.4 Electrochemical properties of peptide films

Films	Oxidation (V)	Reduction (V)	HOMO /eV	LUMO /eV	$E_{g\text{-}ec}$ /eV
Fmoc-LL	1.0±0.1	-1.7±0.1	-5.7±0.1	-3.0±0.1	2.71±0.1
Fmoc-L_3	1.0±0.1	-1.6±0.1	-5.6±0.1	-3.2±0.1	2.48±0.1
Fmoc-WL	0.5±0.1	-0.8±0.1	-5.2±0.1	-3.9±0.1	1.33±0.1
Fmoc-YL	0.8±0.1	-0.9±0.1	-5.5±0.1	-3.8±0.1	1.71±0.1

The resistance-temperature profiles of the peptide nanostructures as measured by I-V also showed semiconducting behaviour, i.e., the current increases rapidly with increasing temperature as shown in Figure 4.43. In order to investigate whether the structures were changed by heating, up to 100 ºC, current-temperature curves both by heating (Figure 4.43a) and cooling (Figure 4.43b) were recorded in the vacuum system. Figure 4.45 depicts a temperature dependence Ahrrenius-type equation:

$$\sigma = \sigma_0 \, exp(-E_{act} / RT), \tag{4.7}$$

where E_{act} and T are activation energy and temperature respectively; R is gas constant equal 8.314472(15) J/(K.mol). The current increases with heating up the samples, and decreases with the temperature decrease. The two curves are similar as shown in Figure 4.43a, b and 4.45a, b. E_a values were calculated from the profile of ln(I) against 1/T. The temperature dependence of the resistance on the range 300 to 380 K revealed a semiconductor-like behaviour with activation energy (E_{act}) of 0.5 eV which were calculated from the slope of the linear line as shown in Table 4.5. The two E_a values from both heating and cooling respectively were close, which indicated that the samples were not changed whilst heating. This result provides basic evidence in support of the formation of conducting nanostructures which form a mesh that behaves as a semiconductor in this measurement.

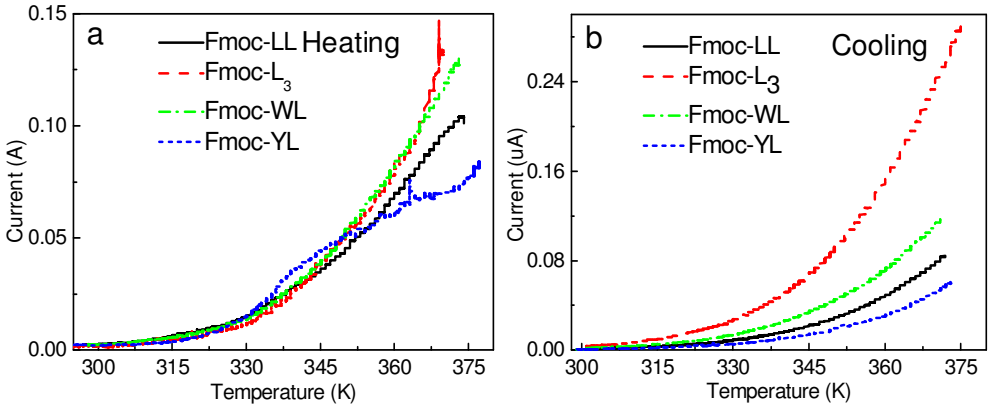

Figure 4.43 The temperature dependence of the current for the hydrogel films in vacuum system. (a) Curves from heating up samples; (b) Curves from cooling samples.

Table 4.5 Activation energy values of Fmoc-LL, Fmoc-L_3, Fmoc-WL and Fmoc-YL from vacuum system.

Samples of diluted films	Fmoc-LL	Fmoc-L_3	Fmoc-WL	Fmoc-YL
E_{act} (eV)	0.54±0.04	0.59±0.02	0.56±0.02	0.55±0.05

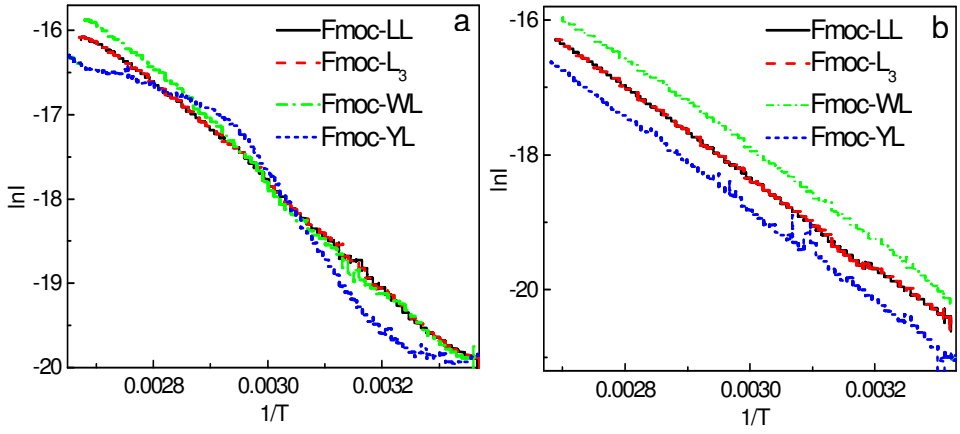

Figure 4.44 Plots of ln(I) versus 1/T: (a) heating up the sample; (b) cooling the samples

The conductivity of the dried films (Fmoc-LL, Fmoc-WL, Fmoc-YL) differed under air environment and vacuum, similar to Fmoc-L_3. A series of experiments were carried out to exam the relationship between conductivity and the relative humidity of dried films. Figure 4.45 shows the

current of the film that changed in response to relative humidity. The current decreased slightly before the vacuum was switched on due to the ion being moved in the film in air. This was because the film adsorbed water in air when a constant potential (3 V) was applied to the film. However, the current became constant under vacuum, indicating that the conductivity of film resulted from electronic conduction, which presumably arises from the delocalized electron system. In addition, the current of films increased after the vacuum was switched off and the resistance were able to recover to their initial value after one day in air.

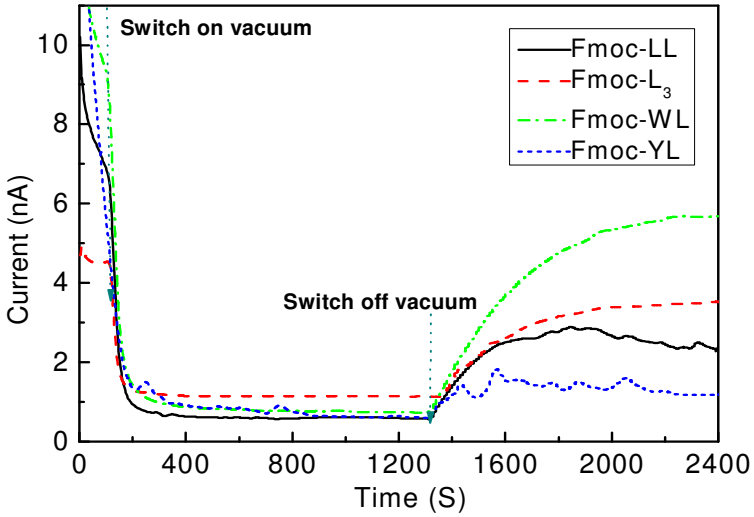

Figure 4.45 Currents changing at different environment at the same voltage at 3V.

In order to investigate the stability of the films, resistances were measured by impedance spectroscopy at different times (first day, second day and third day) both in air and vacuum, as shown in Figure 4.46. Resistance changed at different experimental times in air due to the relative humidity (RH) changing in the lab (Figure 4.46); by contrast, in vacuum, the changing range of resistances became stable. There was a slope at the second arc because of the mass transfer in air; while there is no slope present in vacuum. Figure 4.46 also shows the impedance data from the Fmoc-LL, Fmoc-L_3, Fmoc-WL and Fmoc-YL hydrogel films that were initially held under vacuum and then placed in air for 24 hours before their impedance was measured. This process was repeated for three days to assess the repeatability of the hydration process. The resistances of Fmoc-WL changed on each day and the two arcs in the curve from the second day

due to its inhomogeneous structure in Figure 4.46a, c (green curves). This result is possible from two kinds of nanostructures (nanofibres and large disorder aggregates) in the film, as observed by the AFM (Figure 4.9c). The measurements demonstrated that the film hydrated rapidly and reversibly, and the adsorption of water is responsible for the increased conductivity. It is impossible that the ionic conductivity would be high enough to contribute significantly to high levels of electronic conductivity. It is therefore concluded that the water enhances charge transport in the films.

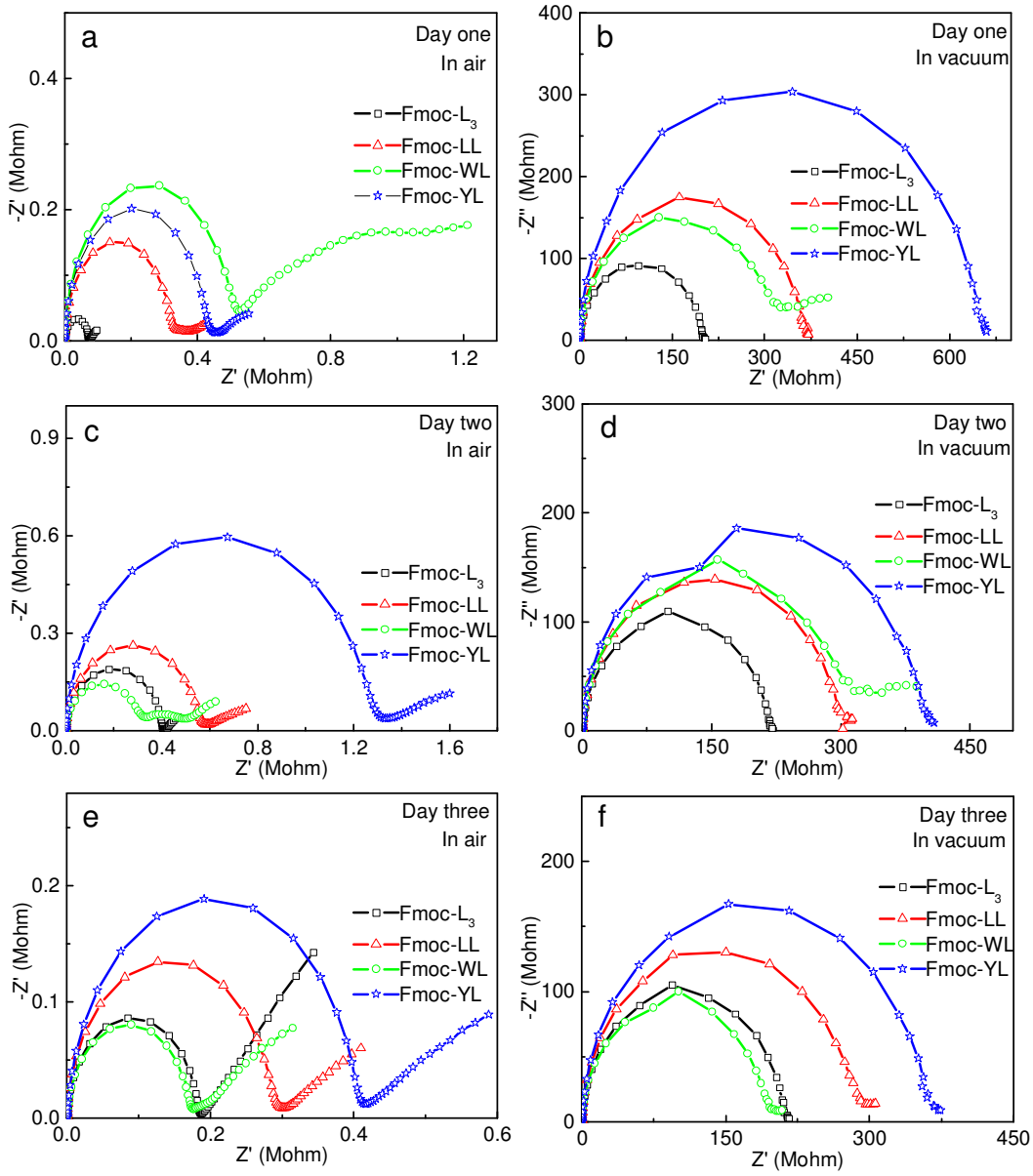

Figure 4.46 Impedance spectroscopy measurements of the hydrogels films at different days in air and vacuum. a: day one in air, b: day one in vacuum, c: day two in air, d: day two in vacuum, e: day three in air, f: day three in vacuum. The samples were put in vacuum for two hours before measurement.

Furthermore, the resistances of films (Fmoc-LL, Fmoc-L_3, Fmoc-WL and Fmoc-YL prepared for three times by the same method) were measured at different times (three days) in air and vacuum, the values for which are shown in Figure 4.47. The resistance points are not on the same level in air because the resistance relied on the RH in Figure 4.47a. In vacuum, the

resistance of Fmoc-L_3 was constant (Figure 4.47b) indicating that the film was stable under vacuum for at least 3 days.

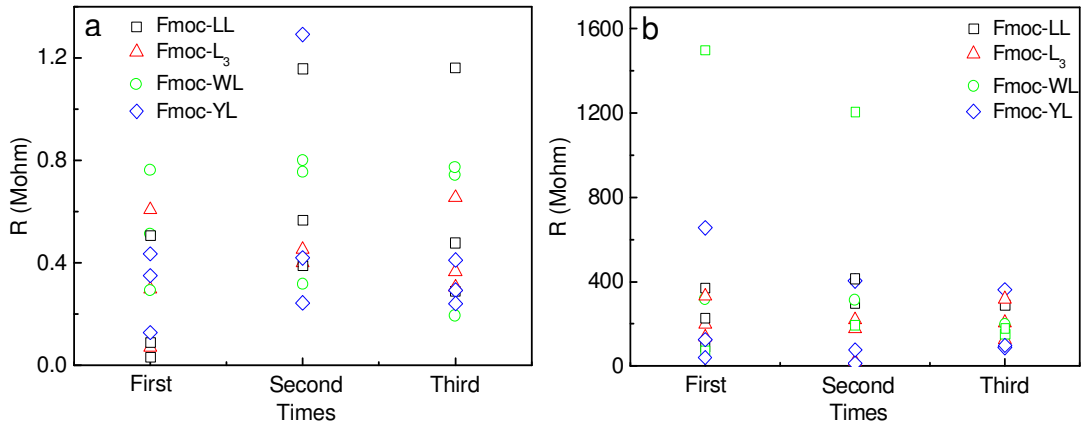

Figure 4.47 Resistance comparisons between four samples (Fmoc-LL, Fmoc-L_3, Fmoc-WL and Fmoc-YL) at different times (a), in air, (b), in vacuum.

4.5 CONCLUSIONS

Current-Voltage (I-V) curves and impedance spectra were used to describe the conductivities of films (Fmoc-LL, Fmoc-L_3, Fmoc-WL and Fmoc-YL), which were about 10^{-2} S/m in air, and 10^{-4} S/m in vacuum. From impedance plot data, it is believed that these films are electronically conductive under vacuum because no mass transfer was observed by impedance spectroscopy. The current of the films increased upon heating, suggesting a semiconductor behaviour. The semiconducting nature was confirmed by measuring the optical band gap (E_g) and activation energy (E_{act}) as 4.0 eV and 0.5-0.6 eV respectively. The band gap was also evaluated electrochemically, and found to be slightly lower. The Fmoc-L_3 networks had the highest conductivity and stability out of the films studied.

Furthermore, Fmoc-L_3 π–β nanotubular networks formed by enzyme-triggered self-assembly of aromatic peptide amphiphiles were demonstrated in detail and found to show significant charge transport. Minimum sheet resistances of bulk peptides of 0.1 MΩ/sq in air and 500 MΩ/sq in

vacuum at room temperature can be achieved. The mechanism of charge transport for these systems is likely to involve electronic transport under vacuum with the introduction of additional ionic transport under ambient conditions due to adsorbed moisture and the presence of buffer salts.

4.6 REFERENCES

1. Y. Yamamoto, T. Fukushina, N. Ishii, A. Saeki, S. Seki, S. Tagawa, M. Taniguchi, T. Kawai, T. Aida, Photoconductive coaxial nanotubes of molecularly connected electron donor and acceptor layers, Science, 2006, 314, 1761-1764.
2. A. P. H. J. Schenning, E. W. Meijer, Supramolecular electronics; nanowires from self-assembled π-conjugated systems, Chem. Commun., 2005, 3245-3258.
3. C. Daniel, F. Makereel, L. M. Herz, F. J. M. Hoeben, P. Jonkheijm, P. H. J. Schenning, E. W. Meijer, R. H. Friend, C. Silva, J. Chem. Phys., The effects of supramolecular assembly on exciation decay rates in organic semiconductors, 2005, 123, 084902.
4. D. A. Stone, L. Hsu, S. I. Stupp, Self-assembling quinquethiophene-oligopeptide hydrogelators, Soft Matter, 2009, 5, 1990-1993.
5. B. Q. Xu, P. M. Zhang, X. L. Li, N. J. Tao, Direct conductance measurement of single DNA molecules in aqueous solution, Nano Lett., 2004, 4, 1105-1108.
6. X. F. Guo, A. A. Gorodetsky, J. Hone, J. K. Barton, C. Nuckolls, Conductivity of a single DNA duplex bridging a carbon nanotubes gap, Nat. Nanotechnol., 2008, 3, 163-167.
7. C. Li, J. Ly, B. Lei, W. Fan, D. Zhang, J. Han, M. Meyyappan, M. Thompson, C. Zhou, J. Data storage studies on nanowires transistors with self-assembled porphyrin molecules, Phys. Chem. B, 2004, Vol. 108, 9646-9649.
8. I. Yanov, Y. Kholod, J. Leszczynski, J. Palacios, Electron transport properties of the porphyrin molecule located between gold electrodes, Chem. Phys. Lett., 2007, Vol. 445, 238-242.
9. R. I. MacCuspie, N. L. S.-Y. Nuraje, A. Runge, H. Matsui, J. Am. Chem. Soc., 2008, 130 (3), 887.
10. M. R. Ghadiri, J. R. Granja, R. A. Milligan, D. E. McRee, N. Khazanovich, Self-assembling organic nanotubes based on a cyclic peptide architecture, Nature, 1993, Vol. 366, 324-327.
11. S. R. Diegelmann, J. M. Gorham, J. D. Tovar, One-dimensional optoelectronic nanostructures derived from the aqueous self-assembly of π-conjugated oligopeptides, J. Am. Chem. Soc., 2008, Vol. 130, 13840-13841.
12. M. Yemini, M. Reches, J. Rishpon, E. Gazit, Novel electrochemical biosensing plattorm using self-assemble peptide nanotubes, Nano Lett., 2005, 5, 183-186.

13. J. D. Hartgerink, J. R. Granja, R. A. Miligan, M. R. Ghadiri, Self-assembling peptide nanotubes, J. Am. Chem. Soc., 1996, Vol. 118, 43-50.
14. K. J. Channon, G. L. Devlin, S. W. Magennis, C. E. Finlayson, A. K. Tickler, C. Silva, C. E. Macphee, Modification of fluorophore photophysics through peptide-driven self-assembly, J. Am. Chem. Soc., 2008, 130 (16), 5487-5491.
15. Y. Zhang, H. Gu, Z. Yang, B. Xu, Supramolecular hydrogels respond to ligand – receptor Interaction, J. Am. Chem. Soc., 2003, 125, 13680.
16. Z. Yang, H. Gu, D. Fu, P. Gao, J. K. Lam, B. Xu, Enzymatic formation of supramolecular hydrogels, Adv. Mater., 2004, 16, 1440.
17. D. J. Adams, M. F. Butler, W. J. Frith, M. Kirkland, L. Mullen, P. Sanderson, A new method for maintaining homogeneity during liquid-hydrogel transitions using low molecular weight hydrogelators, Soft Matter, 2009, Vol. 5, 1856-1862.
18. A. M. Smith, R. J. Williams, C. Tang, P. Coppo, R. F. Collins, M. L. Turner, A. Saini, R. V. Ulijn, Fmoc-Diphenylalanine self assembles to a hydrogel via a novel architecture based on π-π interlocked β-sheets, Adv. Mater., 2008, 20, 37.
19. R. J. Williams, A. M. Smith, R. Collins, N. Hodson, A. K. Das, R. V. Ulijn, Enzyme-assisted self-assembly under thermodynamic control, Nature nanotechnology, Nat. Nanotechnol., 2009, 4, 19.
20. H. Shao, J. R. Parquette, A. π-conjugated hydrogel based on an Fmoc-dipeptide naphthalene diimide semiconductor, Chem. Commun., 2010, 46, 4285-4287.
21. L. Chen, K. Morris, A. Laybourn, D. Elias, M. R. Hicks, A. Rodger, L. Serpell, D. J. Adams, Self-assembly mechanism for a Naphthalene-Dipeptide leading to hydrogelation, Langmuir, 2010, 26 (7), 5232-5242.
22. T. Yamamoto, T. Fukushima, Y. Yamamoto, A. Kosaka, W. Jin, N. Ishii, T. Aida, Stabilization of a kinetically favored nanostructure: surface romp of self-assembled conductive nanocoils from a norbornene-appended hexa-peri-hexabenzocoronene, J. Am. Chem. Soc., 2006, 128, 14337.
23. A. K. Das, R. F. Collins, R. V. Ulijn, Exploiting enzymatic (reversed) hydrolysis in directed self-assembly of peptide Nanostructures, Small, 2008, 4, 279.
24. Z. Yang, H. Gu, D. Fu, P. Gao, J. K. Lam, B. Xu, Enzymatic formation of supramolecular hydrogels, Adv. Mater. 2004, 16, No. 16, 1441-1444.
25. A. Barth, C. Zscherp, What vibrations tell us about proteins, 2002, Vol. 35, 369-430.
26. A. Aggeli, M. Bell, N. Boden, J. N. Keen, P. F. Knowles, T. C. B. Mcleish, M. Pitkeathly, S. E. Radford, Responsive gels formed by the spontaneous self-assembly of peptides into polymeric beta-sheet tapes, Nature 1997, Vol. 386, 259-262.
27. Z. Yang, H. Gu, D. Fu, P. Gao, J. K. Lam, B. Xu, Enzymatic formation of supramolecular hydrogels, Advanced Materials, 2004, 16, 1440-1444.

28. J. W. Sadownik, J. Leckie, R. V. Ulijn, Micelle to fibre biocatalytic supramolecular transformation of an aromatic peptide amphiphile, Chem. Commun., 2010, DOI: 10.1039/c0cc03796f.
29. W. S. Horne, N. Ashkenasy, M. R. Ghadiri, Modulating charge transfer through cyclic D,L-α-peptide self-assembly, Chem. Eur. J. 2005, 11, 1137-1144.
30. N. Ashkenasy, W. S. Horne, and M. R. Ghadiri, Design of self-assembling peptide nanotubes with delocalized electronic states, Small, 2006, 2, 99-102.
31. C.S. Wang, C.L. Sun, Investigation on the individual contributions of N-H…O-C and C-H…O=C interactions to the binding energies of beta-sheet modles, J. Comput Chem. 2010, 1036-1044.
32. Hunter C. A. The role of aromatic interactions in molecular recognition, Chemical Society Reviews, 1994, 101-109.
33. J. Naskar, G. Palui, A. Banerjee, Tetrapeptide-based hydrogels: for encapsulation and slow release of an anticancer drug at physiological pH, J. Phys. Chem. B, 2009, Vol. 113, 11787-11792.
34. K. J. Channon, G. L. Devlin, S. W. Magennis, C. E. Finlayson, A. K. Tickler, C. Silva, C. E. Macphee, Modification of fluorophore photophysics through peptide-driven self-assembly, J. Am. Chem. Soc., 2008, 130, 5487.
35. T. Claire, A. M. Smith, R. F. Collins, R. V. Ulijn, A. Saiani, Fmoc-Diphenylalanine self-assembly mechanism induces apparent pK(a) shifts, Langmuir, 2009, 25 (16), 9447-9453.
36. U. F. Rohrig, A. Laio, N. Tantalo, m. Parrinello, R. Petronzio, Stability and structure of oligomers of alzheimer peptide A beta(16-22): from the dimer to the 32-mer, Biophys. J., 2006, Vol. 91, 3217-3229.
37. J. T. S. Irvine, D. C. Sinclair, A. R. West, Electroceramics: characterization by impedance spectroscopy, Adv. Mater., 1990, 2, 132-138.
38. E. Barsoukov, J. R. Macdonald, Impedance spectroscopy theory, experiment, and application, Second Edition, Wiley-Interscience, 1. 1863-1865.
39. Y. Long, Z. Chen, N. Wang, Electrical conductivity of a single conducting polyaniline nanotubes, Applied Physics Lettters, 2003, Vol. 83, No. 9,
40. A. R. Hopkins, R. A. Lipeles, W. H. Kao, Electrically conducting polyaniline microtube blends, Thin Solid Films, 2004, 474-480.
41. T. Yamamoto, T. Fukushima, Y. Yamamoto, A. Kosaka, W. Jin, N. Ishii, T. Aida, Stabilization of a kinetically favored nanostructure: surface ROMP of self-assembled conductive nanocoils from a norbornene-appended hexa-peri-hexabenzpcoronene, J. AM. CHEM. SOC. 2006, 128, 14337-14340.
42. X. Wu, Y. Tao, L. Dong, J. Hong, Synthesis and characterization of self-assembling (NH4)0.5V2O5 nanowires, J. Mater. Chem., 2004, 14, 901-904.

43. J. R. Macdonald, Impedance spectroscopy, emphasizing solid materials and systems, 1987, Vol. 2.
44. F. yang, P. Xiao, Nondestructive evaluation of thermal barrier coatings using impedance spectroscopy, Int. J. Appl. Ceram. Technol., 2009, 6 [3] 381-399.
45. www.omega.ac.uk
46. R. D. Armstrong, A. T. A. Jenkins, B. W. Johnson, An investigation into the UV breakdown of thermoset polyester coatings using impedance spectroscopy, Corrosion Science, 1995, Vol. 37, 1615-1625.
47. R. Takahashi, H. Wang, J. P. Lewis, Electronic structures and conductivity in peptie nanotubes, J. Phys. Chem. B 2007, 111, 9093-9098.
48. I. Alfonso, M. Bru, M. I. Burguete, E. Garcia-Verdugo, S. V. Luis, Structural Diversity in the self-assembly of pseudopeptidic macrocycles, Chem. Eur. J. 2010, 16, 1246-1255.
49. P. Held, Peptide and amino acid quantification using UV fluorescence in synergy HT multi-mode microplate reader.
50. M. Horie, L. A. Majewski, M. J. Fearn, C. Yu, Y. Luo, A. Song, B. R. Saunders, M. L. Turner, Cyclopentadithiophene based polymers-a comparison of optical, electrochemical and organic field-effect transistor characteristics, J. Mater. Chem., 2010, DOI:10.1039/b924126d.

CHAPTER 5 ALIGNMENT OF SELF-ASSEMBLED PEPTIDE NANOTUBES

5.1 INTRODUCTION

The orientation of nanoscale objects is a key challenge for many applications in the field of supramolecular self-assembly.[1, 2] Most self-assembled materials are randomly oriented, which limits their properties and potential applications. Recently, organic π-electronic nanostructures based on aromatic peptide amphiphiles have emerged as suitable materials for thin film devices.[3] These nanostructures are made from small peptide building blocks that self-assemble through a combination of hydrogen bonding and π-stacking interactions. Much effort has been invested into developing fabrication techniques for growing more organized arrays of the peptide nanostructures based on self-assembly. Peptide nanotubes were grown into vertically well-aligned nanowires in aniline vapour at high temperature[4]. Peptide amphiphile nanofibres have also been self-assembled under a strong magnetic field to give aligned wires.[5, 6] Aligned patterns of self-assembled peptide amphiphile nanofibres were produced by sonication-assisted solution embossing.[7] Peptide-amphiphile self-assembled nanofibres were orientated and patterned by soft lithography[1], and liquid crystalline peptide nanowires were aligned in an electric field[8].

In this chapter, the alignment of the Fmoc-based peptides during electrospinning or assembly under a high electrical potential field is investigated with the aim of improving the conductivity of the resultant networks.

5.2 ELECTROSPINNING

5.2.1 Introduction of electrospinning

Electrospinning is a process designed to use electrostatic force to organize nano or micro scale fibres. In this technique, an electrically charged jet of polymer solution (or so-gel) is fed through a spinneret (hypodermic syringe needle) connected to a high voltage DC supply in the kV range, which draws the jet towards a grounded collection screen (Figure 5.1).[9] A constant rate of

extrusion is achieved by use of a syringe pump. Electrospinning requires a subtle balance between the solvent, the solution concentration, viscosity, surface tension, the voltage applied to the spinneret, and the flow rate. The requirements of electrospinning are as following: 1) electrospun materials require a suitable solvent; 2) the solvent's rate of evaporation must be high enough to precisely regulate the fibre diameter just before it hits the target; 3) the viscosity and surface tension of the solvent should be sufficient to form a jet large enough to prevent excessive draining from the spinneret; 4) the spinneret voltage and the pump rate must overcome the resistance associated with the jet's viscosity and surface tension to form the Taylor cone and jet.[1] Electrospun fibres tend to be deposited as a non-woven network, however alignment can be induced by depositing the fibres onto a rotating mandrel instead of the grounded collecting screen as shown in Figure 5.2.[10, 11]

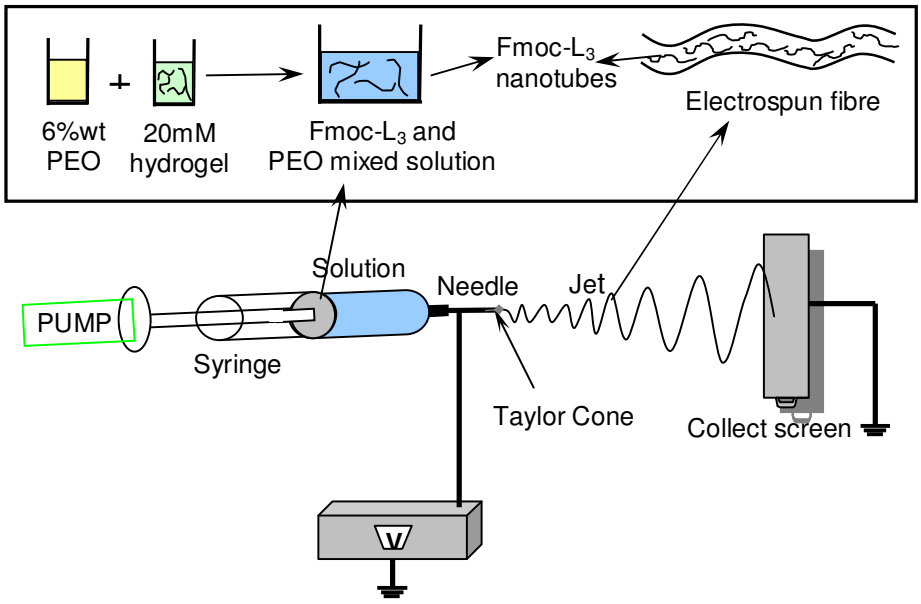

Figure 5.1 Schematic diagram of the electrospinning set up used to spin the Fmoc-L_3(enz) nanotubes.

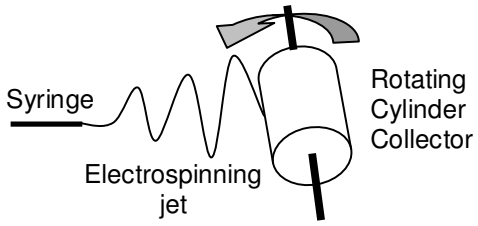

Figure 5.2 A rotating cylinder collector which aligns the fibres along the rotating direction

5.2.2 Electrospinning using Fmoc-L_3(enz) mixed with PEO

Electrospinning was attempted as a method to align the nanotubes produced from Fmoc-L_3 via enzymatic assembly (*(Fmoc-L_3 (enz)*) on a rotating cylinder collector. It was found that it was not possible to spin the Fmoc-L_3 (enz) hydrogel since its low viscosity and low surface tension meant that it could not sustain the requisite jet. PEO (polyethylene oxide) solution (6%wt) was therefore mixed with the Fmoc-L_3 (enz) hydrogel (20 mM) in a 4:1 volume ratio to improve the solution's characteristics.[12] The solution was mixed by vortex to obtain uniform viscous solution for electrospinning. Electrospun fibres were successfully obtained when using a PEO solution concentration up to 1.2%wt. (Electrospun fibres, though, could not be obtained when the concentration was lower than 1.2%wt). The other variables (i.e. distance between the spinneret and collector, DC voltage, pump feed rate and speed of rotating mandrel) also needed fine adjustment to balance with the various solution concentrations. In this experiment, distance, voltage, pump and mandrel speed were optimized at 10 cm, 10 kV, 0.3 ml/h and 1000 rpm respectively, after preliminary trials.

Electrospun fibres only formed when the volumetric ratio of PEO to Fmoc-L_3 was equal or higher than 1:4. Therefore, the author chose the volume ratio of PEO (6%wt) to hydrogel (20 mM) as 1:4 because this was the lowest concentration that could form fibres. Figure 5.3 shows optical micrographs of the fibres spun from the PEO solution and PEO solution mixed with Fmoc-L_3 hydrogel (Fmoc-L_3/PEO) electrospun fibres. The diameter and length of the Fmoc-L_3/PEO electrospun fibres are around 1 μm and 50-100 μm, respectively, which are not uniform due to low viscosity of the mixed solution. FT-IR spectra of the PEO, Fmoc-L_3 (enz) film and Fmoc-L_3

(enz)/PEO film showed that the self assembled structure of the Fmoc-L_3 (enz) was, at least in part, retained after spinning, as highlighted by the 1637 cm^{-1}, 1691 cm^{-1} anti-parallel β-sheet bands (Figure 5.4).

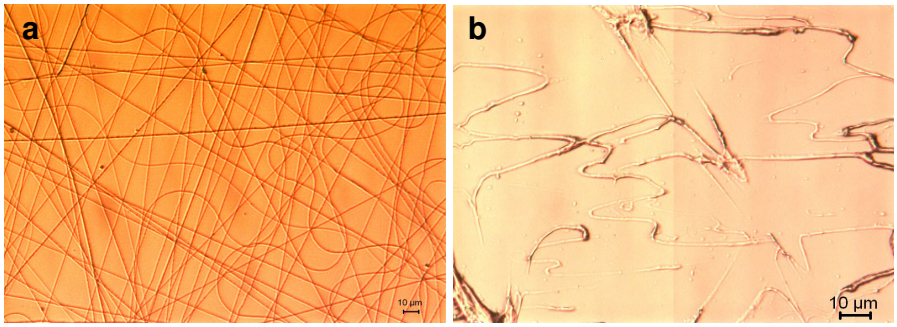

Figure 5.3 Optical microscopy images of electrospun fibres. a. Fibres spun from PEO (6% wt); b. Fibres spun from Fmoc-L_3 gel (enz) (20 mM) mixed with PEO (6% wt) (volume ratio: 4:1).

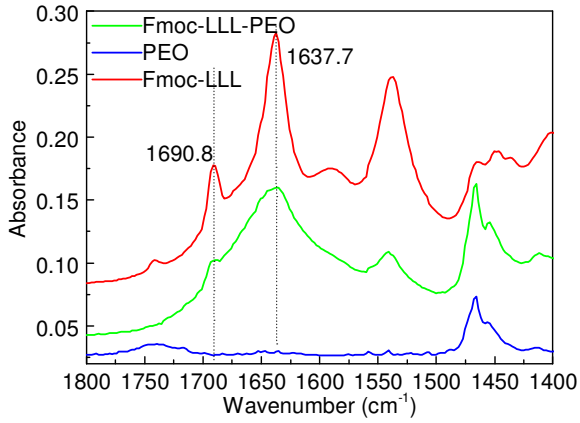

Figure 5.4 FT-IR spectra of Fmoc-L_3 xerogel, Fmoc-L_3 mixed with PEO (6%wt) (volume ratio: 4:1) electrospun fibres, PEO electrospun fibres. Fmoc-L_3 film and Fmoc-L_3 mixed with PEO showing a broad peak at around 1635–1646 cm-1 and a medium intensity band at 1685–1691 cm^{-1} (amide I band), consistent with the antiparallel β–sheet structure.

The optical microscopy images of aligned PEO and Fmoc-L_3-PEO electrospun fibres are shown in Figure 5.5. A number of beads appeared on the Fmoc-L_3-PEO electrospun fibres and discontinuous electrospun fibres as shown in Figure 5.5b due to low viscosity. The tendency for bead formation may be affected by the various parameters used such as the voltage applied, the feed rate and/or distance. A large number of experiments were carried out by changing the various parameters to obtain good fibres. The voltage was varied from 5 kV to 20 kV and the

distance between the needle and collector was varied from 5 cm to 15 cm. The optimum conditions found were a voltage of 8 kV and a distance of 11.5 cm. However, even under these conditions, beads were still produced (Figure 5.6), indicating that the most significant parameter is the solution viscosity and its relative surface tension.[1] With low viscosities used, the spinning dope tend to form droplets, adopting a spherical shape due to the over-riding surface tension effect. Therefore, it was concluded that the Fmoc-L_3 (enz) hydrogel was not suitable for electrospinning on account of its low viscosity and relatively high surface tension.

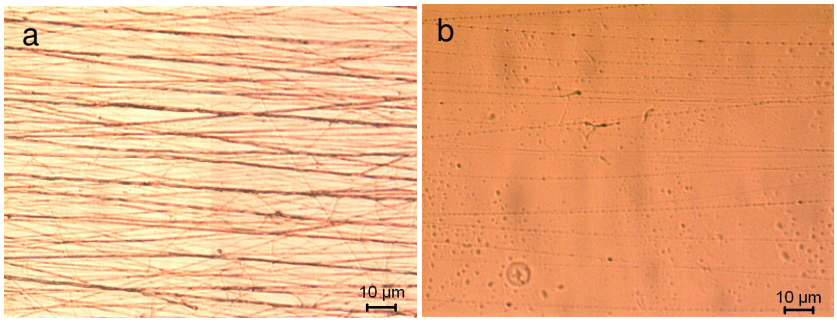

Figure 5.5 Optical images of aligned fibres of PEO (a) and Fmoc-L_3 blended with PEO (1.2% wt) by electrospinning (b)

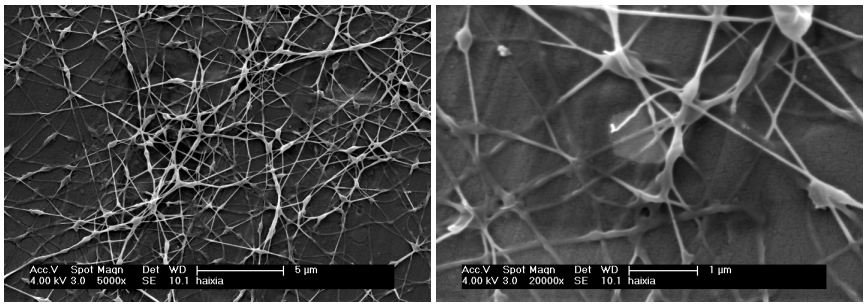

Figure 5.6 SEM images of Fmoc-L_3 mixed with PEO electrospinning fibres

5.3 ALIGNMENT OF FMOC-L_3 NANOTUBES ASSEMBLED UNDER A HIGH ELECTRIC FIELD

5.3.1 Experiments

In view of the fact that alignment of the Fmoc-L_3 (enz) nanotubes could not be achieved by electrospinning, the idea of using an electrostatic technique was tried in order to orientate the Fmoc-L_3 (enz) nanotubes from hydrogel. This is because strong electrostatic field gradients can produce forces which overcome the surface tension in the hydrogel and align the nanotubes.[13] A diagram of the experimental set-up used is shown in Figure 5.7. In these experiments, the insulator was a piece of glass slide with a 4 cm gap separating the two metal plates. The hydrogel was deposited onto the insulator substrate under a high electric field until dry. Varying electric field strengths were applied in the experiments, e.g. 0.25 kV/cm, 1.25 kV/cm, 2.5 kV/cm and 3.75 kV/cm.

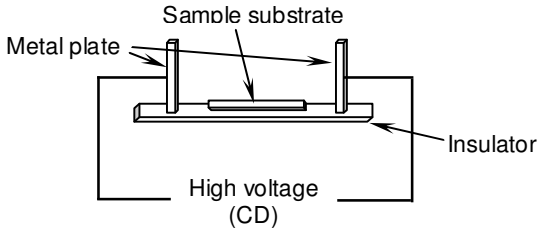

Figure 5.7 Diagram of the high electronic field setup used to induce for alignment.

5.3.2 Fmoc-L_3 (pH) aligned at various electric field strengths

The Fmoc-L_3 (pH) hydrogel (20 mM) was used for the preliminary experiments for the electrostatic technique. The Fmoc-L_3 (pH) hydrogel was vortexed for 3 minutes, dropped onto a glass slide substrate and then immediately placed within the electric field. Atomic Force Microscopy (AFM) on the resultant, thin Fmoc-L_3 (pH) films found dense networks of nanotubes (Figure 5.8). The AFM micrograph also shows that a highly aligned morphology was produced (Figure 5.8 a), under an electric field strength of 0.75 kV/cm. However, under a lower field strengths, the networks consisted of randomly distributed nanotubes (0.5 kV/cm) (Figure 5.8b, c).

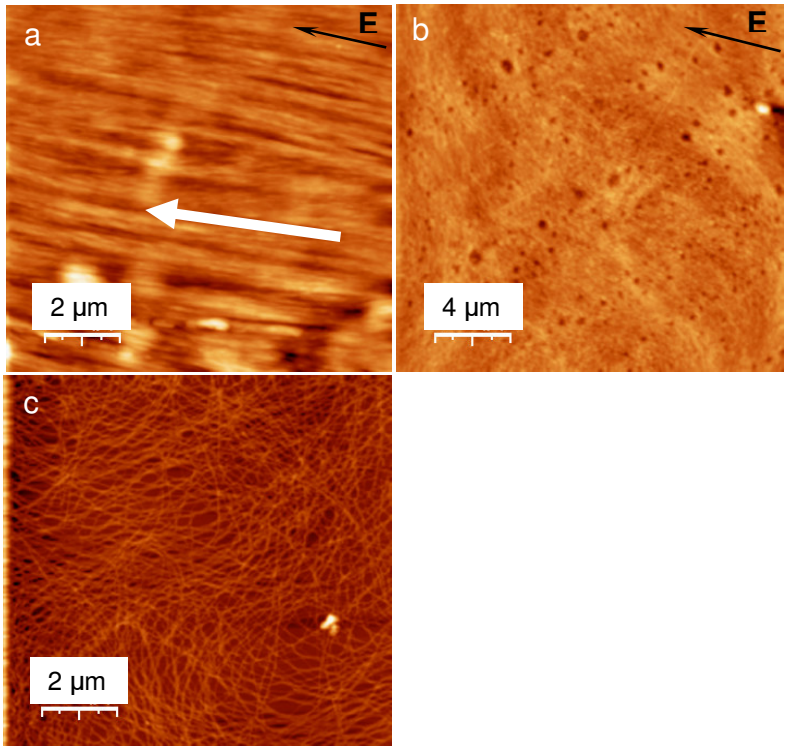

Figure 5.8 AFM images of Fmoc-L_3 (pH). a. alignment nanotubes aligned in 0.75 kV/cm electric field, b. random nanotubes aligned in 0.5 kV/cm electric field, c. random networks formed without electric field.

5.3.3 Alignment of Fmoc-L_3 (enz) nanotubes under various electric field strengths

Given the promising preliminary data discussed above, more detailed experiments were conducted on the alignment of the nanostructures assembled under an electric field. For these experiments, Fmoc-L_3 (enz) nanotubes was used, rather than Fmoc-L_3 (pH), as the former is more conductive (see Chapter 4). 20 mM/L Fmoc-L_3 (enz) hydrogel was vortexed and then spread onto thin glass slide and dried under a 3.75 kV/cm electric field. The level of ordering of the nanostructures under 3.75 kV/cm electric field was clearly observable using Scanning Electron Microscopy (SEM) (Figure 5.9a, b and c). This alignment contrasts against Figure 5.9d, where, without the electric field, the nanotubes are cross-connected and have formed random networks in the film. Herman's orientation function (f) is simply a mathematical construct to

describe the degree or extent of orientation of the chain axis relative to some other axis as shown in Figure 5.10. The formula is:

$$f = (3\cos 2\Phi - 1)/2 \tag{5.1}$$

where Φ is the angle between the chain axis and other axis. The value of f determines the degree of alignment: completely aligned f=1, randomly oriented f=0 and perpendicular f=-0.5. The angle between electric field direction and nanotubes was obtained by ImageJ from SEM image (Figure 5.9 b). The distribution of angle with an average value of 3.7 ° is shown in Figure 5.11. f was calculated from each angle by using the formula (5.1). The average value of f is around 0.9. The arrows show the electric field direction. Furthermore, several micro-tubes with diameter around 1-5 μm were observed (Figure 5.9 a), which may be formed by nanotubes.

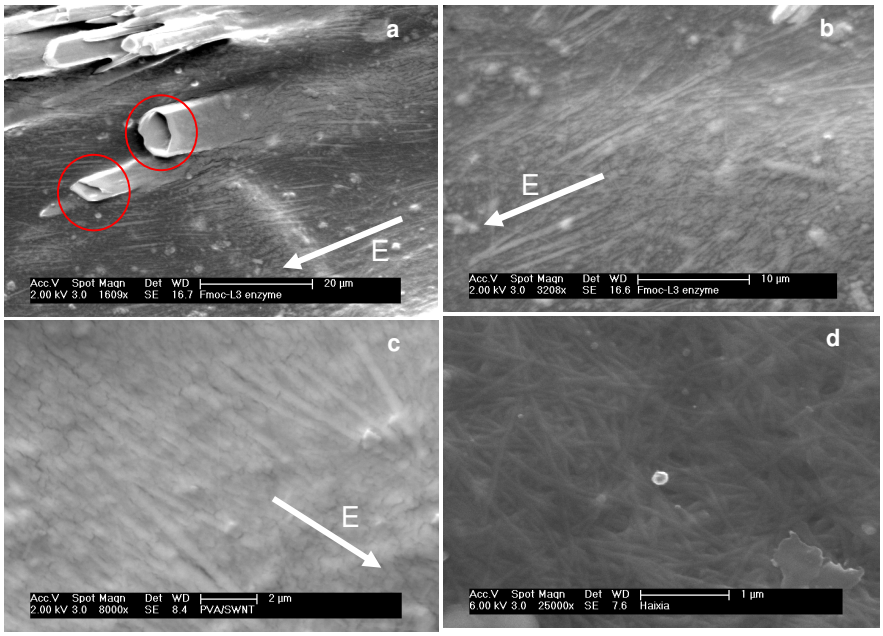

Figure 5.9 SEM images of Fmoc-L_3 (enz): a, b, c: aligned under a 3.75 kV/cm electric field, d: random (no field).

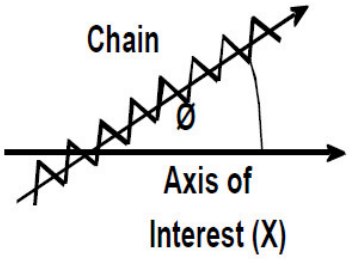

Figure 5.10 Diagram of angle to calculate Herman's orientation function (f).

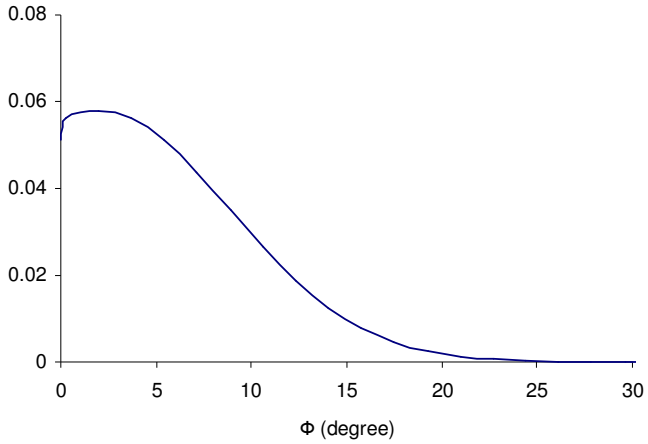

Figure 5.11 Distribution of angle Φ between electric field direction and nanotubes aligned in 3.75 kV/cm electric field.

Impedance spectroscopy was carried out to measure the conductivity of the film, which was prepared by spreading 100 µL Fmoc-L_3 (enz) hydrogel onto a glass slide after vortex, then dried to form a film under a 3.75 kV/cm electric field. Three areas were measured on the same sample. Figure 5.12 shows the impedance plot data which indicated that the resistances are similar in air (Figure 5.12a) and the same in vacuum condition, due to the highly uniformity under the effect of the electric field. The similar measurements of random networks are shown in Chapter 4. The impedance spectra plot data of 100 µL Fmoc-L_3 (enz) hydrogel aligned at various electric fields is shown in Figure 5.13. It is interesting to note that the resistance of random networks is higher than the aligned film at 0.25 kV/cm, 1.25 kV/cm, 2.5 kV/cm and 3.75 kV/cm in Figure 5.13b in vacuum because it is more difficult for the electron to jump between the nanotubes, than along

the nanotubes. The resistance of aligned nanotubes is higher than random nanotubes in air due to ion conduction (Figure 5.13a).

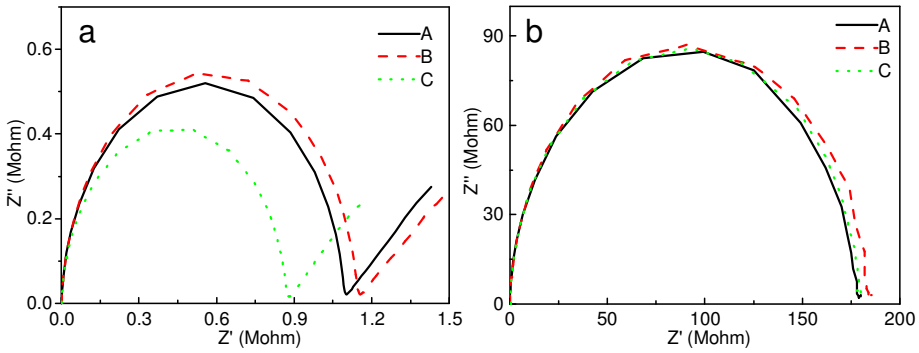

Figure 5.12 Impedance spectra of three areas on the same Fmoc-L_3 (enz) film aligned at 3.75 KV/cm electronic field. a, in air, b, in vacuum.

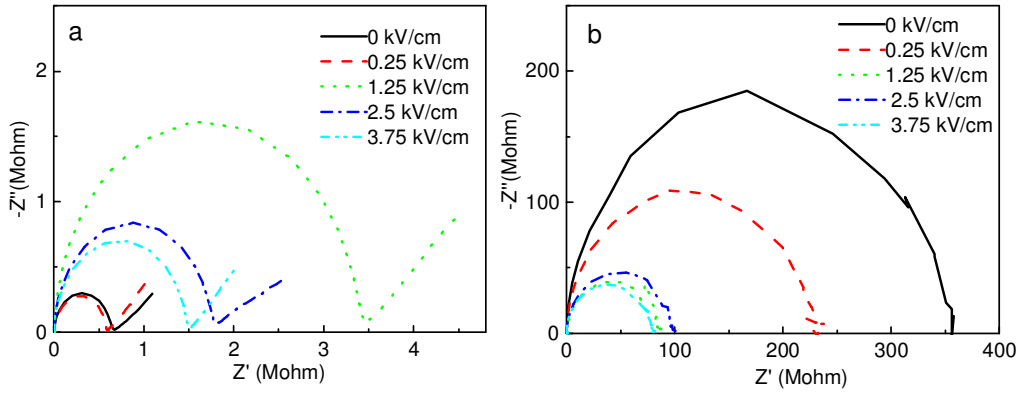

Figure 5.13 Impedance spectra of Fmoc-L_3 (enz) film formed at various electronic field. (0 kV/cm, 0.25 kV/cm, 1.25 kV/cm, 2.5 kV/cm, 3.75 kV/cm) from 100 µL hydrogel : a, in air, b, in vacuum. The impedance was measured parallel to the field direction.

A series of experiments were conducted at varied electric fields. SEM images of Fmoc-L_3 nanotubes aligned at varied electric fields are shown in Figure 5.14. SEM images were chosen from optimal areas because these represent what could be achieved globally, giving further optimum of process (i.e. drying, temperature, humidity). The degree of alignment in the nanotube networks under various electric fields was calculated from the SEM images (Figure 5.14) shown in Figure 5.15. This analysis indicated that the degree of alignment increased with the electric

field strength. The conductivity of films was also found to increase with increasing field strength (Figure 5.16) and correlated to the degree of alignment within the nanotubes networks. The resistance of the aligned networks on the perpendicular direction was found to be higher than in the aligned direction, confirming the anisotropy of the films. Furthermore, the resistance values were scattered for the 0.25 kV/cm, 1.25 kV/cm and 2.5 kV/cm samples due to the alignment being non-uniform and localised. The resistance values of nanotubes aligned at the highest potential (3.75 kV/cm), though, were found to be repeatable. This result suggests that a high field strength is required to get global alignment. The film formed at the highest electric field (3.75 kV/cm) had the highest conductivity properties and its conductance was 3 times higher than that of the random networks.

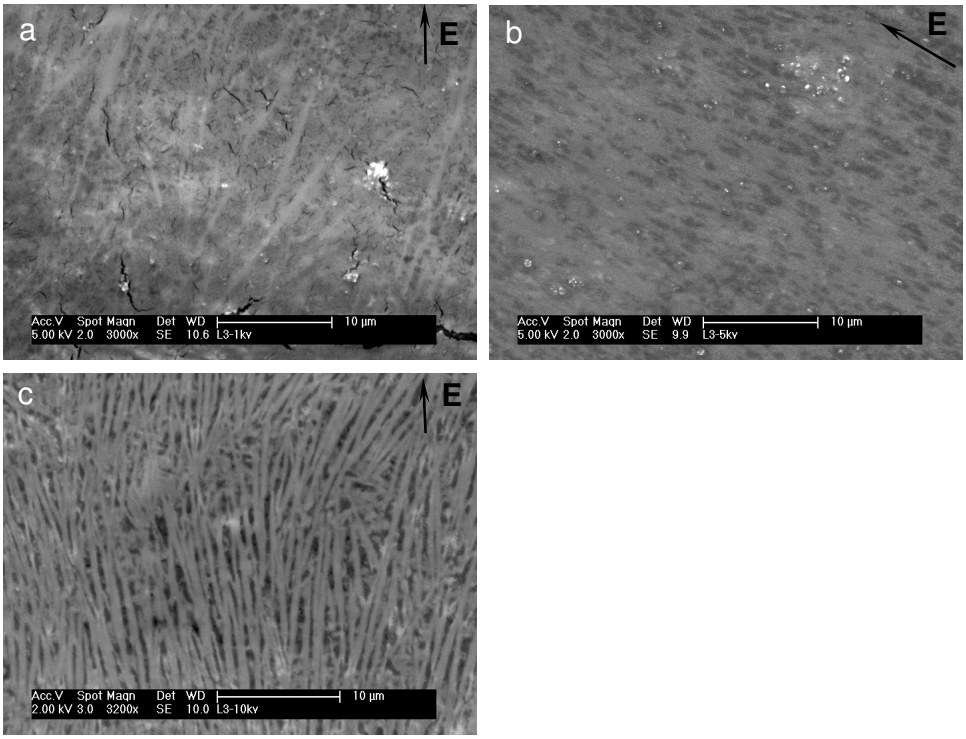

Figure 5.14 SEM images of Fmoc-L_3 aligned at varied electric field: a, 0.25 kV/cm, b, 1.25 kV/cm, c, 2.5 kV/cm

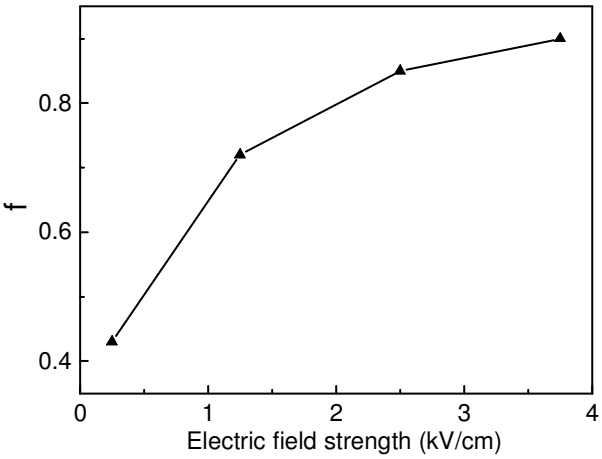

Figure 5.15 Alignment degree f of the networks versus applied electric field strength

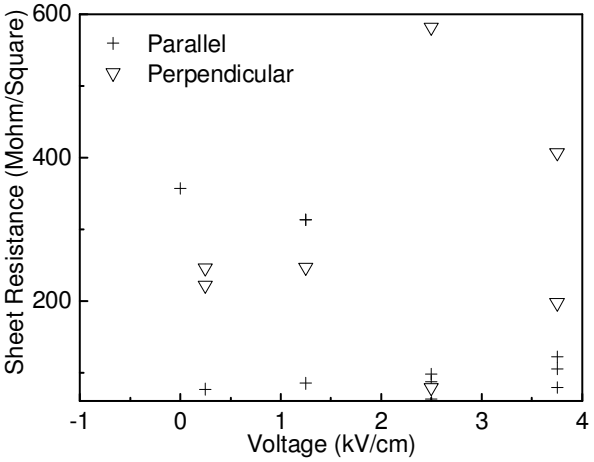

Figure 5.16 Resistances of the Fmoc-L_3 films parallel and perpendicular to the applied electric field . (0 kV/cm, 0.25 kv/cm, 1.25 kV/cm, 2.5 kV/cm and 3.75 kV/cm). Measurements were conducted under vacuum.

5.4 CONCLUSIONS

Electrospinning was studied as a method to align Fmoc-L_3 (enz) nanotubes. Pure hydrogel samples could not be spun due to their low viscosity. Therefore, PEO (1.2%wt) was blended with Fmoc-L_3 (enz) hydrogel (Fmoc-L_3-PEO). Aligned electrospun Fmoc-L_3-PEO fibres were obtained under a certain condition (the distance between spinneret and collector, the voltage, the pump speed and the rotation rate were fixed on 10 cm, 10 kV, 0.3 ml/h and 1000 rpm, respectively). However, the inclusion of the hydrogel was found to disrupt the PEO fibre formation, hence these

aligned composite fibres were short and had poorly defined structure. It was concluded that electrospinning was not a suitable method for the production of Fmoc-L_3 (enz) aligned fibres.

The gels were also dried under an electric field in order to try to align the nanotubes. Preliminary experiments found that Fmoc-L_3 pH nanotubes were aligned in 0.75 kV/cm electric field, but could not be aligned in weaker fields. More detailed studies were then conducted on the Fmoc-L_3 (enz) hydrogels. The alignment of Fmoc-L_3 (enz) nanotubes, formed by drying vortex Fmoc-L_3 (enz) hydrogel under varied electric fields (0.25 kV/cm, 1.25 kV/cm, 2.5 kV/cm, 3.75 kV/cm), was confirmed by SEM images. The degree of alignment, f, increased with the electric field strength. The conductivity of aligned Fmoc-L_3 (enz) nanotubes was measured by impedance spectroscopy. The experiments indicated that Fmoc-L_3 (enz) nanotubes aligned at 3.75 kV/cm electric field have the lowest resistance. The resistance of the aligned film was examined along both the perpendicular and parallel directions to the alignment. The resistance in the perpendicular direction was higher than that in the alignment direction. The conductivity of aligned Fmoc-L_3 (enz) film at the alignment direction increased by a factor of ~ 3 compared to the random networks.

5.5 REFERENCES

1. M. Reches and E. Gazit, Controlled patterning of aligned self-assembled peptide nanotubes, Nature Nanotechnology, 2006, 1, 195-200.
2. A. M. Hung and S. I. Stupp, Simultaneous self-assembly, orientation, and patterning of peptide-amphiphile nanofibres by soft lithography, 2007, Vol. 7, No. 5, 1165-1171.
3. H. Shao, T. Nguyen, N. C. Romano, D. A. Modarelli and J. R. Parquette, Self-assembly of 1-D n-type nanostructures based on naphthalene diimide-appended dipeptides, J. AM. CHEM. SOC., 2009, 131, 16374-16376.
4. J. Ryu and C. B. Park, High-temperature self-assembly of peptides into vertically well-aligned nanowires by aniline vapor, Adv. Mater. 2008, 20, 3754-3758.
5. D. W. P. M. Lowik, I. O. Shklyarevskiy, L. Ruizendaal, P. C. M. Christianen, J. C. Maan and J. C. M. van Hest, A highly ordered material from magnetically aligned peptide amphiphile nanofibre assemblies, Adv. Mater., 2007, 19, 1191-1195.
6. R. J. A. Hill, V. L. Sedman, S. Allen, P. M. Williams, M. Paoli, L. Adler-Abramovich, E. Gazit, L. Eaves and S. J. B. Tendler, Alignment of aromatic peptide tubes in strong magnetic fields, Adv. Mater., 2007, 19, 4474-4479.

7. A. M. Hung and S. I. Stupp, Understanding foctors affecting alignment of self-assembling nanofibres patterned by sonication-assisted solution embossing, Langmuir, 2009, 25(12), 7084-7089.
8. T. H. Han, J. Kim, J. S. Park, C. B. Park, H. Ihee and S. O. Kim, Liquid crystalline peptide nanowires, Adv. Mater., 2007, 19, 3924-3927.
9. S. Ramakrishna, K. Fujihara, W. Teo, T. Lim, Z. Ma, Electrospinning and nanofibres, 15-18.
10. D. Li, Y. Wang, Y. Xia, Electrospinning of polymeric and ceramic nanofibres as uniaxially aligned arrays, Nano Lett, 2003, 3, 1167-1171.
11. D. Li, Y. Wang, Y. Xia, Electrospinning nanofibres as uniaxially aligned arrays and layer-by-layer stacked films, Adv. Matter, 2004, 16, 361-366.
12. A. Aluigi, C. Vineis, A. Varesano, G. Mazzuchetti, F. Ferrero, C. Tonin, Structure and properties of keratin/PEO blend nanofibres, European Polymer Journal, 2008, 44, 2465-2475.
13. E. Schaffer, T. Thurn-Albrecht, T. P. Russell, U. Steiner, Electrically induced structure formation and pattern transfer, Nature, 2000, 403, 874-877.

CHAPTER 6 CONCLUSIONS AND FUTURE WORK

6.1 SUMMARY

Fmoc-LL, Fmoc-L_3, Fmoc-YL, Fmoc-WL hydrogels were produced via self-assembly by hydrolysis of corresponding methyl esters. They were characterized using Fourier transform infrared spectroscopy (FT-IR) and fluorescence spectroscopy. It was shown that the nanostructures were formed by anti-parallel β-sheet and π–π stacking of fluorene. Transmission Electron Microscopy (TEM), Cryogenic Temperature Transmission Electron Microscopy (Cryo-TEM) and Atomic Force Microscopy (AFM) were also used to characterize the morphology of the nanostructures. The gels were found to consist of nanofibres with diameters of 5 nm, 8 nm and 10 nm for Fmoc-LL, Fmoc-YL and Fmoc-WL respectively.

Current-Voltage (I-V) curves and impedance spectra found that the conductivities of the peptide films (Fmoc-LL, Fmoc-WL and Fmoc-YL) were ~ 10^{-2} S/m in air and ~ 10^{-5} S/m in vacuum. Based upon impedance spectroscopy measurements, it was proposed that these films were electronically conducting in vacuum because no mass transfer conductive was observed under these conditions. The resistance of the films was decrease upon heating, which suggested that they had a semiconductor like behaviour. The band gap (E_g) and activation energy (E_{act}) were obtained using UV-Vis spectroscopy and I-V. The band gap was around 4.0 eV and the activation energy is about 0.5-0.6 eV, providing further evidence that the Fmoc-LL, Fmoc-L_3, Fmoc-WL and Fmoc-YL films were semiconductors. The electrochemical band gap as measured by using cyclic voltammetry (CV), which lower than the optical band gap.

Fmoc-L_3 π–β nanotubular networks formed by the self-assembly of aromatic peptide amphiphiles were studied in detail because of their relatively significant charge transport. Wide angle X-ray scattering (WAXS) was used to examine the nanostructures in detail. The reflections of the β-sheets and π-stacking were 4.6 nm and 3.8 nm respectively. Fmoc-L_3 was confirmed to be nanotubes by TEM and Cryo-TEM. The outer and inner diameter of Fmoc-L_3 nanotube is around 18 nm and 9 nm, respectively. The minimum sheet resistances of bulk peptides were 0.1 MΩ/sq

in the air and 500 MΩ/sq in the vacuum at room temperature. Electrochemical Impedance models were simulated for the dried film and hydrogel. In the vacuum, the impedance of the dried Fmoc-L_3 film was found to follow a resistor-capacitor equivalent circuit due to the resistance of peptide networks and the capacitance of the parallel conductive paths. In the air, the simulation suggested that the impedance of the dried Fmoc-L_3 film followed an equivalent resistor-capacitor and Warburg circuit due to the mass transfer between sample and electrode within wet environment. Aqueous solution of Fmoc-L_3 hydrogel was found to follow a model where the impedance spectrum consisted of two aligned semi-circles and a slope: the first semi-circle representing the contribution of peptide nanotubes networks, and the second semi-circle representing the aqueous phase and interfacial capacitance between electrode and electrolyte. Finally, the conductivity of peptide film was found to rely on relative humidity (RH), indicating conductivity increase with RH.

Electrospinning was studied as a method to align Fmoc-L_3 (enz) nanotubes. Pure hydrogel samples could not be spun due to their low viscosity. Therefore, PEO (1.2%wt) was blended with Fmoc-L_3 (enz) hydrogel (Fmoc-L_3-PEO). Aligned electrospun Fmoc-L_3-PEO fibres were obtained under a certain condition (the distance between spinneret and collector, the voltage, the pump speed and the rotation rate were fixed on 10 cm, 10 kV, 0.3 ml/h and 1000rpm, respectively). However, these aligned composite fibres were short and had poorly defined structures. It was concluded that electrospinning was not a suitable method for the production of aligned fibres.

An alternative method was used to align the peptide nanotubes. The gels were also dried under an electric field in order to try to align the nanotubes. Preliminary experiments found that Fmoc-L_3 pH nanotubes were aligned in 0.75 kV/cm electric field, but could not be aligned in weaker fields. More detailed studies were then conducted on the Fmoc-L_3 (enz) hydrogels. The alignment of Fmoc-L_3 (enz) nanotubes, formed by drying vortex Fmoc-L_3 (enz) hydrogel under varied electric fields (0.25 kV/cm, 1.25 kV/cm, 2.5 kV/cm, 3.75 kV/cm), was confirmed by SEM images. The degree of alignment, f, increased with the electric field strength. The conductivity of aligned Fmoc-L_3 (enz) nanotubes was measured by impedance spectroscopy. The experiments indicated

that Fmoc-L_3 (enz) nanotubes aligned at 3.75 kV/cm electric field have the lowest resistance. The resistance of the aligned film was examined along both the perpendicular and parallel directions to the alignment. The resistance in the perpendicular direction was higher than that in the alignment direction. The conductivity of aligned Fmoc-L_3 (enz) film at the alignment direction increased by a factor of ~ 3 compared to the random networks.

6.2 FUTURE WORK

Although the conductivity of Fmoc-L_3 nanotubes networks was increased up to ~3 times after alignment, the nanotubes networks could obtain higher conductivity if the aligned nanotubes could be achieved globally. Different conditions could be applied during the alignment process, such as temperature and humidity. All the nanotubes could be aligned with a high degree before the film dried at an appropriate environment. The aligned nanotubes could be manufactured into devices, such as transistor or photovoltaic cell, to test the materials.

Promising potential could be explored by research on Fmoc-WL due to the inhomogeneous nanostructures (nanospheres and nanofibres). The nanostructures may be changed by different conditions such as concentration, temperature and enzyme. The conductivity of nanospheres and nanofibres may be separated by impedance spectra. Revealling complicated impedance of peptide hydrogels could develop future valuable applications.

Preliminary studies show in the appendix found that the conductivity of the Fmoc-SF-OMe film was very low due to the amorphous structure on its surface. Therefore, the removal of the amorphous structure is an important task for the future. The single layer crystalline nanosheets have potential applications, such as biosensors, smart biomaterials and biologically inspired photovoltaic devices. Scanning probe microscopy techniques may be a method to study this type of nanosheets.

Several methods could be used to improve the conductivity of the peptide nanostructures, such as:

1. Replacing Fmoc by electroactive components, such as naphthalenediimide (NDI);

2. Adding electroactive components on peptide systems, such as thiophene;

3. Doping peptide nanostructure system, providing additional charge carriers to the material.

APPENDICES

A1 PEAKS OF WAXS DATA FROM BUFFER

Table A.1 Peaks and their relative intensities from WAXS data of buffers

Peaks (degree)	Relative Intensities		
	Phosphate	MOPS	HEPES
29.6	0	6130	0
28.6	0	0	3513
28	0	0	3348
27.6	0	3514	0
26.5	0	0	0
26	1101	7084	0
25.5	0	5673	0
25.1	0	0	5882
24.7	0	3013	0
23.9	00	338	0
23.6	0	0	4511
23.2	1559	0	0
22.9	0	0	4428
22.4	3844	0	0
22.2	0	3305	0
21.8	0	0	6797
20.7	0	0	9788
20.3	0	109091	0
19.7	0	0	5717
18.9	0	8621	0
18.4	0	0	3183
18.1	1062	0	0
17.7	0	2059	0
17.3	0	2016	0
17	0	0	5089
15.2	0	28541	1393
12.9	0	0	1729
10.3	0	9331	0
9.3	0	853	0
8.5	0	0	1311
5.2	0	0	6505
4.9	0	7793	0
3.9	0	1393	0
2.2	0	3266	0

d: Fmoc-TL-OMe

Time	Peak positions: Wavelength (nm)			
0	318	377		
12 h	326	377	399	452
40 h	326	378	399	454
60 h	326	378	399	454
1 week	326	378	399	454

A2 ELECTRONIC AND STRUCTURAL PROPERTIES OF NANOSTRUCTURES PRODUCED BY THERMOLYSIN ASSISTED SELF-ASSEMBLY

A2.1 INTRODUCTION

Conductive peptide nanostructure networks formed from Fmoc-peptide self-assembly by enzymatic hydrolysis of methyl esters was introduced in Chapter 4. This system operates under kinetic control and may suffer from kinetically trapped defects which could hamper the formation of extensive π-stacked conducting tracks. As an alternative method, Ulijn's group have introduced enzyme-assisted self-assembly under thermodynamic control. In this system, enzymes convert non-assembling precursors into self-assembling components by amide bond formations (i.e. reversed hydrolysis).[2] For example, the Ulijn group have demonstrated the production of a range of Fmoc-dipeptide esters (denoted Fmoc-XY-OMe), some of which showed significant electron delocalization as inferred from photoluminescence measurements.[3] Therefore, in this section, preliminary experiments were conducted on the Fmoc-SF-OMe, Fmoc-SL-OMe, Fmoc-TF-OMe and Fmoc-TL-OMe systems as these showed the most promising potential as conductive peptide systems from the initial photoluminescence measurements. The morphology of the nanostructures produced from the peptides was found to vary significantly and differ from those found in other Fmoc-dipeptide systems. In particular, 2-D laminar structures were observed for the first time in an Fmoc terminated system. Initial electrical measurements revealed that these systems were insulating. Unfortunately, due to time constraints, only an incomplete understanding could be obtained about the novel microstructures of these peptide nanostructures and their electronic structure. It is expected that this appendix will encourage future work into this interesting system.

A2.2 Background to the self-assembly process

In the condensation system, the combination of the building blocks is reversible, allowing the exchange of blocks towards thermodynamic equilibrium, i.e. the systems should be self correct

for defects. (This was described in detail in Section 2.3.2) The condensation system is therefore fundamentally different from the hydrolysis system used in Chapter 4 which is essentially irreversible. An additional advantage of the system studied here is that the preparation of the hydrogel from condensation does not require heating and thus can form a hydrogel or suspension directly. Herein, the structural and electronic properties of nanostructures produced by thermolysin assisted self-assembly of Fmoc-peptide-esters formed via reversed hydrolysis is studied. Four different systems were studied; Fmoc-SF-OMe, Fmoc-SL-OMe, Fmoc-TF-OMe and Fmoc-TL-OMe. The Fmoc-peptide-esters were created by a catalyzing enzyme and then self-assembled to form anti-parallel β–sheets with the fluorenyl groups presented at alternate sides. Multiple anti-parallel β–sheets were then interlocked through π–π stacking (Figure A.1).

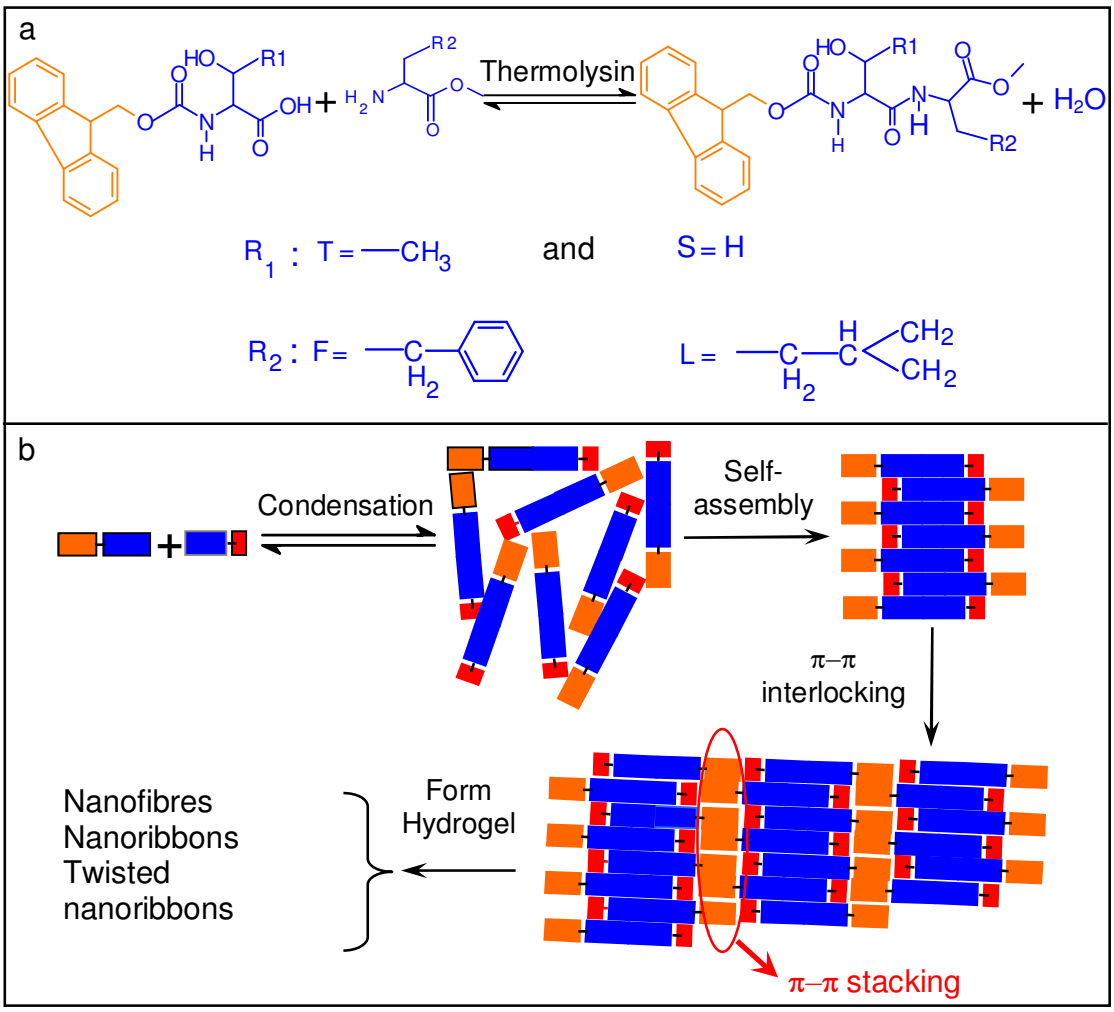

Figure A.1 (a) Reversible amide synthesis/hydrolysis catalysed by thermolysin and building blocks used for enzyme-driven peptide libraries (Fmoc-T-OH, Fmoc-S-OH, F-OMe and L-OMe). (b) Sequential scheme for reverse hydrolysis and self-assembly process to form nanostructures showing anti-parallel β–-sheet and π–π stacking.

A2.3 NANOSTRUCTURES FROM FOUR DIFFERENT FMOC-PEPTIDE ESTERS

A2.3.1 Characterization of the nanostructures

Four different amino acid derivatives were used as the building blocks for the gelator: Fmoc-T, Fmoc-S as C-terminal components and F-OMe and L-OMe as the N-terminal amino acids. Ideally, as in Chapter 4, the evolution of these systems would have been studied using HPLC. In particular, knowing the reaction rate for the formation of the gelator under different reaction

conditions (e.g. time, temperature, peptide structure and enzyme concentration) is essential to fully understand the formation mechanism of the nanostructures produced.

Given the time restraints for this part of the project, it was decided to just focus on establishing how the morphology of the nanostructures varied with the gelator and temperature at a given reaction time. Consequently, the different nanostructures obtained after 96 hours of exposure to thermolysin were analysed using Cryo-TEM (Figure A.2). A wide range of nanostructures (Table A.1) were observed including nanofibres, twisted nanoribbons and nanosheets as analysed by Cryo-Transmission Electron microscopy (cryo-TEM) (Figure A.2) and Atomic Force Microscopy (AFM) (Figure A.3).

The Fmoc-SF-OMe sample was non-homogeneous. Cryo-TEM found both twisted nanoribbons with widths around 35 nm and 2D nanosheets with widths over 200 nm (Figure A.2a). These structures were retained upon drying. For example, AFM observed a nanosheet with a height ~ 160 nm in a dried suspension of Fmoc-SF-OMe (Figure A.3a, e). The inhomogeneity of the sample was an issue and hence temperature-controlled experiments were conducted to produce more uniform structures, as discussed later.

Figure A.2b shows that Fmoc-SL-OMe assembled into straight nanoribbons with widths ~ 60 nm and heights ~ 15 nm. (The height was deduced from AFM imaging, which revealed a flat line cross-section, instead of the sharp peak as shown in Figure A3b and f. The width therefore was deduced from low magnification images in cryo-TEM, as shown in Figure A2d. It should be noted that using images at this resolution can create a reasonable error as one pixel width is 0.8 nm)

Fmoc-TF-OMe hydrogel film comprised of tightly twisted nanoribbons with widths of ~ 25 nm (Figures A.2c and A.3c) and heights of ~ 20 nm (Figure A.3g).

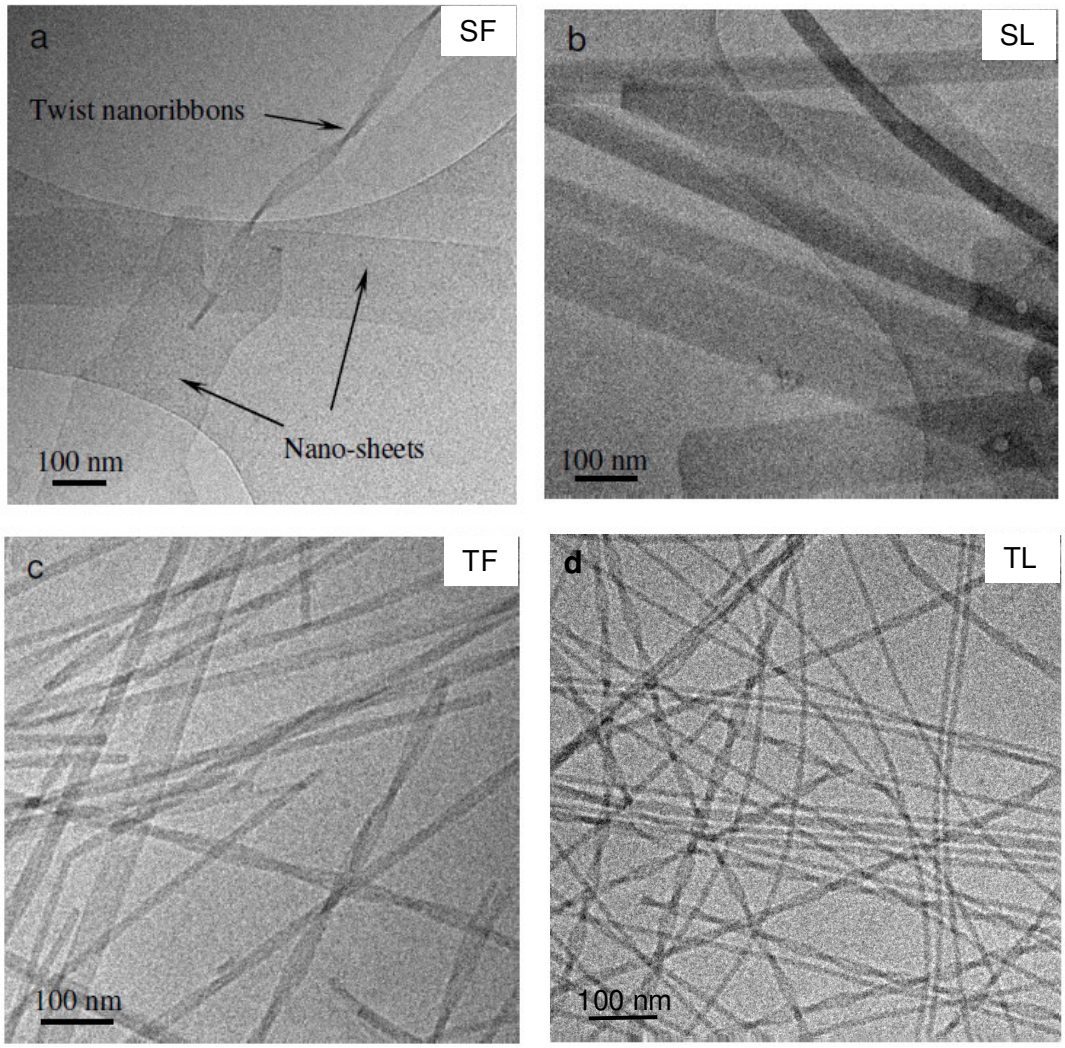

Figure A.2 Cryo-TEM images of the hydrogel. (a) Fmoc-SF-OMe gel showing nanoribbons and twist nanoribbons with diameters of around 35 nm, (b) Fmoc-SL-OMe gel showing nanofibres with diameters of ~60 nm, (c) Fmoc-TF-OMe gel showing naoribbons and twist nanoribbons with widths of ~25 nm, (d) Fmoc-TL-OMe gel showing twisted nanoribbons with widthes of ~ 10 nm.

Cryo-TEM found that the Fmoc-TL-OMe hydrogel was a network of uniform, twisted nanoribbons with a width of ~10 nm (Figure A.2d). AFM also observed these helical nanoribbons, as highlighted in Figure A.3d. The cross section from a single nanoribbon in Figure A.4b was ~ 4 nm, as found by the cross-section between the two red arrows. The pitch of the twist was ~ 16 nm, as obtained from the cross section line in Figure A.3h.

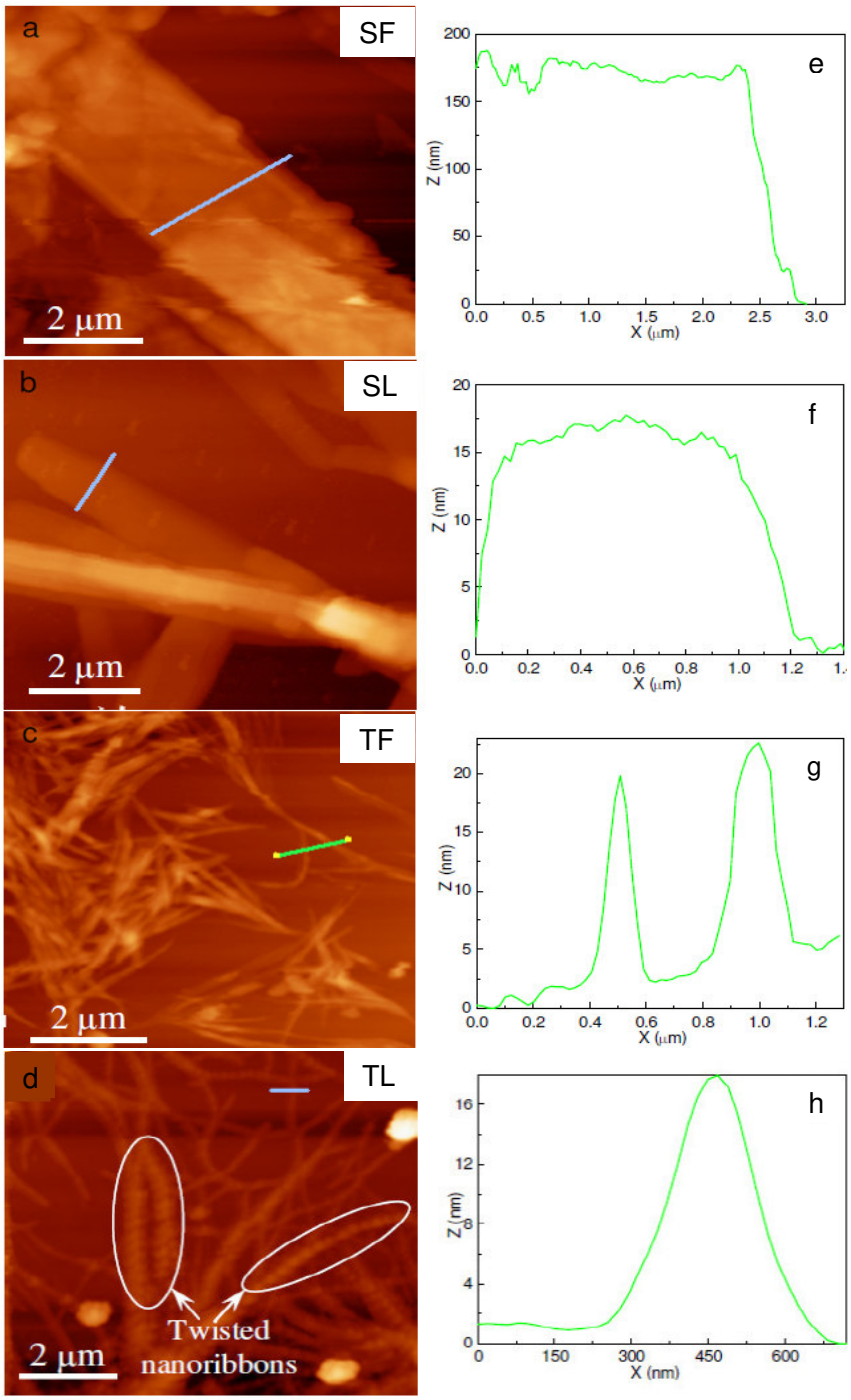

Figure A.3 Taping-mode AFM images of the Fmoc-XY-OMe peptide nanostructures on mica. (a, e). AFM image and cross section of nanosheets of Fmoc-SF-OMe, (b, f). AFM image and cross section of wide nanoribbons of Fmoc-SL-OMe gel, (c, g). AFM image and cross section of nanoribbons Fmoc-TF-OMe gel, (d, h). AFM image and cross section of nanoribbons Fmoc-TL-OMe gel.

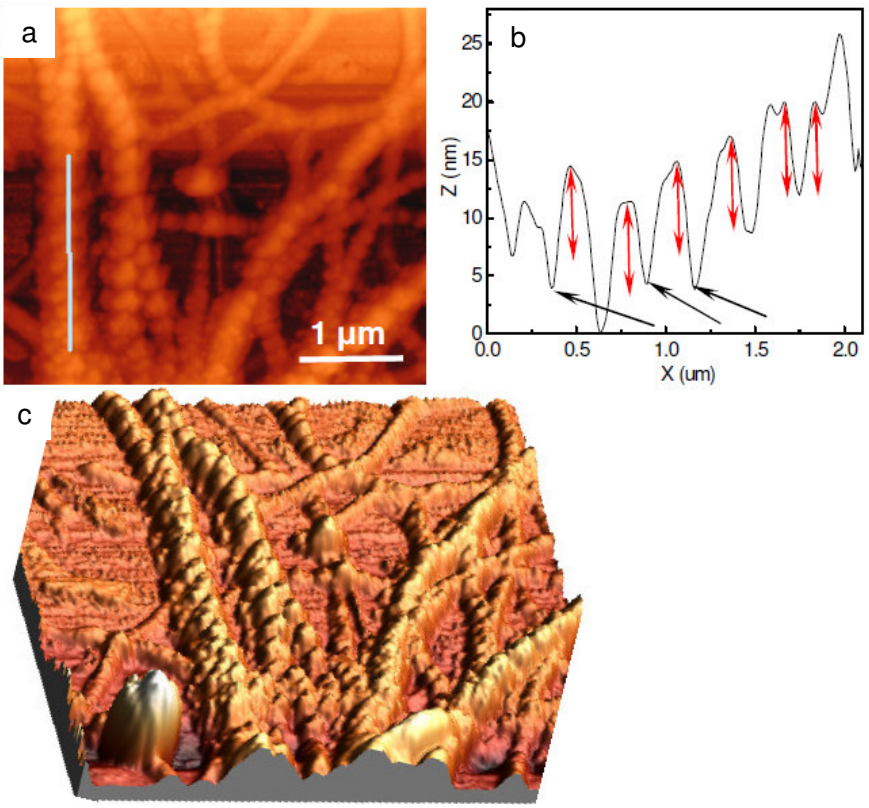

Figure A.4 Taping-mode AFM images and cross section. a, high magnification image from twisted nanoribbons of Fmoc-TL-OMe, b, cross section along one of the nanoribbons, c, 3D structure of Fmoc-TL-OMe twisted nanoribbons

A2.3.2 Dependence of structure on gelator and formation time

Aromatic ring stacking provides the basis for electrons to hop from one gelator to another within a nanostructure, giving rise to the electronic properties observed in the high-order Fmoc-peptides aggregates in Chapter 4. Whereas, electron transfer within a monomer in solution leads to the formation of excimer. Fluorescence spectroscopy was utilized to probe the production of the conjugated motif as the peptides self-assembled, allowing the self assembly process to be followed *in-situ*. The emission spectra from the Fmoc-SL-OMe, Fmoc-TF-OMe and Fmoc-TL-OMe samples are shown in Figure A.5b, c and d. In each case, a red shift and increasing emission intensity were observed over time (0, 6, 24, 40 hours and one week), indicating the formation of π–π stacking. The two peaks at around 379 nm and 398 nm most probably indicate the formation of anti-parallel and parallel dimerization of fluorenyl moieties in the hydrogel. A

broad peak at around 450 nm was found in these three hydrogels and the intensity increased with hydrogel formation time. This result indicates the formation and increasingly extended aggregates of π–π stacking. The Fmoc-SF-OMe may be minimally present in Fmoc-TF-OMe, which is possible due to a role of phenylalanine groups. Fmoc-SL-OMe and Fmoc-TL-OMe may be a different mode of assembly of the Leucine derivatives.

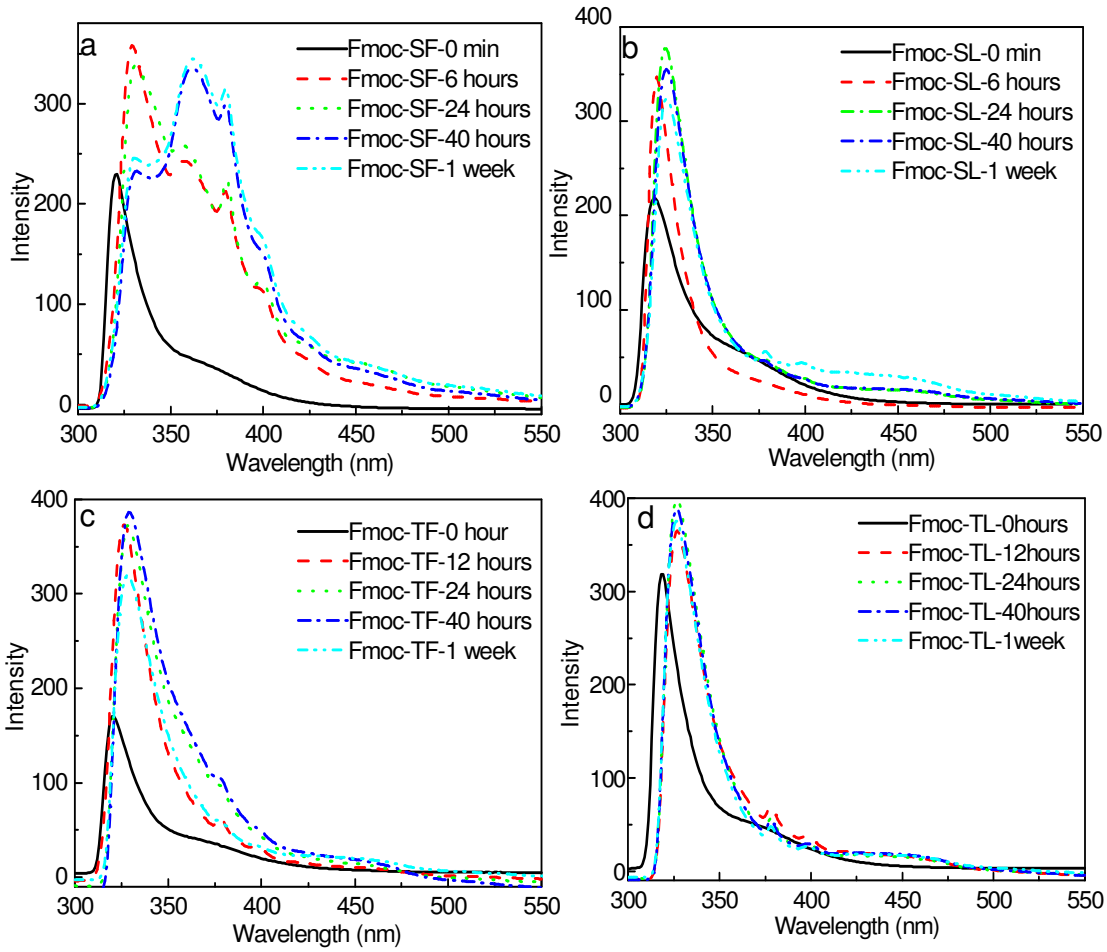

Figure A.5 Emission spectra monitored using photoluminescence spectroscopy characterization immediately after enzyme addition, at 12 hours, at 24 hours, at 40 hours and at one week, (a) Fmoc-SF-OMe, (b) Fmoc-SL-OMe, (c). Fmoc-TF-OME, (d) Fmoc-TL-OMe.

Fourier transform infrared spectroscopy (FT-IR) was used to investigate the structure of peptide nanostructures. The analysis of the nanostructures formed for 1 week from Fmoc-SF-OMe showed well-defined bands centred around 1640 cm^{-1} (CO-stretching bands) and 1685-1691 cm^{-1},

consistent with the formation of anti-parallel β–sheet structures as shown in Figure A.6.[8] The 1639 cm^{-1} peak shifted to 1654 cm^{-1} for Fmoc-TF-OMe and Fmoc-SL-OMe due to the different types of β-sheet (i.e. different bond position and environment). There is no obvious peak around 1691 cm^{-1} from Fmoc-TL-OMe, indicating no anti-parallel β-sheet.

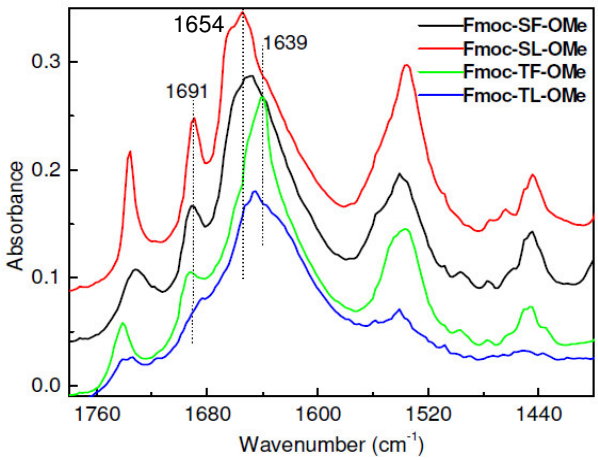

Figure A.6 FT-IR spectra of Fmoc-SF-OMe, Fmoc-SL-OMe, Fmoc-TF-OMe and Fmoc-TL-OMe gel prepared for one week, which reveal consistent evidence of anti-parallel -sheets in the hydrogels or suspension.

Wide angle X-ray scattering (WAXS) analysis of Fmoc-SF-OMe, Fmoc-SL-OMe, Fmoc-TF-OMe, Fmoc-TL-OMe film and buffer film (Figure A.7) was used to further probe their structures. Uniquely, the Fmoc-SF-OMe had a very sharp, high intensity peak at 16 Å, which is similar to the molecular length as shown in Figure A.8. Up to 5 higher orders of this reflection could be observed at spacing corresponding to d/n (n=1 to 5). These higher order reflections are expected to relate to the presence of flat nanosheets formed by the parallel stacked single nanofibres. The other systems also had a reflection corresponding to their molecular length at ~ 15 Å. However, for these systems the peak was much broader and less intense, with no higher order reflections observed.

The two reflections with spacing corresponding to d = 3.6 Å and d = 4.7 Å were observed from Fmoc-SF-OMe and Fmoc-SL-OMe (and not present in buffer salts). It is believed that these peaks relate to the π–π stacking and β-sheets (Figure A.1b and Figure A.8). However, the π–π stacking and β-sheets reflections appeared at d = 3.8 Å and d =4.2 Å respectively for the

Fmoc-TF-OMe and Fmoc-TL-OMe systems. (It should be noted that the Fmoc-TL-OMe system showed no β sheet in FTIR.) The reason for this difference between TF/TL and SF/SL systems is unclear and requires further experimental study and modelling.

The morphology and the nanostructures of Fmoc-XY-OMe are concluded in Table A.2 with details.

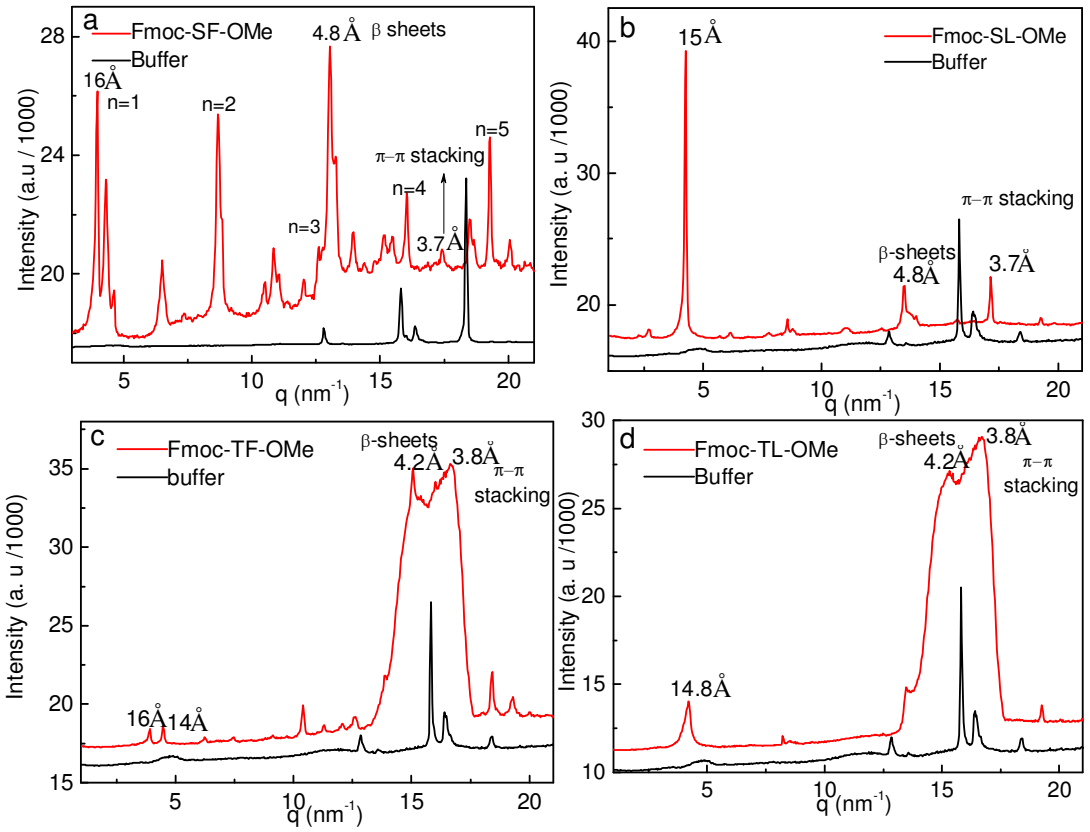

Figure A.7 Analysis of Wide Angle X-ray Scattering (WAXS) of Fmoc-peptides and buffer film on a silica a, Fmoc-SF-OMe and buffer films, b, Fmoc-SL-OMe, c, Fmoc-TF-OMe, d, Fmoc-TL-OMe. Peaks corresponding to the spacing of peptides structures within a β-sheet structure, pairs of fluorenyl groups, and the spacing between π–π stacking.

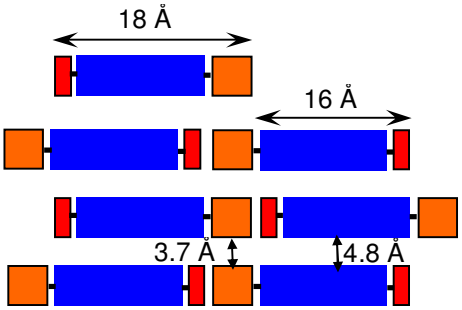

Figure A.8 Molecular lengths and spacing found from WAXS data of a dried sample (Fmoc-SF-OMe)
Yellow: Fmoc; Blue: SF; Red: OMe

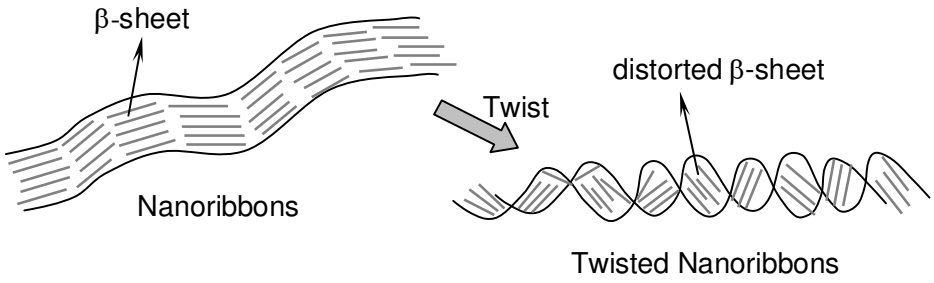

Figure A.9 Schematic representing distorted β–sheets after nanoribbons twisted.

Table A.2 Nanostructures of Fmoc-XY-OMe

Samples	AFM images	Cryo-TEM images	WAXS		FT-IR (cm^{-1})	Fluorescence
			β–sheet	π–π stacking		
Fmoc-SF-OMe	Nanosheets (Height: 160 nm)	Nanosheets (Width: 200 nm) and Twisted nanoribbons (Width: 35 nm)	4.8 Å	3.7 Å	1651; 1691	Significant red shift
Fmoc-SL-OMe	Nanoribbons (Height: 15 nm)	Nanoribbons (Width: 60 nm)	4.8 Å	3.7 Å	1654; 1691	Mini red shift
Fmoc-TF-OMe	Tightly twisted nanoribbons (Height: 20 nm)	Tightly twisted nanoribbons (Width: 25 nm)	4.2 Å	3.8 Å	1639; 1692	Mini red shift
Fmoc-TL-OMe	Twisted nanoribbons (Height: 4 nm; Twisted diameter: 16 nm)	Twisted nanoribbons (Width: 20 nm)	4.2 Å	3.8 Å	1645; 1685	Mini red shift

A2.3.3 Dependence of electrical properties on gelator and formation time

Impedance spectroscopy measurements were performed to determine the conductive behaviour of films of Fmoc-SL-OMe, Fmoc-TF-OMe, Fmoc-TL-OMe hydrogel and Fmoc-SF-OMe suspension formed from different times in vacuum with the frequency range from 0.1 to 10^7 Hz (Figure A.10). Hydrogel or suspension formed for 0 h, 6 h, 24 h, 48 h and 1 week were spread onto glass slides for the measurement. In the complex impedance plot, the diameter of the arc, (obtained under AC bias conditions) is considered to correspond to the electric resistance of the samples.[9] In this case, in the frequency range studied, only part of the arc was obtained from the impedance spectra due to the high resistance of the samples studied here. Software (Zview) was used to fit the part arc to a whole arc to evaluate the resistance of the sample. This presumably arises from delocalized electron through π–π interactions along unidirectional stacks of fluorenyl groups. The resistance values of the films formed over different time periods were lower than

those of the initial materials. Unexpectedly, as shown in Figure A.10, the resistance increased with gelation time. Fluorescence emission data suggested that the formation of unidirectional $\pi-\pi$ stacks increased as the observed increase in emission at 455 nm (Figure A.5). This suggests that the conductivity of samples with longer formation times should be higher because of the higher level of aggregation producing more $\pi-\pi$ interactions. However, the experimental results from impedance spectroscopy (Figure A.10) showed the opposite; the resistance increased with the hydrogel formation time, or the suspension formation time. The hydrogel or suspension with longer formation time contains highly organized nanostructures (nanosheets or nanoribbons) as shown in the Cryo-TEM and AFM images in Figure A.2, A.3 and A.4. The author suspected that the nanostructures were broken when the gel was spread onto the glass slide and dried for examination; and the hydrogel or suspension with shorter formation times were reorganized during glass slide transfer and drying, thus producing the unexpected higher resistances of the longer period samples.

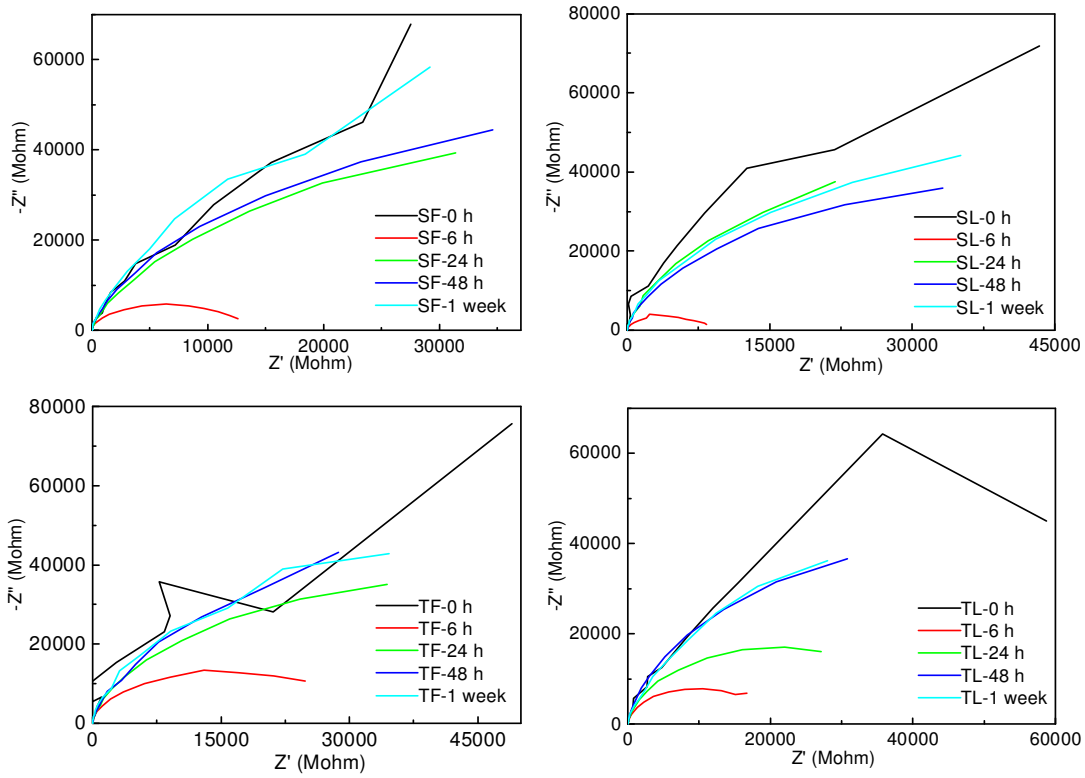

Figure A.10 Complex impedance plot data of 100 µL hydrogel films which have spent different times under vacuum between a frequency range from 0.1 to 10^7 Hz. (suspension formed for 0, 6, 24, 40 hours and one week was spread onto glass, then dried to form film): a, Fmoc-SF-OMe, b, Fmoc-SL-OMe, c, Fmoc-TF-OMe, e, Fmoc-TL-OMe.

The relative resistances of the films formed form different gelators within a 6 hour formation time were found to be: Fmoc-SF-OMe < Fmoc-SL-OMe < Fmoc-TL-OMe < Fmoc-TF-OMe, as shown in Figure A.11. Therefore, Fmoc-SF-OMe had a slightly higher conductivity compared with the other samples. It is possible that the electron transfer is variable between different types of nanostructures. The Fmoc-SF-OMe has a higher conductivity value because it forms nanosheets more easily than other structural types, i.e. it provides more highly conductive pathways with electrons flowing more freely along the nanosheets, instead of having to jump between multiple nanoribbons. More work would be needed to prove this.

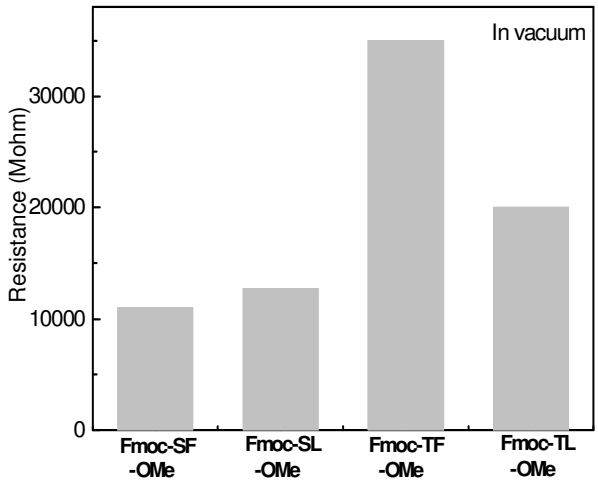

Figure A.11 Comparison of resistance of films formed from hydrogel or suspension with 6 h formation time (Fmoc-SF-OMe, Fmoc-SL-OMe, Fmoc-TF-OMe and Fmoc-TL-OMe).

A2.3.4 Further investigation of Fmoc-SF-OMe nanosheets

A2.3.4.1 Fmoc-SF-OMe film from suspension

Fmoc-SF-OMe was studied further to see if the microstructure of the film could be controlled. As discussed earlier, two kinds of nanostructures were observed under Cryo-TEM. The films were formed from Fmoc-SF-OMe suspension prepared at different temperatures (0 ℃, 20 ℃ and 55 ℃ respectively). The maximum temperature is 55 ℃ due to the enzyme's highest activity at 50 - 55 ℃.[10]

Fmoc-S, F-OMe and thermolysin were dissolved in buffer solution and deposited into three vials, which were placed into different temperatures for different times:

(i) 0 ℃ for 2 days

(ii) 20 ℃ for 2 days

(iii) 55 ℃ for 5 hours.

The three resultant suspensions were then deposited onto glass slides to form dry films at room temperature. The films were labelled as SF-0-Gel, SF-20-Gel, and SF-55-Gel depending on the formation temperature of suspension.

Scanning electron microscopy (SEM) was used to examine the microstructure of the resultant Fmoc-SF-OMe films. Figure A.12 shows the SEM images of microstructure pattern from SF-0-Gel film. The film was covered by spherulites (the red circles in Figure A.12a), which were formed by nanosheets or nanoribbons as shown on the spherulite at the high magnification in Figure A.12b. In the non-spherulite area, both random and crystalline nanosheets appeared (circled in red and blue respectively (Figure A.12c). In addition, a large number of sheets were formed on the bottom of the film (see black arrow in Figure A.12d). The sheets were separated, forming a gap shown at the white rectangle line in Figure A.12d, which could also be found in Figure A.12a, arrowed in white. The gaps could possibly be related to a reduction in conductivity, which will be explained later.

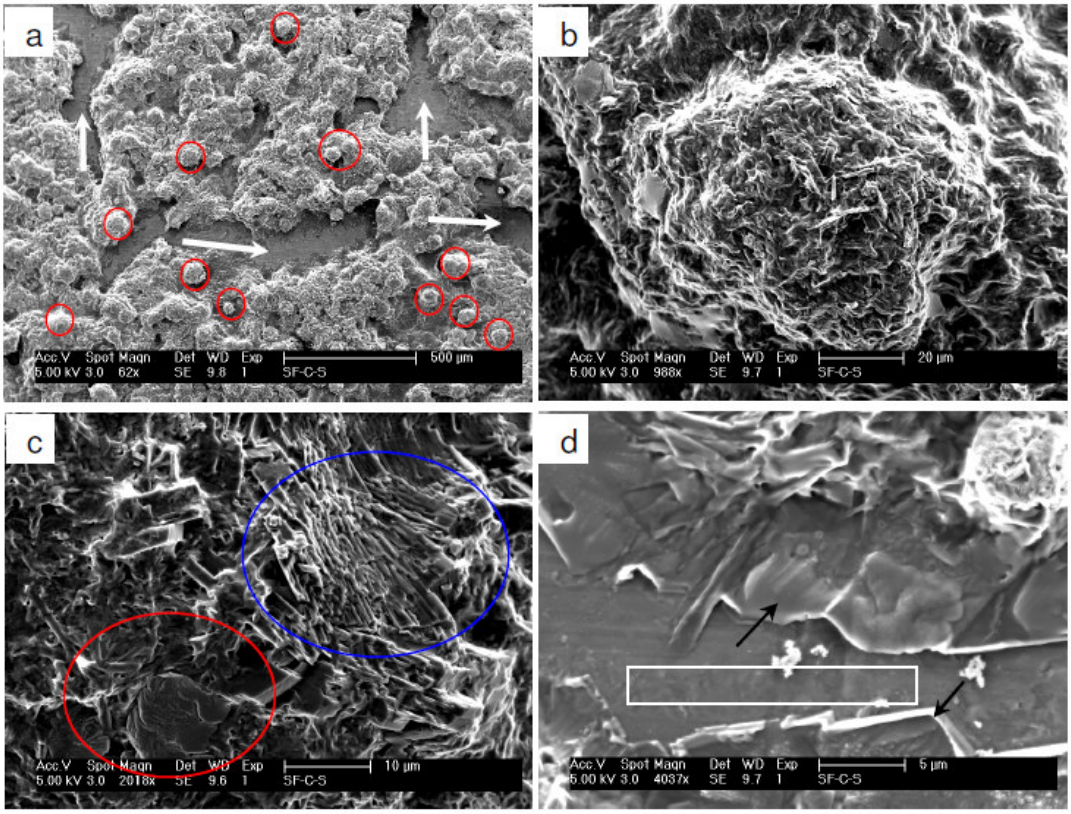

Figure A.12 SEM images of SF-0-Gel film. a, low magnified view of the film covered with spherulites, b, high magnified view of the spherulite, c, high magnified view of the surface of non-spherulite area, d, micro-sheets in the bottom of the film.

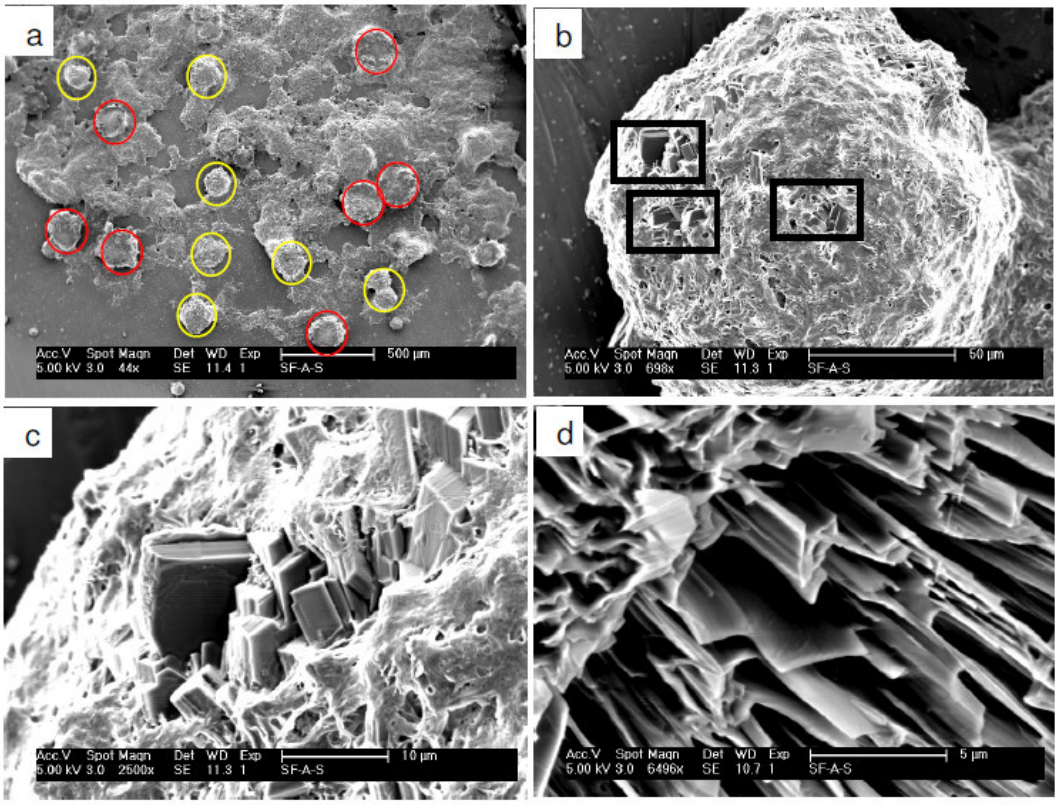

Figure A.13 SEM images of SF-20-Gel film. a, low magnified view of the film covered with spherulites and broken spherulites, b, high magnified view of a whole spherulite, c, high magnification of one point on the spherulite (b), d, high magnified view on the surface of the non-spherulite area.

The microstructure of SF-20-Gel was similar to the SF-0-Gel and contained spherulites (as highlighted by yellow circles in Figure A.13a). Fortunately a few spherulites were fractured (highlighted in red in Figure A.13a) allowing their internal structures to be analysed. The crystalline sheets appeared to grow from their cores, layer by layer, outwards after nucleation initiates as shown in Figure A.14c. The high magnification image in Figure A.14d shows small crystals in the core of the spherulite. Cracks in the films revealed that the spherulites sat on a surface structure of random ribbons and sheets, beneath which were aligned ribbons (Figure A.14b, c). The ordered crystalline sheets (Figure A.13d) had a thickness and width around 500 nm and 5 µm, respectively. It is believed that the difference in the structures of the two samples, in particular the formation of the large sheets, is due to the gelation temperature given that this was the only variable that changed.

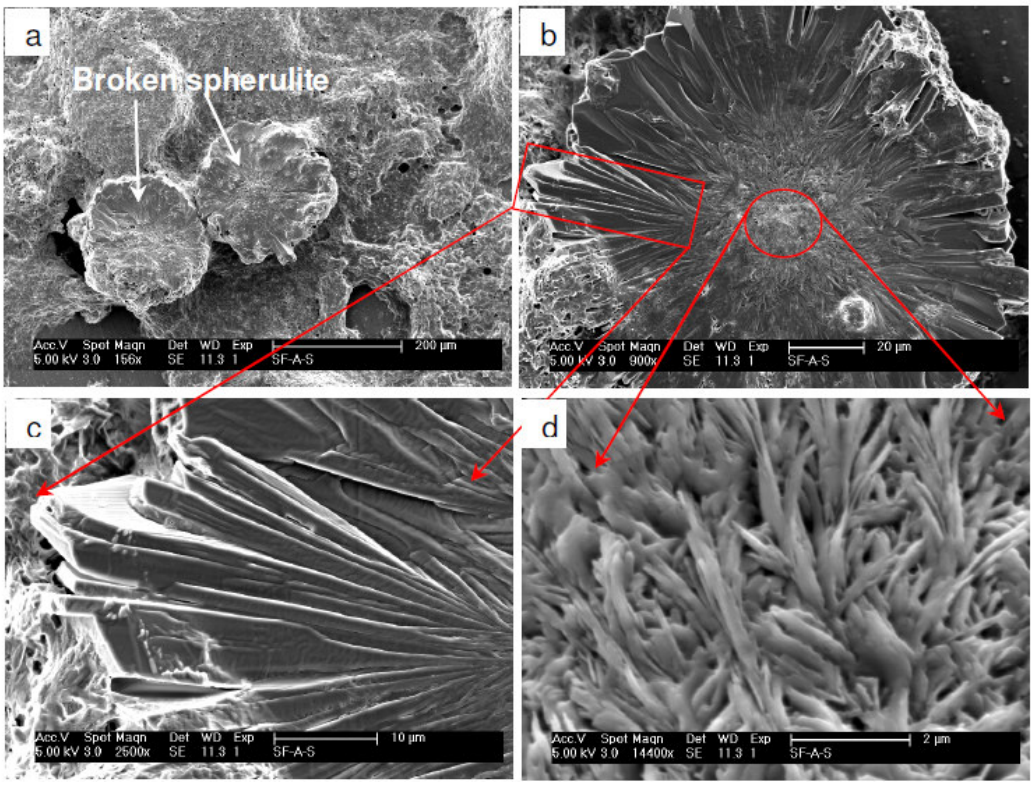

Figure A.14 SEM images of SF-20-Gel film. a, a broken spherulite, b, high magnification of the broken spherulite, c, high magnification of part inside in the broken spherulite, d, high magnified view of the core in the broken spherulite.

The Cryo-TEM showed that the Fmoc-SF-OMe molecules initially self-assembled into nanosheets or nanoribbons in the suspension (Figure A.2a), whereas the SEM of the dried films showed spherulite-like structures (Figure A.12 and A.13). The general process of spherulite formation, consistent with our experimental observation, appears to be: firstly, nanosheets and nanoribbons are assembled in solution (suspension); secondly, the diffusion, subsequent ordering and growth of nanosheets create the spherulite patterns.

In order to fully understand the growth mechanism, a film formed from Fmoc-SF-OMe suspension (SF-55-Gel) was studied. Figure A.15a shows SEM images of SF-55-Gel film, which display the similar spherulites on the film's surface as the SF-0-Gel and SF-20-Gel. A number of fibres with diameter less than 200 nm were formed on the edge of the film in Figure A.15b. It is believed that the concentration of the nanostructures (nanosheets and nanoribbons) on the film's edge is lower than the centre, resulting in insufficient fibres to form the spherulites. As a result, the nanoribbons

self-assembled to form nanofibrous networks. However, a large number of fibres with diameter of around 1 μm and sheets were formed at the high concentration area in the centre of the film as shown in Figure A.15c, confirming the above supposition, with the spherulites patterns forming at even higher concentration in the very centre of the film. The large size sheets with areas around 200 μm^2 were also found in this higher temperature sample (Figure A.15d).

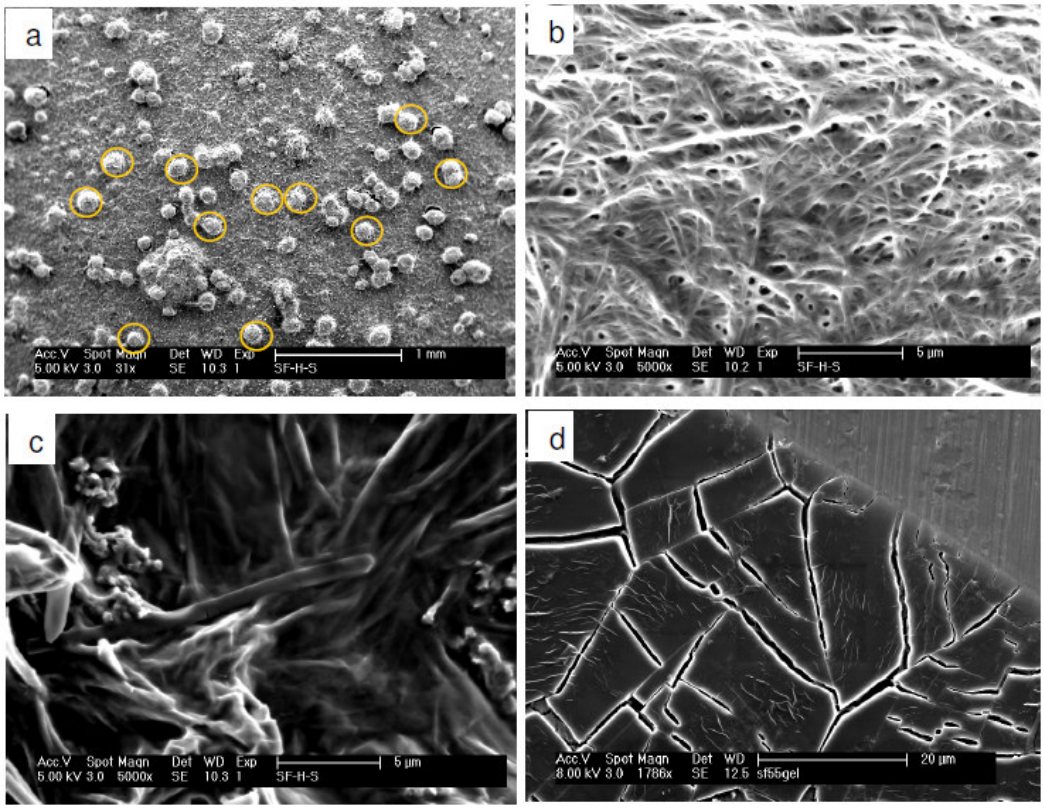

Figure A.15 SEM images of SF-55-Gel film. a, low magnified view of the film covered with spherulites, b, the edge of the nanoribbon film, c, image from the surface without spherulites on the film, d, large sheets on the surface from part of the film without spherulites.

Many surface spherulites were shown in Figure A.15a. A magnified view of a single spherulite was obtained to study the finer detail (Figure A.17a). This spherulite had been assembled, surrounded by a large amount of rigid crystalline ribbons displayed at higher magnification in Figure A.17b. These images indicated how the crystalline spherulite grow from the core. In addition, some spherulites were covered by random ribbons or sheets as shown in Figure A.17 c and d.

Finally, these crystalline spherulites were found to be birefringent under polarized optical microscopy between crossed polarizers (FigureA.16), as found for other spherulite systems.

A plausible process of spherulites formation[11] based on a series of Cryo-TEM, AFM and SEM experimental is shown in Figure A.18 and described below:

1. Reversed hydrolysis process - Fmoc-S and F-OMe were coupled into Fmoc-SF-OMe by thermolysin assistance;

2. Suspension formation process - Nanosheets and nanoribbons were self-assembled by Fmoc-SF-OMe via lateral π–π interlocking of beta sheets. This results in formation of a white suspension state as shown in Figure A.2a and Figure A.3a, e;

3. Drying process on glass slide - Nanosheets or nanoribbons aggregated together from random, small crystalline structures as nucleation initiates in Figure A.14d;

4. Growth under drying conditions - the small crystalline structures centre grows into a spherulite surrounded by crystalline ribbons with diameter around 100 μm, when the nanosheets or nanoribbons attach together at very high concentration as shown in Figure A.14b, c and A.17a, b;

5. Some spherulites were covered by random sheets or ribbons as shown in Figure A.13b, c, while some spherulites had no random structures covered such as Figure A.17a.

Figure A.16 Cross polarized optical microscopy images of SF-55-Gel film in reflectance.

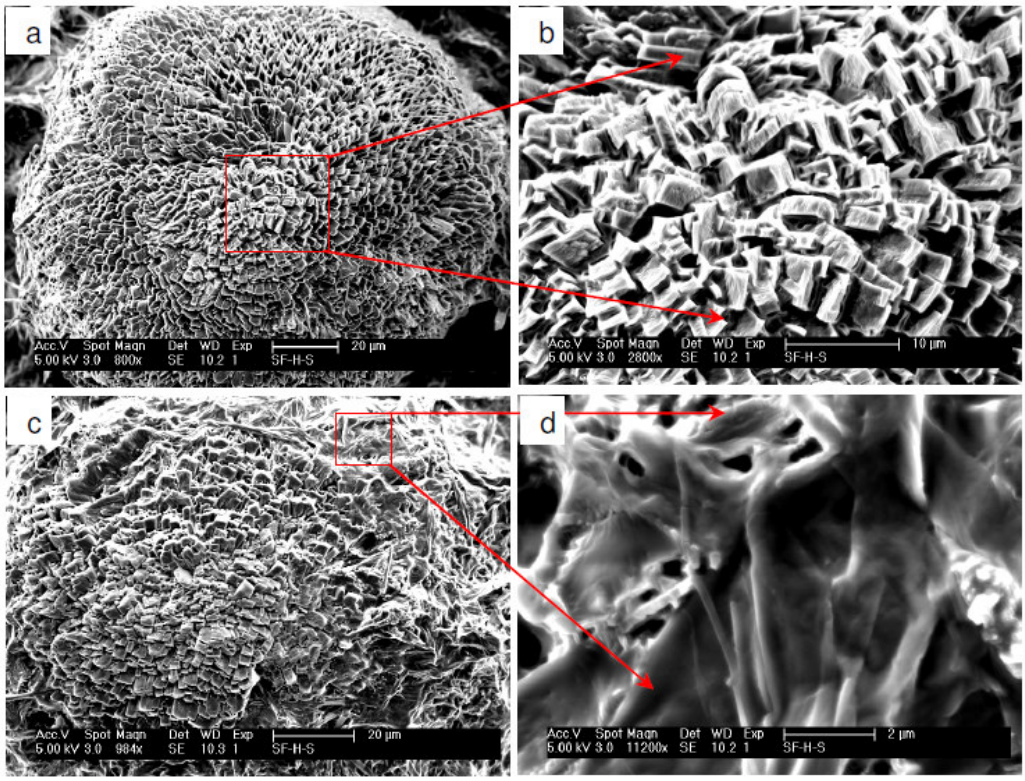

Figure A.17 SEM images of SF-55-Gel film. a, one of the spherulites surround with crystalline ribbons on the film, b, high magnification of the aligned ribbons, c, a spherulites surround with crystalline ribbons but part covered with random sheets, d, high magnified view of the random sheets.

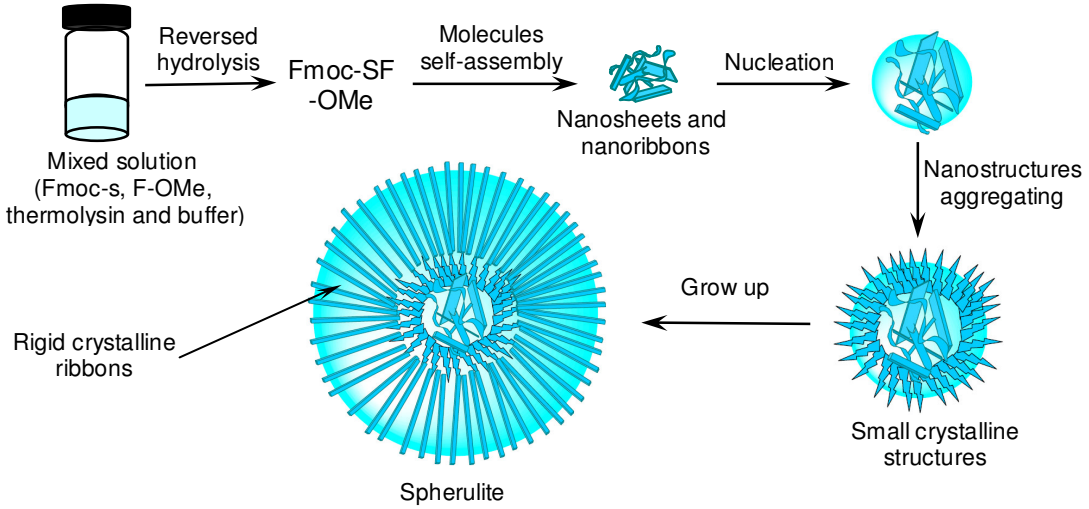

Figure A.18 Diagram of spherulite formation process from mixed solution to Fmoc-SF-OMe, to nanosheets and nanoribbons, to spherulite.

The conductivity of the films formed from 50 μL of Fmoc-SF-OMe suspension was measured by impedance spectroscopy as shown in Figure A.19. Here, the conductivity of the films was measured in air instead of vacuum, due to these samples being easy to dry. The area between the two electrodes was 12 mm × 1 mm. The relative resistances of the films from 50 μL suspension were: SF-20-Gel < SF-0-Gel < SF-55-Gel. A series of resistance measurements are shown in Figure A.20. It is apparent from this figure that the resistances of the films are unstable and massive, which may be due to the gaps between the microstructures shown in Figure A.12a, d and Figure A.15d.

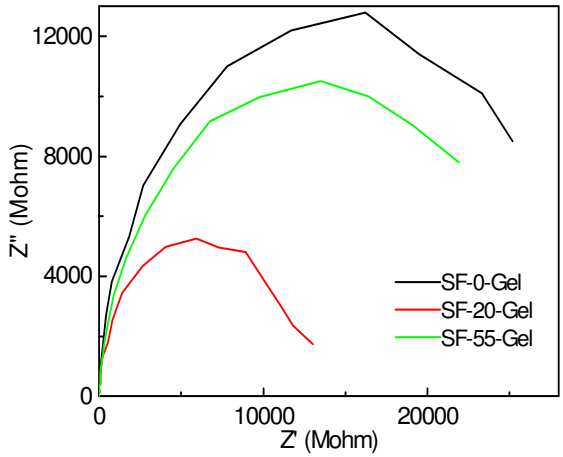

Figure A.19 Impedance plot of film SF-0-Gel, SF-20-Gel and SF-55-Gel from 50 μL suspension.

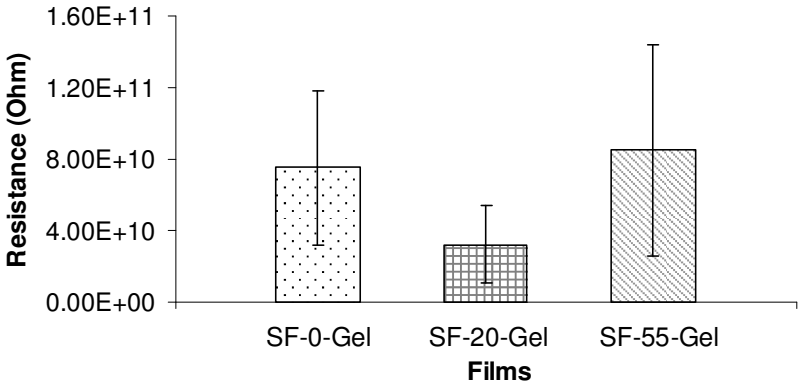

Figure A.20 Resistances of a series of films SF-0-Gel, SF-20-Gel and SF-55-Gel from suspension

A2.3.4.2 Fmoc-SF-OMe film from solution

In order to improve the conductivity, the films were prepared by directly depositing the peptides and enzyme onto the slide rather than an aged suspension. It was decided to do this at 20 ℃ since the SF-20-Gel was found in the last section to have the best conductivity, despite all the samples, including SF-20-Gel, possessing a very high resistivity (Figure A.20).

Fmoc-S, F-OMe and enzyme (thermolysin) were dissolved in buffer, which was spread onto a glass slide to form a film directly in air at room temperature (20 ℃) (labelled SF-20-Sol). Figure A.21 shows the SEM images of the resultant SF-20-Sol film. Interestingly, no spherulites were observed, despite their prevalence in the SF-20-Gel samples. Scratching the film found crystalline ribbons under the film surface, (Figure A.21a). Figure A.21b shows a higher magnification view of the rigid crystalline ribbons. The rigid ribbons were ~ 1 μm thick and ~ 10 μm wide and appeared to be formed from layers of nanosheets or nanoribbons (red arrow in Figure A.21b). A possible mechanism for the crystal growth is described as follows:

1. The mixed solution forms suspension by self-assembly;
2. The micro-structure develops during drying process in Figure A.20, which included both random sheets and ribbons on the surface and crystalline rigid ribbons beneath the surface. It is also possible that nanosheets and nanoribbons sank beneath the sample's surface due to gravity, as there was very low nanostructure concentration on the film's

surface. This would help to explain the random surface microstructure on the surface, and the crystalline ribbons formation below the surface due to the higher concentration.

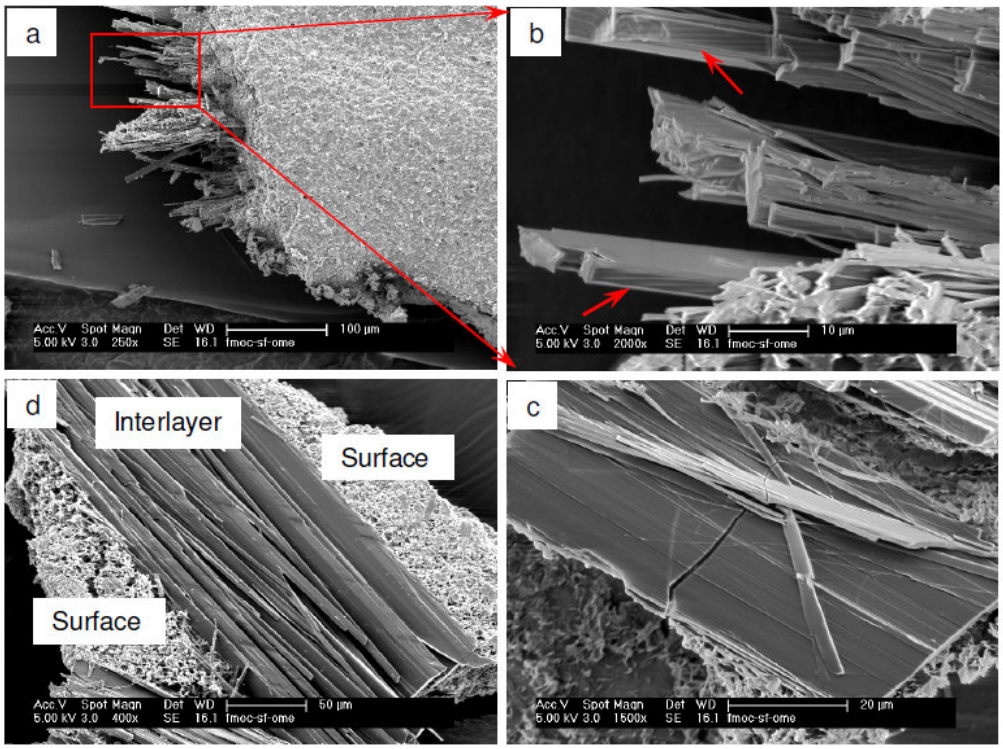

Figure A.21 SEM images of film SF-20-Sol. a, scratch line on the film showing straight crystalline ribbons beneath the surface, b, high magnification view of the crystalline ribbons, c, a piece of the film including both random surface and crystalline sheets, d, a slice of large sheet in the middle layer of the film.

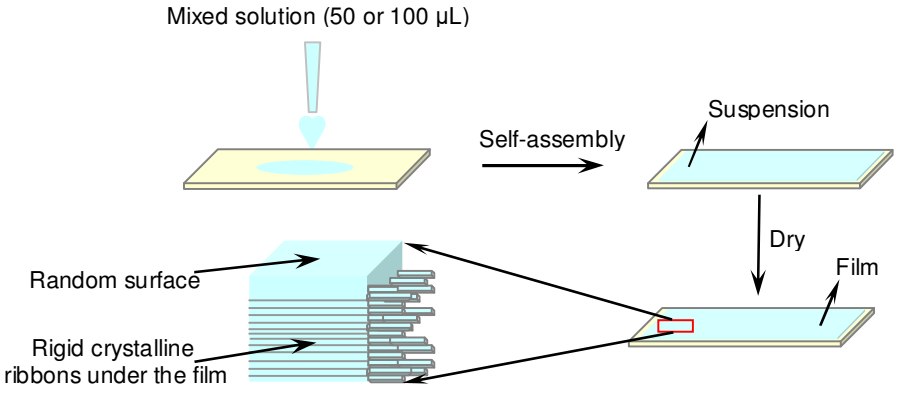

Figure A.22 Diagram of the formation process of the film from mixed solution directly.

The conductivity of the SF-20-Sol film was also measured by impedance spectroscopy to make a comparison with SF-20-Gel film (Figure A.23). The area between two measurement electrodes was 12 mm × 1 mm. Several samples were measured to detect the stability and reproducibility of the measurements (Figure A.24). Also, the conductivity of SF-20-Sol is lower than SF-20-Gel, possibly due to the top surface of the film which is in contact with the electrodes being appreciably different from the bottom surface in Figure A.21.

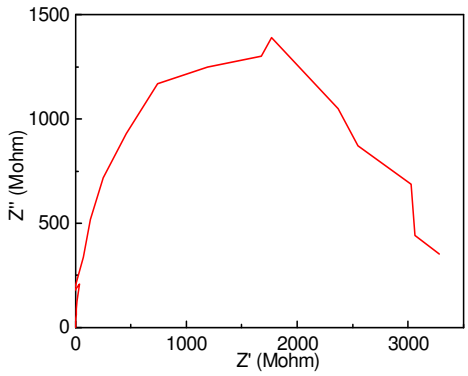

Figure A.23 Impedance plot of a film made from 50 µL volume mixed solution of SF-20-Sol.

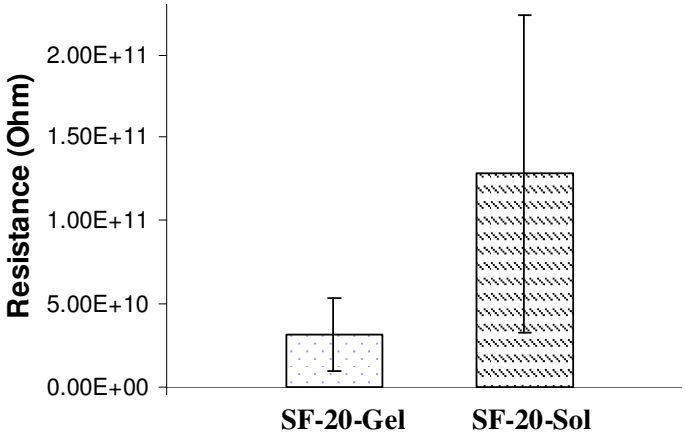

Figure A.24 Comparison of resistance between film SF-20-Gel and SF-20-sol.

A2.4 CONCLUSIONS

In conclusion, the use of reversed hydrolysis reactions assisted by enzyme action was demonstrated to induce self-assembly of peptides units through thermodynamic control. The nanostructures of Fmoc-SF-OMe, Fmoc-SL-OMe, Fmoc-TF-OMe and Fmoc-TL-OMe were

studied by spectra, Cryo-TEM and AFM, which show nanosheets, nanoribbons and twisted nanoribbons (Table A.2). It is clear that more stable peptide self assemblies demonstrate more significant overall shifts in emission spectra. WAXS was also used to detect crystal structure information in detail. Impedance spectra were used to characterize the conductivity of the peptides nanostructures which had to be left in gel for various times. The resistances of the films are high and random. These were explained by the nanostructures being initially broken down by the physical action of depositing hydrogel or suspension.

Fmoc-SF-OMe suspension was studied further because it has a slightly higher conductivity and some interesting nanostructures, including nanoribbons and sheets, as well as spherulites (Table A.3). Different Fmoc-SF-OMe films were prepared from suspension at various temperatures: 0 ℃, 20 ℃ and 55 ℃ (SF-0-Gel, SF-20-Gel and SF-55-Gel), a range chosen in view of the enzyme's (thermolysin) activity. Films formed from various conditions have different structures and conductivity (Table A.3). Spherulites with diameter around 100 μm were formed on the surface of the films, in which formation process mechanism was proposed.

The conductivity of the films formed from suspension was measured by impedance, revealing an unstable resistance pattern. SF-20-Gel obtained the best conductivity among SF-0-Gel, SF-55-Gel (Table A.3). The temperature of film SF-20-Gel formation was the same as when suspension produced. However, resistivity of SF-20-Gel was lower than SF-20-Sol, maybe due to the random surface structure of the film SF-20-Sol.

Table A.3 Summary of all films with conditions, structures and resistance

Films	Formation temperature (℃)	Film precursor	Film structure	Sheet resistance (MΩ/sq)
SF-0-Gel	0	Suspension [a]	Spherulites, random and crystalline nanosheets	9.0×10^5
SF-20-Gel	20	Suspension [a]	Spherulites, crystalline sheets and random ribbons	3.8×10^5
SF-55-Gel	55	Suspension [a]	Spherulites and random sheets	1.0×10^6
SF-20-Sol	20	Mixed solution [b]	Rigid crystalline ribbons	1.5×10^6

[a]: Suspension: Fmoc-S, F-OMe and thermolysin were dissolved in buffer solution, then put in the right temperature shown in the table for two days to form suspension. [b]: Mixed solution: Fmoc-S, F-OMe and thermolysin were dissolved in buffer solution to form mixed solution.

A2.5 REFERENCES

1. S. Toledano, R. J. Williams, B. Jayawarna, R. U. Ulijn, Enzyme-triggerd slef-assembly of peptide hydrogels via reversed hydrolysis, J. Am. Chem. Soc. 2005, 128, 1070-1071.
2. R. J. Williams, A. M. Smith, R. Collins, N. Hodson, A. K. Das and R. V. Ulijn, Enzyme-assisted self-assembly under thermodynamic control, Nature nanotechnology, 4, 2009,19-24.
3. A. K. Das, A. R. Hirst and R. V. Ulijn, Evolving nanomaterials using enzyme-driven dynamic peptide libraries (eDPL), Faraday Discuss, 2009, 143, 293-303.
4. A. M. Smith, R. J. Williams, C. Tang, P. Coppo, R. F. Collins, M. L, Turner, A. Siani and R. V. Ulijn, Fmoc-Diphenylalanine self-assembles to a hydrogel via a novel architecture based on π-π interlocked β-sheets, Adv. Mater., 2007, 1-5.
5. T. Forster, Excimers, Angew. Chem. Int. Ed., 1969, 8, 333-343.
6. D. Schweitzer, K. H. Hausser, M. W. Haenel, Transanular interaction in [2.2] (4,4') diphenylophane and [2.2] (2,7) fluorenophane, Chem. Phys., 1978, 29, 181-185.
7. Z. Yang, H. Gu, D. Fu, P. Gao, J. K. Lam and B. Xu, Enzymatic formation of supramolecular hydrogels, Adv. Mater., 2004, 16, 1440-1444.
8. A. Aggelli, et al. Responsive gels formed by the spontaneous self-assembly of peptides into polymeric β-sheet tapes. Nature 1997, 386, 259-262.
9. T. Yamamoto, A. Ushiro, I. Yamaguchi and s. Sasaki, Synthesis, structure, and chemical

properties of lithium salts of poly(2-methoxyaniline-5-sulfonic acid), Maromolecules, 2003, 36, 7075-7081.

10. Elena V. Kudryashova, Vadim V. Mozhaev, Claude Balny, Catalytic activity of thermolysin under extremes of pressure and temperature: modulation by metals ions, Biochimica et Biophysica Acta. 1386, 1998, 199-210.
11. W. Wang, Y. Chau, Self-assembled peptide nanorods as building blocks of fractal patterns, Soft Matter, 2009, 5, 4845-5048.